TECHNISCHE MECHANIK

Editor:
Magdeburger Verein für Technische Mechanik e.V.
und Otto-von-Guericke-Universität Magdeburg

Volume 39 Issue 1 (2019)

ISSN 0232-3869 (print)
ISSN 2199-9244 (online)

TECHNISCHE MECHANIK

Wissenschaftliche Zeitschrift für Grundlagen und Anwendungen der Technischen Mechanik
Scientific Journal for Fundamentals and Applications of Engineering Mechanics

The journal **Technische Mechanik** publishes refereed original articles on Engineering Mechanics in its broadest sense. It is intended to provide a forum for a rapid transfer of research results to industry and science. In that sense contributions are encouraged which demonstrate the practical application of new results and scientific findings.

In der **Technischen Mechanik** werden begutachtete Beiträge aus allen Gebieten der Mechanik publiziert. Ein Hauptanliegen besteht in der raschen Verfügbarmachung von Forschungsergebnissen für Industrie und Wissenschaft. In diesem Sinne werden vor allem auch solche Beiträge bevorzugt, die neben neuen Ergebnissen und Erkenntnissen auch deren praktische Anwendung beinhalten.

Editorial Board / Herausgeberkollegium:

Holm Altenbach (Magdeburg)
Albrecht Bertram (Magdeburg)
Daniel Balzani (Bochum)
Stefan Diebels (Saarbrücken)
Paweł Dłużewski (Warsaw)
Sascha Duczek (Sydney)
Christoph Egbers (Cottbus)
Victor Eremeyev (Gdansk)
Samuel Forest (Paris)
Michael I. Friswell (Bristol)
Ulrich Gabbert (Magdeburg)
Daniel Juhre (Magdeburg), editor-in-chief
Richard Markert (Darmstadt)
Reinaldo Rodriguez (Havanna)
Miroslav Šilhavý (Prague)
Paul Steinmann (Erlangen-Nuremberg)
Jens Strackeljan (Magdeburg)
Bob Svendsen (Aachen)
Dominique Thévenin (Magdeburg)
Kerstin Weinberg (Siegen)
Elmar Woschke (Magdeburg)

Copyright
Submission of a manuscript implies that the work described has not been published before (except in the form of an abstract or as part of a published lecture, review, or thesis); that it is not under consideration for publication elsewhere; that its publication has been approved by all co-authors, if any, as well as by the responsible authorities at the institute where the work has been carried out. The authors hold and retain the copyright of their papers. They grant the journal the non-exclusive right to publish the papers.
All articles published in this journal are protected by copyright. No material may be reproduced or copied without prior written permission of the copyright holder, except for personal use only.

Urheberrecht
Voraussetzung für die Einreichung eines Manuskriptes an die Redaktion der Zeitschrift ist, dass die Arbeit noch nicht publiziert oder an anderer Stelle zur Publikation eingereicht wurde. Ferner wird vorausgesetzt, dass die Publikation von allen beteiligten Autoren einer Arbeitsgruppe genehmigt ist und dass die Arbeit, wenn sie zur Publikation angenommen wurde, nicht an anderer Stelle in gleicher Form publiziert wird.
Die Urheberrechte für die Artikel liegen bei den jeweiligen Autoren. Sie gewähren der Zeitschrift das nicht-exklusive Recht der Veröffentlichung.
Die Zeitschrift sowie alle in ihr enthaltenen einzelnen Beiträge und Abbildungen sind urheberrechtlich geschützt. Jede Verwertung, die nicht ausdrücklich vom Urheberrechtsgesetz zugelassen ist, bedarf der vorherigen schriftlichen Zustimmung der Rechteinhaber. Ausgenommen sind Kopien für den persönlichen Gebrauch.

Redaktion/Editorial Office
W. Lenz (Chefredakteur)

Bezugsmöglichkeiten

Die Zeitschrift Technische Mechanik erscheint ab dem Jahr 2019 ausschließlich in elektronischer Form. Die Zeitschrift Technische Mechanik ist ein Open Access Journal. Alle Artikel können kostenfrei von unserer Webseite herunter geladen werden.
Für Veröffentlichungen fallen für die Autoren keine Kosten an. Alle Artikel werden einem standardmäßigen Begutachtungsprozess unterzogen.

The journal Technische Mechanik is distributed only electronically with the beginning of 2019. The journal Technische Mechanik is an Open Access journal. All papers are available free of charge for download. Publishing of papers is free of any costs for the authors. Each submitted paper runs through a standard peer review process.

Anschrift der Redaktion/Editorial Office
Redaktion Technische Mechanik
Institut für Mechanik
Otto-von-Guericke-Universität
Postfach 4120
D-39016 Magdeburg
Telefon: +49 391 67–52 459
Telefax: +49 391 67–12 439/–12 863
e-mail: Technische.Mechanik@ovgu.de
http://www.ovgu.de/techmech/

Herausgeber/Publisher
Magdeburger Verein für Technische Mechanik e.V.
und Otto-von-Guericke-Universität Magdeburg
Geschäftsführender Herausgeber: D. Juhre
Stellvertr. geschäftsführender Herausgeber: E. Woschke

Inhalt / Contents

ISSN 0232-3869 (print)
ISSN 2199-9244 (online)

Preface

This volume of *Technische Mechanik* contains selected papers presented at CMFF18, the 17th event of the international conference series on fluid flow technologies now called Conference on Modelling Fluid Flow. This conference took place in Budapest between Sept. 4th and Sept. 7th, 2018, with more than 120 participants from over 25 countries. The next conference is scheduled for September 2021. Please bookmark http://www.cmff.hu if you want to be kept informed.

As reflected in its title, this conference covers many fields of fluid mechanics. Key results from theoretical, numerical, as well as experimental studies have been presented in Budapest, with some of the most significant papers being invited to special issues. Articles dealing with turbomachines are being published separately in the International Journal of Turbomachinery, Propulsion and Power. The present special issue covers the following topics:

- Complex fluids
- Turbulence
- Multiphase flows
- Flows with heat transfer
- Reacting flows

We hope that you enjoy reading the content!

Dominique Thévenin, János Vad, Csaba Horváth, and Gábor Janiga

DOI: 10.24352/UB.OVGU-2019-002 TECHNISCHE MECHANIK, 39, 1, (2019), 3 – 15
submitted: September 4, 2018

Ferrofluid Flow in the Presence of Magnetic Dipole

G. Bognár, K. Hriczó

The aim of this paper is to introduce new results on magneto-thermomechanical interaction between heated viscous incompressible ferrofluid and a cold wall in the presence of a spatially varying magnetic field. Similarity transformation is applied to convert the governing nonlinear boundary layer equations into coupled nonlinear ordinary differential equations. This system is numerically solved using higher derivative method. The effects of governing parameters corresponding to various physical conditions are investigated. Numerical results are represented for distributions of velocity and temperature, for dimensionless wall skin friction and for heat transfer coefficients. Two bifurcate solutions have been obtained and one of the two solutions compares well with previous studies.

1 Introduction

During the last several decades, liquids are intensively investigated by various researchers due to their numerous applications in industry. One of them is the nanofluid, a homogenous combination of base fluid and nanoparticles. These suspensions are prepared with various metals or non-metals e.g., aluminium (Al), copper (Cu), silver (Ag), and graphite or carbon nanotubes respectively, and the base fluid, which includes water, oil or ethylene glycol, glycerol, etc. Ferrofluid is a special type of nanofluid. Magnetic fluids, also called ferrofluids, are stable colloidal suspensions of non-magnetic carrier liquid containing very fine magnetized particles, for example magnetite, with diameters of order 5-15 nm (see Papell (1965)). Ferrofluids are useful for retaining dust from the drive shafts of the magnetic disk drive. Furthermore, these fluids are used in enhancing the heat transfer rate in numerous materials and liquids in the industry.

Nanofluids can be used in many areas in our daily lives and technological processes. Such type of applications includes heat exchanger, vehicle cooling, nuclear reactor, cooling of electronic devices. The magneto nanofluids are also very much helpful in magnetic drug targeting in cancer diseases, hyperthermia, wound treatments, removal of blockage in the arteries, magnetic resonance imaging (MRI) etc. (see Bhatti et al. (2016)).

When magnetizable materials are subjected to an external magnetizing field **H**, the magnetic dipoles or line currents in the material will align and create a magnetization **M**.

Problem of magnetohydrodynamic (MHD) flow near infinite plate has been studied intensively by a number of researchers (see, e.g., Abel and Mahesha (2008), Adiguzel and Atalik (2017), Andersson and Valnes (1988), Bognár (2016a), Bognár (2016b), Siddheshwar and Mahabaleshwar (2005)). Andersson (1992) investigated the heat transfer rate in ferromagnetic fluids. The hydrodynamic flow of MHD fluids was studied when the applied transverse magnetic field is assumed to be uniform.

In recent years various theoretical models have been put forward to study the continuum description of ferrofluid flow. Most of the analytical studies concerning the motion of ferrofluids are based on the formulation given by either Neuringer and Rosensweig (1964) or Shliomis (2004). Neuringer and Rosensweig developed a model, where the effect of magnetic body force was considered under the assumption that the magnetization vector **M** is parallel to the magnetic field vector **H**.

Andersson and Valnes (1988) extended the so-called Crane's problem by studying the influence of the magnetic field, due to a magnetic dipole, on a shear driven motion, on a flow over a stretching sheet of a viscous non-conducting ferrofluid. It has been shown that the effect of the magnetic field is a slowing of the fluid movement compared to the hydrodynamic case. Abraham and Titus (2011) concluded that the presence of heat source (or sink) controls the effect of the magneto-thermomechanical interaction, which decelerates the flow along the stretching

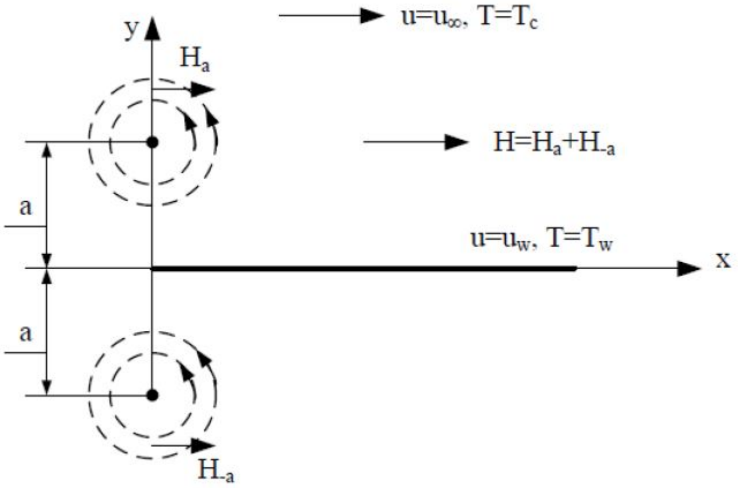

Figure 1: Parallel flow along a cold flat sheet in the presence of magnetic field due two line currents

sheet, thereby influence on the heat transfer rate. Zeeshan et al. (2016) investigated the effects of magnetic dipole and thermal radiation on the flow of ferromagnetic fluid on a stretching sheet.

Neuringer (1966) has examined numerically the dynamic response of ferrofluids to the application of non-uniform magnetic fields with studying the effect of magnetic field on two cases, the two-dimensional stagnation point flow of a heated ferrofluid against a cold wall and the two-dimensional parallel flow of a heated ferrofluid along a wall with linearly decreasing surface temperature.

The aim of this paper is to re-investigate the two-dimensional parallel flow of a heated ferrofluid along a wall with decreasing surface temperature of power-law type and the static behaviour of ferrofluids in magnetic field using similarity analysis. The similarity method is applied for the governing equations to transform partial differential equations to nonlinear ordinary differential equations. Numerical solutions are obtained with higher derivative method. The heat transfer, velocity and temperature distribution in the boundary layer are provided and compared with the results obtained by Neuringer (1966) for constant streaming speed and linearly decreasing wall temperature. The behaviour of the velocity and thermal distribution is presented. We point out for the existence of two different solutions on the base of numerical results to the corresponding boundary value problem. The effects of the parameters involved in the boundary value problem are graphically illustrated.

2 Problem Formulation

Consider a steady two-dimensional flow of an incompressible, viscous and electrically non-conducting ferromagnetic fluid over a flat sheet in the horizontal direction shown in Fig. 1.

The dipole of the magnet is placed at a distance a from the surface, in such a way its center lies on y-axis. The magnetic field (**H**) due to the magnetic dipole is directed towards positive x-direction. The ferrofluid influences by the dipole of the permanent magnet whose scalar potential is

$$\phi(x,y) = -\frac{I_0}{2\pi}\left(\tan^{-1}\frac{y+a}{x} + \tan^{-1}\frac{y-a}{x}\right), \tag{1}$$

where I_0 denotes the dipole moment per unit length and a is the distance of the line current from the leading edge. The wall temperature is a decreasing function of x and is given by $T_w = T_c - Ax^{m+1}$, where T_c denotes the Curie temperature, A and m are real constants.

The negative gradient of the magnetic scalar potential ϕ equals to the applied magnetic field, i.e. $\mathbf{H} = -\nabla\phi$.

Then, the corresponding field components are given by

$$\begin{aligned} H_x &= -\frac{\partial \phi}{\partial x} = -\frac{I_0}{2\pi}\left[\frac{y+a}{x^2+(y+a)^2}+\frac{y-a}{x^2+(y-a)^2}\right], && (2) \\ H_y &= -\frac{\partial \phi}{\partial y} = -\frac{I_0}{2\pi}\left[\frac{x}{x^2+(y+a)^2}+\frac{x}{x^2+(y-a)^2}\right]. && (3) \end{aligned}$$

Moreover, the second derivatives are given by

$$\frac{\partial^2 \phi}{\partial x^2} = -\frac{\partial^2 \phi}{\partial y^2} = -\frac{I_0}{2\pi}\left[\frac{2x\,(y+a)}{\left[x^2+(y+a)^2\right]^2}+\frac{2x\,(y-a)}{\left[x^2+(y-a)^2\right]^2}\right] \tag{4}$$

and

$$\frac{\partial^2 \phi}{\partial x\,\partial y} = -\frac{I_0}{2\pi}\left[\frac{(y+a)^2-x^2}{\left[x^2+(y+a)^2\right]^2}+\frac{(y-a)^2-x^2}{\left[x^2+(y-a)^2\right]^2}\right]. \tag{5}$$

Neuringer and Rosensweig (1964) showed that the existence of spatially varying fields is required in ferrohydrodynamic interactions. We shall have the following assumptions for the exposition of ferrohydrodynamic interaction:

(i) the fluid temperature must be less than Curie temperature,

(ii) the applied magnetic field is inhomogeneous.

Then, the dynamic response of ferrofluids to the application of non-uniform magnetic fields follows from the fact that the force per unit volume on a piece of magnetized material of magnetization **M** (i.e. dipole moment per unit volume) in the field of magnetic intensity **H** is given by the form $\mu_0 M \nabla H$, where $H = \sqrt{\left(\frac{\partial \phi}{\partial x}\right)^2+\left(\frac{\partial \phi}{\partial y}\right)^2}$, μ_0 denotes the free space permeability and M represents the magnitude of **M**. Applying the scalar potential ϕ, ∇H is calculated as follows

$$\nabla H = \left([\nabla H]_x\,,[\nabla H]_y\right) = \left(\frac{\frac{\partial \phi}{\partial x}\frac{\partial^2 \phi}{\partial x^2}+\frac{\partial \phi}{\partial y}\frac{\partial^2 \phi}{\partial x\,\partial y}}{\sqrt{\left(\frac{\partial \phi}{\partial x}\right)^2+\left(\frac{\partial \phi}{\partial y}\right)^2}}, \frac{\frac{\partial \phi}{\partial x}\frac{\partial^2 \phi}{\partial x\,\partial y}+\frac{\partial \phi}{\partial y}\frac{\partial^2 \phi}{\partial y^2}}{\sqrt{\left(\frac{\partial \phi}{\partial x}\right)^2+\left(\frac{\partial \phi}{\partial y}\right)^2}}\right), \tag{6}$$

where $[\nabla H]_x$ and $[\nabla H]_y$ denotes the first and second components of ∇H, respectively. Since $(\partial\phi/\partial x)_{y=0} = 0$ and $\left(\partial^2\phi/\partial y^2\right)_{y=0} = 0$ at the wall, then $[\nabla H]_y$ vanishes.

In the boundary layer for regions close to the wall when distances from the leading edge large compared to the distances of the line sources from the plate, i.e. $x \gg a$, then one gets

$$[\nabla H]_x = -\frac{I_0}{\pi}\,\frac{1}{x^2}. \tag{7}$$

From the above said consideration of the flow analysis, the governing equations (conservation of mass, momentum and energy) of the boundary layer flow are formed according to the following assumptions (Neuringer (1966)):

(i) the intensity of magnetic field is strong enough to drench the magnetic fluid, and the variation of magnetization M is the linear function of temperature as reported by $M = K(T_c - T)$, where K is the pyromagnetic coefficient and T_c denotes the Curie temperature proposed by Amirat and Hamdache (2012),

(ii) the induced field resulting from the induced magnetization compared to the applied field is neglected; hence, the ferrohydrodynamic equations are uncoupled from the electromagnetic equations and

(iii) in the temperature range to be considered, the thermal heat capacity c, the thermal conductivity k, and the coefficient of viscosity ν are independent of temperature.

Then, the governing equations are described as follows

$$\frac{\partial u}{\partial x}+\frac{\partial v}{\partial y}=0, \tag{8}$$

$$u\frac{\partial u}{\partial x}+v\frac{\partial u}{\partial y}=-\frac{I_o\mu_0 K}{\pi\rho}(T_c-T)\frac{1}{x^2}+\nu\frac{\partial^2 u}{\partial y^2}, \tag{9}$$

$$c\left[u\frac{\partial T}{\partial x}+v\frac{\partial T}{\partial y}\right]=k\frac{\partial^2 T}{\partial y^2}, \tag{10}$$

where the x and y axes are taken parallel and perpendicular to the plate, u and v are the parallel and normal velocity components to the plate, respectively, μ_0 means the permeability of the vacuum, ν is the kinematic viscosity and ρ denotes the density of the ambient fluid, which will be assumed constant. Equations (8)-(10) are considered under the boundary conditions at the surface ($y=0$) with

$$u(x,0)=0, \qquad v(x,0)=0, \qquad T(x,0)=T_w, \tag{11}$$

where $T_w=T_c-Ax^{m+1}$ and as y leaves the boundary layer $(y\to\infty)$ with

$$u(x,y)\to u_\infty, \qquad T(x,y)\to T_\infty \tag{12}$$

where $T_\infty=T_c$, and u_∞ is the exterior streaming speed which is assumed throughout the paper to be $u_\infty=U_\infty x^m$ ($U_\infty=const.$). Parameter m is relating to the power law exponent. The parameter $m=0$ refers to a linear temperature profile and constant exterior streaming speed. In case of $m=1$, the temperature profile is quadratic and the streaming speed is linear. The value of $m=-1$ corresponds to no temperature variation on the surface.

Introducing the stream function ψ, defined by $u=\partial\psi/\partial y$ and $v=-\partial\psi/\partial x$, problem (8)–(10) can be formulated as

$$\frac{\partial\psi}{\partial y}\frac{\partial^2\psi}{\partial yx}-\frac{\partial\psi}{\partial x}\frac{\partial^2\psi}{\partial yy}=\nu\frac{\partial^3\psi}{\partial yyy}-\frac{I_0\mu_0 K}{\pi\rho}\left(T_c-T\right), \tag{13}$$

$$c\left[\frac{\partial\psi}{\partial y}\frac{\partial T}{\partial x}-\frac{\partial\psi}{\partial x}\frac{\partial T}{\partial y}\right]=k\frac{\partial^2 T}{\partial yy}. \tag{14}$$

Boundary conditions (11) and (12) are transformed to

$$\frac{\partial}{\partial y}\psi(x,0)=0, \qquad \frac{\partial}{\partial x}\psi(x,0)=0, \qquad T(x,0)=T_c-Ax^{m+1}, \tag{15}$$

$$\frac{\partial}{\partial y}\psi(x,y)\to U_\infty x^m \qquad T(x,y)=T_c \qquad \text{as } y\to\infty. \tag{16}$$

Using the following transformations, the structure of (13)–(16) allows us to look for similarity solutions of a class of solutions ψ and T in the form (see Barenblatt (1996))

$$\psi(x,y)=C_1x^bf(\eta), \qquad T=T_c-Ax^{m+1}\Theta\left(\eta\right), \qquad \eta=C_2x^dy, \tag{17}$$

where b and d satisfy the scaling relation

$$b+d=m \tag{18}$$

and for positive coefficients C_1 and C_2 the relation

$$\frac{C_1}{C_2}=\nu \tag{19}$$

are fulfilled. The real numbers b, d are such that $b - d = 1$ and $C_1 C_2 = U_\infty$, i.e.

$$b = \frac{m+1}{2}, \qquad d = \frac{m-1}{2}, \qquad C_1 = \sqrt{\nu U_\infty}, \qquad C_2 = \sqrt{\frac{U_\infty}{\nu}}. \tag{20}$$

By taking into account (17), equations (13) and (14) and conditions (15) and (16) lead to the following system of coupled ordinary differential equations

$$\frac{d^3 f}{d\eta^3} - m\left(\frac{df}{d\eta}\right)^2 + \frac{m+1}{2}\, f\, \frac{df}{d\eta} - \beta\,\Theta = 0, \tag{21}$$

$$\frac{d^2\Theta}{d\eta^2} + (m+1)\ \mathrm{Pr}\left(\frac{1}{2}\, f\, \frac{d\Theta}{d\eta} - \Theta\, \frac{df}{d\eta}\right) = 0. \tag{22}$$

The boundary conditions reduces to the following equations subjected to the boundary conditions

$$f(0) = 0, \qquad \frac{d}{d\eta} f(0) = 0, \qquad \Theta(0) = 1, \tag{23}$$

$$\frac{d}{d\eta} f(\eta) = 1, \qquad \Theta(\eta) = 0 \qquad \text{as } \eta \to \infty, \tag{24}$$

where $\mathrm{Pr} = c\nu/k$ is the Prandtl number and $\beta = I_0 \mu_0 K A/(\pi \rho U_\infty^2)$.

The components of the non-dimensional velocity $\mathbf{v} = (u, v, 0)$ can be expressed by

$$u = U_\infty\, x^m\, \frac{df(\eta)}{d\eta}, \tag{25}$$

$$v = -\sqrt{\nu U_\infty}\, x^{(m-1)/2}\left(\frac{m+1}{2}\, f(\eta) + \frac{m-1}{2}\frac{df(\eta)}{d\eta}\,\eta\right). \tag{26}$$

The physical quantities that specify the surface drag and heat transfer rate can be derived. Mathematically these quantities are interpreted in the following form

$$\tau_{y=0} = \nu\rho\left(\frac{\partial u}{\partial y}\right)_{y=0} = \rho U_\infty \sqrt{\nu U_\infty}\, x^{\frac{3m-1}{2}}\, \frac{d^2}{d\eta^2} f(0), \tag{27}$$

$$-k\left(\frac{\partial T}{\partial y}\right)_{y=0} = -kA\sqrt{\frac{U_\infty}{\nu}}\, x^{\frac{3m+1}{2}}\, \frac{d}{d\eta}\Theta(0), \tag{28}$$

where $(d^2 f/d\eta^2)(0)$ denotes the skin friction coefficient and $(d\Theta/d\eta)(0)$ stands for the heat transfer coefficient.

According to our knowledge, the coupled boundary-layer equations for the case when $m = 0$ were first examined by Neuringer (1966). If $m = 0$ and $\beta = 0$, equation (21) is equivalent to the famous Blasius equation

$$\frac{d^3 f}{d\eta^3} + \frac{1}{2}\, f\, \frac{df}{d\eta} = 0, \tag{29}$$

which appears when studying a laminar boundary-layer problem for Newtonian fluids (see Barenblatt (1996)).

In the mathematical study of a model describing the dynamics of heat transfer in an incompressible magnetic fluid under the action of an applied magnetic field, the fluid is assumed nonelectrically conducting and the obtained solutions are valid only for distances greater than a.

3 Results and Discussion

There are several methods for the numerical solution of boundary value problems of similar type of coupled strongly nonlinear differential equations as (21)–(22). Bhatti et al. (2016) applied the successive linearization method to solve the boundary value problem, where the unknown functions are obtained by iteratively solving the linearized version of the governing equation. Using a selection of initial guesses, auxiliary linear operators are quite essential to find the homotopic solutions for flow analysis (see Hayat et al. (2015)). Tzirtzilakis and Kafoussias (2003) obtained numerical results by a numerical technique based on the common finite difference method. Zeeshan et al. (2016) and Abraham and Titus (2011) solved the highly non-linear differential equation subjected to boundary conditions by shooting method when the higher-order ordinary differential equations are converted into the set of first-order simultaneous equations, which can be integrated as an initial value problem using the well known Runge-Kutta Fehlberg fourth-order scheme. The initial guesses for the unknown functions were adjusted iteratively by Newton-Raphson's method.

Due to the difficulties involved in two-point boundary value problems, several researchers have explored different approaches for solving these types of problems. The differential transformation method has been proved to be effective to provide approximate analytical solutions as it does not require many computations as carried out in Adomian decomposition method (ADM), homotopy analysis method (HAM), homotopy perturbation method (HPM), and variational iteration method (VIM). Also, the differential transformation method introduced by Zhou (1986) has been used in many engineering and scientific research papers due to its comparative advantages over the other approximate analytical methods. These numerical method could be used to solve differential equations, difference equation, differential-difference equations, fractional differential equation, pantograph equation and integro-differential equation, to solves nonlinear integral and differential equations without restrictive assumptions, perturbation and discretization or round-off error.

The system of equations (21)–(22) with the corresponding conditions (23)–(24), is interpreted numerically using BVP solution technique built in Maple.

In this paper, the coupled ordinary differential equations (21)–(22) are solved numerically with boundary conditions using a special type of BVP technique, namely, the higher derivative method (HDM) with A-stability property. The HDM method can be applied for the determination of efficient solution to some boundary value problems, which are described by nonlinear ordinary differential equations (see Chen et al. (2017)). The discretization of boundary value problems based on HDM scheme. It is experienced that most of the test runs quickly, in a few seconds. The Maple code is attached in the Appendix.

During our investigations, the velocity and temperature changes in the boundary layer are examined and the effects of the parameters on the solution are illustrated on the figures.

The boundary value problems can have the situation that either no solution or multiple solutions exist even for the simple set of differential equations (see Bognár (2012) and Hussaini and Lakin (1986)). Here, the boundary value problem in Maple with applying the HDM method was solved. From the implementations we realized that two differential solutions exist, call them an upper and a lower solutions for velocity distribution, these are denoted by green and yellow curves and exhibited on Fig. 2 for $m = 0$, $Pr = 10$, $\beta = 0.1$ and for the length of $\eta_{max} = 6$. The Prandtl number $Pr = 10$ is fixed as a typical value of kerosine based ferrofluid. The obtained solutions of thermal distribution can be seen on Fig. 3, where we have lower and upper solutions, same as in the case of velocity, but in this case, the lower solution is in a good agreement with published by Neuringer (1966).

The ferromagnetic parameter β highlights the effect of the external magnetic field. The variation of β is shown on Figs. 4-5. It is can also be noticed that the boundary layer thickness is different for different values of β. The thermal boundary-layer thickness is smaller than the corresponding velocity boundary-layer thickness.

The effect of parameter m is presented in Fig. 6 for the shear stress at the wall, and the impact on the heat transfer at the wall in Fig. 7. It can be checked from the figures that for the increasing values of m the surface shear stress $f''(0)$ decreases, and the effect is opposite for the heat transfer rate $\Theta'(0)$.

Figure 8 shows the dependence of temperature profiles on the Prandtl number. Greater values of Pr result in thinning of thermal boundary layers. It is observed that an increasing in the Prandtl number decreases the temperature profile in the flow region.

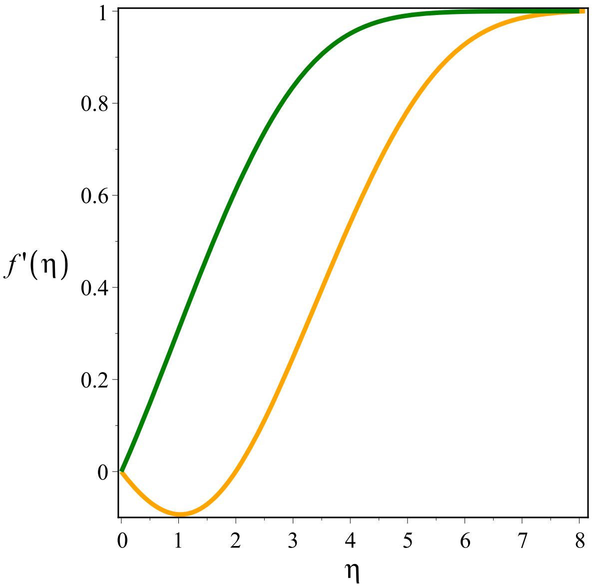

Figure 2: The effect of β on the velocity distribution for $m = 0$, $Pr = 10$, $\beta = 0.1$

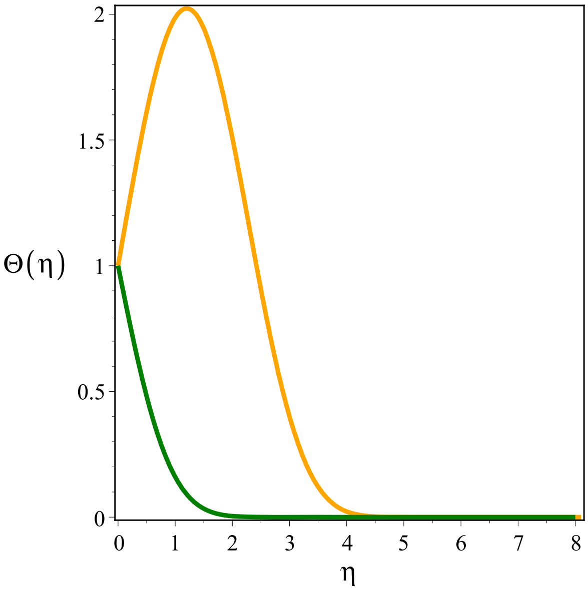

Figure 3: The effect of β on the temperature distribution for $m = 0$, $Pr = 10$, $\beta = 0.1$

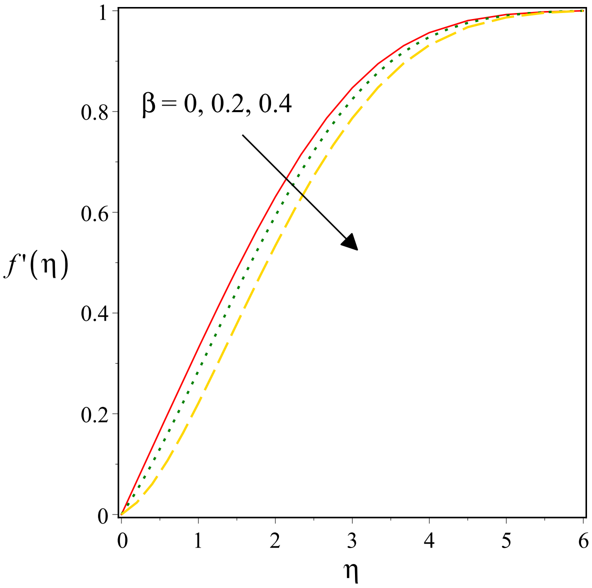

Figure 4: The velocity distribution for varying β ($m = 0$, $Pr = 10$)

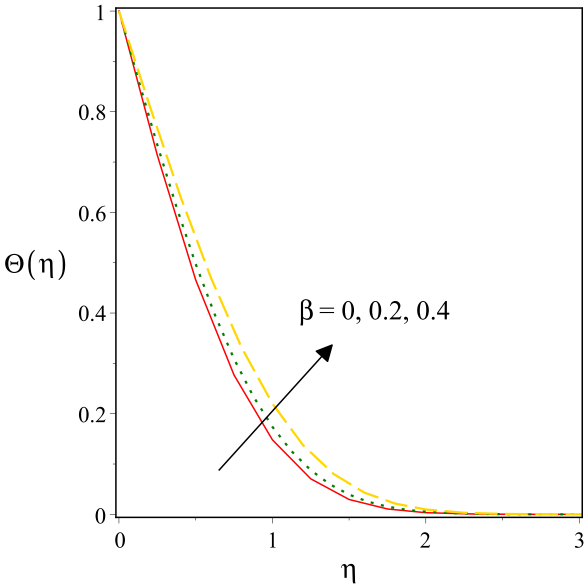

Figure 5: The temperature distribution for varying β ($m = 0$, $Pr = 10$)

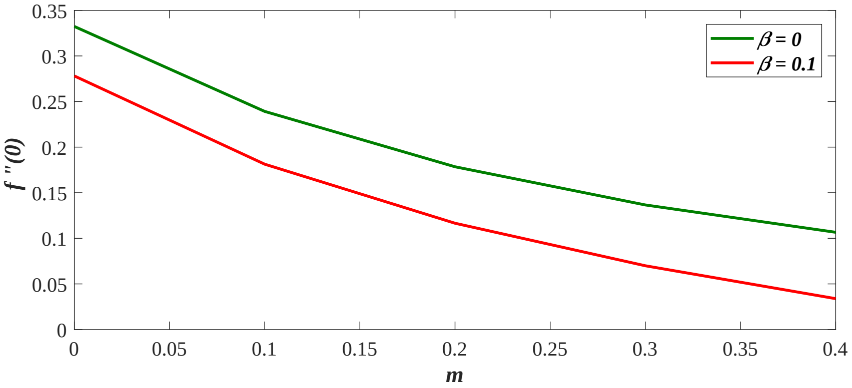

Figure 6: The shear stress at the wall for $Pr = 10$, $\beta = 0$ and $\beta = 0.1$

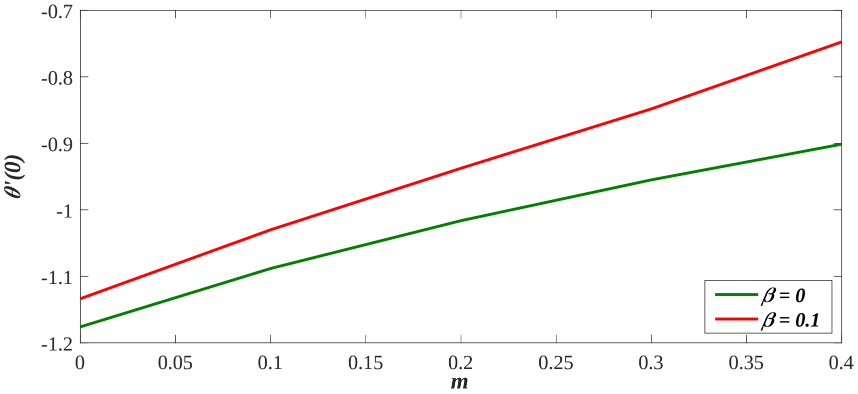

Figure 7: The heat transfer at the wall for $Pr = 10$, $\beta = 0$ and $\beta = 0.1$

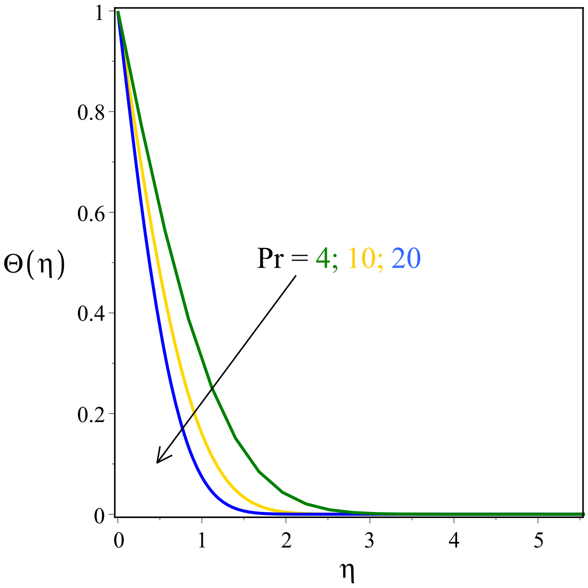

Figure 8: The effect of the Prandtl number $m = 0$ and $\beta = 0.1$

4 Conclusions

This paper presents similarity solution of the boundary layer flow and heat transfer over a cold wall of a ferrofluid fow in the presence of spatially varying magnetic field. By means of similarity transformation, the governing mathematical equations are reduced into ordinary differential equations which are then solved numerically using a higher derivative method. The effects of some governing parameters namely ferromagnetic parameter β, Prandtl number and power law parameter on the flow, and heat transfer characteristics are graphically presented and discussed. The findings of the numerical results can be summarized as follows:

(i) Dual solutions exist for the system of equations (21)–(22) with the corresponding conditions (23)–(24).

(ii) The effect of the external magnetic field is shown by he ferromagnetic parameter β. The boundary layer thickness is different for different values of β. The thermal boundary-layer thickness is smaller than the corresponding velocity boundary-layer thickness.

(iii) The increasing of parameter m is to decrease the surface shear stress $f''(0)$, and the effect is opposite for the heat transfer rate $\Theta'(0)$ on the wall.

(iv) The increase of the Prandtl number leads to a decrease of the temperature profile in the flow region.

Acknowledgements

This work was supported by project no. 129257 implemented with the support provided from the National Research, Development and Innovation Fund of Hungary, financed under the $K-18$ funding scheme.

Nomenclature

a	$[m]$	distance
A	$[K*m^{-(m+1)}]$	coefficient
c	$[J/K]$	thermal heat capacity
C_1, C_2	[-]	parameters
f	[-]	similarity velocity function
H	$[A/m]$	magnetic field strength
I_0	$[A]$	dipole moment per unit length
k	$[W/mK]$	thermal conductivity
K	$[A/mK]$	pyromagnetic coefficient
m	[-]	constant
M	$[A/m]$	magnetisation of the field
T	$[K]$	temperature
T_c	$[K]$	Curie temperature
T_w	$[K]$	wall temperature
T_∞	$[K]$	fluid temperature far from the wall
u_∞	$[m/s]$	fluid velocity
u, v	$[m/s]$	velocity components
u_w	$[m/s]$	wall velocity
x, y	$[m]$	distances parallel and perpendicular to the wall, respectively

Greek symbols

η	[-]	similarity variable
Θ	[-]	similarity temperature function
μ_0	$[Vs/Am]$	permeability of the vacuum
ν	$[m^2/s]$	kinematic viscosity
ρ	$[kg/m^3]$	density of the fluid
ϕ	$[A]$	scalar potential
ψ	$[m^2/s]$	stream function

References

Abel, M. S.; Mahesha, N.: Heat transfer in MHD viscoelastic fluid flow over stretching sheet with variable thermal conductivity, non-uniform heat source and radiation. *Appl. Math. Modelling*, 32, (2008), 1965–1983.

Abraham, A.; Titus, L. S. R.: Boundary layer flow of ferrofluid over a stretching sheet in the presence of heat source/sink. *Mapana J. Sci.*, 10, (2011), 14 – 24.

Adiguzel, A. B.; Atalik, K.: Magnetic field effects on Newtonian and non-Newtonian ferrofluid flow past a circular cylinder. *Appl. Math. Modelling*, 42, (2017), 161 – 174.

Amirat, Y.; Hamdache, K.: Heat transfer in incompressible magnetic fluid. *J. Math. Fluid Mech.*, 14, (2012), 217 – 247.

Andersson, H. I.: MHD flow of a viscoelastic fluid past a stretching surface. *Acta Mechanica*, 95, (1992), 227 – 230.

Andersson, H. I.; Valnes, O. A.: Flow of a heated ferrofluid over a stretching sheet in the presence of a magnetic dipole. *Acta Mechanica*, 128, (1988), 39 – 47.

Barenblatt, G.: *Scaling, self-similarity, and intermediate asymptotics: dimensional analysis and intermediate asymptotics*. Cambridge University Press, Cambridge, MA (1996).

Bhatti, M. M.; Abbas, T.; Rashidi, M. M.: Numerical study of entropy generation with nonlinear thermal radiation on magnetohydrodynamics non-newtonian nanofluid through a porous shrinking sheet. *J. Magnetics*, 21, (2016), 468 – 475.

Bognár, G.: On similarity solutions to boundary layer problems with upstream moving wall in non-Newtonian power-law fluids. *IMA J. Appl. Math.*, 77, (2012), 546 – 562.

Bognár, G.: Magnetohydrodynamic flow of a power-law fluid over a stretching sheet with a power-law velocity. *Differential and Difference Equations with Applications (Springer Proceedings in Mathematics and Statistics; 164. ICDDEA, Amadora, Portugal, 2015)*, pages 131 – 139.

Bognár, G.: On similarity solutions of MHD flow over a nonlinear stretching surface in non-Newtonian power-law fluid. *Electron. J. Qual. Theory Differ. Equ.*, 2016, (2016b), 1 – 12.

Chen, J.; Sonawane, D.; Mitra, K.; Subramanian, V. R.: Yet another code for boundary value problems- higher derivative method. *manuscript*.

Hayat, T.; Muhammad, T.; Shehzad, S. A.; Alsaedi, A.: Similarity solution to three dimensional boundary layer flow of second grade nanofluid past a stretching surface with thermal radiation and heat source/sink. *AIP Advances*, 5, 1, (2015), 017107.

Hussaini, M. Y.; Lakin, W. D.: Existence and nonuniqueness of similarity solutions of a boundary-layer problem. *Quart. J. Mech. Appl. Math.*, 39, (1986), 177 – 191.

Neuringer, J. L.: Some viscous flows of a saturated ferrofluid under the combined influence of thermal and magnetic field gradients. *J. Non-linear Mech.*, 1, (1966), 123 – 127.

Neuringer, J. L.; Rosensweig, R. E.: Ferrohydrodynamics. *Phys. Fluids*, 7, (1964), 1927 – 1937.

Papell, S. S.: Low viscosity magnetic fluid obtained by colloidal suspension of magnetic particles. *U.S. Patent*, 3, (1965), 3,215,572.

Shliomis, M.: Comment on ”ferrofluids as thermal ratchets”. *Phys. Rev. Lett.*, 92, (2004), 188901.

Siddheshwar, P. G.; Mahabaleshwar, U. S.: Effect of radiation and heat source on mhd flow of a viscoelastic liquid and heat transfer over a stretching sheet. *Int. J. Non-Linear Mech.*, 40, (2005), 807 – 820.

Tzirtzilakis, E. E.; Kafoussias, N. G.: Biomagnetic fluid flow over a stretching sheet with non-linear temperature dependant magnetization. *ZAMP*, 54, (2003), 551 – 565.

Zeeshan, A.; Majeed, A.; Ellahi, R.: Effect of magnetic dipole on viscous ferro-fluid past a stretching surface with thermal radiation. *J. Mol. Liq.*, 215, (2016), 549 – 554.

Zhou, J.: *Differential Transformation and Its Applications for Electrical Circuits*. Huazhong University Press, Wuhan, China (1986).

Address: University of Miskolc, Miskolc-Egyetemváros, Miskolc, H–3515, Hungary
email: `v.bognar.gabriella@uni-miskolc.hu`

Appendix

The HDM adapt procedure is applied to determine the approximate numeric solution. The simulation gives the value of unknown parameters B and C, and then we get the figure of all solution functions.

```
> restart:
> read("HDM.txt");
> Digits:=15;
> EqODEs:=[diff(y1(x),x) = y2(x),diff(y2(x),x) = y3(x),
diff(y3(x),x) = m*y2(x)*y2(x)-(m+1)/2*y1(x)*y3(x)+b*y4(x),
diff(y4(x),x) = y5(x),
diff(y5(x),x) = -Pr*((m+1)/2*y1(x)*y5(x)-(m+1)*y4(x)*y2(x))];
> bc1:=evalf([y1(x),y2(x),y3(x)-B,y4(x) - 1,y5(x)-C]);
> bc2:=evalf([y2(x)-1,y4(x)]);
> Range:=[0.,5.6];
> pars:=[m=0.00,beta=0.1,Pr=4];
> unknownpars:=[B,C]; nder:=5;nele:=20;
> atol:=1e-6;rtol:=atol/100;
> sol:= HDMadapt(EqODEs,bc1,bc2,pars,unknownpars,nder,nele,Range,atol,rtol):
> sol[1][(nops(sol[3])+1)*nops(EqODEs)+1..nops(sol[1])];
> sol[4];
> sol[5];
> NN:=nops(sol[3])+1; print(y5(x));
> node:=nops(EqODEs);

> odevars:=select(type,map(op,map(lhs,EqODEs)),'function');
> xx:=Vector(NN):
> xx[1]:=Range[1]:
> for i from 1 to nops(sol[3]) do xx[i+1]:=xx[i]+sol[3][i]:  od:
> for j from 1 to node do

> plot([seq([xx[i],rhs(sol[1][i+NN*(j-1)])],i=1..NN)],
axes=boxed,labels=[x,odevars[j]],style=point);

> end do;
```

DOI: 10.24352/UB.OVGU-2019-003
TECHNISCHE MECHANIK, 39, 1, (2019), 16 - 29
submitted: September 4, 2018

Planar Elongation Flow Analysis of Non-Newtonian Fluids Using a Disk-Shaped Bob

S. Ito, S. Iwata, Y. Sugihara, T. Takahashi

Planar elongation viscosity is a material property involved in extensional deformation, which plays a significant role in many processes such as film-casting and coating. As for the elongation behavior of a polymeric film, some commercial measurement methods are available. However, these measurement methods cannot be applied to liquids with lower viscosities. A method of measuring planar elongation viscosity, especially for low viscosity liquids, has been proposed, which generates a planar elongation flow by pushing a bullet-shaped bob into a cup filled with the sample liquid. The pushing force, which can be measured by a conventional rheometer, reflects the responses of shear, planar extensional deformation, and buoyancy. However, measurements using a bullet-shaped bob may be strongly affected by the shear flow between the bob and the cup. Therefore, an alternative measurement using a flat disk-shaped bob is proposed, in order to significantly reduce the influence of shear flow. However, such improvements cannot be estimated numerically. In this study, we performed numerical simulations of viscoelastic fluids for both measurement methods to clarify the shear flow effects.

Nomenclature

$\mathbf{E}$	[Pa]	elastic stress tensor
F	[N]	applied force
g	[m/s^2]	gravity acceleration
$\mathbf{g}$	[m/s^2]	gravity vector
G	[Pa]	relaxation modulus
h	[m]	gap between bob and cup
L	[m]	representative length
p	[Pa]	pressure
Q	[m^3/s]	volume flow rate
R	[m]	radius
S	[m^2]	surface area
$\mathbf{S}$	[s^{-1}]	rate of deformation tensor
u, w	[m/s]	velocity in r, z direction
$\mathbf{v}$	[m/s]	velocity vector
V_b	[m/s]	bob sliding velocity
α, s	[-]	Giesekus model parameter
$\dot{\gamma}$	[s^{-1}]	shear rate
$\boldsymbol{\delta}$	[-]	unit tensor
$\dot{\varepsilon}$	[s^{-1}]	elongation velocity
η_0	[Pa$\cdot$s]	zero-shear viscosity
θ	[rad]	radial angle
λ	[s]	relaxation time
ρ	[kg/m^3]	density
$\boldsymbol{\tau}$	[Pa]	extra stress tensor
∇	[m^{-1}]	gradient operator
II_d	[s^{-2}]	second invariant of deformation tensor
III_d	[s^{-3}]	third invariant of deformation tensor

Subscripts and Superscripts

b	bob
c	cup
hd	hydraulic mean depth
m	smallest
M	largest
PE	planar elongation
r, z	direction
T	transpose
∇	contravariant convective derivative

1 Introduction

Planar elongation flow of viscoelastic fluids can be observed in film-casting, blow molding, and coating processes, among others. Such processes can be affected by the material response under extensional deformation, which is different from the response under shear deformation. To evaluate the planar elongation behavior of such fluids is important for the design and operation of the processes. However, useful planar elongation viscosity measurements are not available, because it is difficult to generate a steady planar elongation flow field, especially for low viscosity fluids. Sugihara et al. [1] proposed a method of measuring the planar elongation viscosity, which uses the planar elongation flow generated by pushing a bullet-shaped bob into a cup filled with the sample liquid. A commercial stress-controlled rheometer was used to measure the normal force at a given bob speed. The normal force is equivalent to the summation of resistance forces acting on the bob, such as a buoyancy force, pressure, and extra stresses due to the elongation and shear flows. The bullet-shaped bob and cup are precisely manufactured to generate a planar elongation flow at a desired planar elongation rate, as shown in Figure 1. This method is useful for lower viscosity liquids. However, the Trouton ratio of the planar elongation viscosity of the Newtonian fluid was approximately 10^3 times higher than the theoretical value of 4. On the other hand, Sugihara et al. [1] also showed numerical results, such as the streamline and shear rate profiles shown in Figure 2. They pointed out that the resistance force on the bob is dominated by shear flow due to the longer narrow gap between the bob and cup, and it is necessary to reduce the influence of the shear flow for accurate planar elongation viscosity measurements.

To reduce the effect of the shear flow at the gap, a flat disk-shaped bob with a knife-edged rim was proposed [2]. Figure 3 shows a schematic view of the disk-shaped bob. This technique was intended to reduce the influence of the shear flow significantly because the length of the narrow gap is infinitesimally short. However, it was necessary to assume a representative length L of the shear and elongation flow region instead of the length of the test section in order to estimate the resistance force to evaluate the planar elongation viscosity. The choice of this representative length is important to increase the accuracy of the elongation viscosity measurement. They used the hydraulic mean depth as the representative length, so that Trouton ratio of the flow channel of Newtonian fluids agrees with the theoretical value of 4. Ideally, the representative length characterizing the flow field should be determined based on an analytically or experimentally obtained velocity distribution. The flow field occurring around the disk-shaped bob and the cup, however, has not yet been revealed. In this study, we perform a numerical simulation of a viscoelastic fluid for the flat disk-shaped bob to clarify the effect of the shear flow region on the resistance force and the validity of using the hydraulic mean depth as the representative length.

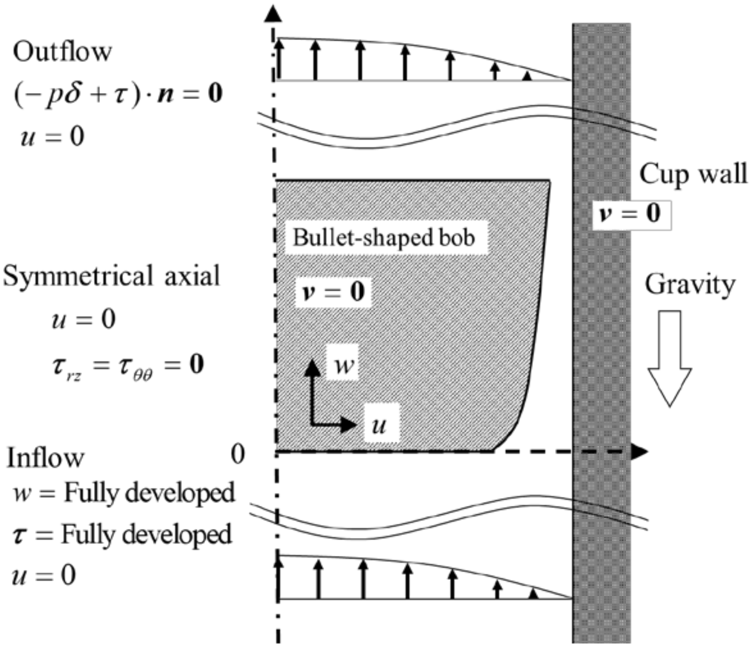

Figure 1. Boundary conditions of flow analysis in the bullet-shaped bob geometry.

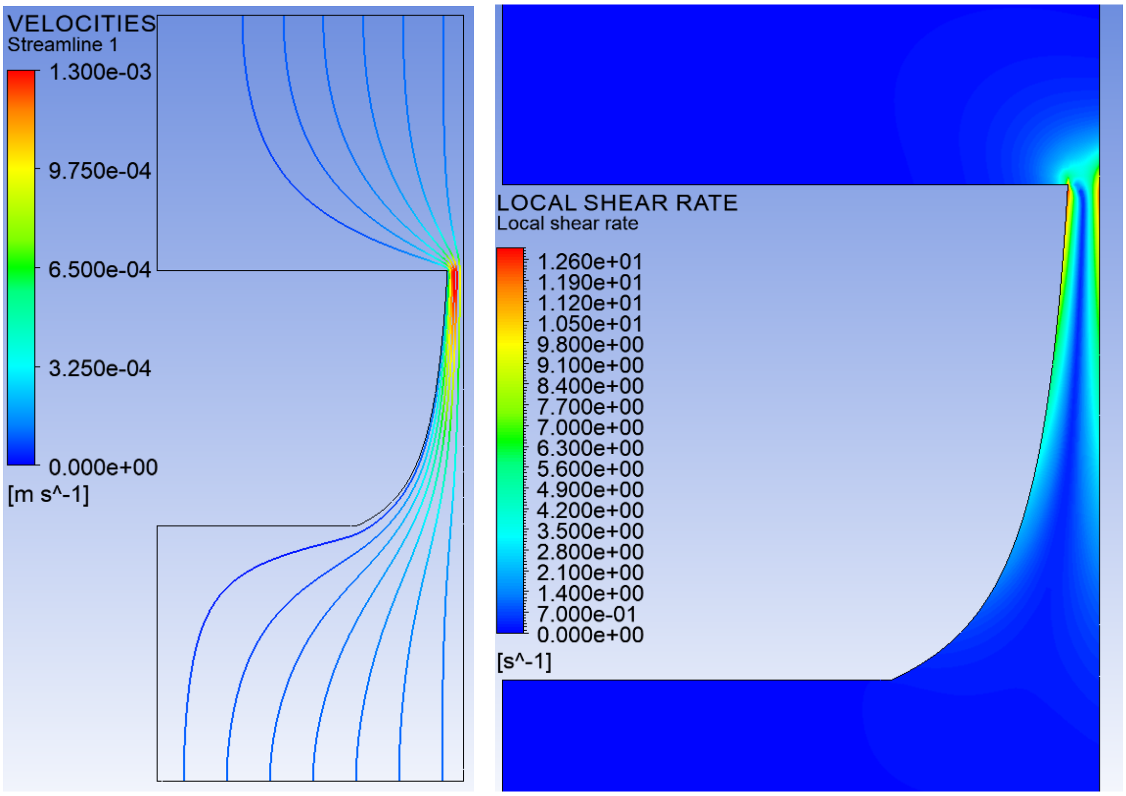

Figure 2. (a) Streamlines and velocity profile and (b) shear rate profile of the flow channel between the cup and bullet-shaped bob sliding at V_b=0.1 mm/s.

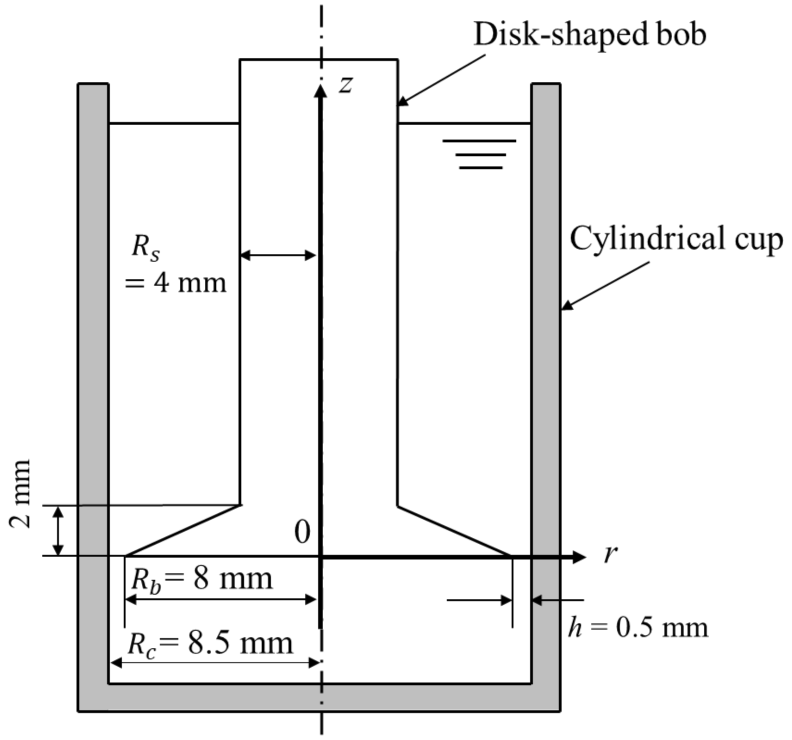

Figure 3. Schematic of flow problem between the disk-shaped bob and cylindrical cup.

2 Numerical Analysis

2.1 Governing Equations

The isothermal and steady state flow of a viscoelastic fluid is governed by the following basic equations, i.e., equation of continuity (1), momentum equation (2) and constitutive equations (3) and (4) as follows.

$$\nabla \cdot \boldsymbol{v} = 0 \tag{1}$$

$$\rho \boldsymbol{v} \cdot \nabla \boldsymbol{v} = -\nabla p + \nabla \cdot \boldsymbol{\tau} + \rho \boldsymbol{g} \tag{2}$$

$$\boldsymbol{\tau} = 2\eta_0 s \boldsymbol{S} + \boldsymbol{E} \tag{3}$$

$$\boldsymbol{E} + \lambda \overset{\nabla}{\boldsymbol{E}} + \left(\alpha / G\right) \boldsymbol{E}^2 = 2\eta_0 \left(1 - s\right) \boldsymbol{S} \tag{4}$$

where $\boldsymbol{S}$ is the deformation tensor ($2\boldsymbol{S} \equiv \nabla \boldsymbol{v} + \nabla \boldsymbol{v}^{\mathrm{T}}$) and the upper convected derivative of the elastic stress $\overset{\nabla}{\boldsymbol{E}}$ defined in equation (5), which is the elastic part of the extra stress $\boldsymbol{\tau}$. The unit mode Giesekus model [3] is employed as a constitutive equation with a zero-shear viscosity η_0, a relaxation time λ, model parameters α, s and relaxation modulus $G \equiv \eta_0 \left(1 - s\right) / \lambda$.

$$\overset{\nabla}{\boldsymbol{E}} \equiv \boldsymbol{v} \cdot \nabla \boldsymbol{E} - \left(\nabla \boldsymbol{v}^{\mathrm{T}} \cdot \boldsymbol{E} + \boldsymbol{E} \cdot \boldsymbol{v}\right) \tag{5}$$

The elastic–viscous–split–stress (EVSS) method [4] for viscoelastic flows is used to improve the convergence of the analysis. Biquadratic interpolation and linear interpolation are used for the velocity and the pressure field, respectively. A 4×4 sub element scheme and stream up winding method [5] are employed for discretization of constitutive equations using the Galerkin finite element method by POLYFLOW software ANSYS 19.0.

2.2 Boundary Conditions

Figure 3 is a schematic illustration of the flow geometry with a disk-shaped bob. 2D asymmetrical flow was assumed in this simulation. The radius of the disk-shaped bob, the rod, and the inner cup are R_b, R_s, and R_c, respectively. The upper part of the disk is slightly conical in shape.

Boundary conditions are summarized in Figure 4. The flow at the inlet boundary is taken to be fully developed at a given flow rate with a specified profile velocity and components of the elastic stress $\boldsymbol{E}$, as well as the total stress are set to vanish at the outlet. No-slip conditions are assumed along the surfaces of the cup wall and the bob. The bob is fixed, and the cup wall moves up at the bob sliding speed V_b.

Figure 5 shows a mesh profile of the calculation domain consisting of 7,620 elements. A close-up of the mesh profile around the tip of the disk-shaped bob is shown on the right side. The tip of the disk-shaped bob is slightly rounded to relax the singularity effect.

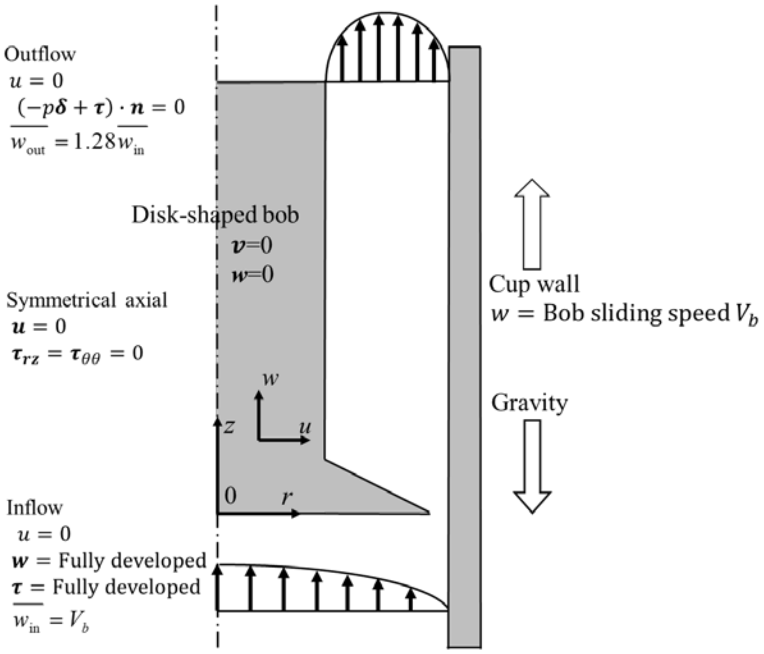

Figure 4. Boundary conditions for flow analysis between the cup and disk-shaped bob.

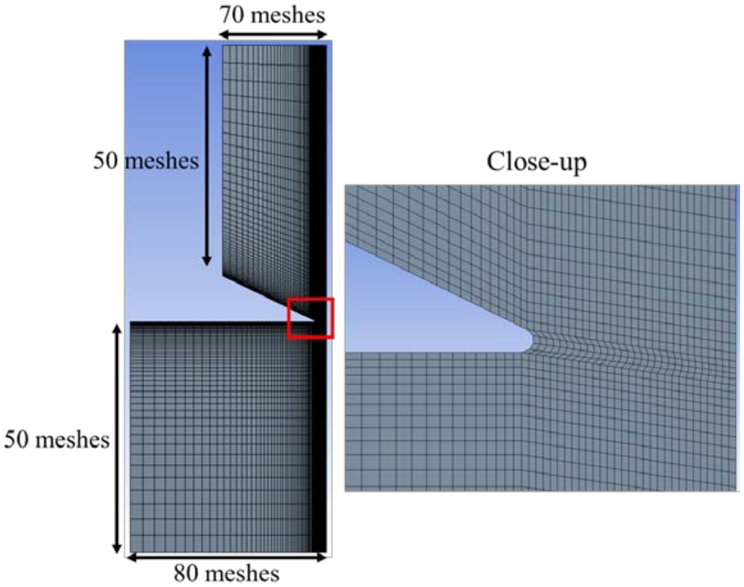

Figure 5. Overview of mesh profile (left side) and its close-up view around the tip of the disk (right side).

2.3 Material

M1 fluid [7, 8] was used as a low-viscosity viscoelastic liquid, and was measured by a rheometer MCR301 (Anton Paar Corp.). Figure 6 shows the rheological properties of the M1 fluid. The M1 fluid shows an almost constant shear viscosity over the tested shear range but exhibits slightly shear-thinning behavior (Figure 6). The data of storage modulus *G’* and loss modulus *G”* are replotted from Te Nijenhuis et al. [10].

We also fit parameters of the unit mode Giesekus model to the experimental data. The rheological curves obtained by this fitting are shown as the solid lines in Figure 6. The model parameters used in the simulations are $\eta_0 = 1.64$ Pa·s, $\lambda = 0.200$ s, $\alpha = 0.500$, and $s = 0.595$.

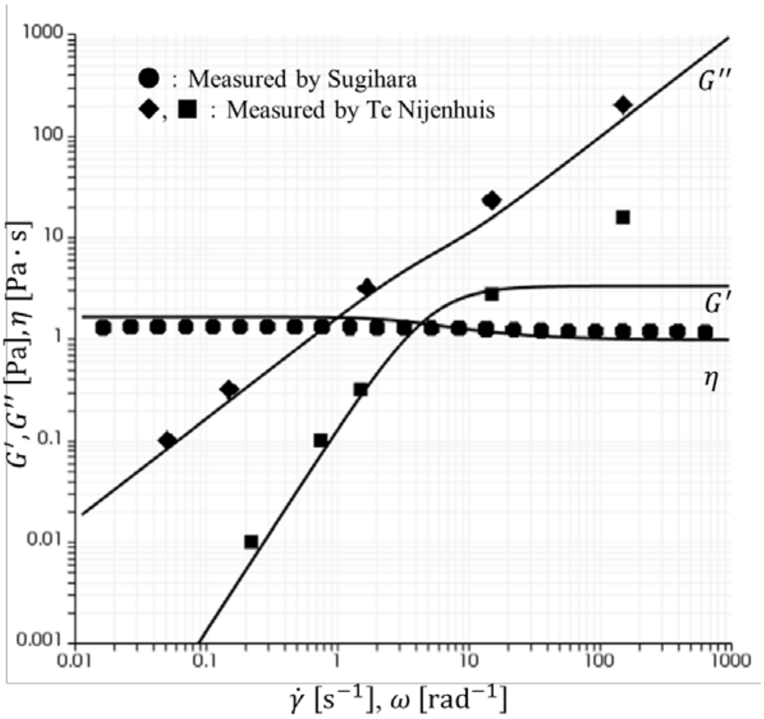

Figure 6. Rheological properties of the M1 fluid: Storage modulus *G’*, Loss modulus *G”*, Shear viscosity η.

2.4. Estimation of Resistance Forces

In the case of the disk-shaped bob, the summation of the apparent resistance force *F’* can be written as:

$$F' = F - F_b = F_{ss} + F_{sn} + F_{PE} \tag{6}$$

where *F* is the net resistance force, F_b is the buoyancy force, F_{ss} is the contribution of the shear stress acting on the aspect of the bob, F_{sn} is the contribution of the pressure drops of the shear flow, and F_{PE} is generated by the planar elongation flow in the test section [2]. In the case of the bullet-shaped bob, F_{sn} will be the dominant force, because the shear stress acting on the bullet-shaped bob is much bigger due to the longer channel, as shown in Figure 2(a). However, the shear stress acting on the surface of the disk-shaped bob can be neglected because of the knife-edged rim, giving F_{ss}=0. In addition, shear stress will be generated on the cup surface in the narrow gap region. Sugihara et al. [2] assumed that F_{sn} is given as follows:

$$F_{sn} = \pi R_b^2 \int_0^L \left(-\frac{dp}{dz} \right) dz = \pi R_b^2 \left(-\frac{dp}{dz} \right) L \tag{7}$$

In the experimental measurement of planar elongation, we treat the M1 fluid as a power-law fluid (flow coefficient power-law index K=1.25 Pa·s^n) [2]. Assuming a power-law fluid, the pressure gradient over a representative length L can be calculated. Finally, the planar elongation rate can be given as follows:

$$\dot{\varepsilon}_{PE} = \frac{Q}{\pi\left(R_c{}^2 - R_b{}^2\right)} \times \frac{1}{L} = \frac{R_c{}^2 V}{L\left(R_c{}^2 - R_b{}^2\right)} \tag{8}$$

Here, the choice of representative length L is important for the disk-shaped bob. Sugihara et al. [2] used the hydraulic mean depth L_{hd} as L [9], which gave the experimentally obtained Trouton ratio of the Newtonian fluid the theoretically predicted value of 4.

$$L_{hd} = \frac{\pi\left(R_c{}^2 - R_b{}^2\right)}{2\pi\left(R_c + R_b\right)} = \frac{R_c - R_b}{2} \tag{9}$$

L_{hd} is half of the width between the tip of the disk-shaped bob and the cup wall.

3 Results and Discussion

3.1 Results of Numerical Simulation

Figure 7 shows the apparent resistance force F' generated by the flow between the cup and the bob. The solid line with open circles indicates experimental values replotted from [2]. The dashed line with solid circles indicates F' obtained by the numerical simulation. F' increases linearly and agrees well with the experimental data. The relative error with respect to the experimental value at V_b=10 mm/s is -0.73%. Therefore, the validity of the numerical simulation is confirmed.

Figure 8(a) shows streamlines in the flow field. The magnitude of velocity is indicated on each streamline by the color scale. Fully developed flow enters from the bottom of the cup. The mean inlet velocity in the z-direction $\overline{w_{in}}$ is 0.1 mm/s, which is the same as the bob sliding velocity V_b. The streamlines are parallel to each other. The streamlines are gradually concentrated and smoothly enter the narrow gap between the disk-shaped bob and cup. However, no vortex was found in the calculation domain. Approaching the gap from the bottom, the flow velocity is dramatically increased up to about 8.76 times faster than the mean inlet velocity. The value is dependent on the flow geometry. After passing through the narrow gap, the streamlines diverge smoothly and the velocity profile changes again to parallel flow. Numerical results at V_b = 10 mm/s are similar to those at V_b = 0.1 mm/s.

Figure 8(b) shows a contour plot of the elongation rate, which can be evaluated by equation (10) [6],

$$\dot{\varepsilon}_{PE} = 3III_d / II_d \tag{10}$$

where II_d and III_d are the second and third invariants of the deformation tensor $\boldsymbol{S}$, respectively. It was found that strong elongation flow is clearly generated in the entrance region of the narrow gap.

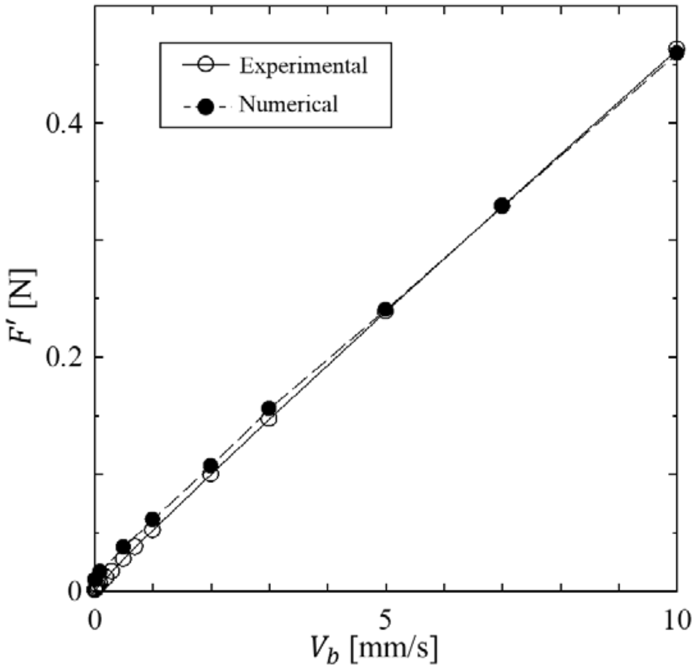

Figure 7. Apparent resistance force generated by flow between the cup and the bob.

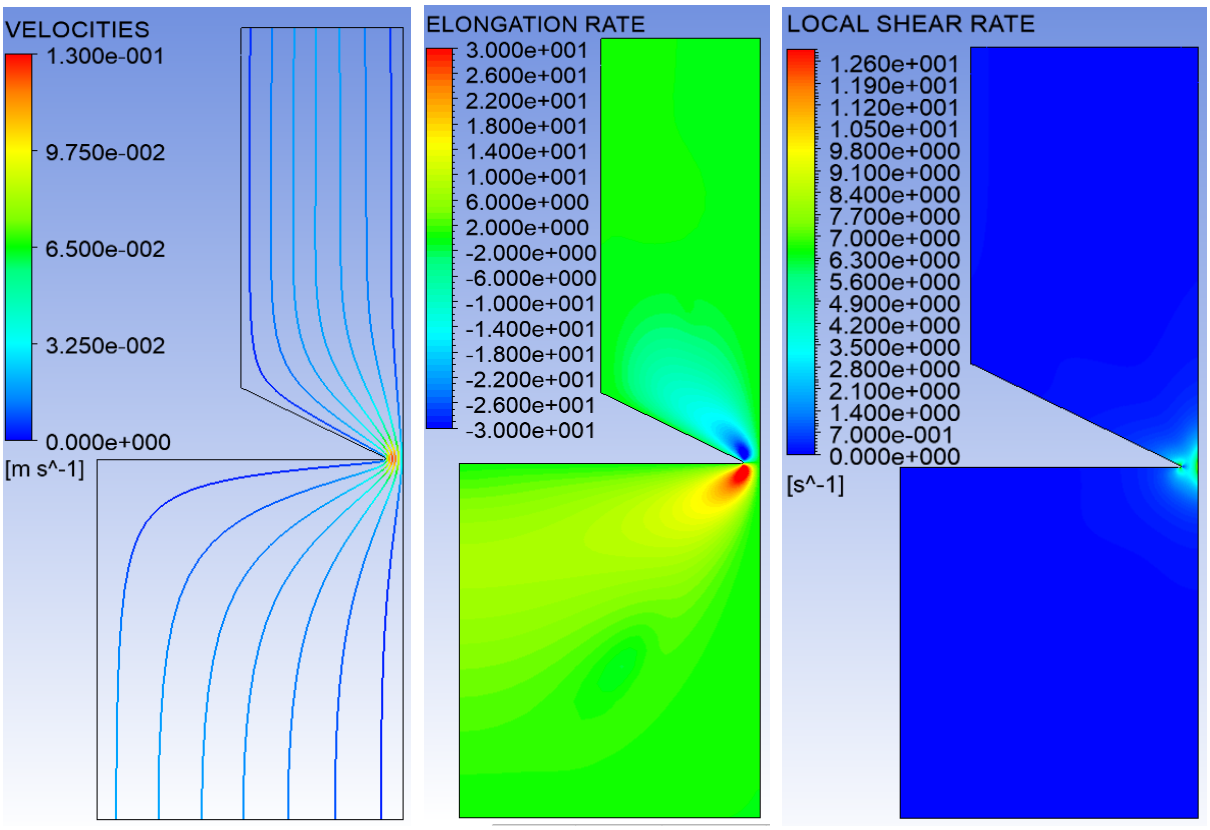

Figure 8. (a) Streamlines and velocity profile of the M1 fluid. Sliding velocity of the disk-shaped bob was V_b=0.1 mm/s. (b) Elongation rate profile at V_b=0.1 mm/s. (c) Shear rate profile at V_b=0.1 mm/s.

3.2 Validity of Representative Length

A shear rate profile for the calculation domain is given in Figure 8(c). It is readily apparent that the area of shear flow in the disk-shaped geometry is much smaller than in the bullet-shaped bob geometry shown in Figure 2(b).

An enlarged view of the shear rate contour plot around the edge of the disk is shown in Figure 9. The wall shear on the cup is biggest just beside the tip and falls off rapidly with increasing distance from the tip. Figure 10 shows the normalized wall shear rate along the cup surface near the tip. The shear rates at four sliding speeds (V_b=0.1, 1, 5, 10 mm/s) were normalized by the maximum value. The lines are very similar in shape near the tip. This means that the normalized shear region is independent from the bob sliding velocity V_b. Therefore, it is reasonable to determine the representative length from the shear rate profile on the cap wall. The hydraulic mean depth L_{hd} matches the range of high shear rate, $\dot{\gamma}/\dot{\gamma}_{\max} \geq 0.9$. Thus, the assumption of representative length is reasonable in the estimation of elongation viscosity.

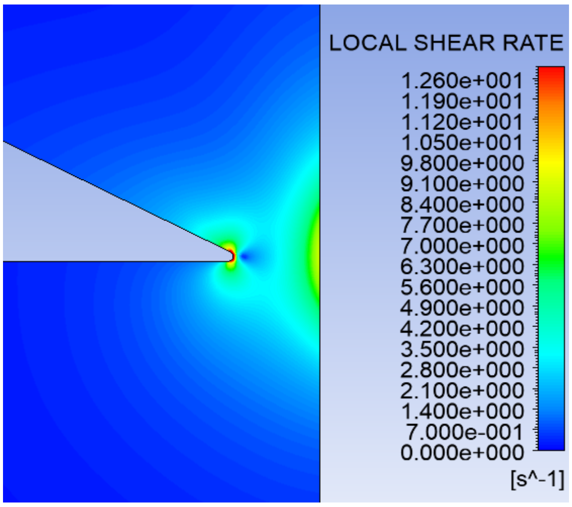

Figure 9. Shear rate profile around the edge of a disk-shaped bob at V_b=0.1 mm/s.

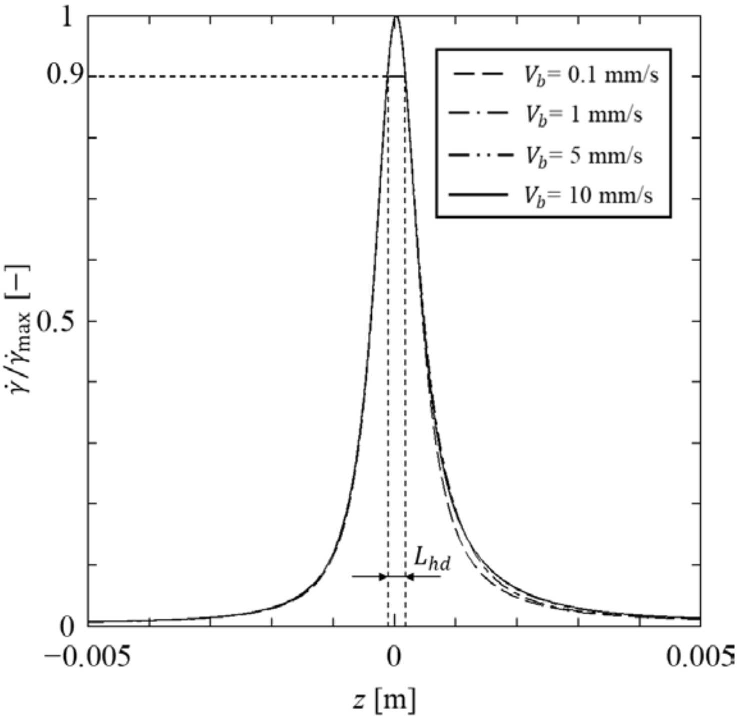

Figure 10. Effect of bob velocity V_b on normalized shear rate on the cup wall surface. R_b=8 mm, R_c=8.5 mm, h=0.5 mm, L_{hd}=0.25 mm.

3.3 Effect of Bob Geometry on Representative Length

We examined the effect of the radius and gap geometry on the shear rate profile along the cup wall. The bob geometry was changed gradually in two ways: (1) R_c and R_b were changed with constant gap h, and (2) the gap h between the bob and cup was changed with constant cup radius R_c. Figure 11 shows the calculation results for the constant gap cases. The shear rate on the cup wall is normalized by its maximum value. Twenty lines overlap in Figure 11, and they are all very similar to each other near the tip. Each hydraulic mean depth L_{hd} agrees with the range of over 90% of its maximum shear rate value.

Figure 12 shows the simulations result for the constant R_c cases. The bob radii are varied as R_b=6.5, 7.5, 8, 8.1 mm, and the gaps are varied as h=2, 1, 0.5, 0.4 mm. The shear rate on the cup wall is normalized by its maximum value. When the horizontal axis of the figure is normalized by the gap h, the similar profiles were obtained. These simulation results indicate that the choice of L_{hd} is applicable to various bob geometries.

R_b [mm]	R_c [mm]	h [mm]
8	8.5	0.5
5	5.5	0.5
11	11.5	0.5
20	20.5	0.5
25	25.5	0.5
8.1	8.5	0.4
7.5	8.5	1
6.5	8.5	2

Table 1. Geometric parameters of the disk-shaped bob.

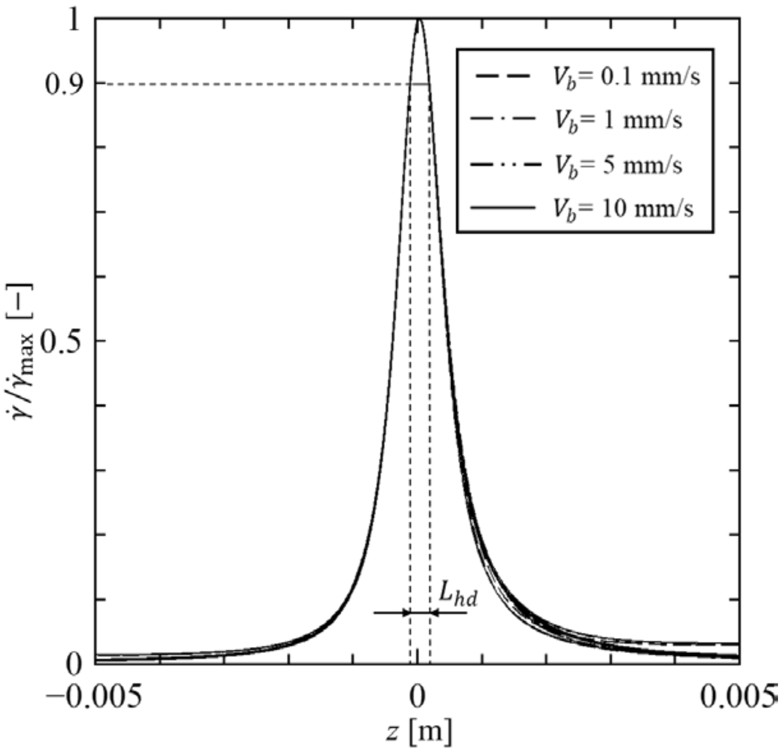

Figure 11. Normalized shear rate on cup wall surface near the tip. R_b=5, 8, 11, 20, 25 mm. L_{hd}=0.25 mm.

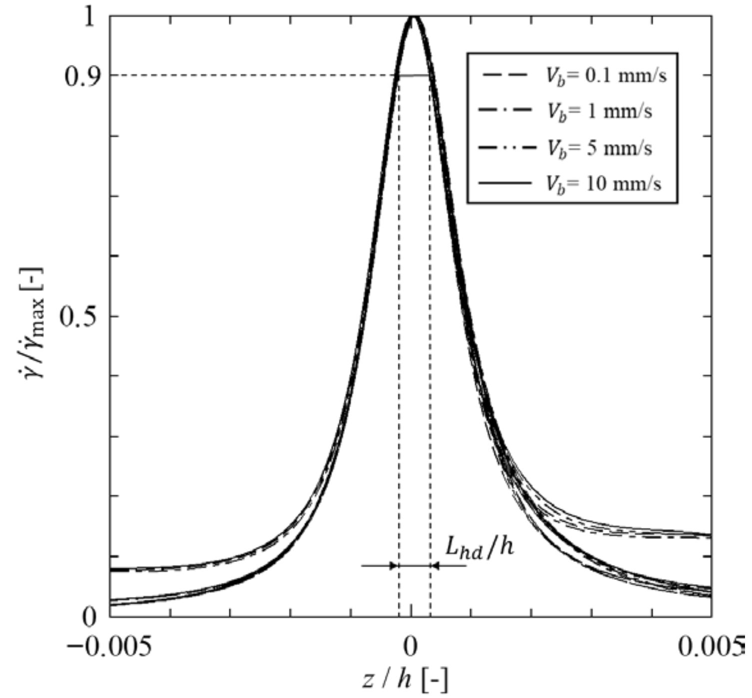

Figure 12. Normalized shear rate on cup wall surface near the tip. R_b=6.5, 7.5, 8, 8.1 mm. L_{hd}/h=0.5 mm.

3.4 Effect of Thickness of the Disk-shaped Bob on Resistance Force

The accuracy of the estimation of planar elongation viscosity can be improved by increasing the contribution of the planar elongation stress F_{PE} compared to the resistance force F'. In the case of the bullet-shaped bob, the ratio of F_{PE} to F' is about 0.4% [1] due to the bigger shear region as shown in Figure 2(b). However, in the case of the disk-shaped bob, the ratio can be dramatically improved up to 44.8% at V_b=10 mm/s, because the region of shear flow near the narrow gap is eliminated. We numerically evaluated the effect of the longitudinal length (bob thickness l) of the narrow gap, as shown in Figure 13, on the ratio of F_{PE} to F'.

Figure 14(a) shows streamlines in the flow field at l=5 mm and V_b=0.1 mm/s. Figure 14(b) shows a contour plot of the elongation rate. The maximum elongation rate is almost the same as that at l=0 mm and V_b=0.1 mm/s. A shear rate profile for the calculation domain is shown in Figure 14(c). Strong shear flow is obvious in the narrow gap region depending on the length of l and that increases the shear contribution, F_{ss} and F_{sn}. Figure 15 shows the effect of the thickness length l and the bob sliding speed V_b on the apparent resistance force F'. The numbers on the right side indicate the ratio of the elongation stress term F_{PE} to the apparent resistance force F' at V_b=10 mm/s. It is clear that the thinner disk-shaped bob is preferable for the measurement of elongation viscosity.

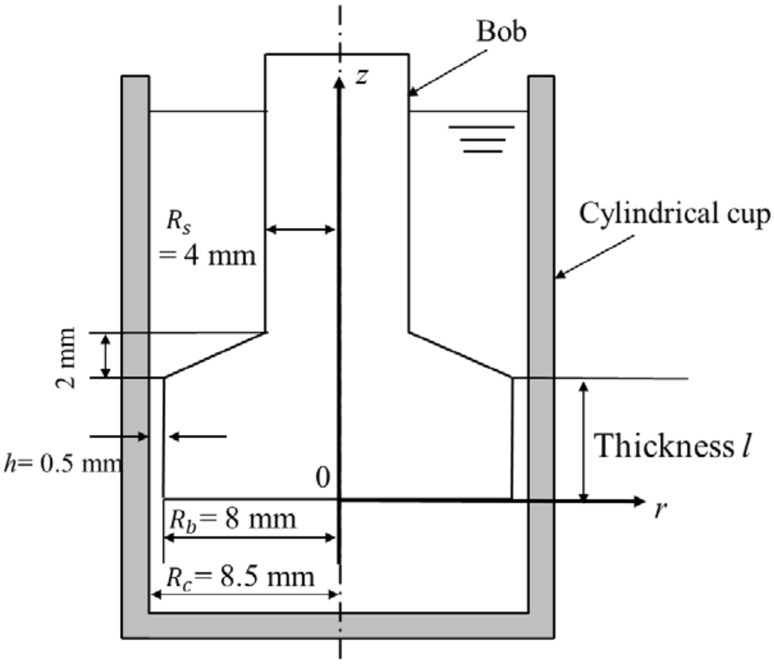

Figure 13. Schematic of flow with a disk-shaped bob and a cylindrical cup. The disk-shaped bob has thickness l.

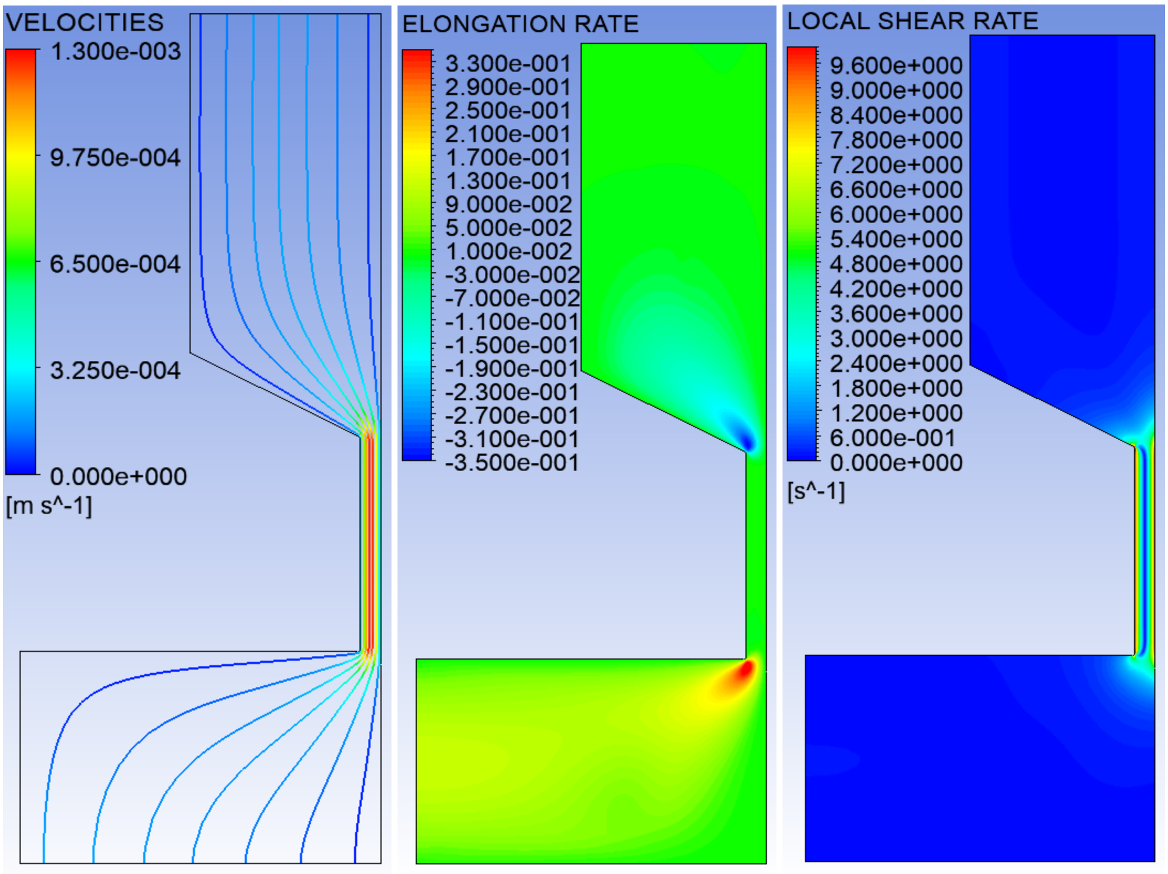

Figure 14 (a). Streamlines and velocity profile of the M1 fluid. Thickness of the disk-shaped bob is l=5 mm. Sliding velocity of the disk-shaped bob is V_b=0.1 mm/s, (b) Elongation rate distribution. l=5 mm, V_b=0.1 mm/s, (c) Shear rate distribution. l=5 mm, V_b=0.1 mm/s.

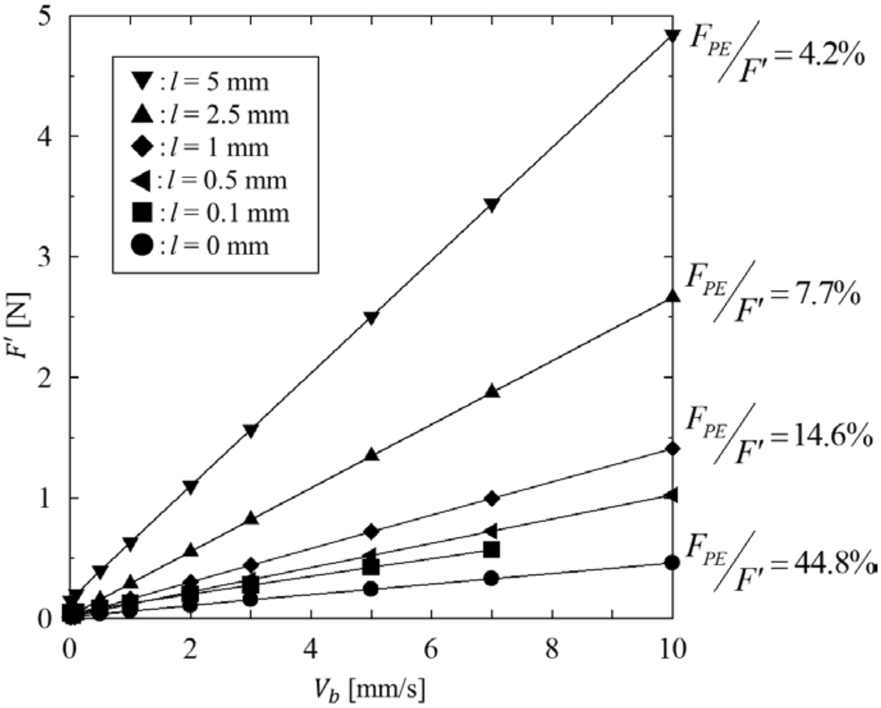

Figure 15. Apparent resistance force generated by flow between the cup and the bob. Left numbers indicate the contribution of planar elongation at a bob velocity V_b of 10 mm/s.

Conclusions

We performed a numerical simulation of a viscoelastic fluid for the measurement method using a disk-shaped bob developed by Sugihara et al. [2]. Approaching the gap, flow velocity increases dramatically, and a strong elongation velocity is clearly generated in the entrance region of the narrow gap.

The wall shear rate profiles near the tip are similar for four different bob sliding speeds. The width of the normalized strong shear region was the almost same as the hydraulic mean depth. Therefore, the validity of this assumption in the calculation of elongation viscosity for the disk-shaped bob was confirmed.

The effects of bob and cup geometry were examined. The hydraulic mean depth matched the region of high wall shear rate, confirming the validity of the use of the hydraulic mean depth as the representative length.

Shear rate distributions for the disk-shaped bob and the bullet-shaped bob are compared. The effect of shear in the disk-shaped geometry is much smaller than that in the bullet-shaped bob. The thinner disk-shaped bob is preferable for the measurement of elongation viscosity, because the influence of shear flow along the wall surface is significantly reduced.

Acknowledgements

The authors would like to thank Ms. Akiko Onishi and Mr. Wataru Kubota for technical assistance with the experiments. This work was supported by JSPS KAKENHI Grant Numbers (No. 17K06152) from the Japan Society for the Promotion of Science (JSPS).

References

[1] Sugihara, Y.; Kubota, W.; Yoshitake, Y.; Takahashi, T.; Iwata, S.; Nagumo, R.; and Mori, H.: Development of Mechanical Measurement Technique for Planar Elongation Viscosity Using Resistance Force on Pushing Bullet Bob. *Nihon Reoroji Gakkaishi*, 44, (2016), 175-183.

[2] Sugihara, Y.; Iwata, S.; and Takahashi T.: Evaluation of planar elongation viscosity of low-viscosity liquids using annular abrupt contraction flow around a sliding disk-shaped bob. *Rheologica Acta*, 57, (2018), 97-104.

[3] Giesekus, H.: A Simple Constitutive Equation for Polymer Fluids Based on the Concept of Deformation-Dependent Tensorial Mobility. *J. Non-Newtonian Fluid Mech.*, 11, (1982), 69-109.

[4] Rajagopalan, D.; Armstrong, R.; and Brown, R.: Finite element methods for calculation of steady, viscoelastic flow using constitutive equations with a Newtonian viscosity. *J. Non-Newtonian Fluid Mech.*, 36, (1990) 159-192.

[5] Marchal, J. M.; and Crochet, M. J.: A new mixed finite element for calculating viscoelastic flow. *J. Non-Newtonian Fluid Mech.*, 26, (1987), 77-113.

[6] Debbaut, B.; and Crochet, M. J.: Extensional effects in complex flows. *J. Non-Newtonian Fluid Mech.*, 30, (1988), 169-184.

[7] Nguyen, D. A.; and Sridhar, T.: Preparation and some properties of M1 and its constituents. *J. Non-Newtonian Fluid Mech.*, 35, (1990), 93-104.

[8] Binding, D. M.; Jones D. M.; and Walters, K.: The shear and elongation flow properties of M1. *J. Non-Newtonian Fluid Mech.*, 56, (1990), 121-135.

[9] Ushida, A.; Kawami, M.; Uchiyama, H.; Narumi, T.; Kayaba, R.: Flow properties of microbubble/polyethylene glycol mixtures passing through orifices and slits. *Nihon Reoroji Gakkaishi*, 40, (2012), 61-68.

[10] Te Nijenhuis, K.; Van Benschop, H. J.: Glass transition temperature, specific gravity, viscosity and viscoelastic properties of the test fluid M1. *J. Non-Newtonian Fluid Mech.*, 35, (1990), 179-187.

Addresses: Shunsaku Ito, Department of Life-Science and Applied Chemistry, Graduate School of Engineering, Nagoya Institute of Technology, Gokiso-cho, Showa-ku, Nagoya, Aichi 466-8555, Japan. email: ito.shunsaku@chemeng.nitech.ac.jp

Prof. Dr. Shuichi Iwata, Department of Life-Science and Applied Chemistry, Graduate School of Engineering, Nagoya Institute of Technology, Gokiso-cho, Showa-ku, Nagoya, Aichi 466-8555, Japan. email: iwa@nitech.ac.jp

Dr. Yukinobu Sugihara, Department of Electronic Control Engineering, National Institute of Technology, Nagaoka College, 888 Nishikatakai, Nagaoka, Niigata 940-8532, Japan. email: ysugi@nagaoka-ct.ac.jp

Prof. Dr. Tsutomu Takahashi, Department of Mechanical Engineering, Nagaoka University of Technology, 1603-1, Kamitomioka Nagaoka, Niigata 940-2188, Japan. email: ttaka@nagaokaut.ac.jp

DOI: 10.24352/UB.OVGU-2019-004
TECHNISCHE MECHANIK, 39, 1, (2019), 30 - 38
submitted: November 1, 2018

Shear Layer Generation in Yield Behavior of Gels

Y. Sato, I. Homma, T. Takahashi

The shear layer generation at the yield point and its recovery process are observed by the twin-drive rheometer. When the stress-ramp test or the shear rate-ramp test is applied to the colloidal gels, the stresses acting on the plates show different values under certain conditions. The bottom plate is used as a driving side, and the stress is controlled. Additionally, the upper plate side is a fixed side. The stress acting on the upper plate increases with the bottom plate, but at the occurrence of the yield behavior the different curve from the bottom plate is suddenly revealed. The stress acting on the upper plate becomes low, and the difference between the two stresses increases with an increasing stress or shear rate. This means that the shear stress is not constant over the gap, and a shear layer is generated. In the case of a small stress-ramp rate, the stress on the upper plate becomes the bottom value from the bottom plate stress at the yield point, but it returns to the same curve a few seconds later. The two layers of the shear layer generated at the yield point are adhered by the structure recovery, and the shear layer then disappeared.

1 Introduction

There are many fluids which show this yield-like behavior while having flowability in our daily life. Food products such as margarine and mayonnaise, cosmetics such as skincare cream, and a type of grease are such examples of this yield-like behavior. Oils, particles, and bubbles in the products form the macro structure from the weak binding force and maintain their shape from a weak force like gravity. Furthermore, when the force exceeds a certain value, the fluid suddenly begins to flow. The concept of the yield was presented by Bingham (Bingham ES, 1916). This sudden change is similar to the yield point in the metal, soft matter can recover it up to the mechanical property before the yield by the static time, which is completely different from the yield of metal. These phenomena are closely related to the functionality of the product. For example, the handling property in the cosmetics field such as skincare cream is controlled by the yield stress before taking the sample from the container (Nikko Chemicals Co. Ltd., 1996). However, the research related to the mechanism of the yield behavior on the functionality of the soft matter is still being studied (Okamoto T et al., 2014; Nabata Y et al., 2014; Watanabe K et al., 2012; Ovarlez G et al., 2012; Garcia MC et al., 2016; Dinkgreve M et al., 2016; Ovarlez G et al., 2013; Brown JR et al., 2011; Boujel J et al., 2012).

Although a previous research paper written by Barns claimed the materials considered as “Bingham’s plastic material” did not show the true yield stress (meaning the material continues to flow under the yield stress), it was not considered to be the wall slip (Barns et al., 1985). The apparent viscosity increases up to an infinitely high value over time by using the rough plate (Coussot et al. 2006; Moller et al. 2009). The flow, including the wall slip, shear-banding, and the shear-layer is an important factor when the industrial products are used. It is investigated by using special facilities and techniques. (Pérez-González, J et. al, 2012; Coussot P et. al, 2015).

The author has reported that the shear layer at the yield-like behavior is evaluated by the twin-drive rheometer, which is equipped with a conventional measurement system in the upper and the bottom plates. Each of the plates can independently control the torque applied to the sample and measure the strain that is generated. Thus, it is possible to simultaneously measure the shear stress acting on the upper plate while applying the shear stress to the bottom plate. The stress-ramp test and the shear-rate-ramp test were carried out with various acceleration values, and the stress difference between the upper plate and the bottom plate was measured. Based on these results, we discussed the generation of the shear layer in the gels (Sato Y, 2018). In this research study, we have focused on the generation of the shear layer in yield behavior of gels using the twin-drive rheometer in clay dispersing colloidal gels.

2 Materials and Experimental Methods

2.1 Sample

The colloidal gels used in this experiment consisted of silicone oil, hectorite, and PEO. The concentration of the hectorite (800×80×1~3 nm) is 8wt%, and the PEO concentration is 2wt%. The microscope image is shown in Figure 1. The black lump (seen on the right side) of approximately 0.1 mm is an agglomerate of hectorite. The silicone oil was used as a Newtonian fluid (Shin-Etsu Chemical Co., Ltd.).

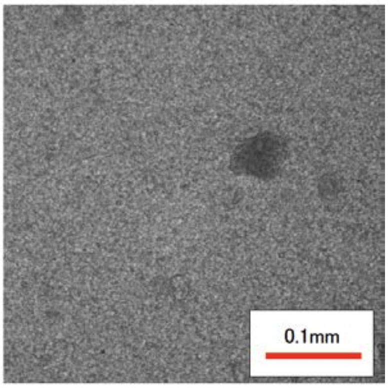

Figure 1. The observed microscope image in clay dispersing colloidal gels.

2.2 Rheometer

In this study, we used the rheometer which is MCR702 (Anton Paar Co., Ltd.) which is twin-drive stress-controlled rheometer. As we have already described above, the rheometer can measure independently each of the stress in the upper and the bottom plates. In this research, "2EC isolation transducer mode" which rotates only the bottom plate while fixing the upper plate was used as shown in Figure 2. Both of the upper and the bottom plates are the flat disk of 25 *mm* in diameter and they consist the parallel plate geometry. Both plates are made from the stainless steel. The gap between the plates is constant at 0.5 *mm* in all test. 0.5 *mm* is enough large to the particle size of the colloidal gels.

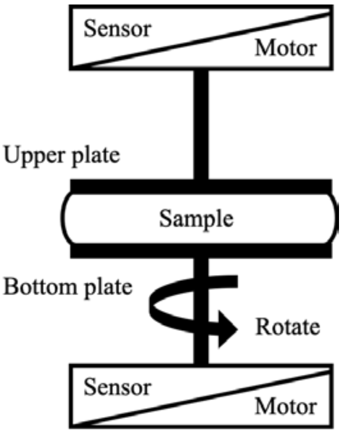

Figure 2. The outline drawing of the twin-drive rheometer.

2.3 Stress-ramp Test

The accurate value of the yield stress cannot be evaluated using the step shear test due to the destroyable discontinuous rapid acceleration that occurs at the start of the test. Therefore, the generation of the yield behavior is observed by the stress-ramp test in this study. The stress-ramp test is a rheological test, which increases the shear stress gradually from zero to a certain value in the same stress-ramp rate. The stress-ramp rate is an important parameter related to the time-dependent characteristics of the samples.

In the stress-ramp test using the twin-drive rheometer, it seems possible to detect the generation of the shear layer by measuring and comparing the stress acting on the upper and the bottom plate, in addition to the yield behavior. In a steady shear flow field, Couette flow generally occurs. In this steady flow state, the same shear stress should be acting on the upper and the bottom plates. Even if the shear band is formed, there is no difference in shear stress acting on the upper and the bottom plate in the steady flow field. On the other hand, a stress difference between the upper and the bottom plates would be observed in the transient flow field by the stress-ramp test, because of the delay of the development of the flow field. Furthermore, there is a possibility to detect the generation of the non-uniformity in the velocity profile caused by the shear-band or the shear layer, by monitoring the occurrence of the stress difference.

In this experiment, the influence of the transient flow field on the stress of the upper and bottom plates in the stress-ramp test was investigated. By substituting the torques $\boldsymbol{M_{upper}}$ and $\boldsymbol{M_{bottom}}$ that are acting on the upper and the bottom plates during the flow into the equations (1) and (2), the stresses acting on each of the upper and bottom plates were calculated.

$$\boldsymbol{\tau_{upper}}\left(\boldsymbol{M_{upper}}\right) = \frac{4\boldsymbol{M_{upper}}}{3\pi \boldsymbol{d}^3} \tag{1}$$

$$\boldsymbol{\tau_{bottom}}(\boldsymbol{M_{bottom}}) = \frac{4\boldsymbol{M_{bottom}}}{3\pi \boldsymbol{d}^3} \tag{2}$$

Here, d is the radius of the plate used for the measurement.

The stress-ramp test with a stress-ramp rate of 0.5 Pa/s was carried out after the pre-shear to eliminate the influence of the loading sample in each test. The static time was set after the stress-ramp test to recovers up to the mechanical property and the sample can show the same yield behavior again by the static time. All tests confirmed the repeatability from multiple experiments.

2.3 Shear rate-ramp Test

In the stress-ramp test, the viscosity decreases suddenly due to the occurrence of the yield behavior. In the case of a stress-controlled test, the plate on the driving side increases the rotation speed with rapid acceleration in order to reach the corresponding shear rate according to a sudden viscosity drop. The stress difference measured at the time of the sudden change in the transient rotation may not only include the yield behavior, but also the effect due to the rheometer such as the inertial force of the plate. The shear rate-ramp test (which increases the rotational speed at a constant ratio) was conducted to confirm the inertial effect. The shear rate increased from zero to 100 s^{-1} for the colloidal gel at a specific ratio. The parameter to consider is the shear rate-ramp rate *b*, the stress acting on the shear layer, and other layers in the transient test. The pre-shear and the static time are also applied, such as the stress-ramp test. All the tests were able to confirm the repeatability from multiple experiments.

3 Result and Discussion

3.1 Stress-ramp Test

Figure 3 shows the transient behavior of the upper stress at each stress increase ratio. In addition, the value of the yield stress estimated from stress-strain curve (where the slope of the curve suddenly changes) is pointed out by an arrow in each plot in Figure 3. Here, τ_{y1} and τ_{y2} are the first and second yield stress, respectively. The bottom stress acting on the bottom plate is applied as the input condition. The upper stress acting on the upper plate, which is the fixed side for this test, is followed with the bottom stress on the lower plate. However, the upper stress cannot follow the bottom stress when the stress exceeds a certain stress level. The sudden stress difference between the upper and bottom plates is in good agreement with the yield stress estimated from stress-strain curve, which shows that the stress distribution of the sample in the plates became non-uniform due to the sudden viscosity decrease at the yield behavior. Figures 4 shows the time change of the upper and bottom stress for the stress-ramp test for the silicone oil. The upper stress shows a slightly lower stress than the bottom stress as the stress-ramp rate increases, but the stress difference is much smaller than the colloidal gel shown in Figure 3.

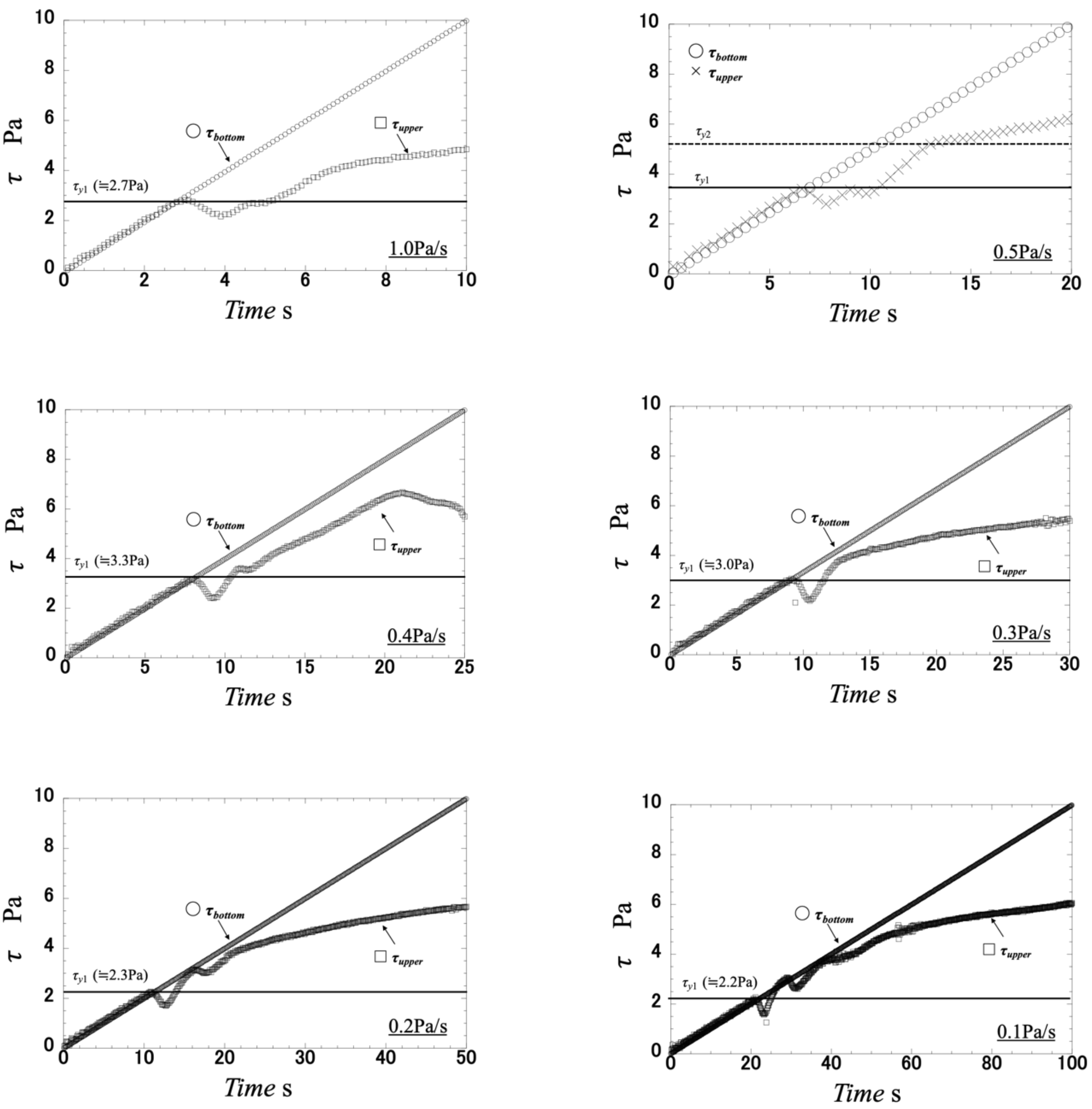

Figure 3. Bottom stress τ_{bottom} and upper stress τ_{upper} during the stress-ramp test by MCR702 on the colloidal gels.

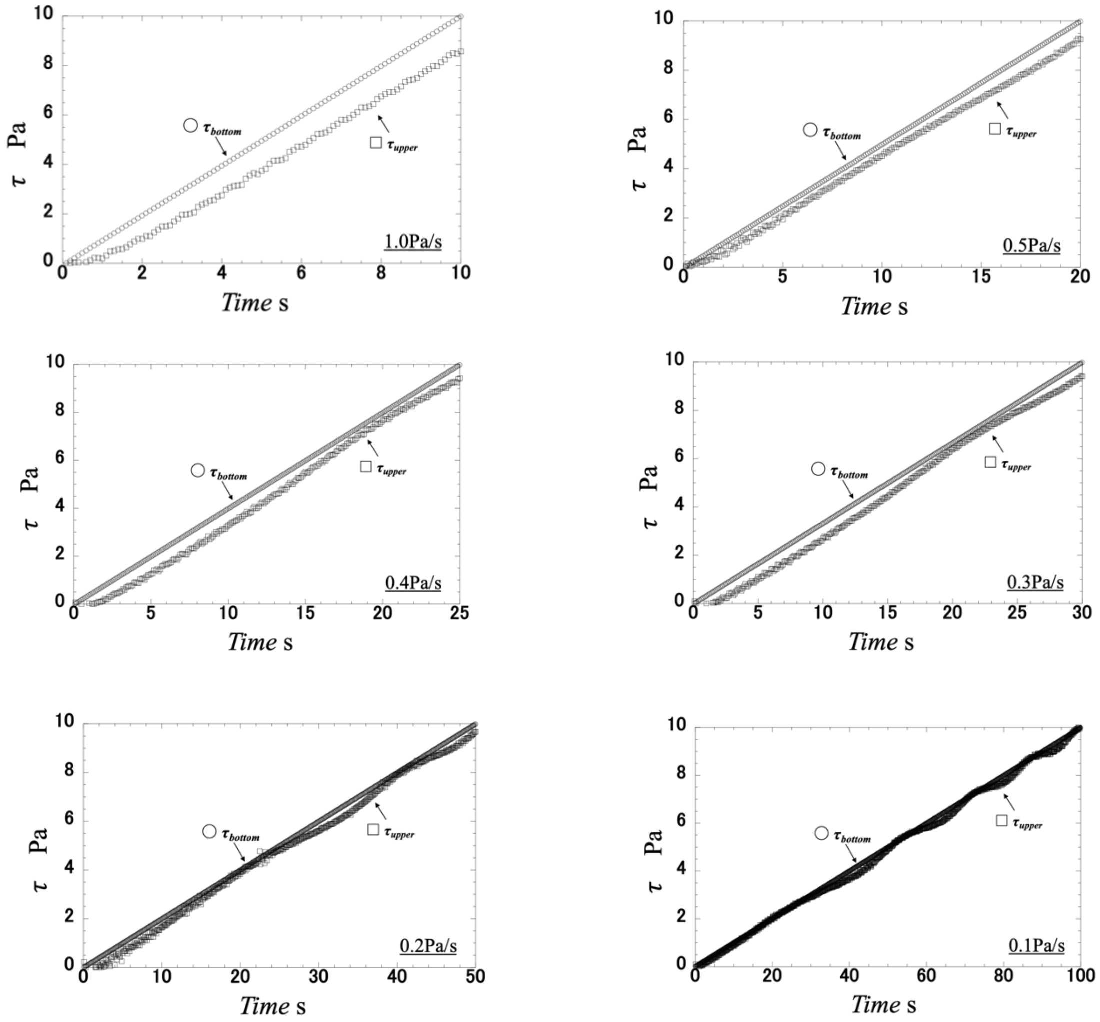

Figure 4. Bottom stress τ_{bottom} and upper stress τ_{upper} during the stress-ramp test by MCR702 on the silicone oil.

The results were observed in more detail in Figure 3. Regarding the behavior after the stress difference occurred between the plates, the stress difference generated at the first yield recovered immediately and exhibited almost the same stress value as the bottom plate once again in the case of the 0.3 or less stress-ramp rate. After that, the upper stress acting on the upper plate decreased at the second yield and increased again after showing the minimum value. In the weak bond which formed the structure, it is considered that the shear layer is formed due to crack propagation, such as the dislocation of the metal fracture after the first yield generated the fracture from a weak part. In the region where the macrostructure is destroyed, the viscosity of the sample decreases and the shear rate increases. This does not occur throughout the entire flow path, but rather just the shear layer. However, when the stress increase ratio is low, the shear layer is thin and the rotation speed is low. The shear layer disappears immediately, and the stress difference between the upper and bottom plates ends only at the moment the yield behavior occurs. After that, the structure breaks incrementally until the second yield, and the viscosity decreases slowly. On the other hand, the shear layer formed by the first yield rapidly increases the rotational speed of the plate and decreases the viscosity of the fluidization when the stress increase ratio is 1.0 *Pa/s*. Therefore, the stress difference between the upper and the bottom plates at a stress-ramp rate of 0.3 or less does not occur. In addition, the second yield was observed only at 0.5 *Pa /s*. The second yield is considered, as some macroscopic / microscopic structure is formed during shear flow and it occurs when it rapidly breaks, even though the formation of the structure related to the second yield is inhibited when the stress increase rate is high. This is also considered as an influence of the shear layer. The authors reported the following as a previous study (Homma I, 2017). The high-speed optical microscopy which can observe the structure within several hundred microns was conducted in order to analyze the velocity of the oil particle. From the start of the flow to 1.5

seconds, the particle close to the stationary plate moves at almost the same velocity as the rotational bottom plate. This means that the shear-layer is generated in the vicinity of the stationary plate, and the sample above the shear-layer moves at the velocity close to the rotational bottom plate as a bulk. Over 1.5 seconds, the velocity decreases suddenly and approaches zero. The shear-layer expands to the entire gap and forms a Couette flow. Eventually the particle velocity approaches zero near the stationary upper plate. It was verified to quantitatively evaluate the occurrence of the shear layer generation, the increase of the thickness of the shear layer, and the development of the velocity distribution over time. This result shows that a thin shear layer was formed in the vicinity of the fixed plate at the beginning of the flow, and is the reason for the above consideration.

Next, we examine the relationship between the upper stress and the strain obtained in Figure 3. The result is shown in Figure 5. All the results of the stress-ramp rate are plotted on the one curve. The upper stress maintains a nearly constant value over a wide strain range. At all stress-ramp rates, the stress increases almost in proportion to the strain in the low strain region and the region dominated by elastic behavior before the first yield have been detected, which was not seen in other results. The upper stress decreases after the first yield and reaches the same curve as the other results. After that, the upper stress starts to increase again for the second yield. Furthermore, the viscosity was calculated based on the shear stresses measured on the upper and the bottom plates, respectively. The relationship between the shear rate and viscosity was investigated. Figure 6 shows the relationship between the upper viscosity, the bottom viscosity, and the shear rate. The elastic behavior of the low strain region observed in Figure 5 is not discussed because the shear rate is too small. A significant viscosity was measured immediately after the first yield, and a much higher viscosity than the other results was obtained. As the stress rate increases, it shows low viscosity from the start of flow. Although it seems that the bottom viscosity increases as the stress increase ratio increases, when evaluated by the shear stress of the upper plate fixed side all results appear to agree very well. Although the detailed reason is still unknown, there is a possibility that the conventional rheometer cannot measure the accurate viscosity in the gels exhibiting the yield behavior.

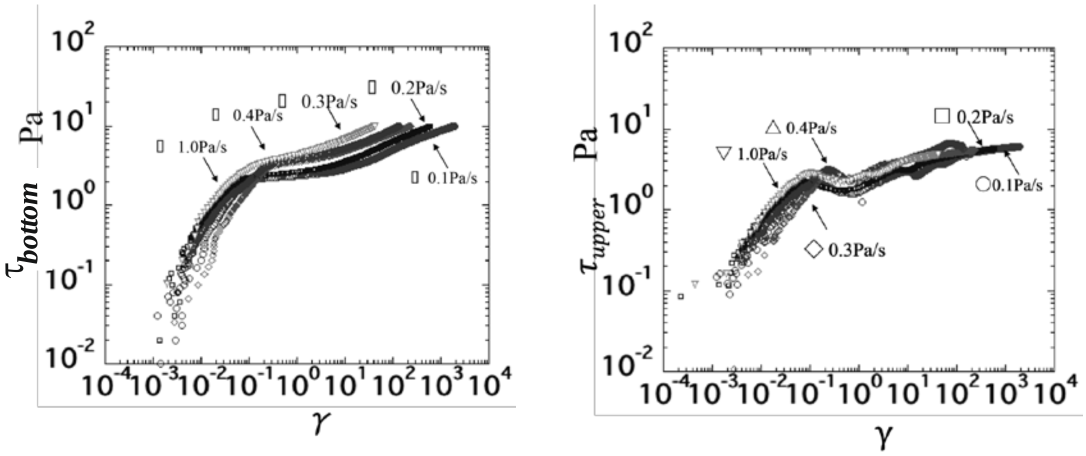

Figure 5. Bottom stress τ_{bottom} and upper stress τ_{upper} -straint by MCR702 on the colloidal gels.

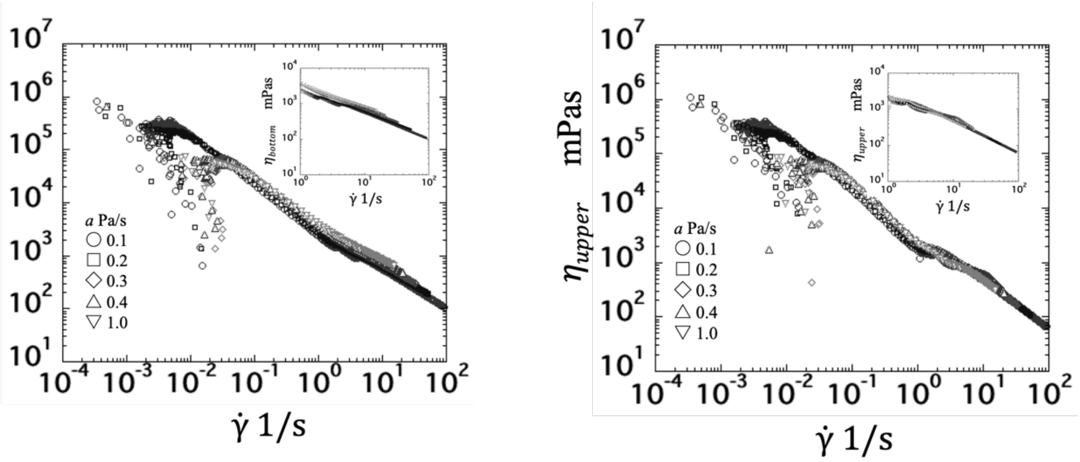

Figure 6. Bottom viscosity η_{bottom} and upper viscosity η_{upper} -shear rate curve on the colloidal.

3.2 Shear rate-ramp Test

In the stress-ramp test, the viscosity decreases and the rotational speed increases suddenly by the formation of the shear layer after the yield behavior. The shear rate-ramp test was carried out to confirm whether the stress difference is caused by the problem of the control system of the rheometer, or the property of the sample. Figure 7 shows the stress-strain curve and the time change of the stress during the test. At a shear rate-ramp rate b = 5.0 s^{-2}, the stress difference between the plates is very small after the occurrence of the yield. It is thought that the stress non-uniformity is present because the strain is greatly smaller than the stress-ramp test, so that the restructuring was influenced relatively strongly and the flow field is in a closely static state. The bottom stress exhibits the periodic fluctuation, but it is due to the control of feedback system to reach the shear rate to a certain value. From the above results, the stress difference during the stress-ramp test is not caused by the sudden change of the rotational speed, but is due to the formation of the shear layer by the yield behavior and the flow after the yield. In addition, the stress difference between the upper and the bottom plates is easier to generate in the stress-ramp test, which applies the strain with an acceleration rather than the shear rate-ramp test which applies the strain at a constant ratio. The shear layer develops due to the accelerated flow, which does not disappear by the restructuring, and results in the stress non-uniformity appearing strongly.

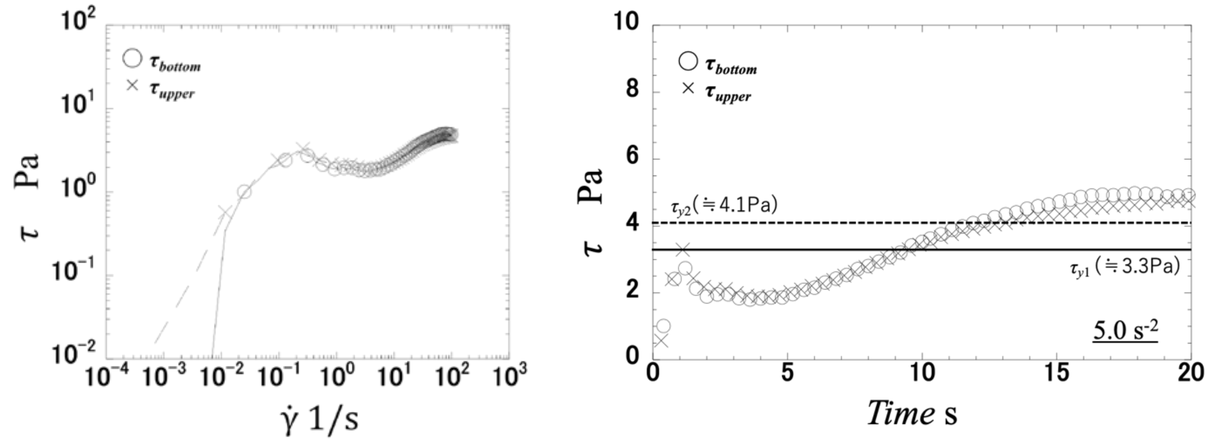

Figure 7. Bottom stress $\boldsymbol{\tau_{bottom}}$ and upper stress $\boldsymbol{\tau_{upper}}$ during the shear rate sweep test by MCR702 on the colloidal gels.

4 Conclusions

In this study, the stress-ramp test and the shear rate-ramp test was conducted using the twin-drive rheometer to the colloidal gel, which results in the yield behavior being recognized. Additionally, the stress acting on the upper and the bottom plate was measured, as well as the evaluation of the formation of the shear layer in the flow. The obtained results are summarized below.

In the colloidal gel, the bottom stress was applied as the input condition during the stress-ramp test, but the upper stress deviated from the bottom stress after the yield behavior. When the stress-ramp rate is sufficiently small, the elastic behavior before the yield was observed and the upper stress reached the same value, even though the stress difference occurred after the first yield. When the stress-ramp rate is high, the elastic behavior was not observed and the relationship between the upper stress acting on the fixed plate and the strain appeared on the same curve at any stress-ramp rate. Furthermore, the bottom viscosity evaluated by the driving plate shows the different value depending on the stress-ramp rate, but the upper viscosity was in good agreement regardless of the stress-ramp rate. It also means that the accurate viscosity could not be evaluated by a conventional rheometer, because of the influence of the shear layer in the case of such fluids that exhibit the yield behavior.

References

Barnes H., Walters K.: The yield stress myth., *Rheol. Acta*, 1985, Vol. 24, 323.

Bingham ES: An investigation of the laws of plastic flow, 1916, *Bull US*.

Brown JR, Callaghan PT: *Soft Matter*, 2011, Vol. 7, 10472.

Boujel J., Coussot P.: Measuring yield stress: A new, practical, and precise technique derived from detailed penetrometry analysis, *Rheol. Acta*, 2012, Vol. 51, 867.

Coussot P., Tocquer L., Lanos C., Ovarlez G.: Macroscopic vs. local rheology of yield stress fluids, *J. Non-Newtonian Fluid Mechanics*, 2015, Vol. 158, 85.

Dinkgreve M., Paredes J., Denn MM, Bonn D.: On different ways of measuring "the" yield stress, *J. Non-Newtonian Fluid Mechanics*, 2016, 238, 233.

Garcia MC, Alfaro MC, Munoz J.: Creep-recovery-creep tests to determine the yield stress of fluid gels containing gellan gum and Na+, *J. Biological Eng.,* 2016, Vol. 114, 257.

Homma I., Takahashi T., Noda K., Sekine T., Kitajima M., Sogabe A.: Macroscopic Structure Change and Optical Anisotropy Induced by Yield Behavior of Clay Dispersing Colloidal Gel, *Nihon Rheoloji Gakkaishi (J. Soc. Rheol. Jpn)*, 2017, Vol. 45, 277.

Moller PCF, Fall A., Bonn D.: Origin of apparent viscosity in yield stress fluids below yielding, *EPL*, 2009, Vol. 87, 38004

Nabata Y., Saito T., Tetsu M.: Rheological Properties of α -Gel Lamellar Samples with Different Morphology, *Proc. 62th Rheol. Symp*., 2014, Vol. 306, (in Japanese).

Nikko Chemicals Co. Ltd., Nippon Surfactant Indusiries Co Ltd.: *Keshouhin Handbook*, Toshiki Pigment Co., Ltd, , Chuo Printing Co., Ltd, Niigata (in Japanese). 1996.

Okamoto T.: *Netsu Sokutei*, 2010, Vol. 37 (3), 124, (in Japanese).

Ovarlez G., Bertrand F., Coussot P., Chateau X.: Shear-induced sedimentation in yield stress fluids, *J. Non-Newtonian Fluid Mechanics*, 2012, Vol.177, 19.

Ovarlez G., Cohen-Addad S., Krishan K., Goyon J., Coussot: On the existence of a simple yield stress fluid behavior, *J. Non-Newtonian Fluid Mechanics*, 2013, Vol.193, 68.

Pérez-González J., López-Durán JJ, Benjamin MM, Rodríguez-González F.: Rheo-PIV of a yield-stress fluid in a capillary with slip at the wall, *Rheol. Acta*, 2012, Vol. 51, 937.

Yasunori Sato, Homma I., Takahashi T., Noda K., Sogabe A.: Evaluation Method of Shear Layer Generation at Yield Behavior of Softmaters, *Nihon Rheoloji Gakkaishi (J. Soc. Rheol. Jpn),* 2018, Vol. 46, 67.

Watanabe K., Inoue H., Teshigawara T., Kimura T.: Gel Prepared in Sodium Methyl Stearoyl Taurate/ Behenyl Alcohol/Water System-Characterization of Structural Changes with Water Concentration, *J. Oleo Sci*, 2012, Vol. 61, (1), 29.

Address: 662 Mechanical Engineering Depertment, 1603-1 Kamitomioka, Nagaoka-city, Niigata, Japan
email: s143039@stn.nagaokaut.ac.jp

DOI: 10.24352/UB.OVGU-2019-005 TECHNISCHE MECHANIK, 39, 1, (2019), 39 – 50
submitted: November 01, 2018

The Influence of Different Arrangements of Shallow Dimples on the Resistance of Plates Subjected to Relative Fluid Motion

J. Praß, H. Wannmacher, J. Franke, S. Becker

Shallow dimples have long been a scientifically investigated topic to reduce the flow resistance of objects subjected to overflow. Most of the investigations on the influence of dimples on flow resistance have so far been carried out experimentally. Although the arrangements and flow conditions are often similar, different research activities conclude differently concerning the effect of the surface structures. This also leads to disagreement regarding the causes of flow resistance reductions. In this paper, time-resolved Large Eddy Simulations on two different, already experimentally investigated setups of dimples have been carried out to better understand the effects of dimples on the surface being subjected to relative fluid motion. In one case the dimples were examined in overlapping arrangement, in the other case in a non-overlapping arrangement. We were able to show that the formation of streaks near the surface significantly influences the local contribution to the flow resistance. For the overlapping arrangement, only a slight resistance reduction of 0.12 % was determined. For the non-overlapping arrangement, the mean resistance reduction was found to be 3.16 %. Regardless of the resistance reduction determined, a clear interaction between longitudinal vortices near the plate and local contributions to flow resistance could be demonstrated. Since these longitudinal vortices are directly influenced by the dimples, it is very likely that an optimized arrangement of the dimples, adapted to the flow conditions, can reduce the resistance.

Nomenclature

A	m^2	wetted area projected parallel to flow direction
C_w	-	WALE constant
D	m	dimple diameter
F_t	$\mathrm{kg\,m\,s^{-2}}$	total resistance force
H	m	height of computational domain
L_s	m	mixing length
R_c	-	correlation coefficient
S^d_{ij}	s^{-2}	traceless symmetric part of the square of the velocity gradient tensor
$\hat{S}_{ij}$	s^{-1}	rate-of-strain tensor for the resolved scale
T	-	dimensionless period time
V	m^3	volume of a cell
c_F, c_{F0}	-	total drag coefficient, total drag coefficient of smooth plate
d	m	distance to the wall
$\hat{g}_{ij}$	s^{-1}	velocity gradient tensor
h	m	dimple depth
l_x	m	streamwise distance
l_z	m	spanwise distance
p	$\mathrm{kg\,m^{-1}\,s^{-2}}$	pressure
r	m	dimple edge radius
s	m	spacial displacement
s_z	m	spanwise shift
t	s	time
u	$\mathrm{m\,s^{-1}}$	velocity
u, v, w	$\mathrm{m\,s^{-1}}$	velocity components in x, y and z-direction
x, y, z	m	spatial coordinates
y^+	-	dimensionless wall distance
δ_{ij}	-	kronecker delta

Δx^+	-	dimensionless streamwise distance
Δz^+	-	dimensionless spanwise distance
κ	-	von Kármán constant
μ_t	$\mathrm{kg\,m^{-1}\,s^{-1}}$	eddy viscosity
ν	$\mathrm{m^2\,s^{-1}}$	kinematic viscosity
ρ	$\mathrm{kg\,m^{-3}}$	density
τ_w	$\mathrm{kg\,m^{-1}\,s^{-2}}$	wall shear stress
τ_{ij}	$\mathrm{m^2\,s^{-2}}$	sub-grid structure stresses
ξ	m	spatial coordinate
NOL		non-overlapping dimple arrangement
OL		overlapping dimple arrangement
WALE		Wall-Adapting Local Eddy-Viscosity Model

Subscripts and Superscripts

$\bar{\square}$	temporal average of a quantity
$\hat{\square}$	spatially filtered quantity
$\square'$	fluctuating part of a quantity
in	inlet
max	maximum
mean	temporal average
ref	reference
i, j	index
∞	bulk

1 Introduction

Flow-induced resistance in viscous fluids is an important phenomenon that affects the efficiency of many technical systems. A distinction is usually made between form and friction resistance. As friction losses occur wherever fluids of any kind – such as air or water – show relative velocities to walls they interact with, the amount of power expended globally to overcome these losses is significant. While the form resistance is determined by the projected area of a body perpendicular to the direction of the relative movement – i. e. shape and cross-section – friction resistance is mainly dependent on dimension and properties of the surface that is overflown. While form resistance is only important in the case of bodies surrounded by flow, friction resistance plays an important role in both the flow around and through objects. Since the flow resistance of moving objects such as a car or an airplane as well as of fluid transport, for example through pipelines, has to be overcome by means of energy consumption, many research projects deal with investigations on the reduction of resistance.

In order to reduce the frictional resistance active and passive methods exist. Classical active methods are characterised by the fact that the flow near the wall is influenced by actuators in order to keep the flow resistance low. Recent research aims to flatten the velocity profile by increasing the flow velocity near the wall, which destabilizes the turbulence downstream and relaminarizes the flow (Kühnen et al. (2018)). So far, however, this effect could only be observed in pipe flows. Passive methods, such as the use of riblets (e. g. Garcia-Mayoral and Jimenez (2011)), protrusions (e. g. Sirovich and Karlsson (1997)), tabs (e. g. Park et al. (2006)) or grooves (e. g. Krieger et al. (2018)), are aimed at changing the wall geometry or structure in order to also modulate the flow, and thereby decreasing the resistance. The potentials for resistance reduction through active methods such as boundary layer suction (e. g. Antonia et al. (1994)), boundary layer blowing (e. g. Park and Choi (1999)), moving walls (e. g. Baron and Quadrio (1996)) and boundary layer influencing (e. g. Cimarelli et al. (2013)) are higher than with passive methods, but this effect is often relativized in the overall energy balance by the energy consumption of the actuators (Quadrio and Ricco (2004)). In addition, actuators are susceptible to failures, require maintenance and additionally increase the total weight of a system, which is why passive resistance reduction methods are no less important in research.

A promising and controversially debated approach is the use of dimples, which, in addition to reducing drag, offers other advantages such as weight reduction of the system and low sensitivity to pollution (Turow (2012)). Dimples were originally studied in terms of their ability to increase convective heat transfer from walls. While this aspect was intensively examined, only relatively few scientific papers deal with the potential of the drag reduction of dimples (Nesselrooij et al. (2016)). Since the mechanisms responsible for the reduction of drag are not yet fully understood and as various scientists use different test setups, the published results are inconsistent and sometimes even contradictory. Some scientists found in their investigations only resistance increases (e. g. Lienhart et al. (2008); Lashkov and Samoilova (2002)), while others found reductions of up to 20 % for low Re (Veldhuis and Vervoort (2009)) and 17 % for high Re in experiments (Kiknadze et al. (2012)). However, the results of the authors Kiknadze et al. (2012) are discussed critically, as the experiments and related results could not yet be reproduced and thus validated. Resistance reductions have been demonstrated for dimples with depth to diameter (h/D) ratios of less than 10 % in different arrangements (Nesselrooij et al. (2016); Veldhuis and Vervoort (2009); Tay (2011); Tay et al. (2015)). Tay et al. (2015) discovered in invasive (hot-wire anemometry) experiments that longitudinal vortices introduced by the dimples near the wall have similar effects on drag reduction as active methods. Since these structures depend very strongly on the flow conditions and it is difficult to measure them from a measurement point of view – invasive methods show interactions with the flow, laser-based methods can only be carried out close to the wall with considerable effort – numerical methods are required to investigate the near-wall structures in detail. In this work we therefore use time-resolved Large Eddy Simulations (LES) to examine the effects of two geometries already experimentally investigated by Nesselrooij et al. (2016). Additionally, a flat plate without dimples was simulated with the same mesh resolution and boundary conditions as a reference case in order to compare the results of the dimpled plates with.

2 Numerical Setup

In the present work, all simulations were carried out with Ansys Fluent (v17.2). In order to adequately represent the near-wall flow, an adaptive mesh and a wall-adapting local eddy-viscosity (WALE) model for sub-grid scale structure modeling were used.

2.1 Governing Equations

In Eq. 1 and 2 mass conservation and momentum conservation in filtered, incompressible form are given, respectively.

$$\frac{\partial \hat{u}_j}{\partial x_j} = 0 \tag{1}$$

$$\frac{\partial \hat{u}_j}{\partial t} + \frac{\partial \hat{u}_i \hat{u}_j}{\partial x_i} = -\frac{\partial \hat{p}}{\partial x_j} + \frac{\partial}{\partial x_i}\left(2\nu \hat{S}_{ij}\right) - \frac{\partial \tau_{ij}}{\partial x_i} \tag{2}$$

Here, $\hat{S}_{ij}$ denotes the rate-of-strain tensor for the resolved scale (Eq. 3), ν denotes the kinematic viscosity and τ_{ij} the sub-grid structure stresses that have to be modeled, in the current paper this was done using a WALE model as proposed by Nicoud and Ducros (1999) implemented in Fluent, i. e. the eddy viscosity μ_t is modeled according to Eq. 4,

$$\hat{S}_{ij} = \frac{1}{2}\left(\frac{\partial \hat{u}_j}{\partial x_i} + \frac{\partial \hat{u}_i}{\partial x_j}\right) \tag{3}$$

$$\mu_t = \rho L_s \frac{\left(S_{ij}^d S_{ij}^d\right)^{3/2}}{\left(\hat{S}_{ij}\hat{S}_{ij}\right)^{5/2} + \left(S_{ij}^d S_{ij}^d\right)^{5/4}} \tag{4}$$

where the mixing length L_s and the traceless symmetric part of the square of the velocity gradient tensor S_{ij}^d are defined as in Eqs. 5 and 6, respectively:

$$L_s = \min\left(\kappa d, C_\mathrm{w} V^{1/3}\right) \tag{5}$$

with the von Kármán constant $\kappa = 0.41$, the distance to the wall d, the WALE constant $C_\mathrm{w} = 0.325$ and the volume of the cell V,

$$S_{ij}^{d} = \frac{1}{2}\left(\hat{g}_{ij}^{2} + \hat{g}_{ji}^{2}\right) - \frac{1}{3}\delta_{ij}\hat{g}_{kk}^{2} \tag{6}$$

with the velocity gradient tensor $\hat{g}_{ij} = \partial\hat{u}_i/\partial x_j$.

2.2 Computational Setup

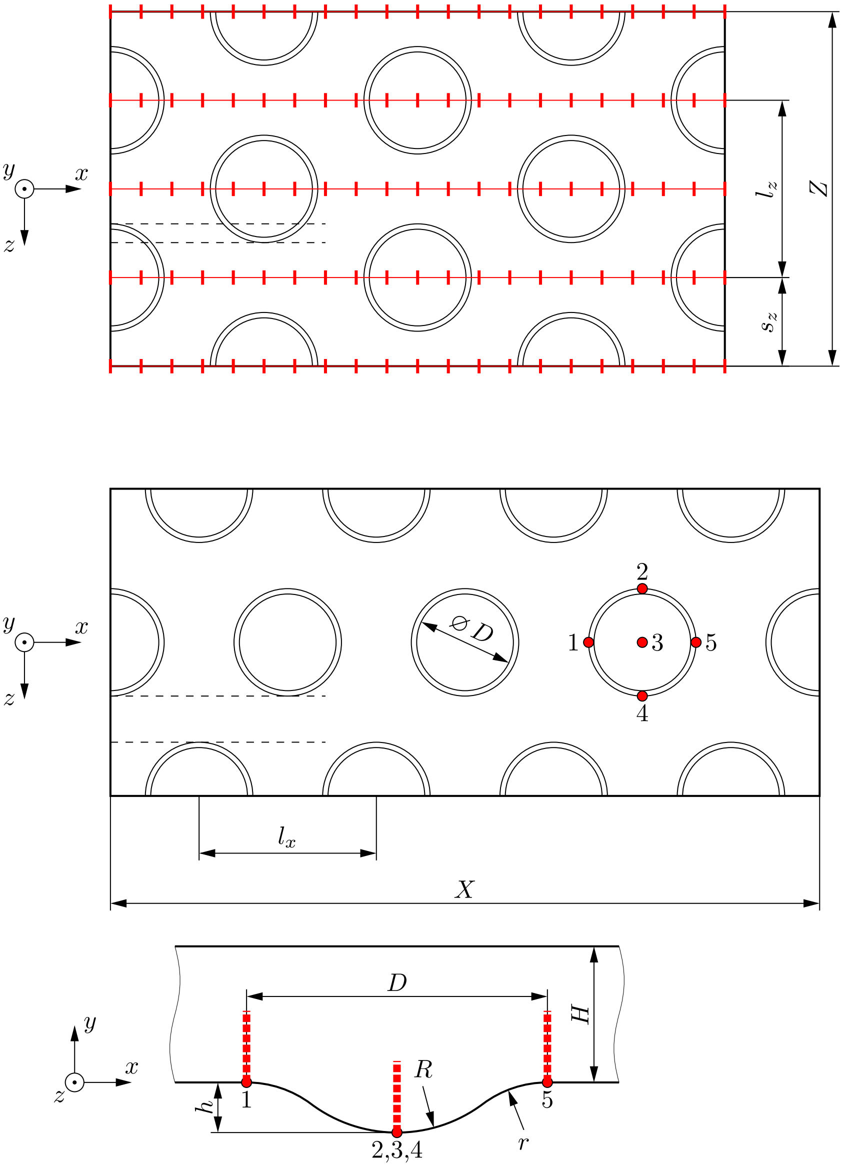

Figure 1: Arrangement and relations of dimples in the domain: overlapping (OL) arrangement with positions of monitor points for correlation analysis indicated (*top*), non-overlapping (NOL) arrangement with positions 1–5 for velocity analysis indicated at an arbitrary dimple (*middle*) and cross-section of a dimple with a path of measurement line for velocity analysis indicated (*bottom*)

To describe the dimples and their arrangement on a surface, six parameters are sufficient: The diameter D, the depth h, edge radius r, streamwise distance l_x, spanwise distance l_z and spanwise shift s_z. In the current paper, two staggered arrangements were used, meaning that $s_z = l_z/2$. In the first arrangement dimples were positioned overlapping (OL), in the second arrangement a non-overlapping (NOL) setup was used. The used setups and mentioned parameters are shown in Fig. 1, the corresponding unit-laden values are given in Tab. 1. The domains have been chosen large enough to be able to capture large-scale structures. The height was set to $H = \max(2\,l_x; 2\,l_z)$.

The dimpled wall was defined as a no-slip wall, the upper wall was defined as free-slip wall in order to simulate a free overflown plate and the boundaries in z-direction and x-direction as translational periodic boundary conditions. The Reynolds number based on dimple diameter $Re = D \cdot u/\nu$ was set via a pressure gradient in x-direction and was fixed at $Re \approx 35\,000$.

Table 1: Geometrical Setup as experimentally investigated by Nesselrooij et al. (2016)

case	D in mm	h/D in %	l_x/D	l_z/D	r/D
OL	20	2.5	2.859	1.650	0.5
NOL	20	2.5	1.650	2.859	0.5

Special attention was paid to the used mesh. To achieve values of $y^+ < 1$ as well as $\Delta x^+ < 10$ and $\Delta z^+ < 10$, the mesh near the wall was refined adaptively as shown in Fig. 2. In every adaptive layer perpendicular to the wall at least four cells were used. With these restrictions, a mesh convergence study was conducted to ensure that the results are not affected by discretization errors.

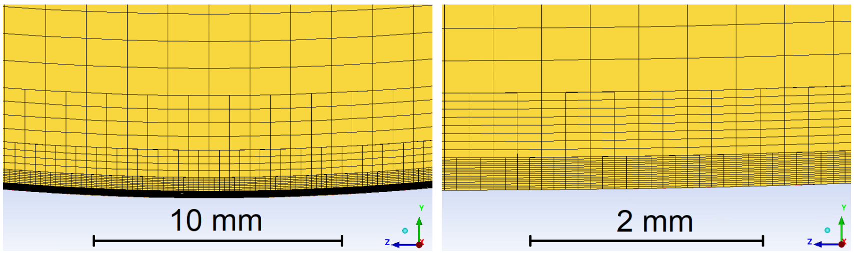

Figure 2: Detail of the computational mesh in direct proximity of a dimple (*left*) and magnified view of boundary layer resolution (*right*)

2.3 Validation

In addition to conditions $y^+ < 1$, $\Delta x^+ < 10$ and $\Delta z^+ < 10$ (Fröhlich (2006)) two other criteria for validation have been taken into account. First, the appropriate resolution of the boundary layer was proven since the correct representation of physical effects in direct proximity of the wall were of major interest. For this purpose, the dimensionless streamwise velocity of the simulation of the non-dimpled channel was compared with literature values of Moser et al. (1999). As shown in Fig. 3 the results are consistent with the literature values, meaning that the physical effects close to wall can well be captured by the conducted LES.

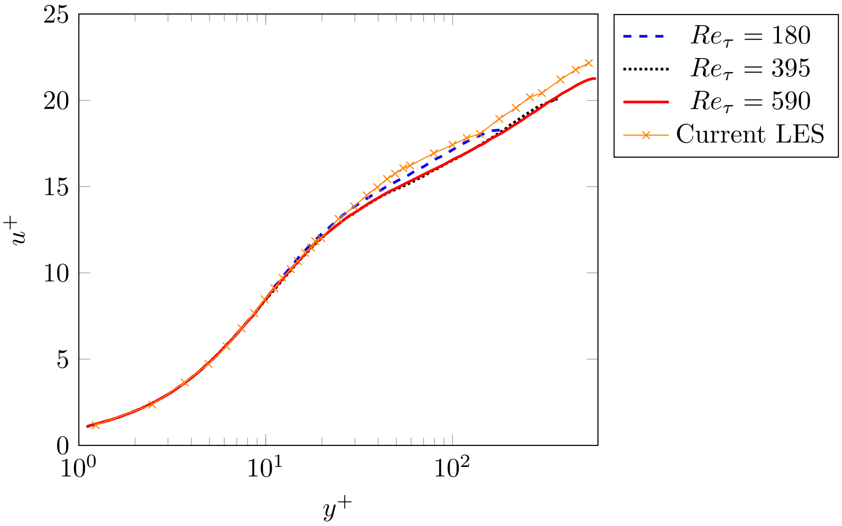

Figure 3: Comparison of boundary layer profile of the current LES with data for turbulent boundary layers by Moser et al. (1999)

Second, it was shown that the domain size is sufficient by considering the correlation coefficient given in Eq. 7 (Herwig and Schmandt (2015)) at different wall distances. According to Kiš et al. (2015) R_c should have a zero crossing when using periodic boundary conditions, since the correlation naturally increases to unity when approaching the periodic boundary condition and can thus not stay at zero as it is proposed for non-periodic boundary conditions (Fröhlich (2006)). For the correlation analysis, monitor points in four different y^+-ranges were evaluated at five z-values, each with 21 x-values distributed evenly over the entire domain. The x- and z-locations are given in Fig. 1. The positions in y^+-direction were selected such that one measuring path lies in each of the different ranges of the boundary layer. These ranges are i) the viscous sub-layer ($y^+ \lesssim 5$), ii) the buffer-layer ($5 \lesssim y^+ \lesssim 30$), iii) the log-law region ($30 \lesssim y^+ \lesssim 100 \ldots 800$) and iv) the outer layer ($y^+ \gtrsim 1000$). Therefore, y^+-positions 4, 15, 137 and 1073 were chosen. As shown in Fig. 4 R_c reached zero well before $x = 0.4 \cdot X$, which was the same for all z-locations investigated, as well as for the shown average taken over the five paths, indicating that the domain size is chosen big enough to avoid non-physical phenomena stemming from correlated velocity fluctuations.

$$R_\mathrm{c} = \frac{\overline{u'(x,t)\, u'(x+s,t)}}{\sqrt{\left(\overline{u'(x,t)^2}\right)\,\left(\overline{u'(x+s,t)^2}\right)}} \tag{7}$$

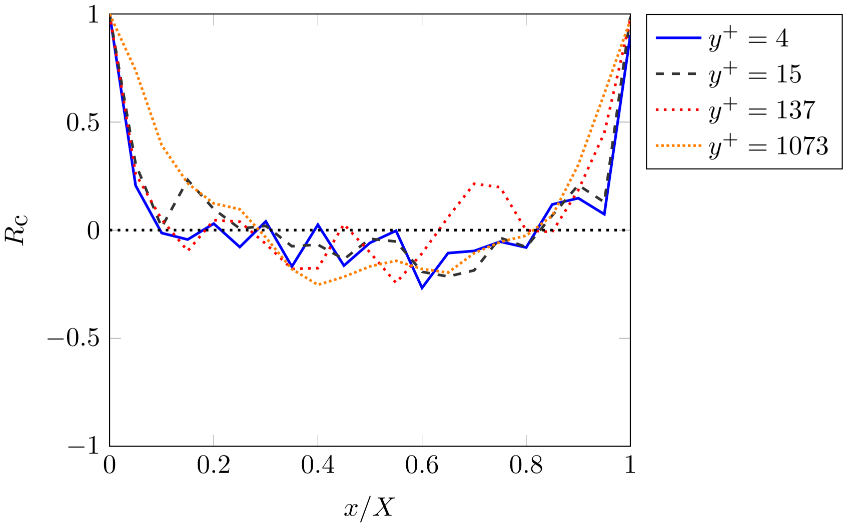

Figure 4: Comparison of correlation coefficient R_c for different y^+-locations averaged over five equally spaced z-positions

All simulations were initialized using results from RANS simulations carried out on the same mesh superimposed with synthetic turbulence in order to accelerate convergence. The bulk velocity u_∞ as well as the pressure p at the periodic boundary condition at $x = 0$ and the maximum velocity u_max at a point just below the free-slip boundary condition were considered to find the point in time at which the flow no longer shows any influence from the initial conditions. Velocities were made dimensionless using bulk velocity u_∞. As no such quantity exists for pressure p, pressure was shifted by its mean value and scaled by reference pressure $p_\mathrm{ref} = 20\,\mathrm{Pa}$. As shown in Fig. 5, the point from which on the quantities fluctuate around a constant value occurs from about ten flow-through times (calculated value: 10.57)[1], which is why averaging was started from this time on. For the non-overlapping arrangement (not shown) time for averaging was reached at 9.16 flow-through times. Each of the simulations took about 70 000 to 72 000 CPU hours to complete.

---

[1] This is the point from which on fluctuations were so small that all values fulfilled the criteria $|u_\mathrm{in}/u_\infty - 1| \leq 0.15\,\%$.

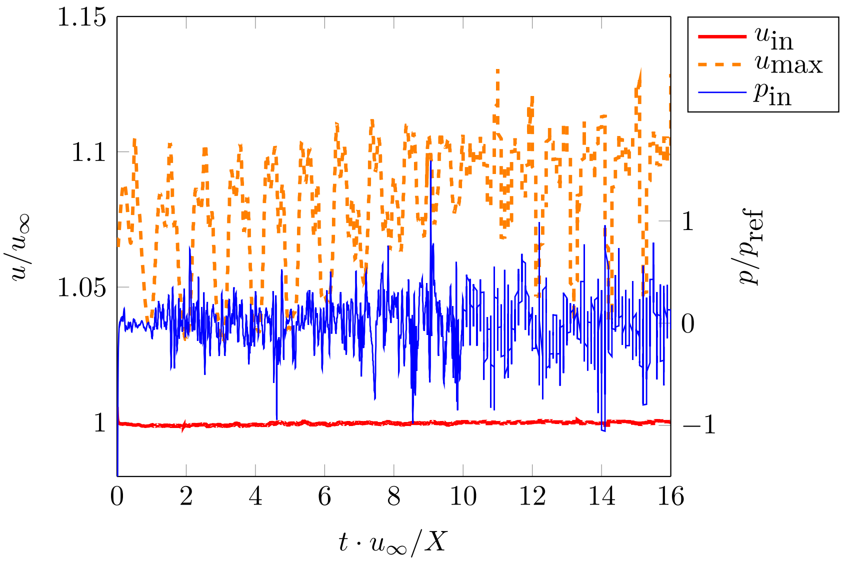

Figure 5: Determination of the statistically averaged state of the LES shown for dimpled plate with overlapping arrangement (OL)

3 Results

3.1 Drag Reduction

The flow resistance of a body subjected to fluid flows is composed of form and friction resistance. Since no wetted, projected surface perpendicular to the direction of flow is present on a smooth, parallel overflowed plate, the component of form resistance vanishes. The total resistance force F_t of the plate is thus determined exclusively by the resulting wall shear stress $\tau_\mathrm{w} = F_\mathrm{t}/A$. The total drag coefficient can be determined according to Eq. 8. The area A is the wetted area projected parallel to the direction of flow, which in the case of the smooth plate is identical to the wetted area. In the case of the dimpled plates, the total resistance force F_t comprises not only the friction component but also the form resistance component. The dimple also increases the wetted surface of the plate. Since the focus of this paper is on influencing the resistance of a surface, the total resistance coefficient c_F according to Eq. 8 using the total resistance force F_t related to area A of the smooth plate was used as a reference value. For the dimpled case, this area corresponds to the wetted area projected parallel to the direction of flow. This type of evaluation took into account all possible influences on the resistance. In addition, the comparability with the results given by Nesselrooij et al. (2016) is improved, since it corresponds to the procedure in their experiments. Fig. 6 shows the ratio of total drag coefficient c_F to drag coefficient of the undimpled plate c_{F0} for the investigated arrangements OL and NOL as well as the time-averaged values indicated by index ’mean’.

$$c_F = \frac{2F_\mathrm{t}}{\rho u_\infty^2 A} \tag{8}$$

It can be seen that – similar to velocity and pressure in Fig. 5 – the values fluctuate around this average value. Interestingly, however, the dimensionless period times T of c_F/c_{F0} are in the range of $T \approx 7 \ldots 8$ flow-through times and are thus considerably longer than those of velocity and pressure fluctuations. The oscillation is furthermore overlaid by higher frequency fluctuations and the amplitudes are higher than those of the average velocity would suggest, but the maximum expansion is still less than 10 %. For arrangement OL at $Re \approx 35\,000$ Nesselrooij et al. (2016) found a drag reduction of approximately 3 %. In the current LES, the reduction in drag observed for this setup was not more than 0.12 % and is therefore hardly existent. Better results concerning drag reduction were obtained with arrangement NOL, where resistance was reduced by as much as 3.16 %. However, Nesselrooij et al. did not find any resistance reduction for this setup, but even a slight increase in resistance of little more than 2 %. From this point of view, the results of the current LES are at first sight not in good agreement with the literature. Since the expected and also the found differences are in the range of single-digit percentages, this fact becomes less pronounced as the difference between simulation and experiment is ≈ 3 % for arrangement OL and ≈ 5 % for arrangement NOL, while the measurement repeatability was already up to 2 % (Nesselrooij et al. (2016)).

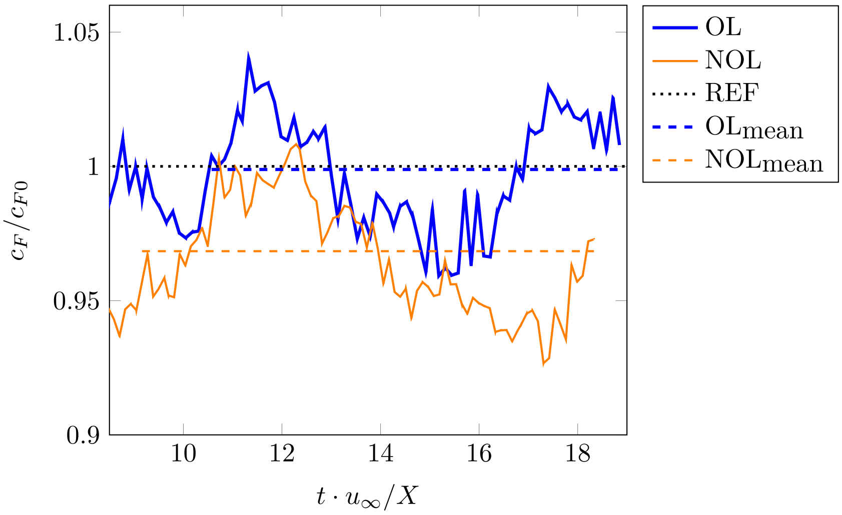

Figure 6: Total drag coefficient c_F for the plate without dimples (REF), plate with overlapping dimple arrangement (OL) and plate with non-overlapping dimple arrangement (NOL) related to c_{F0}

3.2 Flow Structures and Pressure Distribution

Regardless of the actual reduction of resistance, the main focus lies on investigating the physical mechanisms of action that influence the resistance of dimpled surfaces. For this purpose, the flow structures close to the wall are examined in detail below. Fig. 7 (*top*) shows the velocity field in a section plane at $y^+ = 20$. Clear differences in magnitude arranged in streaks can be seen here, which are structures stretched and parallel aligned in the streamwise direction. Kline et al. (1967) found from their investigations of turbulent boundary layers that these streaks are caused by rotating longitudinal vortices. The longitudinal vortices are self-maintaining in turbulent flows and draw the necessary energy from the main flow (Kim (2011)). By different directions of rotation of longitudinal-vortices lying alongside each other, fluid of higher velocity is either transported from the main flow into direction of the wall (*sweep*) or fluid transport of slow fluid away from the wall into direction of the main flow (*burst*) occurs. These mechanisms are shown in Fig. 7 (*bottom*). The practical relevance of these theoretical phenomena are shown in Fig. 7 (*middle*). Streamlines are used to visualize the global fluid movement in the area around the streaks. At areas of low wall shear stress, fluid is transported away from the wall in the direction of the main flow. By contrast, in areas with high wall shear stress, fluid of higher velocity is transported towards the wall. The influence of streaks on wall shear stress and thus on frictional drag has already been shown (Fröhlich (2006)). According to Kim (2011) longitudinal vortices are responsible for a considerable part of the wall friction. It is assumed that *sweep* in particular has a strong negative effect on friction resistance, as the transport of fluid with a high streamwise velocity to the wall increases the velocity gradient and thus also the wall shear stress which can be confirmed with the shown results of the presented LES.

Since the velocity and pressure ratios in the direct vicinity of the plate influence the wall shear stress and thus also the local frictional resistance, these are examined in detail below. Both Tay et al. (2015) and Nesselrooij et al. (2016) assume that the dimples produce secondary flows that are responsible for the effect of the dimple on the frictional resistance. Therefore, the flow in direct vicinity of the dimple by means of pressure and velocity analysis is considered. Due to the observed strong local variations in the quantities from dimple to dimple, measurements were taken on all dimples and averaged afterwards. In Fig. 8, the pressure distribution on the wall for the two arrangements studied is shown. The qualitative course of the related graphs is almost identical for both arrangements. For case OL, lower pressure values can be observed on the front and back of the dimple (indicated by dotted black lines) in both streamwise and spanwise direction. In streamwise direction the local maxima are approximately at the same level which leads to steeper pressure gradients for the OL arrangement. These are likely to be involved in loss generation, which is a possible reason for the lower resistance reduction of this arrangement. The pressure curve in spanwise direction is subject to higher local variations than in streamwise direction. This deviation is caused by local differences in flow velocity due to streaks. Nevertheless, the differences in the pressure characteristics are very small overall and do thus not allow for any concrete conclusions regarding the mechanisms of resistance influence of the dimples.

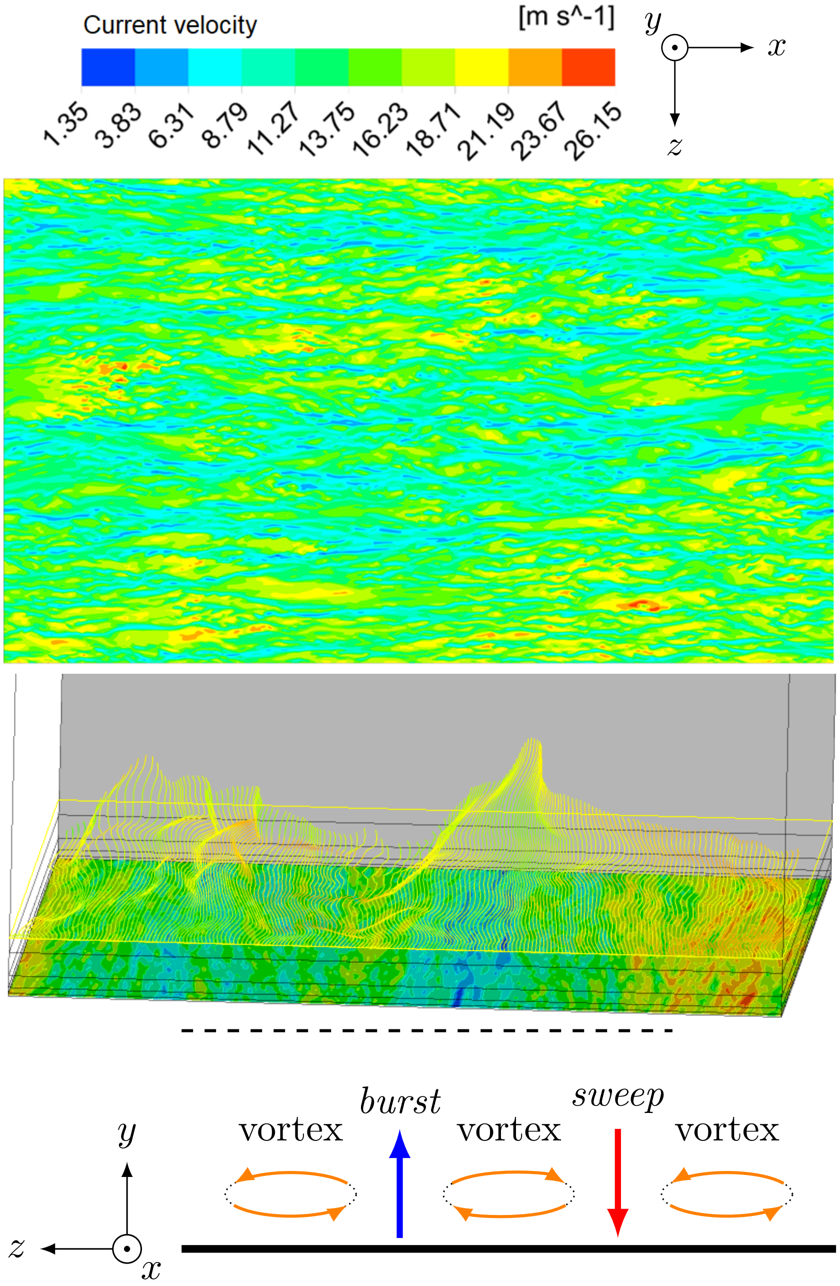

Figure 7: Streaks found as result of a LES visualised by velocity u in a section plane at $y^+ = 20$ (*top*), isometric view (flow approximately in direction of the drawing plane) with streamlines visualising *burst* and *sweep*, undimpled plate coloured by dimensionless wall shear stress, yellow line indicates the height of the starting points of the streamlines (*middle*) and schematic development of the streaks according to Kim (2003) (*bottom*)

3.3 Wall Shear Stress and Flow Velocity Perpendicular to the Wall

Fig. 9 shows the wall shear stresses τ_w in streamwise (x) and spanwise (z) direction on the surface for the dimpled arrangements OL and NOL as well as for the smooth reference channel. Here, a local increase in the wall shear stress in streamwise direction at the intake and a significant increase in shear stress at the end of the dimples can be observed for both dimpled plates. The entire curve and both peaks are higher for OL than for NOL, which fits very well with the overall higher observed c_F value for this arrangement. Also, most of the curve of the NOL arrangement is below the reference curve, which is also very well in accordance with the c_F values. This shows that the effects of drag reduction are related to the dimpled areas rather than the surrounding area of the dimples. The increase in wall shear stress at the entrance of a dimple can be attributed to acceleration of fluid in these areas (Isaev et al. (2010)). The subsequent strong decrease right behind it indicates that flow can follow the wall within

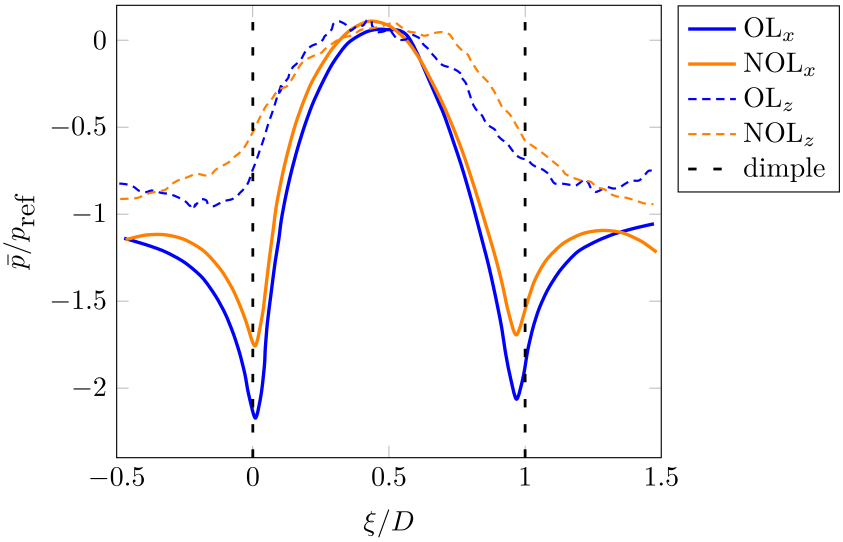

Figure 8: Static pressure at the dimpled wall in direct proximity of the dimples

that area only limitedly. Since the values remain above 0, there is no flow separation as would be the case with dimples of higher h/D. Such a detachment would increase the form resistance and is thus to be avoided (Tay et al. (2015)). The wall shear stresses in spanwise direction show a locally fluctuating but comparable course for all three cases. Fluctuations show the influence of the streaks and the resulting secondary currents close to the wall. The wall shear stress in this direction is not influenced by the dimples.

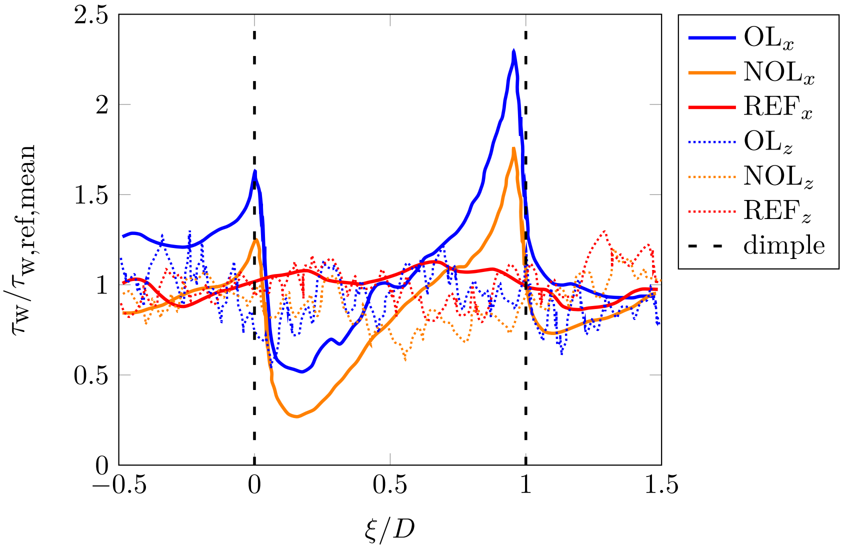

Figure 9: Normalized τ_{w} in streamwise (x) and spanwise (z) direction for the plate without dimples (REF), plate with overlapping dimple arrangement (OL) and plate with non-overlapping dimple arrangement (NOL) in direct proximity of the dimple

In order to examine the velocity distribution around the dimples, these were evaluated over five measuring points as depicted in Fig. 1 (*middle*). For this purpose, the velocity components u, v and w along lines in the y-direction and starting from the measuring points were analysed. In this case too, the evaluation was performed for all dimples and the values were averaged afterwards. The y-component (v) of fluid velocity proved to be of particular interest here because the most significant differences occurred between the configurations OL and NOL. Since the influence of the dimples is particularly pronounced near the wall, but the velocity components on the wall due to the no-slip condition are 0, the range $10 \leq y^+ \leq 800$ is shown in Fig. 10. It can be seen that above point 3, i. e. in the middle of the dimple, the mean wall-normal velocity component over the entire boundary layer is oriented in the direction of the wall. This is due to the expansion of the flow cross-section by the dimple. It is interesting to note that above the lateral borders of the dimples (points 2 and 4) the values for v for the arrangement NOL are clearly more symmetrical around the zero line than for the arrangement OL. This means that the streaks in arrangement NOL are much better aligned with the dimples. This observation suggests that this stabilization of the streaks can have a positive effect on the flow resistance if the intensity of the streaks is kept low.

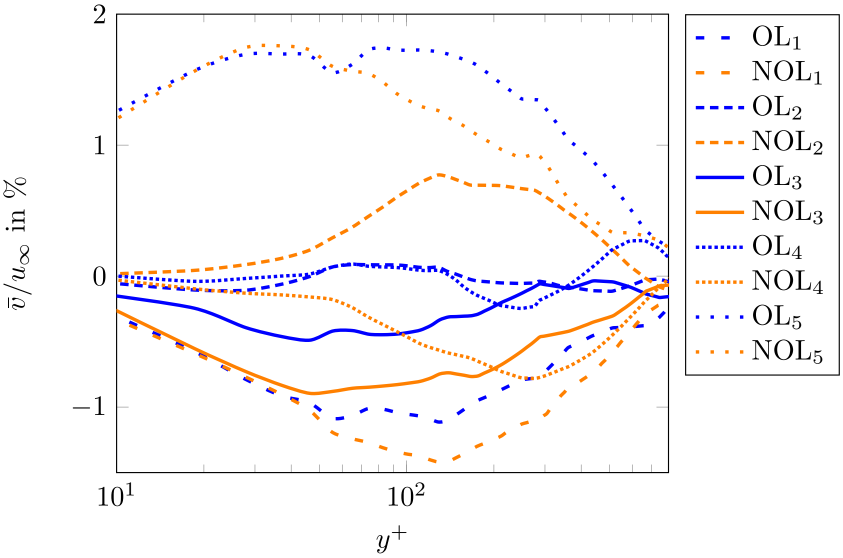

Figure 10: Average velocity $\bar{v}$ perpendicular to the wall scaled with bulk velocity u_∞ for the overlapping (OL) and non overlapping (NOL) arrangements at different physical positions 1–5 inside a dimple as indicated in Fig. 1

4 Conclusion

In this paper, two different arrangements of dimples on a plate were investigated numerically via Large Eddy Simulations with respect to their drag reduction potential. It was found that, in absolute terms, the results were consistent with available literature values for these setups, but only a minimal resistance reduction of 0.12 % could be achieved with one setup, while a reduction of 3.16 % was possible with the other. According to literature, however, the first case should have resulted in higher drag reduction while the second case should have resulted in a slight increase in resistance. Investigation of the flow structures in the immediate vicinity of the dimples revealed that the setup with higher drag reduction also showed lower wall shear stresses locally in the area of the dimples. The analysis of wall normal velocity also suggested that in this case existing longitudinal vortices can be stabilized. Even if these longitudinal vortices can have negative effects on flow resistance, these results lead to the assumption that a stabilization of the vortices by dimples is possible and advantageous. In order to investigate this assumption further, there is a need for additional investigations in this area. A time-resolved comparison of the local resistance components with the associated flow phenomena due to dimples would be of particular interest.

References

Antonia, R. A.; Spalart, P. R.; Mariani, P.: Effect of suction on the near-wall anisotropy of a turbulent boundary layer. *Physics of Fluids*, 6, 1, (1994), 430–432.

Baron, A.; Quadrio, M.: Turbulent drag reduction by spanwise wall oscillations. *Applied Scientific Research*, 55, 4, (1996), 311–326.

Cimarelli, A.; Frohnapfel, B.; Hasgawa, Y.; de Angelis, E.; Quadrio, M.: Prediction of turbulence control for arbitrary periodic spanwise wall movement. *Physics of Fluids*, 25, 075102.

Fröhlich, J.: *Large Eddy Simulation Turbulenter Strömungen*. B. G. Teubner Verlag, 1 edn. (Sep. 2006).

Garcia-Mayoral, R.; Jimenez, J.: Drag reduction by riblets. *Philosophical Transactions of the Royal Society A: Mathematical, Physical and Engineering Sciences*, 369, (2011), 1412–1427.

Herwig, H.; Schmandt, B.: *Strömungsmechanik*. Springer Vieweg, 3 edn. (2015).

Isaev, S.; Kornev, N.; Leontiev, A.; Hassel, E.: Influence of the reynolds number and the spherical dimple depth on turbulent heat transfer and hydraulic loss in a narrow channel. *International Journal of Heat and Mass Transfer*, 53, 1-3, (2010), 178–197.

Kiknadze, G. I.; Gachechiladze, I. A.; Barnaveli, T. T.: The mechanisms of the phenomenon of tornado-like jets self-organization in the flow along the dimples on the initially flat surface. In: *Proceedings of the ASME 2012 International Mechanical Engineering Congress & Exposition*, vol. 7, pages 3017–3026, ASME (Nov. 2012).

Kim, J.: Control of turbulent boundary layers. *Physics of Fluids*, 15, 5, (2003), 1093–1105.

Kim, J.: Physics and control of wall turbulence for drag reduction. *Philosophical Transactions of the Royal Society A: Mathematical, Physical and Engineering Sciences*, 369, 1940, (2011), 1396–1411.

Kiš, P.; Jin, Y.; Herwig, H.: The physics of stripe patterns in turbulent channel flow determined by DNS results (2015), arXiv:1511.07753.

Kline, S. J.; Reynolds, W. C.; Schraub, F. A.; Runstadler, P. W.: The structure of turbulent boundary layers. *Journal of Fluid Mechanics*, 30, 4, (1967), 741–773.

Krieger, V.; Perić, R.; Jovanović, J.; Lienhart, H.; Delgado, A.: Toward design of the antiturbulence surface exhibiting maximum drag reduction effect. *Journal of Fluid Mechanics*, 850, (2018), 262–303.

Kühnen, J.; Song, B.; Scarselli, D.; Budanur, N. B.; Riedl, M.; Willis, A. P.; Avila, M.; Hof, B.: Destabilizing turbulence in pipe flow. *Nature Physics*, 14, (2018), 386–390.

Lashkov, Y. A.; Samoilova, N.: On the viscous drag of a plate with spherical recesses. *Fluid Dynamics*, 37, 2, (2002), 231–236.

Lienhart, H.; Breuer, M.; Köksoy, C.: Drag reduction by dimples? - A complementary experimental/numerical investigation. *International Journal of Heat and Fluid Flow*, 29, (2008), 783–791.

Moser, R. D.; Kim, J.; Mansour, N. N.: Direct numerical simulation of turbulent channel flow up to $Re_\tau = 590$. *Physics of Fluids*, 11, 4, (1999), 943–945.

Nesselrooij, M. v.; Veldhuis, L. L. M.; Oudheusden, B. W. v.; Schrijer, F. F. J.: Drag reduction by means of dimpled surfaces in turbulent boundary layers. *Experiments in Fluids*, 57, 142, (2016), 1–14.

Nicoud, F.; Ducros, F.: Subgrid-scale stress modelling based on the square of the velocity gradient tensor. *Flow, Turbulence and Combustion*, 62, (1999), 183–200.

Park, H.; Lee, D.; Jeong, W.-P.; Hahn, S.; Kim, J.; Kim, J.; Choi, J.; Choi, H.: Drag reduction in flow over a two-dimensional bluff body with a blunt trailing edge using a new passive device. *Journal of Fluid Mechanics*, 563, (2006), 389–414.

Park, J.; Choi, H.: Effects of uniform blowing or suction from a spanwise slot on a turbulent boundary layer flow. *Physics of Fluids*, 11, 10, (1999), 3095–3105.

Quadrio, M.; Ricco, P.: Critical assessment of turbulent drag reduction through spanwise wall oscillations. *Journal of Fluid Mechanics*, 521, (2004), 251–271.

Sirovich, L.; Karlsson, S.: Turbulent drag reduction by passive mechanisms. *Nature*, 388, (1997), 753–755.

Tay, C. M.: Determining the effect of dimples on drag in a turbulent channel flow. In: *49th AIAA Aerospace Sciences Meeting including the New Horizons Forum and Aerospace Exposition AIAA 2011-682 4 – 7 January 2011, Orlando, Florida* (Jan. 2011).

Tay, C. M. J.; Khoo, B. C.; Chew, Y. T.: Mechanics of drag reduction by shallow dimples in channel flow. *Physics of Fluids*, 27, 035109.

Turow, J.: *Flow structures and heat transfer on dimpled surfaces*. phdthesis, University of Rostock (2012).

Veldhuis, L. L. M.; Vervoort, E.: Drag effect of a dented surface in a turbulent flow. In: *27th AIAA Applied Aerodynamics Conference AIAA 2009-3950 22 - 25 June 2009, San Antonio, Texas* (Jun. 2009).

Address: Institute for Factory Automation and Production Systems, Faculty of Engineering, Friedrich-Alexander-University Erlangen-Nuremberg. Fürther Straße 246b, 90429 Nuremberg, Germany.
email: `Julian.Prass@faps.fau.de`

DOI: 10.24352/UB.OVGU-2019-006 TECHNISCHE MECHANIK, 31, 1, (2019), 51-63
submitted: January 6, 2019

Prediction of Aerodynamic Coefficients of Road Vehicles on Bridge Deck with and without Wind Protection by Means of CFD for Crosswind Stability Investigations

V. Krämer, B. Pritz, E. Tempfli, M. Gabi

While planning a new bridge construction the risk of traffic accidents due to critical wind conditions should be carefully considered. The determination of aerodynamic forces and moments on vehicles is indispensable for stability investigations. However, the aerodynamic coefficients of vehicle-bridge systems depend on many factors which make it difficult to generalise the procedure. This paper is focusing on analysing a particular bridge geometry whereby aerodynamic coefficients were predicted by means of CFD. The accuracy of the numerical model was validated with the aid of experimental data from wind tunnel tests. Specifically, this work was conducted to investigate the effect of the wind barrier considering various wind flow angles and vehicle speeds. Mean forces and moments on the vehicle were analysed depending on both absolute and relative wind flows. The impact of performing relative motion between vehicle and bridge deck was investigated. Simulation results without wind barrier are qualitatively in good agreement with results found in literature. Nevertheless, the flow situation with wind barrier and relative motion is significantly more complex. Thus, CFD modelling has dominating advantages over wind tunnel tests in terms of both parameter variation and model accuracy. In this particular case CFD modelling is indeed essential in order to represent all possible wind flow angles and the relative motion between the vehicle and the bridge deck which remains difficult or rather hardly possible to perform in the wind tunnel.

1 Introduction

When starting to plan a new bridge construction the study and the analysis of the effects of crosswinds on road vehicles are indispensables in order to reduce the risk of wind-induced accidents. For stability analysis, force and moment coefficients are required as input parameters as shown by Baker at al. (2009) and Proppe et al. (2010). Such stability investigations serve to determine the probability of road accidents due to overturning, sideslip or rotation of the vehicle under various conditions. Thereby, the final goal is to identify the maximum safe vehicle speed on the bridge deck for a specific wind situation and for a certain vehicle type. As a result, the traffic on the bridge could be easily regulated if necessary.

Also for the newly planned bridge construction on the Kiel Canal in the north of Germany this procedure is essential. Especially lightweight high-sided vehicles and vehicles with a trailer represent critical cases being situated on a bridge in such a wind prone region. Consequently, this is an important safety and economic issue, as such accidents can cause life-threatening situations as well as traffic and infrastructure disruptions. In the past, many experimental as well as numerical studies have already been conducted concerning similar problems with vehicles in crosswinds in order to identify the aerodynamic characteristics.

Baker et al. (1991, 1996) carried out the mean aerodynamic force and moment coefficients of several ground vehicles in high crosswinds. According to Baker (1991), to all six aerodynamic forces and moments should be paid attention when considering a vehicle. The influence of the relative motion between the bridge deck and the vehicle needs to be assessed as well. Baker and Humphreys (1996) came to the conclusion that the relative motion must have a strong effect on some of the aerodynamic coefficients. Wang et al. (2013) showed, however, that this has only small influence on the aerodynamic results considering bridge geometry without wind barrier. In fact, the difference between simulations with and without relative motion in the case with an existing impermeable wind barrier was not tested in his study. Furthermore, Zhu et al. (2012) demonstrated that there is a significant difference between the aerodynamic characteristics of a vehicle over a bridge deck compared to a vehicle on a ground. In particular, different vehicle types, different wind directions as well as several vehicle positions were investigated in wind tunnel tests and partly strong variations in results were found. Dorigatti et al. (2012) proved the high impact of the bridge deck geometry on the aerodynamics. Some more various essential factors are mentioned and investigated by Malviya and Mishra (2014), such as acceleration and braking conditions, inclined ground planes, road surface curvature, centrifugal cornering effects and surrounding environment. Bettle et al. (2003) conducted numerical simulations which showed that vehicle speed and vehicle position (windward lane vs. leeward lane) have especially a large impact on the side force and roll moment coefficients. In addition, Coleman et al. (1992) showed that at least the variation of the side force and lift force coefficients with yaw angle is quite different with wind barriers than without. Thereby, it was confirmed that on the one hand the solidity and on the other hand the height of the wind barrier are decisive factors for the reduction of forces and moments on the vehicle. This fact was also ascertained by Guo et al. (2015). By conducting wind tunnel tests, Chen et al. (2015) demonstrated that wind barriers generally have a positive impact on the vehicle stability. Still the investigated wind barriers were permeable and had a low height ratio relative to the vehicle.

Regarding all the mentioned studies it can be concluded that the results actually cannot be compared with each other. There are too many aspects having a significant impact on the results, for instance bridge geometry, wind barrier type, vehicle types, vehicle position and speed, vehicle manoeuvring, reference dimensions etc. Consequently, determination of the force and moment coefficients should definitely be conducted for every specific bridge construction. Nevertheless, there is a number of assumptions that have to be studied in order to standardise the analysis.

Concerning the mentioned investigations CFD offers a number of advantages over the wind tunnel tests. The major advantage is the possibility to simulate a moving vehicle-bridge deck system which is rather difficult to perform in a wind tunnel. Furthermore, the determination of forces and moments is more precise given the fact that they are calculated over the complete surface of the vehicle. Even though this can also be achieved by conducting experiments with a special balance, this procedure is quite expensive and has to be extremely accurate. Consequently, in wind tunnel tests forces and moments usually are carried out by measuring pressure in several local positions on the vehicle surface which results in a very coarse integration. Further, the Reynolds number for a situation with real bridge dimensions differs significantly from a scaled model usually used for wind tunnel tests. Therefore, the accuracy of wind tunnel investigations can be doubted. Sterling et al. (2009) carried out full-scale experiments on a high-sided lorry and compared the results with wind tunnel tests and CFD simulations. Thereby, especially for the rolling moment coefficient, the full-scale measurements and CFD values were in very good agreement, whereas wind tunnel tests provided discrepant results. Nevertheless, a wider range of yaw angles can be considered by performing numerical simulations. Indeed, because of the finite model length the influence of the cut-off ends of the bridge model increases when positioned parallel to the wind tunnel.

Concerning numerical calculation, Krajnovic et al. (2012) proved that despite fine computational grid and unrealistically small wind velocities, RANS models show better results compared to LES simulation because of the wall treatment. Finally, Alonzo-Estébanez et al. (2017) showed that steady state approach instead of unsteady analysis guarantee sufficiently accurate results without require high computational effort.

The present study deals with determination of mean force and moment coefficients for a specific bridge deck geometry. Further, the general effect of wind barriers and the importance of the relative motion of the vehicle-bridge system were investigated. The established numerical model was successfully validated. The main focus of the study lies on the illustration of advantages and partly even indispensability of CFD regarding studies on this issue.

2 Model Geometry

The simplified horizontal bridge deck geometry, the wind barrier as well as the vehicle position are depicted in Figure 1. In the current study, this vehicle position on the outside road lane on the windward side of the bridge deck (hard shoulder being quite large in this case) was chosen for a better comparison with literature results as this was the most frequently investigated position. The cross section of the bridge was analysed first as a two-dimensional geometry (see Figure 2).

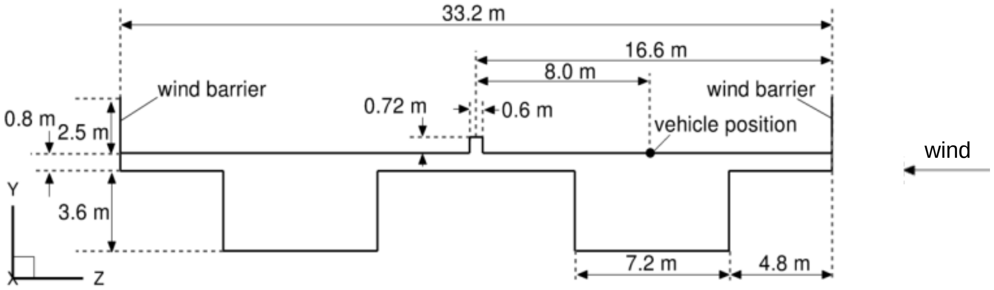

Figure 1. Cross section of the modelled bridge deck, vehicle position and overall dimensions

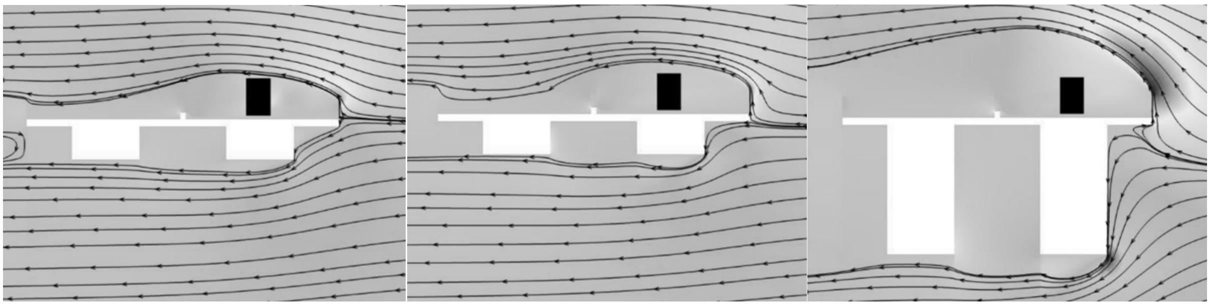

Figure 2. Effect of the bridge deck and wind barrier heights (left: 4 *m* high bridge deck and 2 *m* high wind barrier; middle: 4.4 *m* high bridge deck and 2.5 *m* high wind barrier; right: 15 *m* high bridge deck and 2.5 *m* high wind barrier). The truck geometry of 4 *m* height is not included in the simulation; it is depicted only for comparison purpose. The wind velocity is thereby 20 m/s.

Thereby, as shown in Figure 2, it was confirmed that the lower the bridge geometry or the wind barrier the more critical in the stability situation of the vehicle. In the present study a commonly used wind barrier of 2.5 *m* height was investigated which offers enough protection also for higher truck geometries (Figure 2, middle) and which has already been in a parametric study for a similar vehicle-bridge system (Ingenieurgesellschaft Niemann & Partner GbR, 2007). For the entire analysis three different vehicle types were examined: van, truck with a trailer and passenger car with a trailer. However, in this paper only the van geometry is exemplarily discussed, which is shown in Figure 3. The real geometry was approximated with rectangular block shape in order to cover all of the critical vehicle shapes (e.g. vehicles with nearly sharp edges).

In the further part of the present paper the results of the study of the three-dimensional configuration of the van at the position shown in Figure 1 will be presented.

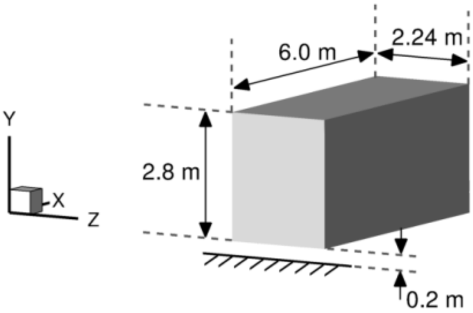

Figure 3. Van model

3 Flow Conditions

The vehicle is moving on bridge deck with the constant speed u whereas the wind is blowing at an absolute angle α with velocity c. Consequently, the relative wind velocity w at the angle β, which is acting on the vehicle, results from the velocity triangle shown in Figure 4.

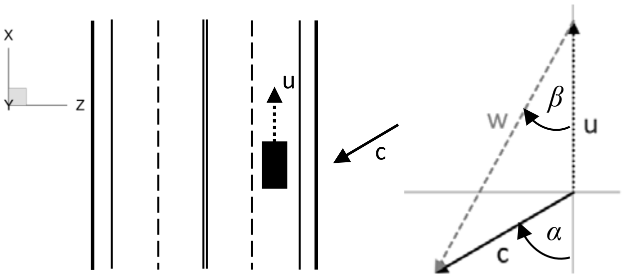

Figure 4. Velocity triangle

The cases computed in the present investigation are listed in Table 1. A key aspect was to achieve a wide range of relative angles *β* (see cases 1 to 9). As confirmed later in Section 7, the force and moment coefficients are described more universally in function of this angle rather than of the absolute angle *α*. Thereby, the evaluated relative angles remain between 0° and 90° as driving against the wind are the most critical configurations for the stability investigations. Especially in cases with a wind barrier, the relative wind angles of attack between 0° and 60° generally show higher values of aerodynamic coefficients (see Figure 12). In cases 3.1 to 3.3 and 4.1 to 4.3 (see Table 1) the variation of the absolute angle *α* was examined while the relative angle *β* remained constant. The variation of the relative angle *β* with the absolute angle *α* being constant could be analysed as well when considering cases 2, 3.2, 4.2, cases 3.1, 4.1, 5, 6 and cases 3.3, 4.3, 7, 8, 9, respectively (see Table 1). Cases marked with an asterisk represent calculations without relative motion between the vehicle and the bridge deck ($u = 0$ *m/s*). This corresponds to an usual wind tunnel test when the vehicle is fixed on the bridge deck. For these calculations either an absolute (**, vehicle speed completely neglected) or relative (*, hypothetical vehicle speed according to velocity triangle from Figure 4) angle of attack was defined.

Table 1. Investigated configuration cases: *α*, *β* in [°] and *c*, *u*, *w* in [*m/s*]

	absolute system			**relative system**	
case	***α***	***c***	***u***	***β***	***w***
1	30	20	130	**11**	54
2	60	20	130	**21**	49
3.1	90	20	130	**29**	41
3.2	60	34	130	**29**	61
3.3	120	18	130	**29**	31
4.1	90	14	60	**40**	22
4.2	60	31	60	**40**	42
4.3	120	11	60	**40**	15
5	90	23	80	**45**	32
6	90	30	60	**61**	34
7	120	21	60	**70**	19
8	120	26	60	**81**	23
9	120	20	60	**94**	10
3.1*	-	-	0	29	41
3.1**	90	20	0	-	-
3.2*	-	-	0	29	61
5*	-	-	0	45	32
6*	-	-	0	61	34

4 Aerodynamic Coefficients

For the safety analysis the mean forces and moments in each coordinate direction must be determined over all surfaces of the vehicle. Figure 5 illustrates all forces and moments on the vehicle model as well as the wind and vehicle movement directions. Thereby, F_D, F_L and F_S are the drag force, the lift force and the side force, respectively, and M_R, M_Y and M_P are the rolling moment, the yawing moment and the pitching moment, respectively.

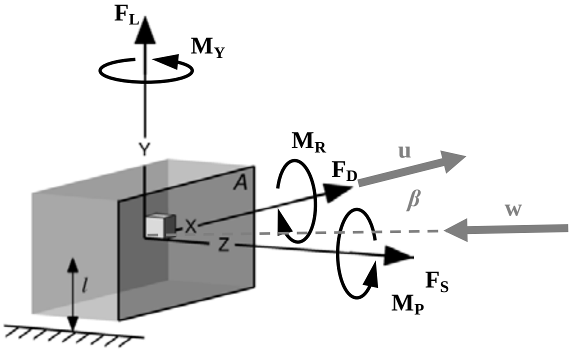

Figure 5. Aerodynamic forces and moments on a vehicle

All six aerodynamic forces and moments refer to the geometric centre point of the vehicle. With air density ρ_{air}, relative velocity of the wind *w*, reference area *A*, reference length *l* and the calculated forces and moments the six non-dimensional aerodynamic force and moment coefficients are defined as:

$$c_i = \frac{F_i}{\frac{\rho}{2} w^2 A} \tag{1}$$

$$c_{M_i} = \frac{M_i}{\frac{\rho}{2} w^2 A l} \tag{2}$$

Concerning the reference area *A* as well as the reference length *l* there are widely varying specifications given in the literature (front surface of the vehicle or some arbitrary reference area, vehicle length, vehicle height or some arbitrary length, respectively). For all of the calculations in the present study the side surface of the vehicle was chosen as reference area *A* (see Figure 5). Given the fact that the wind direction varies considerably (see *β* in Table 1), the side surface is the largest possible windward surface of the vehicle. Particularly with regard to the side load being the most critical one. As reference length *l* the distance between the geometrical centre of the vehicle and the bridge deck was considered (see Figure 5).

5 Numerical Model

Steady-state numerical simulations have been performed using the commercial software ANSYS CFX© which is based on finite volume method. The block-structured numerical grid was generated using ANSYS ICEM-CFD©. The calculations were carried out with air under normal conditions at ambient temperature of 25 *°C* and pressure of 1 bar. Consequently, the density of the air ρ_{air} was equal to 1,185 kg/m^3 for the present study.

The computational domain consists of three independently meshed subdomains as shown in Figure 6: the first domain in close proximity to the vehicle, the second domain around the bridge and the third domain representing the farfield. The subdomains are connected by interfaces.

As mentioned in Section 1, the cut-off ends of the bridge geometry can have a significant impact on the flow dynamics on the bridge deck and on the aerodynamic coefficients on vehicle surface when $\beta \neq 90°$. In contrast to wind tunnel tests, CFD allows to avoid this problem by using periodic boundary conditions in driving direction. The computational domain is thus virtually ordered periodically along the x-axis in order to design a quasi-infinitely long bridge with vehicles at a fixed distance to each other on it. The vehicle is situated in the first area in the middle of the entire domain along the x-axis. The length of one periodic section of 325 *m* was carefully examined. Thus, it could be guaranteed that the flow fields of two running vehicles do not significantly influence each other, even for small values of *β*. The height and the length of the computational domain were both set in such a way that the boundary conditions (BCs) do not affect the flow field around the bridge deck.

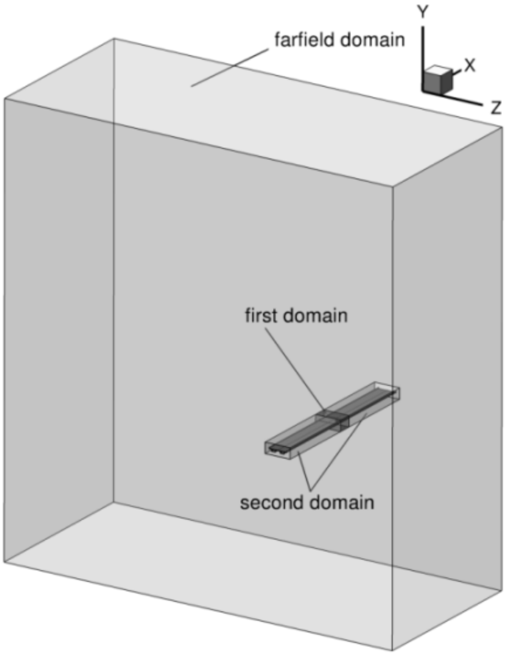

Figure 6. Computational domains

In order to prove that the accuracy of the solution is not dependent on the grid resolution, four different grid sizes were tested for the case 3.1: with 600 000, 3 million, 20 million and 34 million cells. Figure 7 presents all six force and moment coefficients as a function of the grid size. As it can be seen, there is still a significant difference between the results of the 3 million and the 20 million cells meshes. On the other hand, the slight deviation between the results of the 20 million and the 34 million cells meshes is negligibly small. Thus, to guarantee both accurate results and reasonable computing time the final mesh comprised approximately 20 million cells.

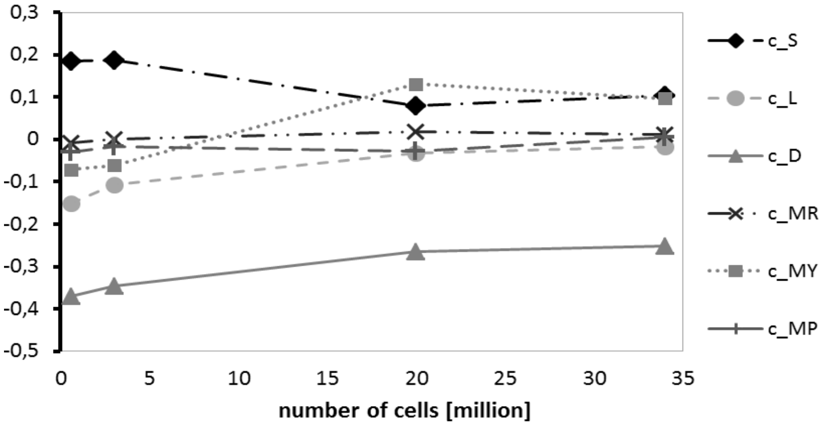

Figure 7. Grid dependence, case 3.1

The reference frame for CFD calculations was attached to the vehicle. Thus, the vehicle surface was defined as no-slip wall. Whereas a moving wall BC was chosen for the bridge deck, considering the motion between the bridge deck and the vehicle. The overview of boundary conditions for the current study is presented in Figure 8.

The relative wind velocity w under the angle β was specified at the inlet with a turbulence intensity of 5%. It should be noted that the atmospheric boundary layer was neglected in the current study as the bridge deck is placed approximately 40 m above the ground. Thus, a homogeneous inflow was realised. At the outlet static pressure was defined. The top and the bottom faces of the domain were set as a free slip wall. As mentioned previously, for the faces at the ends of the bridge section periodic BCs were chosen.

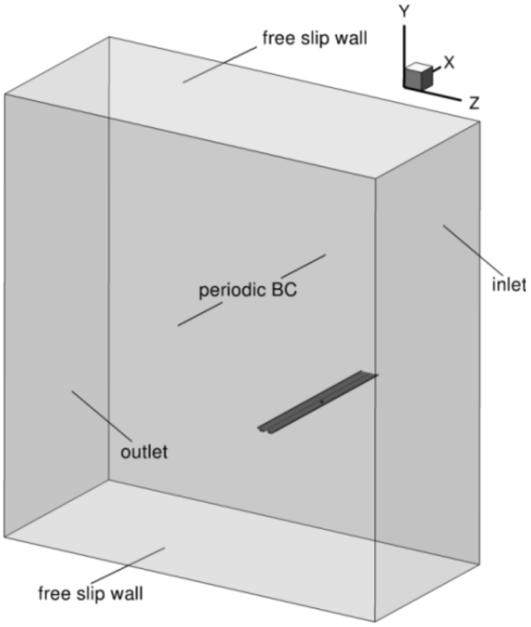

Figure 8. Boundary conditions

All calculations were based on RANS equations and were carried out using the eddy viscosity transport equation turbulence model according to Menter (ANSYS CFX-Solver Theory Guide, 2011). Thereby, scalable wall functions were used in order to make the solution in the near-wall regions independent of the refinement of the grid. The size of the first cell near the wall was kept at $y^+ < 50$ for regions around the vehicle and the road surface. In the present study, the high resolution scheme (a second order upwind scheme) implemented in ANSYS CFX© was used for the advection terms and the turbulence (ANSYS CFX-Solver Theory Guide, 2011).

6 Validation

For the validation of the designed numerical model against experimental results, wind tunnel tests were performed at the Institute of Fluid Machinery at KIT. The tests were carried out in a closed return wind tunnel which can produce air speeds up to 60 *m/s*. The diameter of the outlet nozzle is 1.8 *m* and thus limited the scaling of the examined model. Therefore, the geometric scale for the wind tunnel vehicle-bridge model was set 1:40. The average air speed was set to 20 *m/s*. Local pressure measurements were carried out in the measuring positions defined in Figure 9.

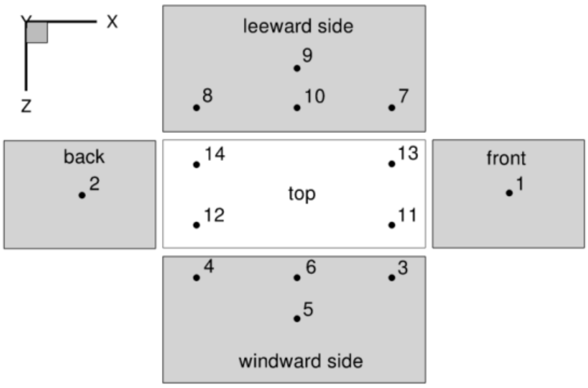

Figure 9. Wind tunnel test measuring positions on surface of the van model (the coordinate axes are valid for the top side)

As already discussed, the possibilities to vary the model settings in wind tunnel tests are rather limited. Consequently, to compare numerical with experimental results, an equally scaled vehicle-bridge system without

relative motion and with the yaw angle of 90° had to be simulated. Finally, pressure values on vehicle surface were extracted from simulation results for the same positions as shown in Figure 9.
In order to analyse the results the non-dimensional pressure coefficient using the density of air ρ_{air}, the freestream velocity U_∞ and the static freestream pressure p_∞ was determined as follows:

$$c_p = \frac{p - p_\infty}{\frac{1}{2}\rho_{air} U_\infty{}^2} \tag{3}$$

Figure 10 shows both pressure coefficients from the wind tunnel tests and CFD in each of the measuring positions. The results are presented in each case with and without wind barrier.

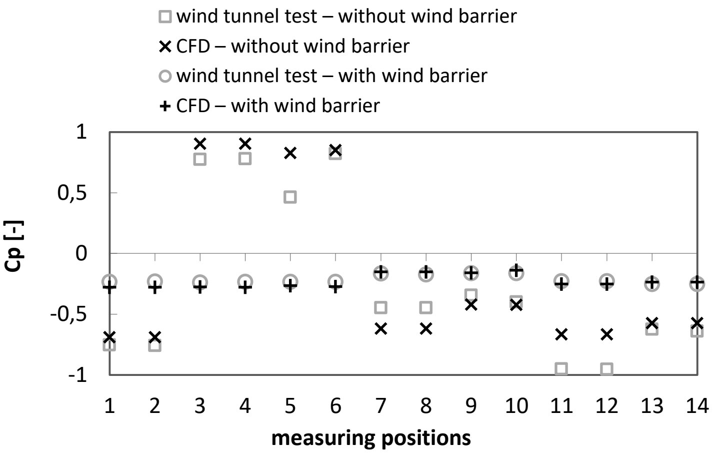

Figure 10. Comparison between results obtained from CFD and from wind tunnel tests

It can be seen that in the absence of the wind barrier the pressure coefficient values are considerably higher than in the case with wind barrier. This proves that a wind protection of 2.5 *m* height generally leads to an improvement in stability situation of the vehicle. Generally, wind tunnel and CFD results are in very good agreement for the case with wind barrier. However, also without wind barrier there are only few measuring positions with larger deviations between numerical and experimental pressure coefficient values (see positions 5, 11 and 12 in Figure 10). This is due to the high flow gradients because of the flow separation on sharp edges as there is no wind protection. Measuring positions 11 and 12 are situated near the separation edge on the windward side and thus are directly in the separation zone. Position 5 is strongly influenced by the separation on the bridge edge. Consequently, already small deviations between simulation and experiment referring to the size of the separation bubbles can cause major discrepancies in results.

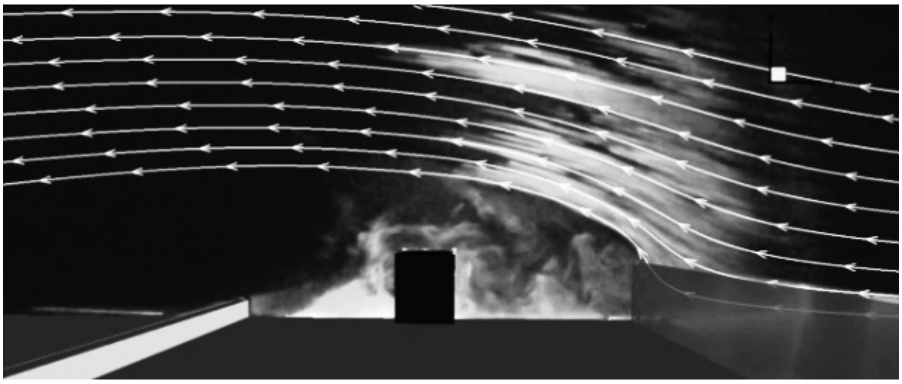

Figure 11. Comparison between results obtained from CFD and from wind tunnel tests

Further, also the overall flow fields from numerical and experimental results are in good agreement. According to Figure 11, streamlines visualized in the wind tunnel are quite similar to computed streamlines. The flow separation on wind barrier is in very good agreement.

7 Results

The results of the study are summarised in Figures 12 to 14. In Figure 12, calculations considering the relative motion between vehicle and bridge deck with wind barrier as well as without wind barrier are presented. The force and moment coefficients are plotted over both the relative wind angle β and the absolute wind angle α. Figures 13 to 14 outline the comparison between vehicle-bridge systems with and without relative motion. However, the causes for the particular distribution of the coefficients are not the focus of the present paper.

Figure 12 illustrates the six force and moment coefficients in function of relative wind angle β (left column) and absolute wind angle α (right column). For the same angle α there is almost always a large variation of results depending on vehicle velocity as well as on wind speed. In particular, in the case without wind barrier the scattering of results is stronger than in the case with wind barrier. This is due to the fact that wind barrier significantly influences the flow field on the bridge deck und thus more or less equalizes it for different configurations. Conversely, the dependence on the relative angle β presents a clear curve shape despite various vehicle velocities and wind speeds (see $\beta = 29°$ and $\beta = 40°$ with wind barrier). It could be ascertained that the aerodynamic coefficients show a meaningful dependency on the relative angle β obtained from the velocity triangle (Figure 4).

As can clearly be seen and was already detected in validation results (Figure 10), the force coefficients as well as moment coefficients are significantly higher in the case without wind barrier (cf. Figure 12 (a) and (c), (e) and (g)). The side force is the highest one if there is no wind protection. Due to the presence of the wind barrier its magnitude not only decreases up to approximately 75%, but also changes its direction. Thus, the vehicle is rather pushed towards the wind barrier. The lift force coefficient has very small values compared to the two other ones. The values of the drag force coefficient do not change much by adding wind protection, as expected. Concerning the moments, the most critical one for the stability analysis is usually the roll moment. As it can be observed in Figure 12 (e) and (g), with the presence of the wind barrier this coefficient could be reduced considerably.

The cases marked with * and ** in Table 1 omit relative motion between the bridge deck and the vehicle which correspond the most common configurations in wind tunnel tests. In the wind tunnel test either the relative angle β (*) or the absolute angle α (**) can be realised between flow direction and the bridge model. From Figure 13 it can be seen that in the case without wind barrier the relative motion between the vehicle and the bridge deck has a negligible effect on the results when relative wind flow is set at the inlet (case 3.1*). However, when the vehicle speed is neglected and the absolute angle is defined at the inlet (case 3.1**), significant deviations can be detected.

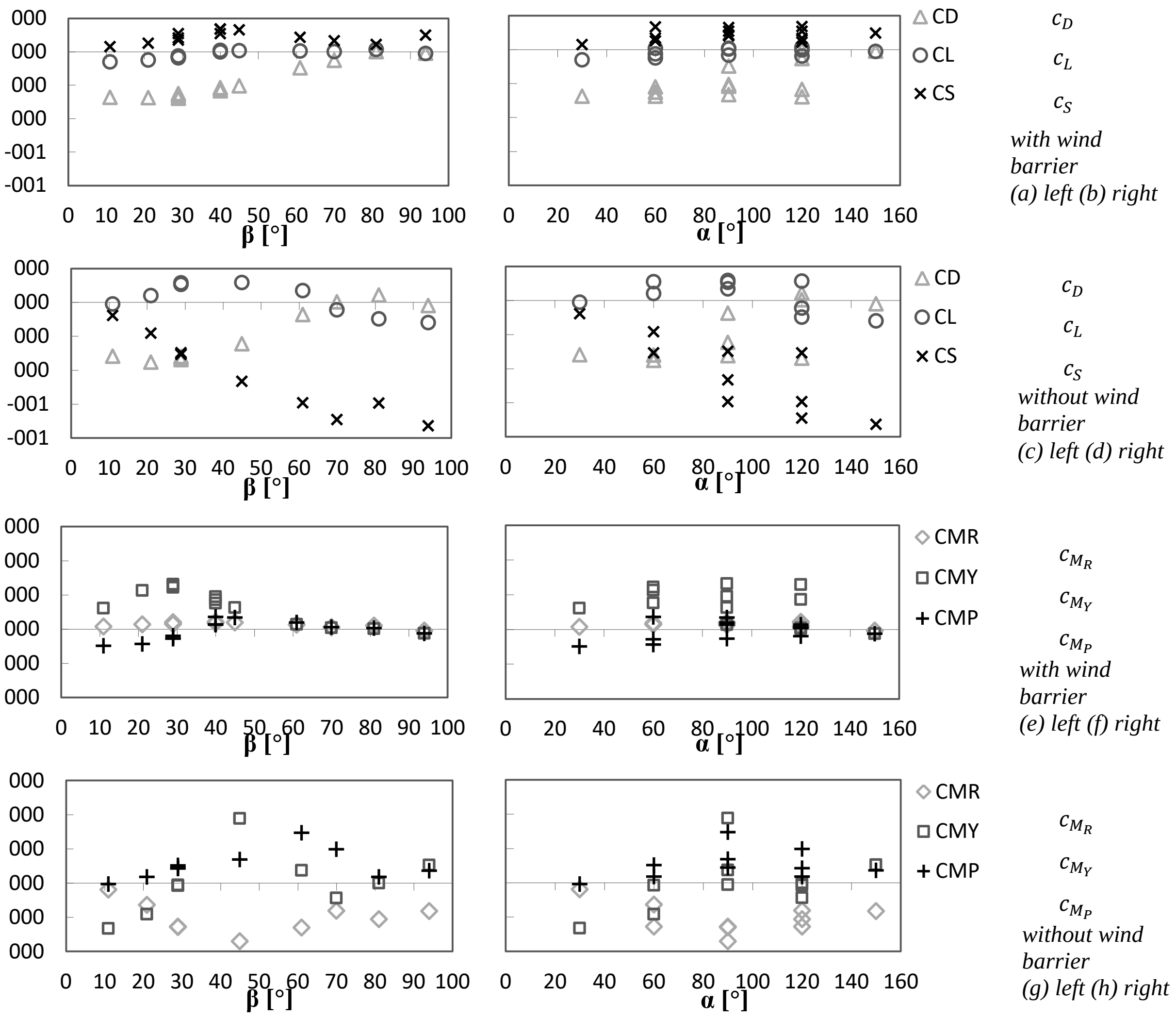

Figure 12. Computed force and moment coefficients on the vehicle on a bridge deck with and without wind barrier; plotted over the relative angle β (left) and the absolute angle α (right)

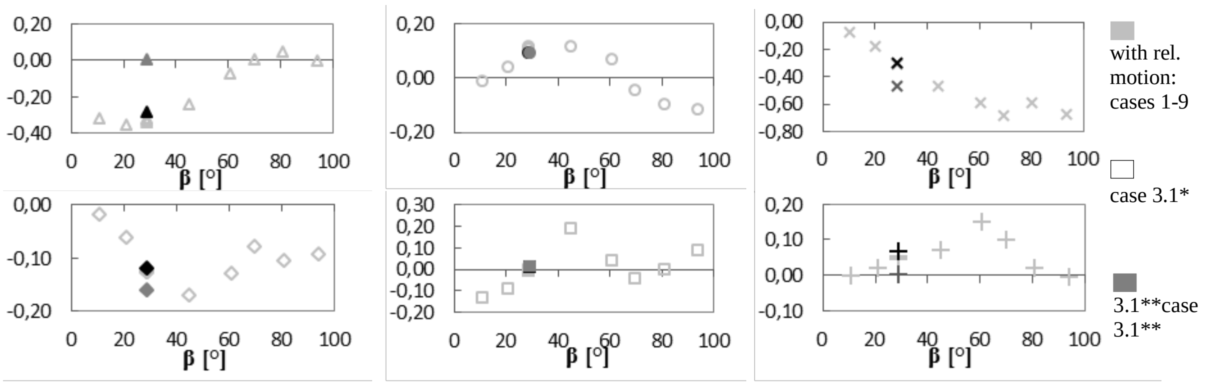

Figure 13. Results with and without relative motion (without wind barrier)

On the contrary, according to Figure 14 the relative motion has a stronger impact on the results when wind barrier is present. Case 3.1** shows large discrepancies here as well. Additionally the deviations for all cases with asterisks are significant. In particular, the distributions of the side force as well as for the roll moment coefficients are substantially different (c_S and c_{M_R} in Figure 14). These two coefficients are particularly important for the stability analysis.

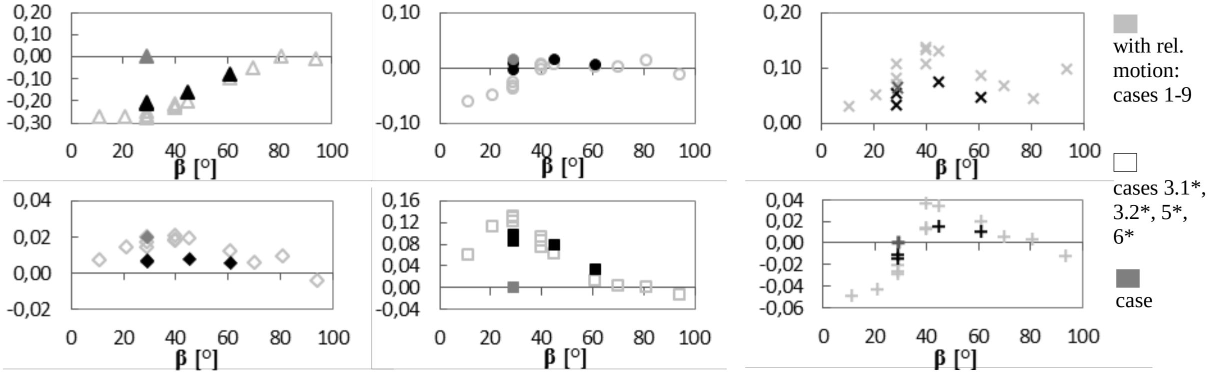

Figure 14. Results with and without relative motion (with wind barrier)

To sum up, if a wind barrier exists and accurate results are required, the relative motion is indispensable.

8 Conclusions and Outlook

Six aerodynamic coefficients under different wind conditions were determined for a van model on a bridge deck with and without wind barrier by means of CFD. The numerical model was first validated through wind tunnel tests. Furthermore, the effect of wind barrier was evaluated and the impact of relative motion between the vehicle and the bridge deck was investigated. Finally, following conclusions could be obtained:

(1) Force and moment coefficients show clearly defined characteristic curves if plotted over the relative angle of attack β which represents the relative wind flow acting on the vehicle.

(2) Wind barrier of 2.5 m height significantly reduces force as well as moment coefficients on the vehicle surface.

(3) Modelling the relative motion of the vehicle-bridge system has only slight influence on aerodynamic coefficients of the vehicle on a bridge deck without wind barrier but it has a noticeable impact in the case of an existing wind protection.

To conclude, it can definitely be said that CFD has clear advantages over wind tunnel tests and is essential for accuracy of such investigations because:

- Relative motion is not that obvious to reproduce experimentally;
- Wide range of yaw angles is not practicable in wind tunnels without influencing the flow field by the finite length of the bridge model;
- Scaling is not necessary and real dimension Reynolds numbers can be realised;
- Variations of the vehicle-bridge system can be evaluated more easily and faster;
- Generally larger data sets are obtained, and namely in every point on the vehicle surface.

Eventually, the main goal of the current and the future researches is to generalise the methodology of predicting the aerodynamic coefficients for the stability investigations. Whereas at the same time, it is demonstrated that the generalisation of the results themselves is not possible because of a huge number of various conditions and the complexity of the flow field around the vehicle when wind barrier and relative motion being modelled. Figure 15 exemplarily illustrates the flow for the case 3.1 from Table 1 by means of streamlines. The outer flow (strong lines) generates a recirculation vortex between the wind barriers, which is strongly disturbed by the van and is split in two vortices.

Consequently, for instance the general effects of wind barrier and vehicle velocity on the flow on the bridge deck as well as a parametric study of the interaction between wind direction and vehicle velocity could be subjects for analysis in future studies. Moreover, the vehicle position on the other outer side of the bridge deck is currently analysed in order to cover all wind direction that can occur on a bridge deck. This also serves to investigate the impact of the wind barrier on the leeward side of the bridge deck on aerodynamic coefficients in the case with a wind barrier higher than the vehicle. The implementation process of aerodynamic coefficients for the actual stability analysis will be published separately.

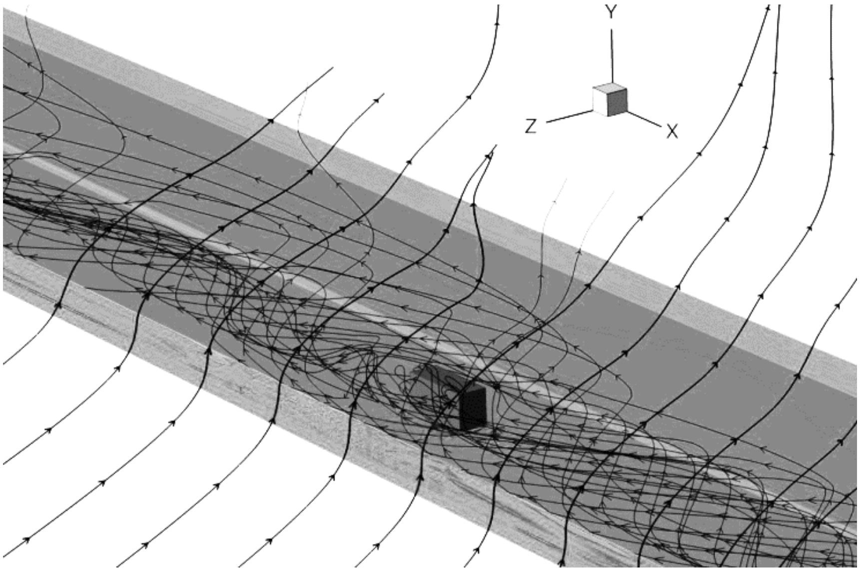

Figure 15. Complex flow around the vehicle caused by the wind barrier and the relative motion between vehicle and the bridge deck exemplarily visualised for wind angle of attack of 90° (case 3.1 in Table 1)

Acknowledgements

The writers are grateful to have the possibility of working on the Kiel Canal bridge project with DEGES Deutsche Einheit Fernstraßenplanungs- und –bau GmbH.

References

Alonso-Estébanaz, A.; Del Coz Díaz, J. J.; Álvarez Rabanal, F. P.; Pascual-Muñoz, P.: Numerical simulation of bus aerodynamics on several classes of bridge decks. *Engineering Applications of Computational Fluid Mechanics*, 11(1), (2017), 435-449.

ANSYS CFX-Solver Theory Guide, (2011).

Baker, C. J.: Ground vehicles in high cross winds. Part I: Steady aerodynamic forces. *Journal of Fluids and Structures*, 5, (1991), 69-90.

Baker, C. J.; Cheli, F.; Orellano, A.; Paradot, N.; Proppe, C.; Rocchi, D.: Cross wind effects on road and rail vehicles. *Vehicle System Dynamics*, 47(8), (2009), 983-1022.

Baker, C. J.; Humphreys, N. D.: Assessment of the adequacy of various wind tunnel techniques to obtain aerodynamic data for ground vehicles in cross winds. *Journal of Wind Engineering and Industrial Aerodynamics*, 60, (1996), 49-68.

Bettle, J.; Holloway, A. G. L.; Venart, J. E. S.: A computational study of the aerodynamic forces acting on a tractor-trailer vehicle on a bridge in cross-wind", *Journal of Wind Engineering and Industrial Aerodynamics*, 91, (2003), 573-592.

Chen, N.; Li, Y.; Wang, B.; Su, Y.; Xiang, H.: Effects of wind barrier on the safety of vehicles driven on bridges. *Journal of Wind Engineering and Industrial Aerodynamics*, 143, (2015), 113-127.

Coleman, S. A.; Baker, C. J.: The Reduction of Accident Risk for High Sided Road Vehicles in Cross Winds. *Journal of Wind Engineering and Industrial Aerodynamics*, 41-44, (1992), 2685-2695.

Dorigatti, F.; Sterling, M.; Rocchi, D.; Belloli, M.; Quinn, A. D.; Baker, C. J.; Ozkan, E.: Wind tunnel measurements of crosswind loads on high sided vehicles over long span bridges. *Journal of Wind Engineering and Industrial Aerodynamics*, (2012), 214-224.

Guo, W. W.; Wang, Y. J.; Xia, H.; Lu, S.: Wind tunnel test on aerodynamic effect of wind barriers on train-bridge system. *Science China Technological Sciences*, 58, No. 2, (2015), 219-225.

Ingenieurgesellschaft Niemann & Partner GbR; Ruhr-Universität Bochum, Arbeitsgruppe Aerodynamik und Strömungsmechanik im Bauwesen: WINDTECHNOLOGISCHES GUTACHTEN ZUR BAB A71; Entwicklung von Windschutzeinrichtungen für die Talbrücke Zahme Gera, (2007).

Krajnovic, S.; Ringqvist, P.; Basara, B.: Comparison of Partially Averaged Navier-Stokes and Large-Eddy Simulations of the Flow Around a Cuboid Influenced by Crosswind. *ASME. Journal of Fluids Engineering*, 134, (2012).

Malviya, V.; Mishra, R.; Development of an analytical multi-variable steady-state vehicle stability model for heavy road vehicles. *Applied Mathematical Modelling*, 38(19-20), (2014), 4756-4777.

Menter, F. R.: Eddy Viscosity Transport Equations and Their Relation to the k-ε Model. *ASME, Journal of Fluids Engineering*, 119(4), (1997), 876-884.

Proppe, C.; Wetzel, C.: A probabilistic approach for assessing the crosswind stability of ground vehicles. *Vehicle System Dynamics*, 48(1), (2010), 411-428.

Sterling, M.; Quinn, A. D.; Hargreaves, D. M.; Cheli, F.; Sabbioni, E.; Tomasini, G.; Delaunay, D.; Baker, C. J.; Morvan, H.: A comparison of different methods to evaluate the wind induced forces on a high sided lorry. *Journal of Wind Engineering and Industrial Aerodynamics*, 98, (2009), 10-20.

Wang, B.; Xu, Y.; Zhu, L.; Cao, S.; Li, Y.: Determination of aerodynamic forces on stationary/moving vehicle-bridge deck system under crosswind using computational fluid dynamics. *Engineering Applications of Computational Fluid Mechanics*, 7(3), (2013), 355-368.

Zhu, L. D.; Li, L.; Xu, Y. L.; Zhu, Q.: Wind tunnel investigations of aerodynamic coefficients of road vehicles on bridge deck. *Journal of Fluids and Structures*, 30, (2012), 35-50.

Address: Institute of Fluid Machinery, Karlsruhe Institute of Technology. Kaiserstr. 12, 76131 Karlsruhe
email: pritz@kit.edu

DOI: 10.24352/UB.OVGU-2019-007 TECHNISCHE MECHANIK, 39, 1, (2019), 64 – 71
submitted: July 6, 2018

Energy Cascade in a Nonlinear Mechanistic Model of Turbulence

B. D. Bak, T. Kalmár-Nagy

Energy transfer plays an essential role in many natural and engineering processes which include different scales. Understanding how the energy cascade (which refers to the energy transfer among the different scales) works is of primary importance. One notable example is the energy cascade in turbulent flow whose kinetic energy is transferred from large eddies to smaller ones. Below a threshold scale the energy is dissipated due to viscous friction. We introduce a nonlinear phenomenological mechanistic model of turbulence which consists of masses connected by springs arranged in a binary tree structure. To represent the various scales, the masses are gradually decreased in lower levels. The bottom level of the model consists of nonlinear energy sinks to provide dissipation. Based on previous research, we choose the system parameters and analyze its behavior for simple impulsive excitations. The decay of the total mechanical energy and the discrete energy spectrum of the system are compared for different impulse magnitudes. It is demonstrated that the dissipation is much more significant compared to the linear model, if the input energy is large enough. The energy spectra are compared with that of the linear model. We find that the energy spectrum of the nonlinear model better highlights the cut-off feature of the Kolmogorov spectrum.

1 Introduction

There are many complex phenomena both in nature and in engineering processes which include energy transfer among a wide range of different scales. Many studies dealt with examining systems exhibiting energy cascades, see e.g. Vakakis et al. (2008). Frequently studied examples include nonlinear chain oscillators (Gendelman et al. (2001); Vakakis and Gendelman (2001)) and the Fermi-Pasta-Ulam problem described by Fermi et al. (1955). An energy cascade describes energy transfer primarily from large scales to small ones. There also exist inverse cascade models in which the energy is transferred from small scales to larger scales. A notable example is the forest fire model of Turcotte et al. (1999) which describes how small clusters of fires combine and form larger fires.

In fluid mechanics the well-known example of such a process is the turbulent energy cascade. According to Richardson (1922) there are vortices of different sizes in a turbulent flow. The larger vortices are unstable and break up to form several smaller vortices. Thus, the kinetic energy of the flow is transferred to smaller scales. The turbulent energy cascade is characterized by the energy spectrum $\hat{E}(\kappa)$ which shows the distribution of the total energy E of the flow among the different scales. In other words, the spectrum is a Fourier-transform of E, i.e.

$$E = \int \hat{E}(\kappa) d\kappa, \tag{1}$$

where the wavenumber $\kappa \sim 1/L$ is associated with the vortex having characteristic size L.

The spectrum of 3D homogeneous isotropic turbulence (also known as Kolmogorov spectrum, see Kolmogorov (1941)) is shown in Fig. 1.

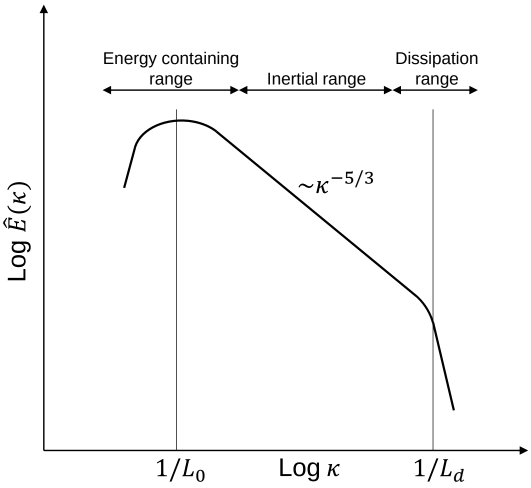

Figure 1: The Kolmogorov spectrum.

This spectrum corresponds to “pure turbulence”: there are no force fields, boundary influences or any kind of disturbance. The flow statistics are spatially homogeneous and isotropic, temporally stationary or decaying. The energy spectrum shown in Fig. 1 describes the main features of the turbulent energy cascade. Energy production mainly affects the large scales (characterized by L_0), most of the energy is contained in the large eddies (energy containing range). There is an intermediate wavenumber range ($1/L_0 < \kappa < 1/L_d$) in which the energy spectrum is described by the scaling law

$$\hat{E}(\kappa) \sim \kappa^{-5/3}. \tag{2}$$

This part of the spectrum is called the inertial range. Dissipation becomes significant due to viscosity below the so called Kolmogorov length scale L_d. This is why the spectrum cuts off by large wavenumbers (dissipation range). A more detailed description of the Kolmogorov spectrum is given by Pope (2000).

The viability of the Kolmogorov spectrum was confirmed by means of both experimental and simulation techniques. For instance, various grid turbulence measurements are reported in the literature, e.g. Stalp et al. (1999); Kurian and Fransson (2009); Ertunç et al. (2010) and the results agree with Kolmogorov’s notion of turbulence. Simulation tools are also extensively used to predict the statistics of turbulent flows, e.g. large eddy simulation was used by Kang et al. (2003), Galanti and Tsinober (2004) performed direct numerical simulations, Ditlevsen (2010) and Biferale (2003) reviewed the shell-models of turbulent energy cascade.

Our goal in this paper is to present a purely phenomenological model of turbulence which includes nonlinearity. Our mechanistic turbulence model is a binary tree of masses and springs (see Fig. 2), in which the masses represent the different scales, and the springs provide the connection among them. In a previous paper (Bak and Kalmár-Nagy (2018b)) we analyzed the response of a linear version of the system for impulsive and continuous harmonic excitations. We showed that among the scales of the linear system there is a qualitatively similar energy distribution as the Kolmogorov spectrum, if the model parameters are adequately chosen.

This paper is structured as follows: in Section 2 the phenomenological mechanistic model is described in details. In Section 3 we show how the energy dissipation depends on the input energy in the nonlinear mechanistic model. Furthermore, the energy spectrum of the model is described, and the characteristics of this spectrum is analyzed with different input energy levels. The energy spectra of the linear and nonlinear systems are compared. In Section 4 we draw conclusions. Throughout the analysis we consider every quantity to be dimensionless and/or normalized by a reference value.

2 Mechanistic Turbulence Model

2.1 Introduction of the Model

We introduce a mechanistic model of turbulence which is a binary tree of masses connected by springs. The tree has n levels, there are 2^{l-1} masses ($l = 1, ..., n$) in the lth level. The total number of masses is $N = 2^n - 1$. The model for $n = 3$ is depicted in Fig. 2.

The masses represent the different scales of vortices. The top mass (the largest vortex) is connected to the motionless ceiling with a spring. In the bottom level the masses (associated with the smallest, energy dissipating scale) are connected to the previous level with either linear or nonlinear springs and linear dampers.

In the nonlinear version of the model the parts responsible for the dissipation are nonlinear energy sinks (NES) as opposed to the linear model in which those are tuned mass dampers (TMD). Considering impulsive excitation, a fundamental difference between NES and TMD is that the effectiveness of the NES depends on the input energy magnitude, while the TMD is effective if it is tuned to the natural frequencies of the primary system. The behavior of a purely linear system is completely independent of the input energy magnitude.

Considering a system having at least 4 levels, the equations of motion for the masses in the different levels are

$$m_i\ddot{x}_i = \begin{cases} k_{2i}(x_{2i} - x_i) + k_{2i+1}(x_{2i+1} - x_i) - k_i x_i, \quad i = 1, \\ k_{2i}(x_{2i} - x_i) + k_{2i+1}(x_{2i+1} - x_i) - k_i(x_i - x_{\lfloor i/2 \rfloor}), \quad i = 2, ..., 2^{n-2} - 1, \\ k_{2i}(x_{2i} - x_i)^{\beta} + k_{2i+1}(x_{2i+1} - x_i)^{\beta} - k_i(x_i - x_{\lfloor i/2 \rfloor}) + \\ \qquad + c_{2i}(\dot{x}_{2i} - \dot{x}_i) + c_{2i+1}(\dot{x}_{2i+1} - \dot{x}_i), \quad i = 2^{n-2}, ..., 2^{n-1} - 1, \\ -k_i(x_i - x_{\lfloor i/2 \rfloor})^{\beta} - c_i(\dot{x}_i - \dot{x}_{\lfloor i/2 \rfloor}), \quad i = 2^{n-1}, ..., N. \end{cases} \tag{3}$$

The symbol $\lfloor . \rfloor$ denotes the floor operation. The exponent β=1 in the linear case and β=3 in the nonlinear case. The number of levels is $n \geq 4$.

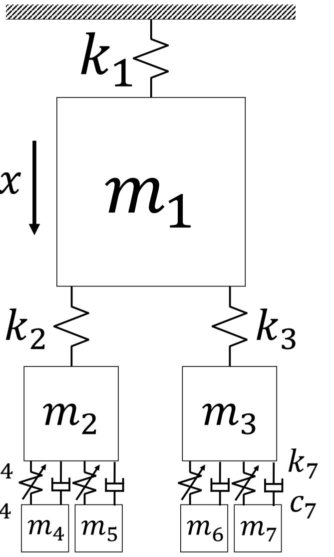

Figure 2: A 3-level mechanistic turbulence model.

2.2 Model Parameters

We set the masses, stiffnesses and dampers to be equal within a level. This allows us to introduce the following notations:

- M_l is the size of each mass in the lth level (i.e. $M_1 = m_1, M_2 = m_2 = m_3, ...$).
- K_1 denotes the stiffness of the top spring. K_l ($l = 2, ..., n$) denotes the stiffness coefficient of every spring which connects a mass of the $l-1$th and a mass of the lth levels.
- Every damper has the same damping coefficient which is denoted by C.

To represent the different length scales of vortices, the masses are gradually decreased in lower levels (a vortex of size L breaks up into smaller vortices). The power-law distribution

$$M_l = 1/2^{l-1}, \quad l = 1, ..., n, \tag{4}$$

specifies the masses in each level. Thus, the sum of masses in each level is 1, since $2^{l-1}M_l = 2^{l-1}(1/2)^{l-1} = 1$. Similarly to the masses, the K_l values are specified with a power-law distribution

$$K_l = \sigma^{l-1}, \quad \sigma > 0, \quad l = 1, ..., n, \tag{5}$$

whose single parameter is σ which is called the stiffness parameter. Thus, the stiffness of the top spring is $K_1 = \sigma^0 = 1$.

We define the damping ratio of the system as

$$\xi = C/2\sqrt{M_n K_n}. \tag{6}$$

The analysis of the previous linear model revealed that the energy spectrum (which we define in Section 3) in effect depends on σ, and is practically independent of ξ. In this paper we use $\xi = 0.001$, because such a weak damping well highlights how the nonlinear system behaves for different input energy magnitudes. Based on previous investigation of the linear model we set $\sigma = 0.45$, since for this σ the energy spectrum has many similarities with the Kolmogorov spectrum (see Bak and Kalmár-Nagy (2018b)). An 8-level system is analyzed for impulsive excitation. Every initial condition is set to zero, except $\dot{x}_1(0)$ (an initial velocity is set for the top mass).

3 Energy Transfer in the Mechanistic Model

3.1 The Total Mechanical Energy

The total mechanical energy $E(t)$ of the system is the sum of the kinetic energy stored in the masses, the potential energy stored in the linear springs, and the potential energy stored in the nonlinear springs, i.e.

$$E(t) = \frac{1}{2}\sum_{i=1}^{N} m_i \dot{x}_i^2 + \frac{1}{2}k_1 x_1 + \frac{1}{2}\sum_{i=2}^{2^{n-1}-1} k_i (x_i - x_{\lfloor i/2 \rfloor})^2 + \frac{1}{\beta+1}\sum_{i=2^{n-1}}^{N} k_i (x_i - x_{\lfloor i/2 \rfloor})^{\beta+1}. \tag{7}$$

The key difference between the linear and the nonlinear system is immediately seen from Fig. 3 which shows the percentage of $E(t)$ compared to the initial energy $E(0) = 1/2\dot{x}_1^2(0)$ for 8-level systems. In this figure the graph corresponding to the linear system ($\beta = 1$) is depicted with a solid line.

In the nonlinear system $E(t)$ strongly depends on the initial mechanical energy. For small $E(0)$ (see Fig. 3a) the dissipation is comparable to that of the linear system. As $E(0)$ increases, the dissipation becomes more significant (see Fig. 3b). This is in accordance with the description in Vakakis et al. (2008) which states that below a certain energy threshold the dissipation of the NES is not significant.

The evidence of a more efficient energy transfer realized by the NES compared to the TMD is shown in Fig. 4. In this figure $E_8(t)$ refers to the energy stored in the 8th level (the last level which includes the dissipating parts). Though the maximum percentage of $E_8(t)/E(t)$ is around 25% in both cases, there are much more spikes reaching this peak by the nonlinear case. The spikes are also wider in the nonlinear case. Thus, even for a moderately small impulse ($E(0) = 1$), more energy is transferred to the dissipating parts of the system in the same amount of time, if NESs are used instead of TMDs.

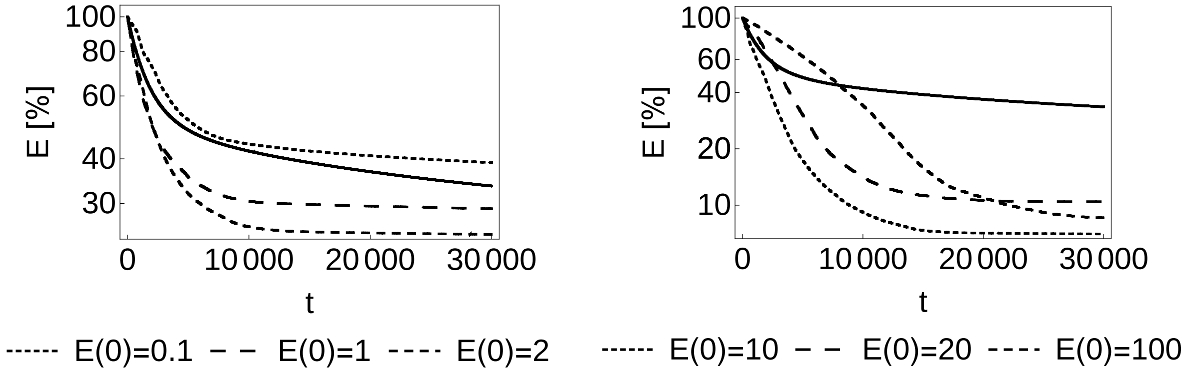

(a) Small input energy.

(b) Large input energy.

Figure 3: The total mechanical energy of 8-level mechanistic models for different amount of initial energies. The continuous line corresponds to the linear system.

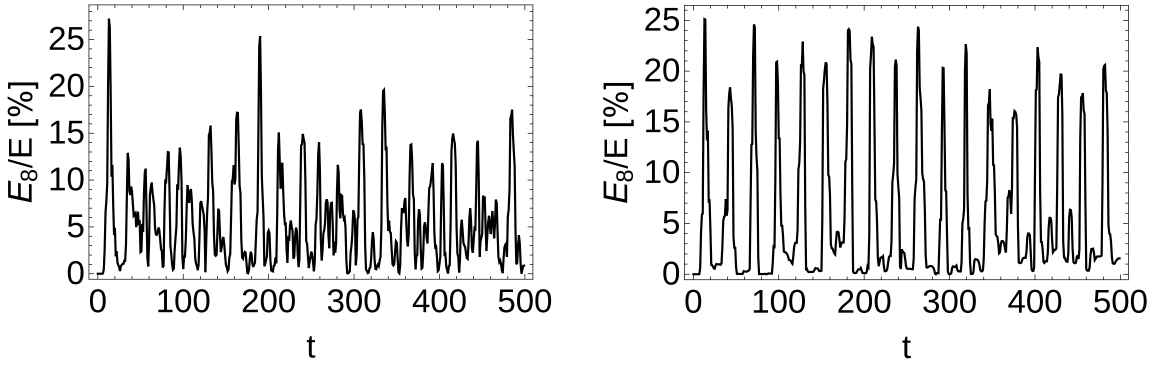

(a) Linear case.

(b) Nonlinear case.

Figure 4: The percentage of the total mechanical energy of an 8-level system stored in the dissipating parts. The initial energy is $E(0) = 1$.

3.2 The Energy Spectrum

We compute $E_l(t)$ which is the mechanical energy stored in level l ($l = 1, ..., n$). Naturally, the kinetic energy of the masses located in level l contribute to $E_l(t)$. By design, the potential energy of the springs connecting two masses is distributed equally between the two levels. The potential energy of the top spring is added to $E_1(t)$. This definition of $E_l(t)$ ensures that $\sum_{l=1}^{n} E_l(t) = E(t)$, and $E_l(t) > 0$ for $t > 0$.

The mean total mechanical energy $\bar{E}$ of the system during the time period $[t_1, t_2]$ is $E(t)$ averaged over this time period, i.e.

$$\bar{E} = \frac{1}{t_2 - t_1} \int_{t_1}^{t_2} E(t)dt. \tag{8}$$

The mean mechanical energy $\bar{E}_l$ stored in level l can be calculated in the same manner, i.e.

$$\bar{E}_l = \frac{1}{t_2 - t_1} \int_{t_1}^{t_2} E_l(t)dt, \quad l = 1, ..., n. \tag{9}$$

In turbulent flow the energy spectrum $\hat{E}(\kappa)$ shows the “contribution” of the different scales to the total energy of the flow, i.e. the mean energy stored in the different wavenumbers κ (see Eq. (2)). Analogously to the wavenumber of a turbulent scale, we define the “wavenumber” of the masses in the lth level as

$$\kappa_l = 1/M_l, \quad l = 1, ..., n. \tag{10}$$

The energy fraction stored in wavenumber κ_l is defined as

$$\hat{E}_l(\kappa) = \bar{E}_l/\bar{E}, \quad l = 1, ..., n, \tag{11}$$

and it shows the "contribution" of a scale to the total mechanical energy of the system (each $\hat{E}_l(\kappa)$ belongs to a different "mass scale" M_l). The $\hat{E}_l(\kappa)$ values ($l = 1, ..., n$) constitute the discrete energy spectrum $\hat{E}(\kappa)$ of the mechanistic model.

Fig. 3 shows that the behavior of the system consists of an initial, highly dissipative part which is followed by a slowly decaying part. In the first part the spectrum heavily depends on the time interval $[t_1, t_2]$ (see Bak and Kalmár-Nagy (2018b)). In Bak and Kalmár-Nagy (2018a) we eliminated this dependence on the chosen time interval by calculating the spectrum of the linear system in the asymptotic limit of $t_1 \to \infty$. In practice we can approximate the spectrum corresponding to the asymptotic limit of $t_1 \to \infty$ by choosing a sufficiently large t_1. Therefore, in this study we extract the energy spectrum from $t \in [59900, 60000]$ for both the linear and nonlinear cases. Our experience is that the energy spectrum of the nonlinear system is also practically independent of the time interval $[t_1, t_2]$, if t_1 is sufficiently large. Typical energy spectra for different initial energies are shown in Fig. 5.

To make the comparison easier, the energy spectrum of the linear case ($\beta = 1$) is depicted in every plot. As Fig. 5 shows, the shape of the energy spectrum depends on the initial energy of the nonlinear system. In general, the cut-off at the largest wavenumber is much more significant in the nonlinear case.

For small initial energy (Fig. 5a) the slope of the spectrum of the nonlinear system is less steep than that of the linear system. The dissipative parts are very efficient for moderately large initial energy (Fig. 5b), and the cut-off at the largest wavenumber is less noticeable in this case. As the initial energy further increased (Fig. 5c) the spectrum of the nonlinear system becomes the same as that of the linear system, except at the largest wavenumber where the cut-off becomes significant again. Comparing Figs. 3 and 5 explains the more serious cut-off in the nonlinear cases. When the system is nonlinear, a plateau is observed in the plots of $E(t)$ after the initial, highly dissipative part. This means that the energy dissipation becomes insignificant. Thus, the energy fraction stored in the largest wavenumber (which corresponds to the dissipating nonlinear part) must be negligible, since otherwise the energy dissipation would be still significant. This is why a spectacular cut-off is present in the energy spectrum by the largest wavenumber. In the linear system the energy is still steadily decaying after the high initial dissipation, hence the cut-off in the energy spectrum is less significant.

Similarly to the Kolmogorov spectrum, the midrange of the energy spectra seemingly obeys a scaling law which is

$$\hat{E}(\kappa) \sim \kappa^{\alpha}, \tag{12}$$

where the scaling exponent α mainly depends on σ. In the nonlinear case α also depends on the input energy. For the linear model the scaling exponent $\alpha = -2.37$, while it is always larger or the same for the nonlinear model.

4 Conclusions

We analyzed a nonlinear mechanistic model of turbulence which is a binary tree of masses connected by springs. The bottom level of the system consists of NESs to model dissipation. The response of the system was studied for impulsive excitations which were applied to the top mass. These impulses had different magnitude to show that the behavior of the nonlinear system strongly depends on the input energy. We defined and showed the energy spectrum of the mechanistic model for linear and nonlinear cases. The parameters of the model (σ and ξ) were chosen to replicate an energy spectrum which is similar to the Kolmogorov spectrum. The choice was based on the analysis of the previously investigated linear model. Compared to the spectrum of the linear model, for small to moderate initial energy the spectrum of the nonlinear model contains more energy in the intermediate and large wavenumbers, except the largest wavenumber. At the largest wavenumber the spectrum cuts off. The cut-off is in general much more serious in the nonlinear case, because after the initially rapid energy dissipation the energy

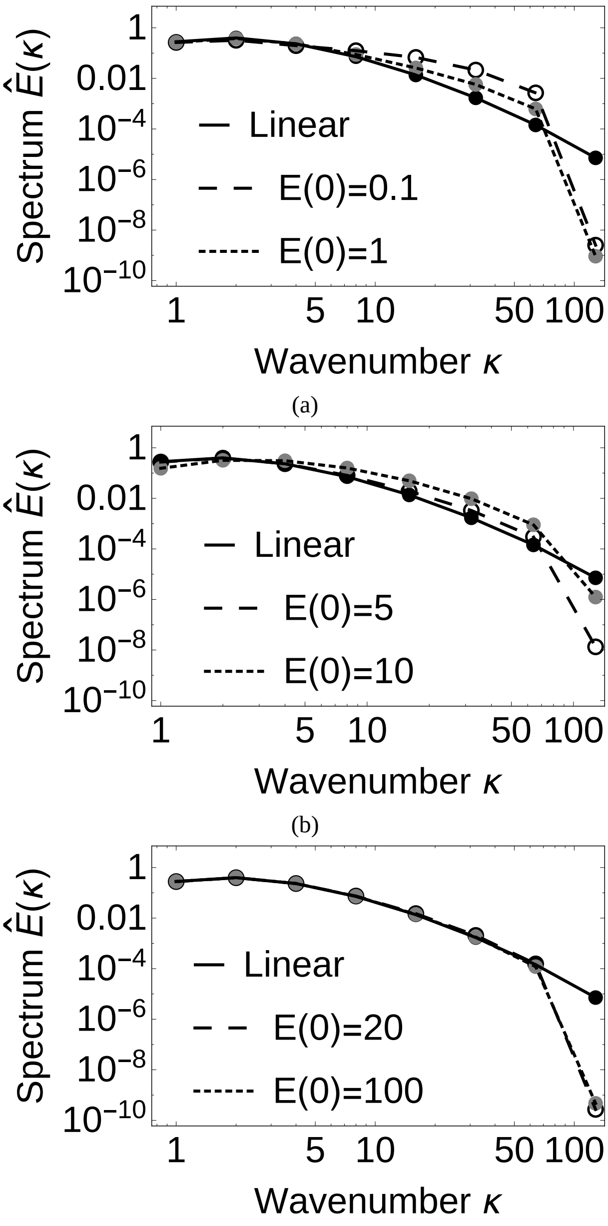

(a)

(b)

(c)

Figure 5: Energy spectra of the linear and nonlinear 8-level mechanistic models for different initial energies.

transfer to the dissipating bottom level becomes negligible. For large initial energy the spectra of the linear and the nonlinear cases are practically the same, except the largest wavenumber. Including nonlinearities in the model “improved” the shape of the spectrum in the sense that it better resembles the Kolmogorov spectrum with the more significant cut-off at the largest wavenumber. In future work we intend to include negative damping (which would correspond to internal energy generation) and more nonlinear springs at higher levels of the model to investigate the energy cascade of those systems.

Acknowledgements

This project was supported by the ÚNKP-17-3-I and ÚNKP-18-3-I New National Excellence Programs of the Ministry of Human Capacities of Hungary. We acknowledge the financial support from TeMA Talent Management Foundation. The research reported in this paper was supported by the Higher Education Excellence Program of the Ministry of Human Capacities in the frame of Water Science & Disaster Prevention research area of Budapest University of Technology and Economics (BME FIKP-VÍZ).

References

Bak, B. D.; Kalmár-Nagy, T.: Energy transfer in a linear turbulence model. In: *ASME 2018 International Design Engineering Technical Conferences and Computers and Information in Engineering Conference* (2018a), V006T09A038.

Bak, B. D.; Kalmár-Nagy, T.: A linear model of turbulence: reproducing the Kolmogorov-spectrum. *IFAC-PapersOnLine*, 51, 2, (2018b), 595–600.

Biferale, L.: Shell models of energy cascade in turbulence. *Annual Review of Fluid Mechanics*, 35, 1, (2003), 441–468.

Ditlevsen, P. D.: *Turbulence and shell models*. Cambridge University Press (2010).

Ertunç, Ö.; Özyilmaz, N.; Lienhart, H.; Durst, F.; Beronov, K.: Homogeneity of turbulence generated by static-grid structures. *Journal of Fluid Mechanics*, 654, (2010), 473–500.

Fermi, I.; Pasta, P.; Ulam, S.; Tsingou, M.: Studies of the nonlinear problems. Tech. rep., Los Alamos Scientific Lab., New Mexico (1955).

Galanti, B.; Tsinober, A.: Is turbulence ergodic? *Physics Letters A*, 330, 3, (2004), 173–180.

Gendelman, O.; Manevitch, L.; Vakakis, A. F.; M'closkey, R.: Energy pumping in nonlinear mechanical oscillators: Part I-dynamics of the underlying hamiltonian systems. *Journal of Applied Mechanics*, 68, 1, (2001), 34–41.

Kang, H. S.; Chester, S.; Meneveau, C.: Decaying turbulence in an active-grid-generated flow and comparisons with large-eddy simulation. *Journal of Fluid Mechanics*, 480, (2003), 129–160.

Kolmogorov, A. N.: The local structure of turbulence in incompressible viscous fluid for very large Reynolds numbers. In: *Dokl. Akad. Nauk SSSR*, vol. 30, pages 301–305, JSTOR (1941).

Kurian, T.; Fransson, J. H. M.: Grid-generated turbulence revisited. *Fluid Dynamics Research*, 41, 2, (2009), 021403.

Pope, S. B.: *Turbulent Flows*. Cambridge University Press (2000).

Richardson, L. F.: *Weather Prediction by Numerical Process*. Cambridge University Press (1922).

Stalp, S. R.; Skrbek, L.; Donnelly, R. J.: Decay of grid turbulence in a finite channel. *Physical Review Letters*, 82, 24, (1999), 4831.

Turcotte, D.; Malamud, B.; Morein, G.; Newman, W.: An inverse-cascade model for self-organized critical behavior. *Physica A: Statistical Mechanics and its Applications*, 268, 3-4, (1999), 629–643.

Vakakis, A. F.; Gendelman, O.: Energy pumping in nonlinear mechanical oscillators: part II-resonance capture. *Journal of Applied Mechanics*, 68, 1, (2001), 42–48.

Vakakis, A. F.; Gendelman, O. V.; Bergman, L. A.; McFarland, D. M.; Kerschen, G.; Lee, Y. S.: *Nonlinear Targeted Energy Transfer in Mechanical and Structural Systems*, vol. 156. Springer Science & Business Media (2008).

Address: Department of Fluid Mechanics, Faculty of Mechanical Engineering, Budapest University of Technology and Economics. Bertalan Lajos u. 4 - 6, H-1111 Budapest, Hungary.
email: `bak@ara.bme.hu, kalmarnagy@ara.bme.hu`

DOI: 10.24352/UB.OVGU-2019-008 TECHNISCHE MECHANIK, 39, 1, (2019), 72 – 84
submitted: July 6, 2018

Heat Transfer across the Free Surface of a Thermocapillary Liquid Bridge

F. Romanò[1], H. C. Kuhlmann[2]

The heat transfer across the free surface of a millimetric thermocapillary liquid bridge is investigated for two dimensional axisymmetric flows, computed by Newton–Raphson iteration. The coupled multiphase flow in the silicone-oil liquid bridge and in the ambient gas (air) is considered for Marangoni and Prandtl numbers of interest for typical space experiments. Based on the space-resolved heat flux of the two-phase flow for a wide range of parameters, we derive a model for the heat flux in form of Newton's heat transfer law for a surrogate single phase flow, in which a space-dependent Biot function is considered. A parametric study for a 2 cSt silicone-oil liquid bridge is conducted for 150 configurations to derive a reliable fit of the Biot function for a wide range of Reynolds numbers and aspect ratios. An explicit form of the parametric fit is provided which takes into account the hot- and cold-wall boundary layers in the liquid.

Nomenclature

$A_{0,1,2,3}$	$[-]$	coefficients for Re-dependent fits
Bi	$[-]$	Biot number and Biot function
Ca	$[-]$	capillary number
Ma	$[-]$	Marangoni number
Pr	$[-]$	Prandtl number
Re	$[-]$	Reynolds number
$\mathcal{V}$	$[-]$	volume ratio of the liquid bridge
$\boldsymbol{J}$	$[-]$	Jacobian matrix
$R,\ R_\mathrm{tc},\ R_\mathrm{gap}$	[m]	radius of rods, test chamber and annular gap around the liquid bridge
$T,\ \Delta T$	[K]	temperature and temperature difference
a	$[-]$	coefficients for z-dependent fits
d	[m]	distance between support rods
$\boldsymbol{f}$	$[-]$	residual of the Newton method
h_fs	$[-]$	free surface deformation
h_g	[W/(m^{2}K)]	heat-transfer coefficient (gas)
$p,\ \boldsymbol{u}$	$[-]$	pressure and velocity field
$r,\ \varphi,\ z$	$[-]$	radial, azimuthal, axial coordinate
$\boldsymbol{x}$	$[-]$	position vector
$\boldsymbol{y}$	$[-]$	solution of the Newton method
$\alpha,\ \beta$	$[-]$	coefficients for Γ-dependent fits
γ	[N/(mK)]	negative surface-tension coefficient
δ	$[-]$	increment of the Newton method
θ	$[-]$	reduced temperature
κ	[m^2/s]	thermal diffusivity
Λ	$[-]$	axial aspect ratio
λ	[W/(mK)]	thermal conductivity
ν	[m^2/s]	kinematic viscosity
ρ	[kg/m^3]	density
σ	[N/m]	surface tension
Γ	[m/s]	radial aspect ratio

Subscripts and Superscripts

0	evaluated at average temperature
$c1,\ c2$	boundary layer at the cold rod
DSD	dynamic surface deformation
m	polynomial fit in the middle of the liquid bridge
cold, hot	hot and cold support rods
fs	free surface
g	gas phase
l	liquid phase
k	k-th iteration of the Newton method
min, max	local minimum and local maximum of Bi
ref	reference (non-dimensional temperature)
h	boundary layer thickness on the hot rod
tc	test chamber
gap	annular gap between the liquid bridge surface and the test chamber wall

1 Introduction

When the interface between two immiscible fluids experiences a tangential temperature gradient, the resulting variable surface tension leads to thermocapillary forces, which can drive the flow in the two phases (1). A natural framework for thermocapillary flows are microfluidic systems, where surface forces become more important than volume forces and buoyancy does not overshadow Marangoni stresses. This is the case, e.g., for small droplets (2) or thin films (3), where the interfacial forces between two immiscible fluids play a key-role for the fluid flow. Thermocapillary convection is also important in industrial processes which involve large temperature gradients, e.g., welding (4), combustion (5) and crystal growth (6). For these reasons, much attention has been paid to thermocapillary flows in simplified configurations such as thermocapillary liquid films (7), cavities (8; 9; 10), annular pools (11) and liquid bridges (12).

Originally, the system of a liquid bridge has been proposed as a model for the floating-zone crystal-growth process (13). Later, it became a paradigm for thermocapillary flows. The multiphase flow is crucially determined by the heat transfer across the liquid–gas interface, because the driving force depends on the tangential temperature gradient. Despite of the importance of the heat transfer, for the sake of computational economy, the flow is typically modelled as a single-phase liquid flow, where an interfacial heat transfer is assumed in form of Newton's law of cooling with some ad hoc temperature distribution in the ambient gas (14; 15). The single-phase modeling limits the computational cost, and the parameter space reduces to the non-dimensional groups for the liquid flow and a few parameters characterizing the heat transfer to the ambient gas, often a constant Biot number only.

Even though the surrounding gas has a strong influence on the liquid flow and its stability (16; 17), most numerical simulations and linear stability analyses have assumed Newton's cooling law with constant Biot number (even zero, i.e. adiabatic conditions) or a fixed given heat flux (15). We shall show that both these assumptions are too simplistic to properly represent the heat transfer and the driving of the thermocapillary flow.

Starting from two-dimensional multiphase simulations, we aim at constructing a refined heat-transfer model in the form of Newton's cooling law. To take into account the thermal effect of the flow in the ambient gas the constant Biot number is replaced by a Biot function which depends on the axial coordinate along the free surface. A new, robust and physically motivated methodology is developed to derive this functional dependence. Moreover, the improved Biot function is given in explicit form which allows to readily supply a single-phase solver with an accurate thermal boundary condition.

In Sec. 2 the multiphase flow problem is defined mathematically; in Secs. 3 and 4 the numerical discretization and the methodology to derive the model are explained. Section 5 presents the improved heat-transfer model and some evidence for its robustness and accuracy is provided. Additional comments are given and conclusions are drawn in Sec. 6.

2 Problem Formulation

A droplet of an incompressible Newtonian liquid is suspended between two coaxial cylindrical rods of radius R, placed at a mutual distance d, forming a liquid bridge. The liquid has a density ρ and a temperature-dependent kinematic viscosity $\nu(T)$ and thermal diffusivity $\kappa(T)$. The rods are differentially heated at constant temperatures $T_{\text{cold}} = T_0 - \Delta T/2$ and $T_{\text{hot}} = T_0 + \Delta T/2$, respectively, where T_0 is the mean temperature and ΔT the temperature difference between the support rods. Due to the thermocapillary effect the temperature gradient along the free surface of the liquid bridge induces a thermocapillary shear-stress which drives the flow along the free-surface from the hot rod to the cold rod. Up to linear order, the temperature-dependent surface tension $\sigma(T)$ reads

$$\sigma(T) = \sigma_0 - \gamma(T - T_0), \tag{1}$$

where $\sigma_0 = \sigma(T_0)$ is the surface tension at the mean temperature T_0 and $\gamma = -\partial\sigma/\partial T|_{T=T_0}$ the negative surface-tension coefficient. Since $\gamma > 0$ is a positive constant for most liquid–gas combinations $\partial\sigma/\partial T < 0$ and the surface tension decreases linearly with the surface temperature.

The liquid bridge is surrounded by an annular chamber space filled with a Newtonian gas (assumed incompressible) with constant density ρ_{g}, kinematic viscosity ν_{g} and thermal diffusivity κ_{g}. The annular chamber has an outer radius $R_{\text{tc}} = R + R_{\text{gap}}$ and a height $d_{\text{tc}} = d_{\text{cold}} + d + d_{\text{hot}}$. The bounding walls are thermally insulating (see fig. 1). In the absence of gravity, thermocapillary stresses at the liquid–gas interface represent the only driving of the flow.

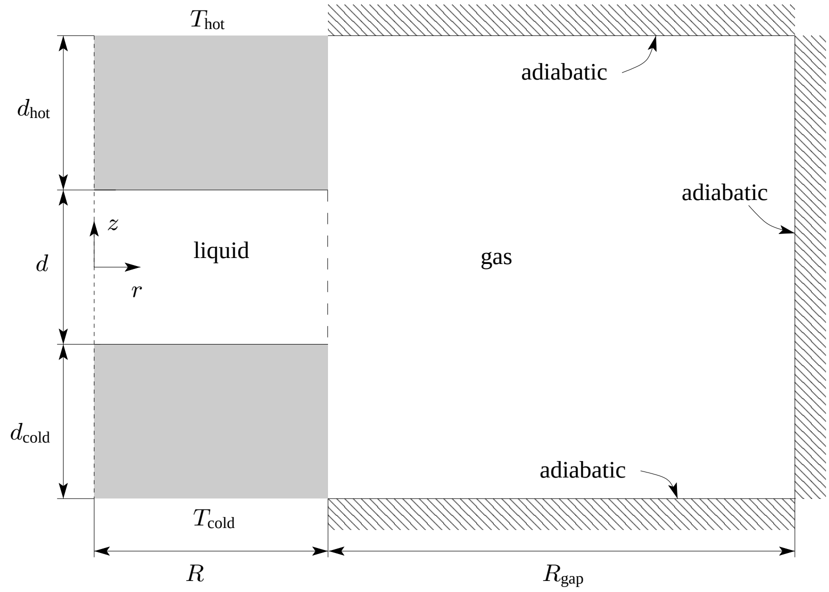

Figure 1: Sketch of the liquid bridge held in place by surface tension between the hot and the cold rod. The liquid bridge is surrounded by an ambient gas confined to an adiabatic test chamber.

Velocity, length, time, pressure and temperature are scaled with $\gamma\Delta T/\rho\nu_0$, d, $d\rho\nu_0/\gamma\Delta T$, $\gamma\Delta T d$ and ΔT, respectively (thermocapillary scaling). The resulting non-dimensional continuity, Navier–Stokes and energy equation for the steady flow are

$$\text{Re}\,(\boldsymbol{u}\cdot\nabla\boldsymbol{u}) = -\nabla p + \nabla\cdot(\nu/\nu_0\nabla\boldsymbol{u}), \tag{2a}$$

$$\nabla\cdot\boldsymbol{u} = 0, \tag{2b}$$

$$\text{Ma}\,(\boldsymbol{u}\cdot\nabla\theta) = \nabla\cdot(\kappa/\kappa_0\nabla\theta), \tag{2c}$$

where $\nu_0 = \nu(T_0)$ and $\kappa_0 = \kappa(T_0)$ are the reference kinematic viscosity and thermal diffusivity, $\boldsymbol{x} = (r, \varphi, z)$ and t are polar space and time coordinates, $\boldsymbol{u} = (u, v, w)$ and p the velocity and pressure fields, and $\theta = (T - T_0)/\Delta T$ is the reduced temperature. Two non-dimensional groups arise, the thermocapillary Reynolds number Re and the Marangoni number Ma

$$\text{Re} = \frac{\gamma\Delta T d}{\rho\nu_0^2}, \quad \text{Ma} = \frac{\gamma\Delta T d}{\rho\nu_0\kappa_0}. \tag{3}$$

For comparison with other work, the Prandtl number $\text{Pr} = \text{Ma}/\text{Re} = \nu_0/\kappa_0$ is defined at the reference temperature. The geometry is characterized by the four aspect ratios (see fig. 1)

$$\Gamma = \frac{d}{R}, \quad \Gamma_{\text{tc}} = \frac{d}{R_{tc}}, \quad \Lambda_{\text{hot}} = \frac{d}{d_{\text{hot}}}, \quad \Lambda_{\text{cold}} = \frac{d}{d_{\text{cold}}}, \tag{4}$$

where, in the following, we fix the three aspect ratios $\Gamma_{\text{tc}} = d/R_{tc} = 0.1$ and $\Lambda_{\text{hot}} = \Lambda_{\text{cold}} = 1$ such that $\Lambda_{\text{tc}} = 1 + \Lambda_{\text{hot}} + \Lambda_{\text{cold}} = 3$, and vary $\Gamma = 0.5$, 0.66 and 1, which are values of common interest in the literature.

A major difficulty in solving (2) is the determination of the shape $h_{\text{fs}}(z)$ of the liquid–gas interface. Here we assume a pinning of the interface at the sharp circular edges of the rods, i.e. $h_{\text{fs}}(z = \pm 1/2) = 1/\Gamma$. Furthermore, we consider the limit of asymptotically large mean surface tension σ_0, for which the capillary number Ca $= \gamma \Delta T/\sigma_0 \rightarrow 0$. Using this approximation is justified for silicone oil liquid bridges: An asymptotic analysis of (18) has shown that the steady flow-induced interface deformations are typically smaller than 0.1% of the radius of the liquid bridge (see also (19)). Oscillatory flow-induced deformations were measured by (20) to be of the order of 0.1 microns. Thus, the dynamic oscillatory deformations were 10^5 times smaller than the length scale $h = 10\,\text{mm}$ of the liquid bridge (see also (21; 22)). Taking the limit Ca $\rightarrow 0$, flow-induced (liquid and gas) interfacial deformations are absent. Therefore, the interfacial shape is independent of the flow and can be determined by solving the Young–Laplace equation (12). In the absence of gravity and for unit non-dimensional volume of liquid

$$\mathcal{V} = \int_{-1/2}^{1/2} h_{\text{fs}}^2(z)\mathrm{d}z = 1, \tag{5}$$

the liquid bridge is cylindrical, i.e. $h_{\text{fs}} = 1/\Gamma$. The cylindrical shape of the liquid bridge is experimentally proven to be a good approximation for silicone oil liquid bridges.

The bulk equations (2) are solved assuming axisymmetry ($\partial_\varphi = 0$) and closed by the boundary conditions. Along the cold and hot support, no-slip and isothermal boundary conditions are enforced

$$\text{hot rod:} \quad \boldsymbol{u} = \boldsymbol{0}, \quad \theta = 1/2, \tag{6a}$$

$$\text{cold rod:} \quad \boldsymbol{u} = \boldsymbol{0}, \quad \theta = -1/2, \tag{6b}$$

whereas no-slip and adiabatic conditions are assumed at the walls of the test chamber

$$r = 1/\Gamma_{\text{tc}}: \quad \boldsymbol{u} = \boldsymbol{0}, \quad \partial_r \theta = 0, \tag{7a}$$

$$z = \pm\Lambda_{\text{tc}}/2: \quad \boldsymbol{u} = \boldsymbol{0}, \quad \partial_z \theta = 0. \tag{7b}$$

Finally, imposing kinematic boundary conditions, balancing the stresses and the heat fluxes and imposing continuity of velocity and temperature at the liquid–gas interface, respectively, yields

$$r = 1/\Gamma: \qquad u = 0, \tag{8a}$$

$$(\nu_0/\nu)\partial_z\theta + \partial_r w = (\mu_{\text{g}}/\mu(T))\partial_r w_{\text{g}}, \tag{8b}$$

$$\partial_r\theta = (\kappa_{\text{g}}/\kappa(T))\partial_r\theta_{\text{g}} \tag{8c}$$

$$\boldsymbol{u} = \boldsymbol{u}_{\text{g}} \tag{8d}$$

$$\theta = \theta_{\text{g}}, \tag{8e}$$

where $\mu_{\text{g}} = \rho_{\text{g}}\nu_{\text{g}}$ and $\mu(T) = \rho\nu(T)$ are the dynamic viscosity of gas and liquid phase, respectively, w_{g} is the axial velocity in the surrounding gas and $\boldsymbol{u}_{\text{g}}$ and θ_{g} denote the velocity vector and the temperature in the gas phase, respectively.

3 Numerical Methods

The mathematical problem defined in Sec. 2 admits axisymmetric steady state solutions which are computed by means of the Newton–Raphson method

$$\boldsymbol{J}\left(\boldsymbol{y}^k\right) \cdot \delta\boldsymbol{y} = -\boldsymbol{f}\left(\boldsymbol{y}^k\right), \tag{9a}$$

$$\boldsymbol{y}^{k+1} = \boldsymbol{y}^k + \delta\boldsymbol{y}, \tag{9b}$$

where $\boldsymbol{J}\left(\boldsymbol{y}^k\right)$ is the Jacobian of (2), $\boldsymbol{y} = (u, w, p, \theta)^T$ the solution vector, k enumerates the iteration step, $\boldsymbol{f}\left(\boldsymbol{y}^k\right)$ is the nonlinear residual and $\delta\boldsymbol{y}$ the solution increment between the k-th and the $(k+1)$-th iteration.

Inserting (9b) in (2) and linearizing with respect to $\delta\boldsymbol{y}$ yields

$$\nabla \cdot \delta\boldsymbol{u} = -\nabla \cdot \boldsymbol{u}^k, \tag{10a}$$

$$\text{Re}\left(\delta\boldsymbol{u} \cdot \nabla\boldsymbol{u}^k + \boldsymbol{u}^k \cdot \nabla\delta\boldsymbol{u}\right) + \nabla\delta p - \nabla \cdot (\nu/\nu_0 \nabla\delta\boldsymbol{u}) = -\text{Re}\left(\boldsymbol{u}^k \cdot \nabla\boldsymbol{u}^k\right) - \nabla p^k + \nabla \cdot \left[\nu(T^k)/\nu_0 \nabla\boldsymbol{u}^k\right], \tag{10b}$$

$$\text{Ma}\left(\delta\boldsymbol{u} \cdot \nabla\theta^k + \boldsymbol{u}^k \cdot \nabla\delta\theta\right) - \nabla \cdot (\kappa/\kappa_0 \nabla\delta\theta) = -\text{Ma}\left(\boldsymbol{u}^k \cdot \nabla\theta^k\right) + \nabla \cdot \left[\kappa(T^k)/\kappa_0 \nabla\theta^k\right], \tag{10c}$$

where the convective term has been linearized by

$$\nabla \cdot \left(\boldsymbol{u}^{k+1}\boldsymbol{u}^{k+1}\right) \approx -\nabla \cdot \left(\boldsymbol{u}^{k}\boldsymbol{u}^{k}\right) + \nabla \cdot \left(\boldsymbol{u}^{k+1}\boldsymbol{u}^{k}\right) + \nabla \cdot \left(\boldsymbol{u}^{k}\boldsymbol{u}^{k+1}\right). \tag{11}$$

Equation (10) is solved using the same grid, initial guesses and convergence criteria as in (23).

4 Heat Transfer Model

The numerical solution of the steady multiphase Navier–Stokes system ensures a full thermal and mechanical coupling between the liquid and the gas phase. Hence, no additional models are required to determine the heat transfer between the liquid bridge and the surrounding gas. Post-processing the flow fields allows to compute the heat transfer across the interface. With θ and $\partial_r\theta|_l$ obtained from the numerical solution and evaluated at the free surface, the heat exchange at the liquid–gas interface can be recast in a Newton's cooling law

$$r = 1/\Gamma: \quad \mathrm{Bi} = \frac{\partial_r\theta|_l}{\theta - \theta_{\mathrm{ref}}}, \tag{12}$$

where the cold rod temperature $\theta_{\mathrm{ref}} = -1/2$ is used as the reference temperature. Equation (12) uses a non-standard definition of the Biot number, such that, if $\mathrm{Bi} > 0$, and $\theta > \theta_{\mathrm{ref}}$, then $\partial_r\theta|_l > 0$. Equation (12) can be understood as a definition of the local Biot number, or Biot function,

$$\mathrm{Bi}(z) = \frac{h_{\mathrm{g}}(z)d}{\lambda}, \tag{13}$$

where λ is the heat conductivity of the liquid and $h_{\mathrm{g}}(z)$ the heat-transfer coefficient of the gas. In this framework, the Biot function not only depends on z, but also on all other governing parameters, i.e. $\mathrm{Bi} = \mathrm{Bi}(z; \mathrm{Re}, \mathrm{Pr}, \Gamma, \mathrm{Pr}_{\mathrm{g}}, \Gamma_{\mathrm{tc}}, ...)$.

The classical Newton's cooling law is based on a constant Biot number ($\mathrm{Bi} = 0$ for adiabatic free surface). This is a poor approximation to the actual heat transfer process. We aim at deriving a robust fit for $\mathrm{Bi}(z; \mathrm{Re}, \mathrm{Pr} = 28.5, \Gamma, \mathrm{Pr}_{\mathrm{g}}, ...)$ assuming air as surrounding gas (i.e. $\mathrm{Pr}_{\mathrm{g}} = 0.71$). Once the Biot function is known, (12) can be interpreted as a boundary condition for θ in the framework of a single-phase flow model. Using the Biot function, the single-phase model would yield almost the same flow and temperature field as the two-phase model, albeit with much less numerical effort.

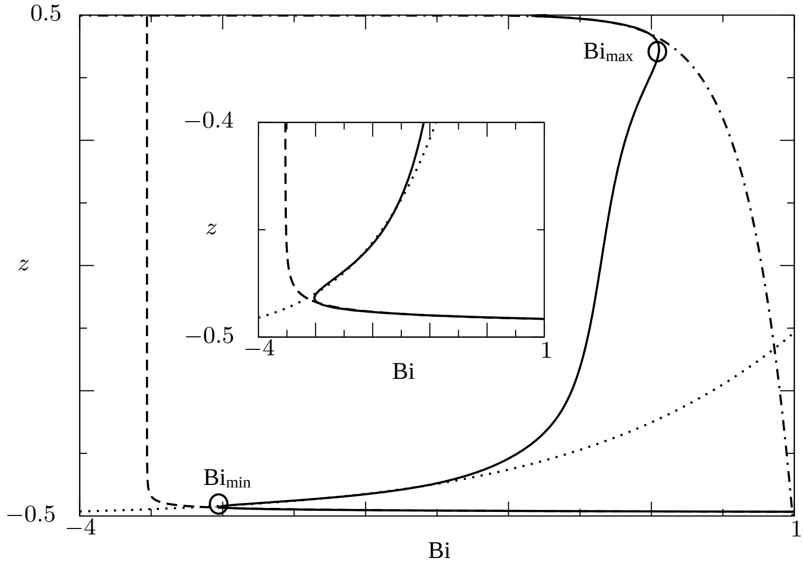

Figure 2: Biot function for $\mathrm{Pr} = 28.5$, $\Gamma = 0.5$, $\mathrm{Re} = 300$ and ambient air (full line). Power-law fits to $\mathrm{Bi}(z)$ in the region of the thermal boundary layers at the hot and cold wall are shown as dashed, dotted and dashed–dotted lines. The circles indicate the stationary points of $\mathrm{Bi}(z)$.

A typical Biot function is shown in fig. 2 (full line) for $\Gamma = 0.5$ and $\mathrm{Re} = 300$. Owing to the high Prandtl number, the temperature field in the liquid is subject to strong convective effects. The corresponding thermal boundary layers on the cold and the hot wall are reflected by the sharp minimum and maximum of the Biot function near the edges $z = \pm 1/2$. The dependence of the Biot function in the boundary layer region is well captured by power laws (dashed, dotted and dashed–dotted lines in fig. 2). Moreover, the locations and the absolute values of the stationary points of Bi(z) (see fig. 2) are well described by the functional dependence

$$\{\delta_{\text{cold}}, \text{Bi}_{\text{min}}, \delta_{\text{hot}}, \text{Bi}_{\text{max}}\} \approx A_0 + A_1 \text{Re} + A_2/\text{Re}^{A_3}, \tag{14}$$

where $\delta_{\text{cold}} = z_{\text{min}}$ and $\delta_{\text{hot}} = 0.5 - z_{\text{max}}$ are the distances from the cold and hot wall of the minimum and maximum of the Biot function, respectively. $A_i = \alpha_i + \beta_i \Gamma$ are fit parameters which, to good approximation, depend linearly on Γ within the range $\Gamma \in [0.5, 1]$. This is demonstrated in fig. 3.

Based on the typical behavior shown in fig. 2, the dependence of Bi(z) in the layers at the hot and cold rods are represented by

$$z \in [z_{\text{max}}, 0.5] : \text{Bi} \approx a_{0h} + a_{1h}(0.5 - z)^{a_{2h}} \tag{15a}$$

$$z \in \left[\frac{-0.5 + z_{\text{min}}}{2}, z_{\text{min}}\right] : \text{Bi} \approx a_{0c1} + a_{1c1}(0.5 + z)^{a_{2c1}} \tag{15b}$$

$$z \in [z_{\text{min}}, z_{\text{min}} + 0.1] : \text{Bi} \approx a_{0c2} + a_{1c2}(0.5 + z)^{a_{2c2}}. \tag{15c}$$

Adding these terms and including a polynomial of degree five to fit the intermediate behavior far away from the edges (middle part of the Biot function, subscript m) yields the functional form of the fit for the Biot function

$$\text{Bi} = [a_{0h} + a_{1h}(0.5 - z)^{a_{2h}}] + \sum_{j=1}^{2} [a_{0cj} + a_{1cj}(z + 0.5)^{a_{2cj}}] + \sum_{i=0}^{5} a_{im} z^i, \tag{16}$$

where a_{ih}, a_{ic1} and a_{ic2} $(i = 0, 1, 2)$ and a_{im} $(i \in [0, ..., 5])$ are fit parameters. The constants can be collected $a_0 = a_{0h} + a_{0c1} + a_{0c2} + a_{0m}$, once the individual subregions have been fitted.

All coefficients are function of the aspect ratio Γ and the Reynolds number Re. By combining results from all simulations, the functional dependence of the fitting coefficients on Γ and Re will be obtained. The functional dependence (14) has been employed for fitting a_{ih}, a_{ic1} and a_{ic2}, and the result is reported in table 1. Such assumption is motivated by the ansatz for the fit of the stationary points of the Biot function. In order to achieve a robust fit, which can also elucidate the boundary layer scaling of Bi(z), we follow a multistage approach.

In a first step only the power laws (15) for the boundary layers are determined. Each fit requires the determination, by least squares, of three fit parameters. Since the fitting function is non-linear, a Newton method is employed to find the solution of the non-linear system resulting from the least squares minimization. Given an initial guess for the coefficients, the iteration is terminated when the absolute norm of the residuals of the fit coefficients is less than 10^{-8}. To obtain a robust fit, the fit protocol follows four stages.

I) all three coefficients are obtained by (15) fitting Bi(z) for each combination of $\Gamma \in \{0.5, 0.66, 1\}$ and Re $\in [30, 1500]$;

II) the coefficient a_{0*} (where $* \in \{h, c1, c2\}$) is fitted by (14) and a successive fit operation is employed to find the coefficients α_i and β_i reported in table 1 (see fig. 4). Inserting the fit of a_{0*} in (15), the other two coefficients are obtained fitting Bi(z) for each combination of $\Gamma \in \{0.5, 0.66, 1\}$ and Re $\in [30, 1500]$;

III) the coefficient a_{1*} is fitted by (14) and a successive fit operation is employed to find the coefficients α_i and β_i reported in table 1 (see fig. 5). The fit of a_{1*} is substituted in (15) together with the fit of a_{0*}. The last coefficient is computed fitting Bi(z) for each combination of $\Gamma \in \{0.5, 0.66, 1\}$ and Re $\in [30, 1500]$;

IV) the coefficient a_{2*} is fitted by (14) and a successive fit operation is employed to find the coefficients α_i and β_i reported in table 1 (see fig. 6).

Once all the fit parameters of the power laws have been determined, (16) is employed to determine a_{im} in a single step using the same least squares and Newton–Raphson method employed for a_{*h}, a_{*c1} and a_{*c2}.

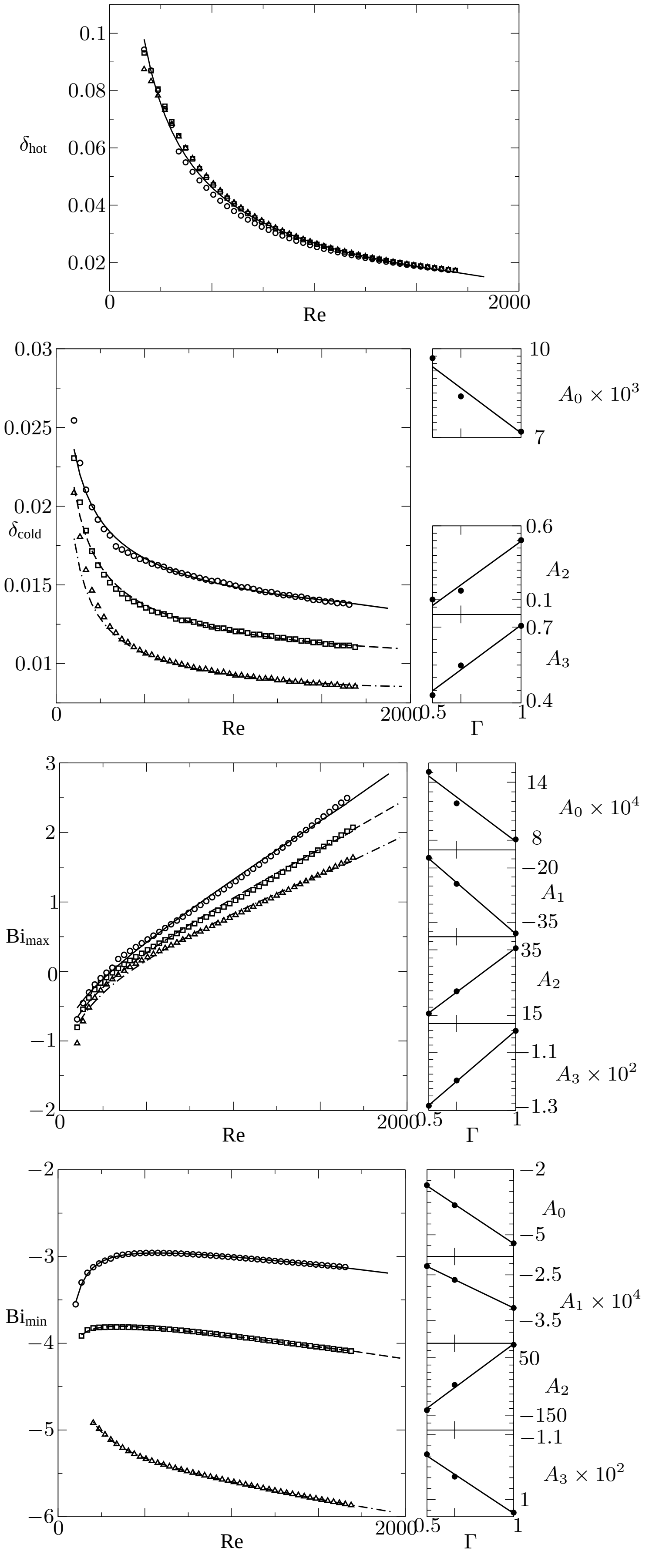

Figure 3: Minimum, $\mathrm{Bi}_{\mathrm{min}}$, and maximum, $\mathrm{Bi}_{\mathrm{max}}$, of the Biot function $\mathrm{Bi}(z)$, and corresponding distance from the cold and hot rod, δ_{cold} and δ_{hot}, respectively. Markers refer to simulation data: $\Gamma = 0.5$ (circles, full line), 0.66 (squares, dashed line) and 1 (triangles, dash-dotted line). The lines refer to least square fits.

5 Results

The three successive fits corresponding to stages II, III, and IV, are demonstrated for $a_{0c2}(\Gamma, \mathrm{Re})$, $a_{1c2}(\Gamma, \mathrm{Re})$ and $a_{2c2}(\Gamma, \mathrm{Re})$ in figs. 4, 5 and 6, respectively. No continuation method is employed for educating the guess of a_{0*}, a_{1*} and a_{2*} depending on their value at a previous Reynolds number. This explains the scatter of a_{0*}, which is due to an underdetermination of the non-linear system to fit (see fig. 4). Reducing the underdetermination of the system by fixing a_{0*} leads to a much smaller scatter in stages III and IV for a_{1*} and a_{2*} (see figs. 5 and 6, respectively). As for the location and absolute value of the stationary points of the Biot function, also for a_{ih}, a_{ic1} and a_{ic2}, the fitting constants A_i are well approximated by a linear fit in Γ.

Table 1: Fit coefficients $A_i = \alpha_i + \beta_i\Gamma$, a_{ih}, a_{ic1} and a_{ic2} are fitted with the ansatz (14).

	a_{0h}	a_{1h}	a_{2h}
α_0	14.971	-14.089	0.00597
β_0	0	-11.215	-0.0124
α_1	-0.115	0.00353	-6.99×10^{-5}
β_1	0	-0.0016	2.86×10^{-5}
α_2	0	-2.277	0
β_2	0	9.190	0
α_3	0	-0.246	0
β_3	0	0.163	0
	a_{0c1}	a_{1c1}	a_{2c1}
α_0	-0.287	0	2.960
β_0	-6.254	0	-27.306
α_1	0	0	8.43×10^{-5}
β_1	0	0	-8.10×10^{-5}
α_2	0	0.743	2.787
β_2	0	0.491	26.183
α_3	0	0.587	0.0607
β_3	0	2.861	-0.0348
	a_{0c2}	a_{1c2}	a_{2c2}
α_0	-2.922	0.574	0.0301
β_0	-47.389	54.748	0.0149
α_1	0	-0.0014	2.70×10^{-6}
β_1	0	0.00410	9.25×10^{-6}
α_2	0	0	-14.204
β_2	0	0	46.087
α_3	0	0	1.079
β_3	0	0	0.599

In the next step all constant coefficients a_{0*} are gathered in a_0 and the remaining coefficients a_{im} for $i = 1, ..., 5$, are determined by inserting a_{1h}, a_{2h}, a_{1c1}, a_{2c1}, a_{1c2} and a_{2c2} into (16). The coefficient a_0 has been obtained by means of a free fitting operation shown in fig. 7. A successive fit of a_0 is done using the ansatz (14) with only $A_{0,1}$ and leads to $A_0 = 13.626 - 52.635\Gamma$ and $A_1 = -0.00297 - 0.00170\Gamma$.

In order to make the polynomial fit more robust, the other coefficients a_{im} have been found by means of a conditioned minimization of the least square distance as follows. Provided that the unconditioned fit for a_{im} (where $i = 1, ..., 5$) has been obtained for the lowest Reynolds number considered, $\mathrm{Re}_{\mathrm{min}} = 30$, the fit coefficients at higher Reynolds numbers are conditioned by $[a_{im}(\mathrm{Re}) - a_{im}(\mathrm{Re}_{\mathrm{min}}) - \mathrm{Re}/\mathrm{Re}_{\mathrm{min}} + 1] \in [-1, 1]$. The resulting fitting coefficients $a_{im}(\mathrm{Re}, \Gamma)$ can be downloaded from
`https://mega.nz/#!hQEmFIwY!9ybtrqWOqPd2NYYnafG0EpC5CeA3oJF5oB3DBUH1WKw`.

Employing the multi-stage methodology described in Sec. 4, a robust and physically motivated fit is obtained to model the Biot function for a wide range of thermocapillary Reynolds numbers and for all three aspect ratios of our study. A comparison between the Biot function obtained by the fit and the Biot function resulting from the multiphase numerical simulation shows a good agreement (fig. 8).

The importance of a robust heat-transfer model, which depends on the surrounding gas, is evident for numerical simulations of the flow in thermocapillary liquid bridges and the onset of three-dimensional instabilities. The

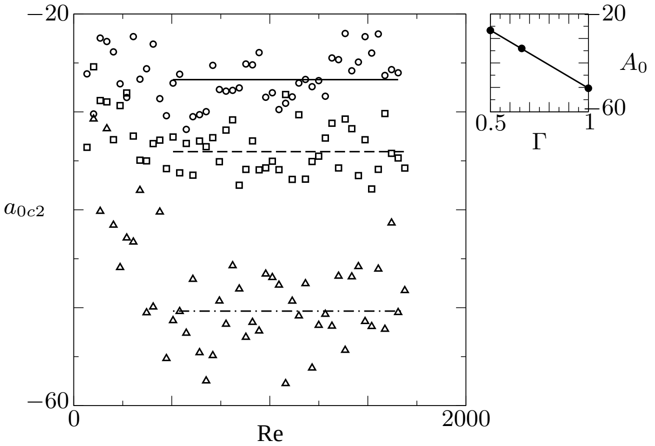

Figure 4: Fit of Bi(z) with respect to $a_{0c2}(\Gamma)$ (stage II, $z \in [z_{\text{min}}, z_{\text{min}} + 0.1]$) which is independent of Re (lines). Shown are data for $\Gamma = 0.5$ (circles, full line), 0.66 (squares, dashed line) and 1 (triangles, dash-dotted line). $A_0(\Gamma)$ is depicted as solid dots and the fit as a solid line in the side panel.

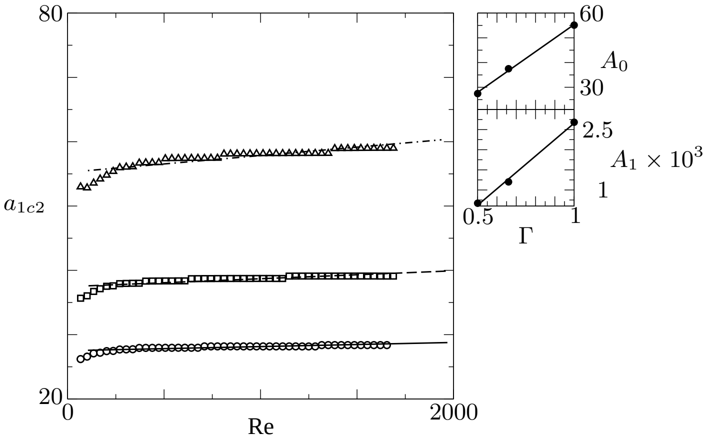

Figure 5: Fit of the coefficient a_{1c2} resulting after stage II. The open markers refer to the fit of the Biot number for $z \in [z_{\text{min}}, z_{\text{min}} + 0.1]$ and $\Gamma = 0.5$ (circles), 0.66 (squares) and 1 (triangles) after that a_{0c2} has been fixed as reported in table 1. The solid, dashed and dashed–dotted lines are the power-law fits employed to fit a_{1c2} for $\Gamma = 0.5$, 0.66 and 1, respectively. $A_{0,1}(\Gamma)$ are depicted as solid dots and the fits as a solid line in the side panels.

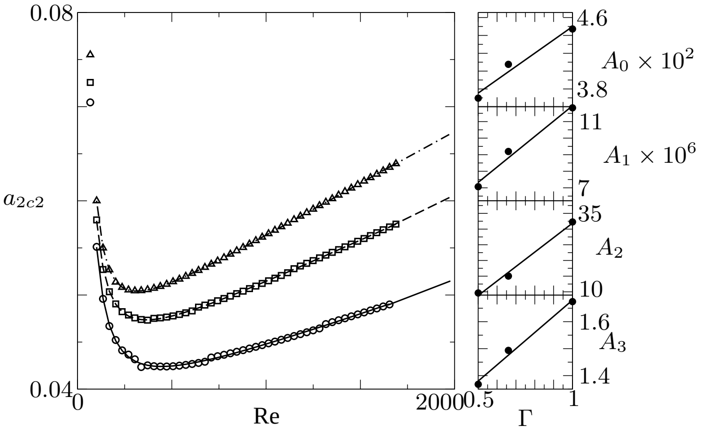

Figure 6: Fit of the coefficient a_{2c2} resulting after stage III. The open markers refer to the fit of the Biot number for $z \in [z_{\text{min}}, z_{\text{min}} + 0.1]$ and $\Gamma = 0.5$ (circles), 0.66 (squares) and 1 (triangles) after that a_{0c2} and a_{1c2} have been fixed as reported in table 1. The solid, dashed and dashed–dotted lines are the fits employed to fit a_{2c2} for $\Gamma = 0.5$, 0.66 and 1, respectively. $A_{0,1,2,3}(\Gamma)$ are depicted as solid dots and the fits as a solid line in the side panels.

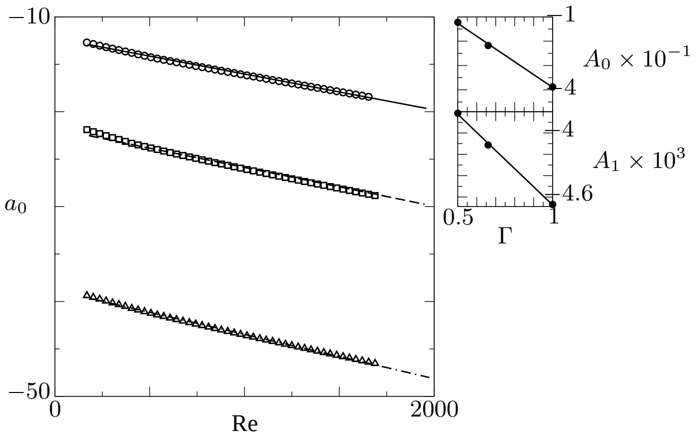

Figure 7: Fit of the coefficient $a_0 = a_{0h} + a_{0c1} + a_{0c2} + a_{0m}$. The open markers refer to the fit of the Biot number for $\Gamma = 0.5$ (circles), 0.66 (squares) and 1 (triangles) after that a_{1h}, a_{2h}, a_{1c1}, a_{2c1}, a_{1c2} and a_{2c2} have been fixed as reported in table 1. The solid, dashed and dashed–dotted lines are the fits employed for a_0 for $\Gamma = 0.5$, 0.66 and 1, respectively. $A_{0,1}(\Gamma)$ are depicted as solid dots and the fits as a solid line in the side panels.

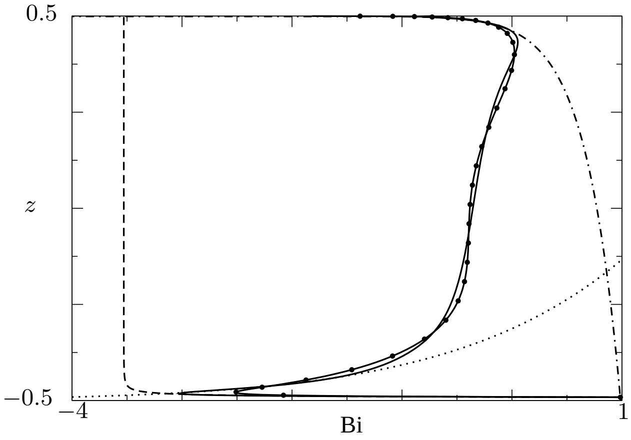

Figure 8: Comparison between the Biot function obtained from the multiphase simulation (solid line) and the corresponding fit obtained by the multi-stage approach of sec. 4 (solid line with full markers) for $\mathrm{Pr} = 28.5$, $\mathrm{Re} = 300$, $\Gamma = 0.5$. The dashed, dotted and dashed–dotted lines indicate the power laws fits within the three subranges.

primary goal of the model is to replace (8c) by a boundary condition (12) which only involves the liquid phase and the Biot function. Since the viscous forces exerted by the gas on the interface can often be neglected ($\nu_\mathrm{g} = 0$) this single-phase approach still leads to a reliable prediction of flow in the liquid bridge. The computational cost of a single-phase solver is much cheaper (saving about 70% for the present simulations cost) than the corresponding multiphase solver employed.

To demonstrate the effectiveness of using the Biot function in combination with a single-phase solver we compare the resulting free-surface velocity $|w_\mathrm{fs}|$ employing different methods in fig. 9. The surface velocity obtained using the Biot function (dots) much better approximates the reference result of the two-phase simulation (full line) than the single phase solver using $\mathrm{Bi} = 0$ (dashed line) or $\mathrm{Bi} = -0.2$ (dashed–dotted line, value suggested by (24)). This clearly demonstrates the superiority of the Biot-function approach over the use of a constant unknown Biot number. The advantage is understood when inspecting a typical Biot function as in fig. 2: Only the region $z \in [-0.4, 0.4]$ may perhaps be approximated by a constant Biot number. The sharp variation of $\mathrm{Bi}(z)$ in the boundary layer region close to the hot and the cold walls, however, cannot be represented by Newton's heat-transfer law with a constant Biot number. The (false) modeling assumption of an adiabatic free surface leads to an increase and thinning of the velocity peak at the cold wall and too low surface velocities near the hot rod. A similar trend is observed for $\mathrm{Bi} = -0.2$, even though the free-surface velocity compares slightly better with the multiphase simulation, in particular, near the cold corner (fig. 9).

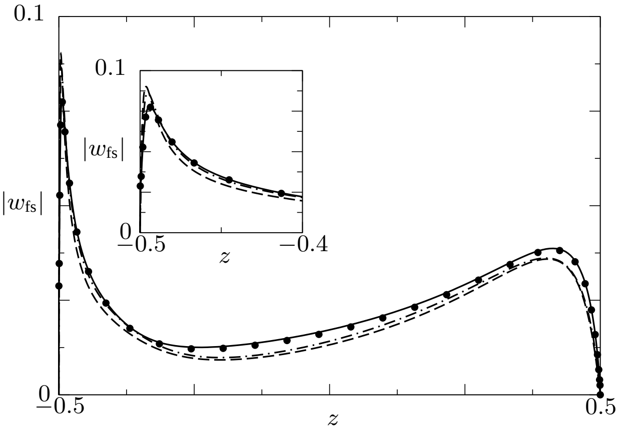

Figure 9: Comparison of the free surface velocity $|w_{\mathrm{fs}}|$ obtained by the multiphase solver (solid line), single-phase adiabatic solver (dashed line), single-phase solver with $\mathrm{Bi} = -0.2$ (dashed–dotted line) and single-phase solver supplied by our heat transfer model (full markers) for $\mathrm{Pr} = 28.5$, $\mathrm{Re} = 300$, $\Gamma = 0.5$.

6 Discussion and Conclusions

A correlation for the space-resolved heat transfer across the free surface between a liquid bridge and the ambient gas phase has been established. To that end fully-coupled, multiphase, axisymmetric simulations for a 2 cSt-silicone-oil liquid bridge surrounded by air have been carried out for a generic adiabatic air chamber. The heat transfer across the liquid–gas interface has been computed for 150 configurations varying the aspect ratio Γ of the liquid bridge and the thermocapillary Reynolds number Re, i.e. the strength of the flow.

Based on the two-phase data computed, a heat transfer model has been proposed in form of Newton's cooling law, but with a space-dependent Biot number which was called Biot function $\mathrm{Bi}(z)$. The Biot function, obtained by a multistage fit, well reproduces the characteristic strong variations of the heat transfer near the edges of the interface which are caused by the thermal boundary layers in the flow. The shape of the Biot function $\mathrm{Bi}(z)$ near the walls can be well represented by power laws. The resulting explicit fit compares very well with the heat transfer obtained from multiphase simulations without any a priori heat-transfer modeling.

Additional accurate calculations of the steady axisymmetric flow for $\mathcal{V} = 1$ have been carried out for $(\Gamma, \mathrm{Re}) \in \{0.5, 1\} \times \{30, 1500\}$, admitting dynamic, flow-induced surface deformations using the material properties of 2 cSt silicone oil. The calculations are based on the code `MaranStable` briefly described in section 4.2 of (17). In all four cases, the difference in the surface temperature when dynamic surface deformations are taken into account as compared to when they are neglected was nowhere larger than 3×10^{-3}. Moreover, computing the Biot function $\mathrm{Bi}_{\mathrm{DSD}}(z)$ taking into account the dynamic surface deformations (DSD) for the above cases, the difference $|\mathrm{Bi}_{\mathrm{DSD}}(z) - \mathrm{Bi}(z)|$ was always two orders of magnitude smaller than the confidence level of the fit used. These tests confirm that dynamic free surface deformations can be safely neglected for the parameters investigated.

The correlation derived in form of a Biot function can be supplied as a boundary condition to any single-phase solver. Corresponding single-phase simulations were shown to much better approximate the results of the fully coupled multiphase solver than any Newton law using a constant Biot number. Beyond the practical advantages of the present model to reduce the computational cost of multiphase solvers by equivalent single-phase solvers, we expect that the use of a Biot function will contribute to clarify the asymptotic scaling of $\mathrm{Bi}(z)$ in the boundary layer regions and help guiding experimental measurements of the heat transfer which are planned to be carried out under microgravity conditions (25).

Future work should aim at extending the parametric study presented, including the effect of gravity forces which are relevant for ground conditions, as the hydrostatic pressure does affect the shape of the liquid bridge. Furthermore, other liquids, gases and chamber geometries might be of interest.

Acknowledgements

We thank M. Stojanovic for calculating flows inclusive of dynamic surface deformations of the liquid–gas interface.

His contribution was made possible through FFG grant number 866027 under the Austrian Space Applications Programme ASAP14.

References

[1] Scriven, L.E., and Sternling, C.V., 1960, “The Marangoni effects”, *Nature*, Vol. 187, pp. 186–188.

[2] Young, N.O., Goldstein, J.S., and Block, M.J., 1959, “The motion of bubbles in a vertical temperature gradient”, *J. Fluid Mech.*, Vol. 6, pp. 350–356.

[3] Smith, M.K., and Davis, S.H., 1983, “Instabilities of dynamic thermocapillary liquid layers. Part 1. Convective instabilities”, *J. Fluid Mech.*, Vol. 132, pp. 119–144.

[4] Mills, K.C., Keene, B.J., Brooks, R.F., and Shirali, A., 1998, “Marangoni effects in welding”, *Philos. T. Roy. Soc. As*, pp. 911–926.

[5] Sirignano, W.A., and Glassman, I., 1970, “Flame spreading above liquid fuels: Surface-tension-driven flows”, *Combust. Sci. Technol.*, Vol. 1, pp. 307–312.

[6] Schwabe, D., 1981, “Marangoni effects in crystal growth melts”, *Physicochem. Hydrodyn.*, Vol. 2, pp. 263–280.

[7] Oron, A., Davis, S.H., and Bankoff, S.G., 1997, “Long-scale evolution of thin liquid films”, *Rev. Mod. Phys.*, Vol. 69, pp. 931–980.

[8] Carpenter, B.M., and Homsy, G.M., 1989, “Combined buoyant-thermocapillary flow in a cavity”, *J. Fluid Mech.*, Vol. 207, pp. 121–132.

[9] Xu, J., and Zebib, A., 1998, “Oscillatory two- and three-dimensional thermocapillary convection”, *J. Fluid Mech.*, Vol. 364, pp. 187–209.

[10] Kuhlmann, H.C., and Albensoeder, S., 2008. “Three-dimensional flow instabilities in a thermocapillary-driven cavity”, *Physical Review E*, Vol. 68, pp. 036303.

[11] Li, Y.-R., Peng, L., Akiyama Y., and Imaishi, N., 2003, “Three-dimensional numerical simulation of thermocapillary flow of moderate Prandtl number fluid in an annular pool”, *J. Cryst. Growth*, Vol. 259, pp. 374–387.

[12] Kuhlmann, H.C., 1999, “Thermocapillary Convection in Models of Crystal Growth”, *Springer*, Vol. 152.

[13] Hurle, D.T.J., and Jakeman, E., 1981, “Introduction to the techniques of crystal growth”, *Physicochem. Hydrodyn.*, Vol. 2, pp. 237–244.

[14] Nienhüser, C.H., and H. C. Kuhlmann, H.C., 2002, “Stability of thermocapillary flows in non-cylindrical liquid bridges”, *J. Fluid Mech.*, Vol. 458, pp. 35–73.

[15] Motegi, K., Kudo, M., and Ueno, I., 2017, “Linear stability of buoyant thermocapillary convection for a high-Prandtl number fluid in a laterally heated liquid bridge”, *Phys. Fluids*, Vol. 29, pp. 044106.

[16] Kamotani, Y., Wang, L., Hatta, S., Wang, A., and Yoda, S., 2003, “Free surface heat loss effect on oscillatory thermocapillary flow in liquid bridges of high Prandtl number fluids”, *Int. J. Heat Mass Transfer*, Vol. 46, pp. 3211–3220.

[17] Shevtsova, V., Gaponenko, Y., Kuhlmann, H.C., Lappa, M., Lukasser, M., Matsumoto, S., Mialdun, A., Montanero, J.M., Nishino, K., Ueno, I., 2014, “The JEREMI-project on thermocapillary convection in liquid bridges. Part B: overview on impact of co-axial gas flow”, *Fluid Dyn. Mater. Process.*, Vol. 10, pp. 197–240.

[18] Kuhlmann, H.C., Nienhüser, C., 2002, “Dynamic free-surface deformations in thermocapillary liquid bridges”, *Fluid Dyn. Res.*, Vol. 31, pp. 103–127.

[19] Shevtsova, V.M., Ermakov, M.K., Ryabitskii, E., Legros, J.C., 1997, “Oscillations of a liquid bridge free surface due to the thermal convection”, *Acta Astronaut.*, Vol. 41, pp. 471–479.

[20] Yano, T., Nishino, K., Matsumoto, S., Ueno, I., Komiya, A., Kamotani, Y., Imaishi, N., 2018. “Report on microgravity experiments of dynamic surface deformation effects on Marangoni instability in high-Prandtl-number liquid bridges”, *Microgravity Sci. Technol.*, Vol. 30, pp. 599–610.

[21] Ferrera, C., Mialdun, A., Shevtsova, V.M., Cabezas, M.G., Montanero, J.M., 2008, “Measurement of the dynamical free surface deformation in liquid bridges”, *Acta Astronaut.*, Vol. 62, pp. 471–477.

[22] Montanero, J.M., Ferrera, C., Shevtsova, V.M., 2008, “Experimental study of the free surface deformation due to thermal convection in liquid bridges”, *Exp. Fluids*, Vol. 45, pp. 1087–1101.

[23] Romanò, F., Kuhlmann, H.C., Ishimura, M., and Ueno, I., 2017, “Limit cycles for the motion of finite-size particles in axisymmetric thermocapillary flows in liquid bridges”, *Phys. Fluids*, Vol. 29, pp. 093303.

[24] Gaponenko, Y., and Shevtsova, V., 2012, “Heat transfer through the interface and flow regimes in liquid bridge subjected to co-axial gas flow”, *Microgravity Sci. Technol.*, Vol. 24, pp. 297–306.

[25] Nishino , K., Yano, T., Kawamura, H., Matsumoto, S., Ueno, I., and Ermakov, M.K., 2015, “Instability of thermocapillary convection in long liquid bridges of high Prandtl number fluids in microgravity”, *J. Cryst. Growth*, Vol. 420, pp. 57–63.

Address: [1]Dept. Biomed. Eng., University of Michigan, 2200 Bonisteel Blvd. Ann Arbor, MI 48109-2099, U.S.A.
Inst. Fluid Mech. Heat Transf., TU Wien, Getreidemarkt 9, 1060 Vienna, Austria.
e-mail: `frromano@umich.edu`

Address: [2]Institute of Fluid Mechanics and Heat Transfer, TU Wien, Getreidemarkt 9, 1060 Vienna, Austria.
e-mail: `hendrik.kuhlmann@tuwien.ac.at`

DOI: 10.24352/UB.OVGU-2019-009 TECHNISCHE MECHANIK, 39, 1, (2019), 85 – 96
submitted: July 6, 2018

Modelling of Heat Transfer and Fluid Flow through a Granular Material and External Wall Barrier

E. Szymanek, A. Tyliszczak

Heat and fluid flow simulations for granular material in wall barriers allow to design them in a way that maximally reduces the expenditures on utilisation of buildings. This paper demonstrates the solution to the problem of the passage of air through the external wall barrier. It shows how the temperature changes inside the wall barriers when the external temperature changes. Two types of partitions are tested: single-layer (granular material) and two-layer (granular and concrete material). The paper presents comparison of the results of the numerical model and in-house code with the experimental data. The numerical model applied is based on the unsteady equation of heat conduction (3D) and the Navier-Stokes equations. A high-order compact method in combination with the WENO scheme and predictor-corrector method are applied for the spatio-temporal discretisation. The flows of air and heat in the granular layers are modelled using immersed boundary technique, which allows to use Cartesian meshes for objects with very complex geometric shapes. The correctness of numerical model applied has been verified by comparisons with ANSYS Fluent results and experimental data obtained from measurements performed in a laboratory and in-situ.

1 Introduction

The process of heat transfer occurs wherever temperature differences exists and a material has conductive properties. It is very common and present in many technological branches. This paper is devoted to an analysis of the heat and fluid flow through granular materials, which are important to a vast array of industries. For instance, in chemical engineering and catalytic reactors, where large surfaces of packed granular beds intensify chemical reactions (Alvarez de Miguel et al., 2014; Yancy-Caballero et al., 2018), in energy production systems, where granulates are promising materials for heat storage and heat transfer media (Baumann and Zunft, 2014; Ma et al., 2014; Ratuszny, 2017), in spray drying and spray granulation installations (Hoffmann et al., 2015; Diez et al., 2018) or in construction industry, where the granular layers are used for wall barrier and heat insulators (Szymanek et al., 2014). In this last example the knowledge of temperature distribution is necessary both to evaluate the efficiency of materials used for wall barrier as well as to assess the correctness of their construction method. In this type of applications the granular materials are currently regarded as one of the most demanding systems. Description of the heat transfer in granulates in the same way as in solids, liquids or gases is impossible and requires the analysis of a number of interrelated processes and the use of increasingly advanced computational and experimental methods. Difficulty is caused by the fact that empty spaces between the granular particles can be filled with gas or water (see Fig. 1) and the heat exchange can take place between them as well as with the granular material, thus leading to a coupled complex problem. Certainly, precise explanations of the phenomena occurring between the constituents in granular systems could be helpful for designing not only new type of wall barriers with improved control of temperature changes but also for all aforementioned industrial branches.

Measurements of the flow behaviour in complex granular structures are often based on sophisticated imaging techniques (Hainswoeth and Aylmore, 1983) including tomographic methods based on X-rays (Computed Tomography, CT) (Breugen et al., 2014). Attempts of theoretical descriptions of the transport processes inside the granular layers are not fully successful and require knowledge of many empirical parameters. Some of the models describing the heat transfer through the granular bed are based on formulas for homegenous medium assuming that over the time the differences between the phases disappear and fluid and solid materials have similar temperatures (Amhalhel and Furmaski, 1997).

In line with rapid development of computational technology the granular layers are more and more studied using numerical methods. Various modelling approaches have been developed for these purposes, they all belong to the

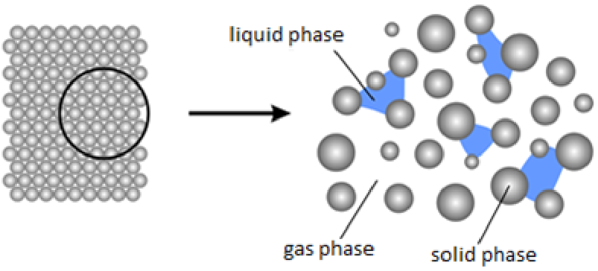

Figure 1: Three-phase granular bed system

CFD (Computational Fluid Dynamics) methods and are based on continuous models (Massoudi, 2006) including finite element/finite volume methods (FEM/FVM), lattice Boltzmann techniques (LBM) or fractional calculus (Szymanek et al., 2014). Vargas and McCarthy (Vargas and McCarthy, 2001) have developed a TPD (thermal particle dynamics) method based on the Discrete Element Method (DEM) allowing analysis of grain-grain interactions. This approach was also used to describe the heat and mass flow in granular beds by Ferrez and Liebling (Ferrez and Liebling, 2001). In their work the granular beds were treated as systems consisting of solid bodies and a system of different pore sizes filled with liquid, gas or a mixture of them. A similar approach to the problem was presented in (Tian and Shu, 2009), where the granular material was described as a homogeneous bed consisting of elements of irregular structure (porous, granular). Ordonez and Alvarado (Ordonez and Alvarado, 2010) proposed a model of heat transfer through a granular bed taking into account the temperature of the solid and gaseous phase separately.

Despite the above mentioned advanced studies the complexity of the flow and thermal processes occurring inside the layer causes that in many cases researchers focus an analyses of simplified problems taking account granular particles with simple shapes. For instance, isolated spheres were studied by Fornberg B. (Fornberg, 1988), while interactions between two spheres being in close proximity were analysed by Dixon et al. (Dixon et al., 2011). Recently, Li et al. (Li et al., 2017), investigated the flows and heat transfer around two spheres using the large eddy simulation (LES) method. An analysis of interactions occurring in this flow type cane can be also found in (Qi et al., 2018), where the flow between two interactive particles was studied using a three-dimensional lattice Boltzmann model.

In the present paper we concentrate on numerical studies of the heat and mass flow in granular layers composed of spherical objects located in a stream of flowing medium or in a wall barrier. The numerical model applied in this paper allows to precisely compute the inner temperature distributions and their variability over time. The solver used in this research is an in-house code called SAILOR. It is based on the unsteady equation of heat conduction (3D) and the Navier-Stokes equations, which allow modeling the airflow in the cases in which the walls are made of permeable granular materials. The analysed problem is treated as unsteady and the flow is assumed to be laminar. The solution algorithm is based on the projection method for determining the pressure field and velocity. A high-order compact method in combination with the WENO scheme and predictor-corrector method are applied for the spatio-temporal discretisation. The flows of air and heat in the granular layers are modelled using immersed boundary (IB) technique, which allows the use of Cartesian meshes for objects with very complex geometric shapes. It was demonstrated that the IB method can be used for modelling of laminar and turbulent flow regimes with domains changing in time and moving objects and with heat exchange (Fadlun et al., 2000, Mittal and Iaccarino, 2005). Concerning discretisation methods it has been successfully applied along with the spectral methods and finite/compact difference methods. In this work we apply probably the simplest variant of the IB method, i.e., the so-called *volume penalisation* method (IB-VP), also known as *fictitious domain* (Mittal and Iaccarino, 2005, Khadra et al., 2000) method. In the IB-VP approach the fluid is penalized from entering a solid part of a domain by adding a continuous forcing term to the equations governing the heat and fluid flow. The forcing extends throughout the entire volume of solid body and is not just confined to a neighbourhood of the solid interface. What makes the IB-VP method very attractive is the simple implementation and the use of an easily definable phase-indicator function (mask function), which by ”switching-on / off” easily identifies the computational nodes as fluid or solid parts. The correctness of applied numerical model has been verified by ANSYS Fluent and by experimental data obtained from measurements performed in a laboratory and using real bulkheads. The purpose of the experiment was to determine the internal temperature distributions and their variability in respect to a changing temperature outside the bulkheads. During the measurements the samples were placed in a climate chamber that could be accurately controlled. It enabled to simulate real outdoor conditions and on the basis of the obtained results, temperature profiles in layers were created.

2 Mathematical Modelling

In this paper we consider variable temperature and variable density flows. The changes of density are caused by increasing/decreasing wall temperature and they are larger than acceptable by Boussinesq approximation. We consider therefore a low Mach number flow described by the continuity equation, the Navier-Stokes equations and the energy equation, which in the framework of an IB-VP approach are defined as:

$$\partial_t \rho + \nabla \cdot (\rho \mathbf{u}) = 0 \tag{1}$$

$$\rho \left(\partial_t \mathbf{u} + (\mathbf{u} \cdot \nabla)\mathbf{u}\right) + \nabla p \mathbf{I} = \nabla \cdot \boldsymbol{\tau} + \mathbf{f}^{\mathrm{IB}} \tag{2}$$

$$\rho C_p \left(\partial_t T + (\mathbf{u} \cdot \nabla) T\right) = \nabla \cdot (\kappa \nabla T) + \mathrm{f}_T^{\mathrm{IB}} \tag{3}$$

The set of Eqs. (1)-(3) is complemented with the equation of state $p_0 = \rho R T$. In open flows with inlet/outlet boundaries p_0 is constant in space and time (Tyliszczak, 2016). The molecular viscosity (μ) within $\boldsymbol{\tau}$ is computed from the Sutherland law. The source terms $\mathbf{f}^{\mathrm{IB}}$ and $\mathrm{f}_T^{\mathrm{IB}}$ originate from the IB method and their role is to act on a fluid in such a way as if there were a solid object immersed in the flow domain.

2.1 Solution Algorithm

The solution algorithm for Eqs. (1-3) is formulated in the framework of a projection method (Fletcher, 1991) for pressure-velocity coupling with a direct forcing approach for the IB method (Mittal and Iaccarino, 2005). The time integration is based on a predictor-corrector approach (Adams-Bashforth/Adams Moulton) and the spatial discretisation is performed using 6th/5th order compact difference and WENO (Weighted Essentially Non-Oscilatory) schemes on half-staggered meshes (Tyliszczak, 2014, Tyliszczak, 2016). In the framework of the IB approach the solution algorithm is defined as follows.

Predictor step. Generally, we assume that the time-step (Δt) can vary as the flow velocity changes in the successive time-steps, $..., n-1, n, n+1, ...$ With this assumption the 2nd order Adams-Bashforth method is given as:

$$\begin{aligned} \frac{\rho \boldsymbol{u}^* - \rho \mathbf{u}^n}{\Delta t^n} &= \left(1 + \frac{\Delta t^n}{2\Delta t^{n-1}}\right) \mathrm{Res}(\mathbf{u}^n) \\ &\quad - \frac{\Delta t^n}{2\Delta^{n-1}} \mathrm{Res}(\mathbf{u}^{n-1}) - \nabla p^n \mathbf{I} + \mathbf{f}^{\mathrm{IB}} \end{aligned} \tag{4}$$

$$\begin{aligned} \frac{T_i^* - T_i^n}{\Delta t^n} &= \left(1 + \frac{\Delta t^n}{2\Delta t^{n-1}}\right) \mathrm{Res}(T^n) \\ &\quad - \frac{\Delta t^n}{2\Delta^{n-1}} \mathrm{Res}(T^{n-1}) + \frac{1}{\rho C_p} \mathrm{f}_T^{\mathrm{IB}} \end{aligned} \tag{5}$$

where Res($\boldsymbol{u}$), Res(T) represents the convection and diffusion terms of the Navier-Stokes and energy equations. The formulas for the source terms $\mathbf{f}^{IB}$ and f_T^{IB} are discussed latter. The velocity field $\boldsymbol{u}^*$ computed from Eq. (4) does not fulfil the continuity equation (i.e. $\partial_t \rho + \nabla \cdot (\rho \boldsymbol{u}^*) \neq 0$) and according to the projection method (see (Fletcher, 1991)) it must be corrected using the gradients of pressure correction (p') according to the following formula:

$$\rho \boldsymbol{u}^{**} = \rho \boldsymbol{u}^* - \Delta t^n \nabla p' \boldsymbol{I} \tag{6}$$

where p' is computed from the Poisson equation:

$$\nabla \cdot (\nabla p' \boldsymbol{I}) = \frac{1}{\Delta t^n} \left[\nabla \cdot (\rho \boldsymbol{u}^*) + \partial_t \rho^*\right] \tag{7}$$

resulting from the condition $\partial_t \rho + \nabla \cdot (\rho \boldsymbol{u}^{**}) = 0$. The density is computed from the equation of state $p_0 = \rho^* R T^*$ and its time derivative needed in (7) is disrcretized using 2nd order formula

$$\begin{aligned} \partial_t \rho^* = \frac{(\Delta t^n \Delta t^{n-1})^{-1}}{(\Delta t^n + \Delta t^{n-1})} \big\{ &\left[(\Delta t^n + \Delta t^{n-1})^2 - (\Delta t^n)^2\right] \bar{\rho}^* \\ &- (\Delta t^n + \Delta t^{n-1})^2 \bar{\rho}^n + (\Delta t^n)^2 \bar{\rho}^{n-1} \big\} \end{aligned} \tag{8}$$

Corrector step. The 2nd order Adams-Moulton method is defined as:

$$\frac{\rho\mathbf{u}^* - \rho\mathbf{u}^n}{\Delta t^n} = \frac{1}{2}(\text{Res}(\mathbf{u}^{**}) + \text{Res}(\mathbf{u}^n)) - \nabla p^n\mathbf{I} + \mathbf{f}^{\text{IB}} \tag{9}$$

$$\frac{T^{n+1} - T^n}{\Delta t^n} = \frac{1}{2}(\text{Res}(T^{**}) + \text{Res}(T^n)) + \frac{1}{\rho C_p}\text{f}_T^{\text{IB}} \tag{10}$$

Again, the velocity field $\mathbf{u}^*$ does not fulfil the continuity equation and its correction is defined as:

$$\rho\mathbf{u}^{n+1} = \rho\mathbf{u}^* - \Delta t^n\nabla p'\mathbf{I} \tag{11}$$

The equation $\rho_t + \nabla\cdot(\rho\mathbf{u}^{n+1}) = 0$ leads to the Poisson equation (7). Its solution allows us to correct the velocity using (11) and to update the pressure field as:

$$p^{n+1} = p^n + p' \tag{12}$$

The density is computed from $p_0 = \rho^* RT^{n+1}$ and the next time step begins.

IB-VP source term. The IB-VP method works through penalizing a difference between the actual and assumed velocity and temperature of the solid body. The role of the source terms $\mathbf{f}^{\text{IB}}$ and f_T^{IB} is to mimmic the presence of solid objects in the flow domain. In the volume penalization variant of the IB method they are defined as:

$$\mathbf{f}^{\text{IB}} = -\frac{\rho}{\eta}\Gamma(\mathbf{x})(\mathbf{u} - \mathbf{u}_s), \quad \text{f}_T^{\text{IB}} = -\frac{\rho C_p}{\eta}\Gamma(\mathbf{x})(T - T_s) \tag{13}$$

where $\eta \ll 1$ is the so-called penalization parameter with dimension of time unit and Γ - the phase indicator defined as:

$$\Gamma(\mathbf{x}) = \begin{cases} 0, & \text{for } \mathbf{x} \in \Omega_f \\ 1, & \text{for } \mathbf{x} \in \Omega_s \end{cases} \tag{14}$$

For $\Gamma(\mathbf{x}) = 1$ with $\eta \ll 1$ Eqs. 4 and 6 reduce to $\mathbf{u}^* \approx \Delta t^n\mathbf{u}_s/(\eta + \Delta t^n)$ and $T^* \approx \Delta t^n T_s/(\eta + \Delta t^n)$ which for $\eta \ll \Delta t^n$ leads to $\mathbf{u}^* \approx \mathbf{u}_s$ and $T^* \approx T_s$. Thus, the forcing terms enforces the no-slip boundary conditions and set the required temperature of the solid objects. Simplicity of the IB-VP method has, however, direct consequences in lower accuracy. Similarly, as in the classical IB method with a stepwise approach (i.e. without the interpolation (Fadlun et al., 2000)) the formal order of the IB-VP method is at most equal to one (Khadra et al., 2000, Kadoch et al., 2012).

3 Experiment/Laboratory Tests

The correctness of the proposed model has been verified by means of data obtained from experimental research. Two configurations of barriers ($120mm$) were analyzed: granular layer ($120mmm$) and granular ($60mm$)/ concrete ($60mm$) layer. The materials used in construction were concrete and granular material (expanded clay) show at Fig. 2b,c.

Temperature measurements were carried out using the thermocouples placed in holes drilled in layers. The empty spaces between the test center and the thermocouple were filled with drilling dust or pieces of expanded clay, so that the thermocouple would closely adhere to the material being tested. The walls constructed in this way were placed in a climatic chamber Series 3 LTCL600 (TASLtd., WestSussex, UK) (see Fig. 2a), which allowed setting the outside temperature and its precise control during the entire experiment. The thermocouples were placed in layers in many spatial locations. The aim of the experiment was to determine the internal temperature distributions for the changing temperature outside the barriers.

4 Results

4.1 Assessment of the IB-VP Accuracy

As it was mentioned in the previous section the accuracy of the IB-VP method is at most of the first order. Here, we verify how this limitation translates on the results obtained for the cases including the heat and mass transfer

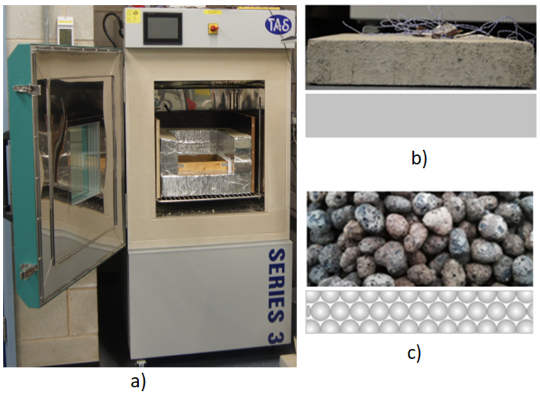

Figure 2: Climatic chamber (a) and material used to wall barrier construction: concrete (b), granular material (c)

in the flows in channels and between or around spheres. The test cases include: (i) an isothermal flow in a channel filled with six layers of spheres, (ii) a flow around heated spheres, (iii) a flow through a bed of granular material and a two-layer bed (granular material with concrete).

In the test case (i), flow through channel filled with a cubic lattice of spheres is examined. The considered configuration consists of six layers of spheres with diameters $D = 28mm$. Their quarters are located in the corners of the channel. The simulations were performed for Reynolds numbers $Re = UD/\nu = 204.74$ (U - inlet velocity, ν - viscosity) $Re = 105.57$, $Re = 59.78$ $Re = 28.88$. The numerical results were compared with experimental data (Suekane et al., 2003) and with the results obtained using the ANSYS Fluent. An important factor affecting the accuracy of the analysis is the density of the mesh. For the SAILOR code the used meshes were regular and uniform and consisted of 40 x 160 x 40 to 80 x 320 x 80 nodes. The simulations performed with ANSYS Fluent were obtained on body-fitted tetrahedral meshes with approximately $2.5 \cdot 10^6$ (mesh M1) and $7 \cdot 10^6$ (M2) tetrahedral cells.

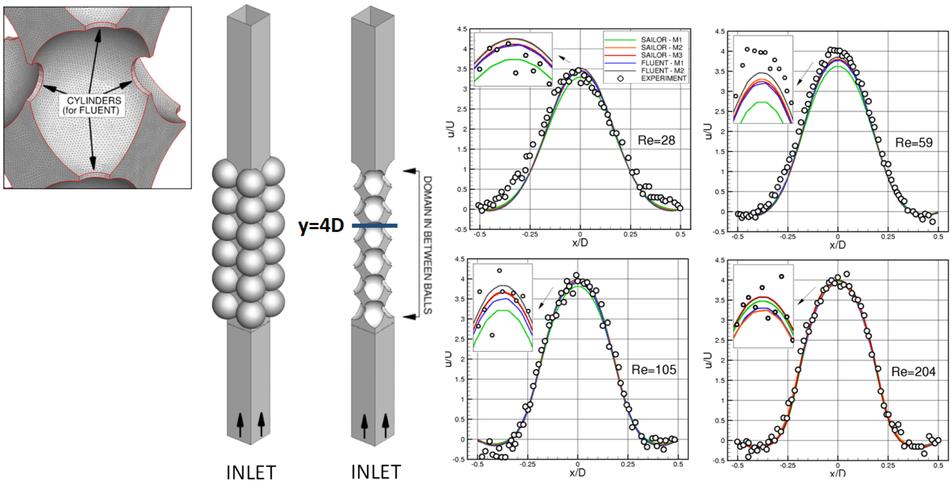

Figure 3: Axial velocity profiles at the location y=4D in a channel filled with six layers of spheres

It can be seen that the results obtained from SAILOR and Fluent practically overlap and are almost independent of the density of the grid. Equally important is that the experimental data are matched very well, see Fig. 3. It can be seen that for the higher the Reynolds number, the convergence of results is better. At $Re = 204$ the computed solutions are in excellent agreement with the experiment. Examination of the profiles at $Re = 28$ reveals a slight discrepancy between the experimental data and numerical results, however, the differences are not large.

In the test case (ii) the flow around three hot spheres ($D = 10mm$) is analysed. The spheres (Fig. 4) have the following coordinates respectively: $(X, Y, Z) = (0.0, 0.0, 0.1)$, $(X, Y, Z) = (-0.0225, 0.0, 0.145)$, $(X, Y, Z) = (0.0225, 0.0, 0.145)$. Temperature of the first sphere is $350K$, while two next have temperature $373K$. The temperature of the incoming flow is $300K$. The flow rate is assigned such that the Reynolds number based on the inlet velocity and sphere diameter is equal to 100.

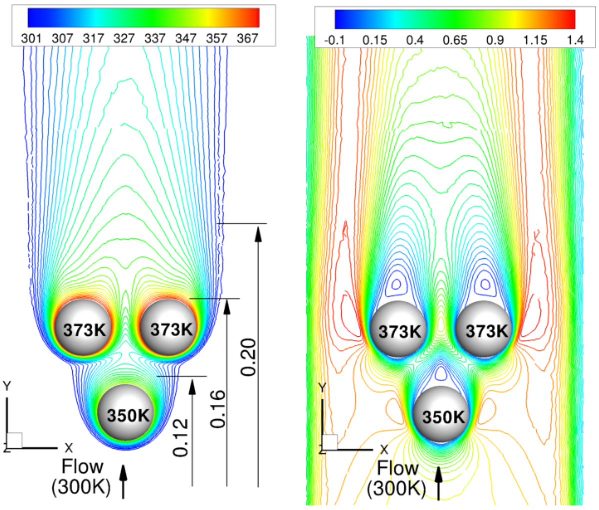

Figure 4: Flow around heated spheres

In this case the grids contained respectively $121 \times 160 \times 121$ (M1) and $121 \times 320 \times 121$ (M2) nodes for the SAILOR code and approximately $4 \cdot 10^6$ cells for simulation using the ANSYS Fluent code. The results of calculations are shown in Fig. 5. Temperature and vertical (V) and horizontal (U) velocity values were compared at selected heights from the inlet. It can be seen that also in this case the compatibility between the results is very good, both the temperature field and the velocities of both simulations are almost identical. It proves that the applied IB-VP method and the solution algorithm are accurate and formulated correctly.

It should be noted that preparing a body-fitted mesh in these relatively simple configurations was not difficult. However, the geometry shown in Fig. 3 required the definition of small, thin cylinders at the point of contact between the spheres. Otherwise, the meshing process caused very distorted cells near the contact points. The applied IB method is free from such problems, i.e. fixed objects can be in any form of contact and even deform each other.

4.2 Heat Transfer in the Single and Double Layer Barriers

The results obtained showed that IB-VP approach could be applied for modelling of the heat and fluid flow in complex domains and around solid objects. In this subsection we analyse the heat transfer inside two industrial configurations of the insulation barriers. They are shown schematically in Fig. 6 along with the locations of the thermocouples used for temperature measurements. The first barrier is composed of single layer granular material (expanded clay, see Fig. 2c), with heat diffusivity equal to $\alpha_g = 8.0 \times 10^{-7} m^2/s$. In the second case there are two-layers composed of granular material and concrete (see Fig. 2b, $\alpha_c = 6.8 \times 10^{-7} m^2/s$). In the experiment the length (L_x), height (L_y) and width (L_z) of the layers were equal to $0.12m$, $0.3m$, $0.3m$, respectively. The layers were insulated from the top and bottom ($y = \pm Ly/2$) and at $z = \pm L_z/2$. In the simulations the dimensions of the barriers were $L_x = 0.12m.$, $L_y = 0.04m$, $L_z = 0.04m$ and at $y = \pm Ly/2$ and at $z = \pm L_z/2$ we assumed adiabatic conditions. Taking smaller layer for the simulations was necessary because of very high computational costs that would be required for the full scale model. For the layer composed of the granulate we assumed the following options: (i) uniform material with an effective heat diffusion coefficient obtained from experiment ($\alpha_g = 5.3 \times 10^{-7} m^2/s$); (ii) spherical ($D = 10mm$) granules with empty spaces filled with air ($\alpha_{\text{air}} = 1.9 \times 10^{-5} m^2/s$); the layer was represented by $13 \times 5 \times 5$ orderly packed spheres. For the latter configuration we considered the cases in which the air was stagnant and when it was flowing from the bottom. In this configuration two buffer layers were added to the domain, i.e. $0.02m$ from the bottom and $0.04m$ from the top. They were required to specify the inlet and outlet boundary conditions and to minimise their impact on the flow in between the spheres. In the performed simulations the mesh was uniform and consisted of $256 \times 208 \times 84$ nodes. The preliminary tests have shown that such a mesh is dense enough to obtain qualitatively consistent solutions.

Initially, the temperature of the barriers was uniform and equal to $298K$. Then, on the right hand side that was treated as an external building side (see Fig. 6), the temperature started to decrease such that at the time $16100s$ it has fallen down to $265K$, we assumed the linear decrease according to $T(t) = 298 - 2.083 \times 10^{-3} t[K]$. The changes of temperature inside the layers were computed by IB-VP approach and were measured by thermocouples

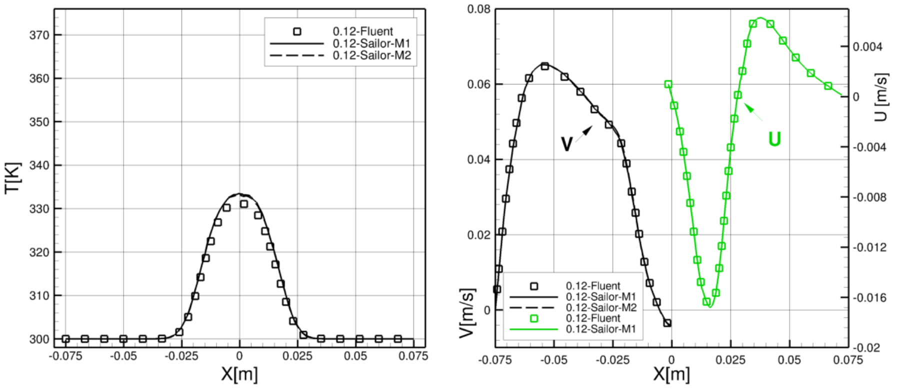

(a) Temperature distribution, h=0.12 (b) Velocity distribution, h=0.12

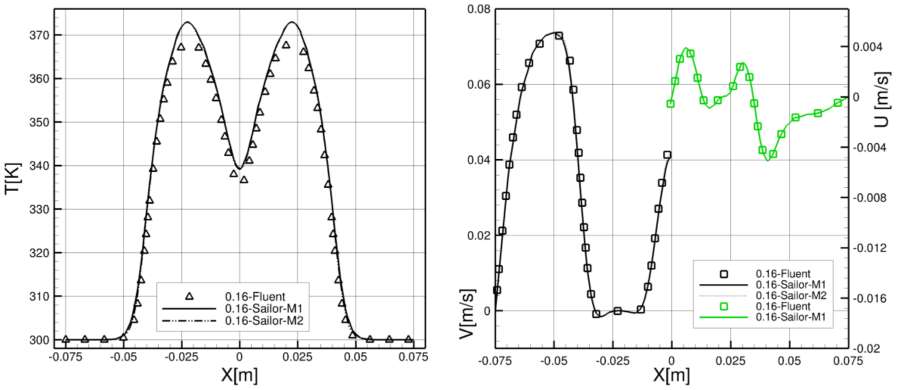

(c) Temperature distribution, h=0.16 (d) Velocity distribution, h=0.16

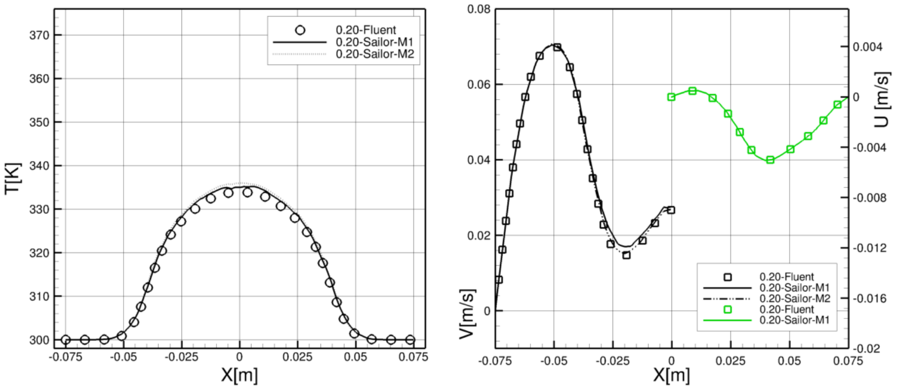

(e) Temperature distribution, h=0.20 (f) Velocity distribution, h=0.20

Figure 5: Temperature and velocity profiles in the flow around heated spheres

for additional verification of the applied IB-VP method. In the following part we first compare which configuration is more effective from the point of view of insulation and next we verify whether the assumption of the granular layer as the uniform material with the effective heat diffusivity is accurate. Then, we analyse what happens inside the layers when the air in between the granules starts to move. Note, that such an internal flow can be caused by the natural convection or can be enforced by external sources, e.g. by air-condition system which removes air from buildings and pumps it outside.

Figures 7 present a comparison of numerical results with experimental data for the single-layer and two-layer barriers, respectively. The results obtained from the SAILOR code were verified by experimental data and simulation results achieved using the ANSYS Fluent package. It should be noted that the values obtained by IB-VP method and the ANSYS Fluent are convergent. A slight difference between the results of numerical calculations and experimental data can be attributed to the complex structure of the granular bed and problems with accurate placement of thermocouples and thus with precise data reading. This may have caused deviations from the numerically obtained temperature distribution. Additionally, Fig. 7(on the left side, single-layer barrier) presents data from the barrier,

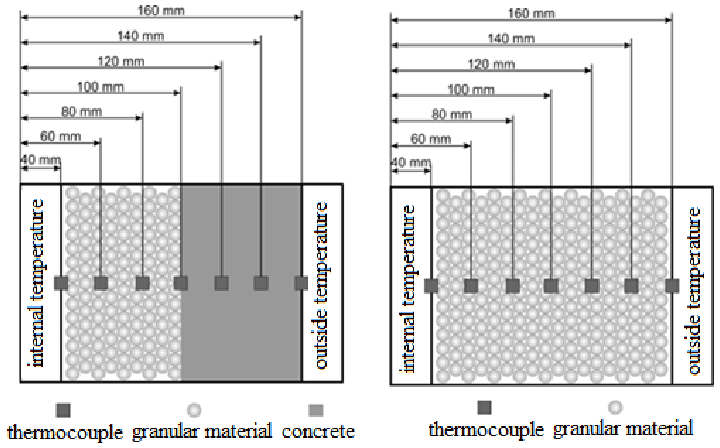

Figure 6: Wall barriers with a schematic distribution of thermocouples

which includes air-filled inter-granular spaces (dashed line denoted as GR+AIR). Differences in the temperature represented by solid lines (uniform material with effective conductivity) are large and originate from the fact that inter-granular spaces filled with air have larger thermal conductivity. This leads to faster temperature change in the entire layer, it is seen that at the end of the layer at the position $x = 0.04m$ at the time $12000s$ the temperature is approximately $10K$ lower compared to the case with effective conductivity. It seems that in this particular case modelling of the heat flow trough the layer assuming an overall heat conductivity is more accurate than treating the layer with different heat conductivities of the solid and air. It can be caused by incorrect specification of the solid material properties provided by the producer.

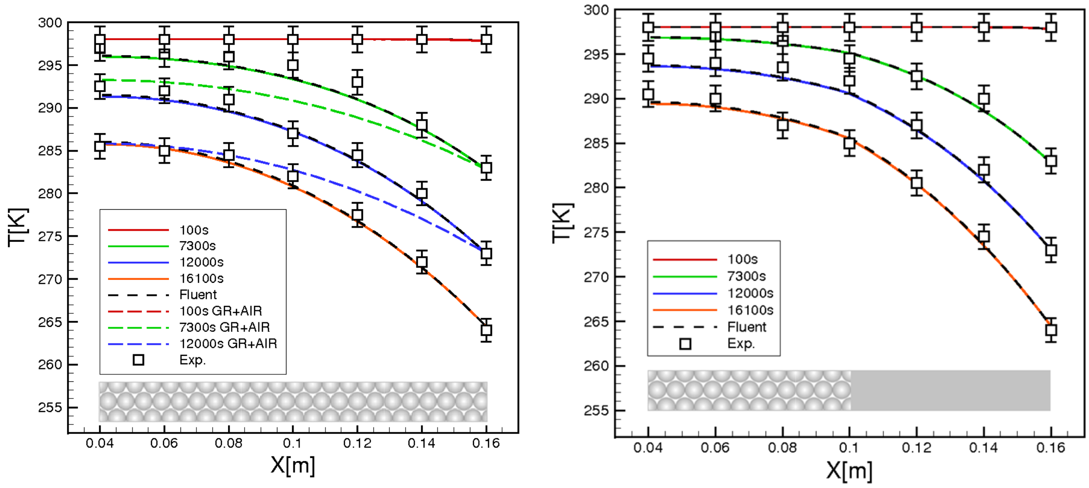

Figure 7: Comparison of numerical results with experimental data: On the left: for a single-layer barrier. On the right: for a two-layer barrier

The results for the two-layer barrier are shown at Fig. 7(on the right side). As in the previous case the differences between numerical and experimental data are small. One can notice that in this configuration the decreasing temperature propagates slower due to smaller heat diffusivity of the concrete. It is worth paying attention to the shape of temperature profiles at the point $x = 0.1m$. This is the point of connected layers of different structure. One can notice a slight inflection, which indicates that the shape of the profiles changes at this point. This test case was used only for validation purpose without involment of the IB method.

4.3 Simultaneous Heat and Flow Fluid in Single Layer Barrier

Next we focus on the case in which the air flows through the barrier. We consider the configuration presented at Fig. 7(on the left side, single-layer barrier) and as the initial solution we take the results at the time instant $12000s$. The air with the temperature $300K$ flows from the bottom side of the barrier with a uniform velocity equal to

$0.1m/s$. Figure 8 shows the temperature and velocity iso-surfaces and velocity vectors for the time 4 seconds from the beginning of the simulation.

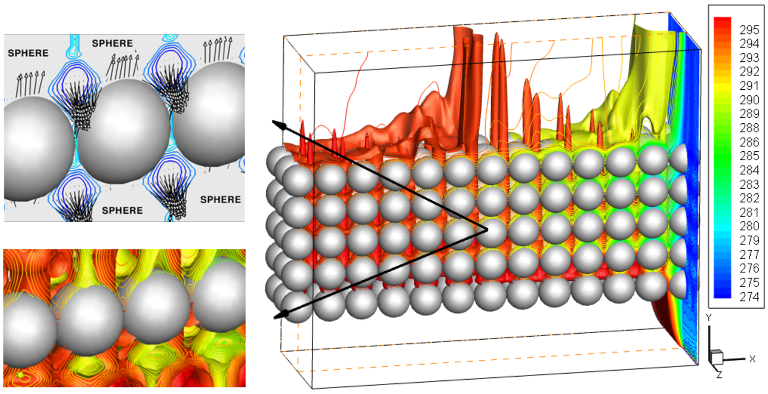

Figure 8: Isosurfaces of temperature and velocity and velocity vectors in the granular bed

The air entering the system is hotter then the barrier temperature and this implies that the temperature distribution should change. Observing the distribution of velocity vectors one can notice local regions of recirculation with locally downward flow. In the direction parallel to the direction of the air inlet one can see clear traces of the low temperature behind the balls. Visibly higher flow temperatures can be observed between granules in inter-granular spaces as evidenced by red iso-surfaces. The red peaks indicate a rapid flow of air. Such an inhomogeneity of flow occurring around individual spheres intensify the heat exchange process. Figure 9 on the right side shows the flow velocity distribution between the spheres and passing through them. It is worth paying attention to the zeroing of the flow velocity in the cross-section, where these regions are marked with white color, and to the places where the local velocity significantly exceeds the inlet velocity (color). This is because in the area of the granular material the spheres occupy most of the volume and the flow must accelerate for the reason of mass conservation. On the contrary, in the plane passing through the spheres (Fig. 9 on the left side) significantly lower velocity values are observed and the spaces between the spheres characterize mostly negative velocity.

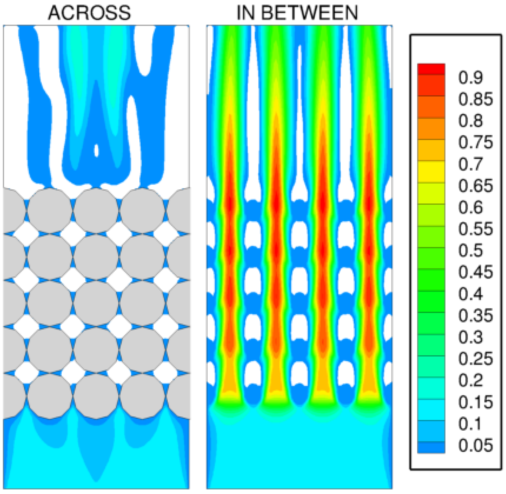

Figure 9: On the left: velocity in the plane passing through the spheres. On the right: velocity in the plane between the spheres.

Figure 10 shows the temperature distribution in the main cross-section ($z = 0$) at the selected time instances. It is seen that it significantly changes across the layer, both along the vertical/horizontal coordinate and between the regions of particular spheres. Compared to the inter-granular spaces they remain colder for long time. Figure 11 show the profiles of temperatures extracted from data presented in Fig. 10 for the time instances $0.1s$, $1s$, $2s$ and $4s$ from the beginning of the simulation. The temperature variations across the layer are shown in two different vertical locations and at four time instances. The dashed line shows the distribution from the location $y = 0.04m$ and the continuous lines correspond to the location $y = 0.06m$. The wavy shape of the profiles reflects varying thermal properties of the granules and air. This shape is readily apparent and becomes more noticeable with time as the cold air from the places in beetwen spheres slowly mixes with the flowing hot air. In the same time the spheres

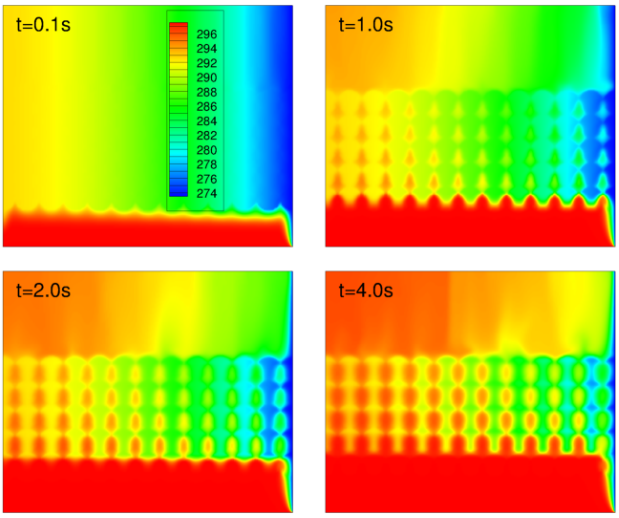

Figure 10: Temperatures in the plane passing through the spheres

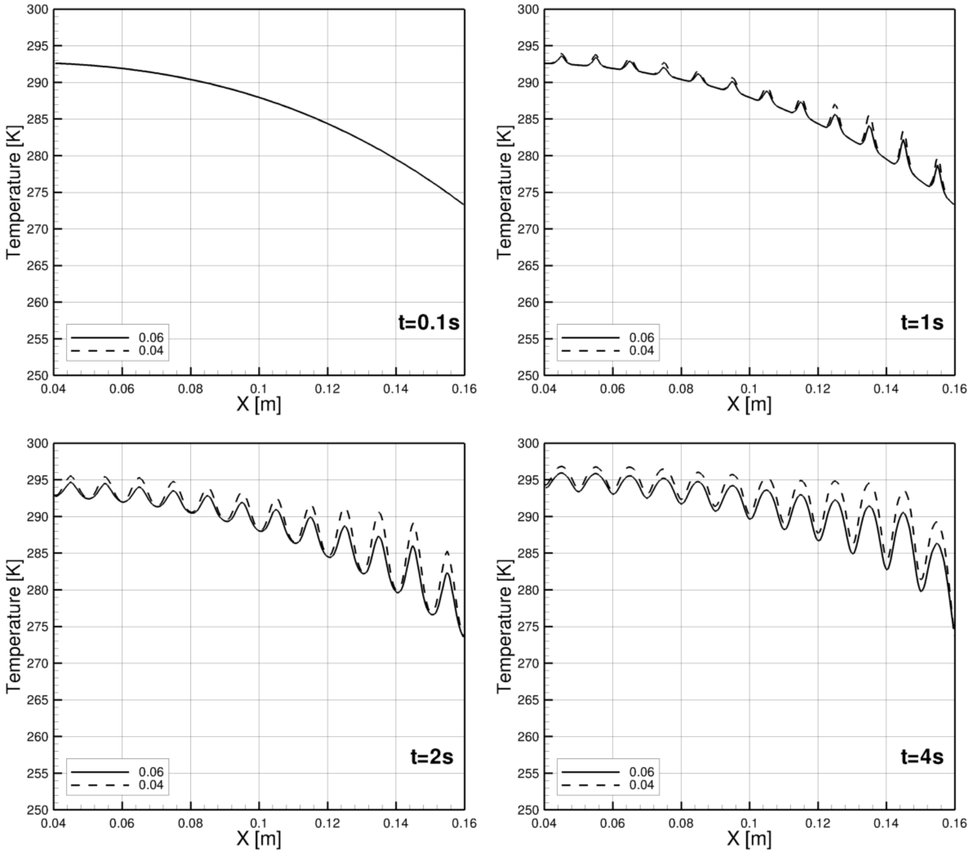

Figure 11: Temperature distribution in the granular bed at four time steps: t = 0.1s, 1.0s, 2.0s and 4.0s in the locations y=0.04m and y=0.06m.

remain cold and get hotter only after while, as it was mentioned above. Although the presented solutions have strongly unsteady character it should be mentioned that for long simulation time the temperature of the flowing air will rise and equalise the temperature of the sphere.

5 Summary

The paper presented numerical and experimental studies on the heat and flow in granular material and external barriers composed of two kind of materials. Comparisons of the numerical and experimental data indicated satisfactory agreement, both for basic test cases as well as for the granular layers and concrete layer used in the barriers. It was shown that treatment of the granulates as uniform layers with effective thermal properties leads to different results than in the case when the granular layer is considered as a complex system of solid material and inter-granular spaces. It was shown that the temperature inside the barriers can be effectively controlled by the motion of air inside the granular layer. In this case the flow and temperature distributions revealed large spatial inhomogeneities where correct predictions are possible only with the help of advanced numerical tools. It is believed that IB-VP method presented and used in this paper is one of them.

Acknowledgements

This work was supported by National Science Centre, Poland (Grant no. 2017/27/N/ST8/02318) and statutory funds of Czestochowa University of Technology under BS/MN 1-103-301/2018/P. PL-Grid infrastructure was used to carry out the computations.

References

[1] lvarez de Miguela, S., Gonzalez-Aguilara, J., Romero, M.; 100-Wh multi-purpose particle reactor for thermochemical heat storage in concentrating solar power plants, *Energy Procedia*, 49, (2014), 676 683.

[2] Yancy-Caballeroa, D.M., Biegler, L.T., Guirardello, R.; Large-scale DAE-constrained optimization applied to a modified spouted bed reactor for ethylene production from methane, *Computers and Chemical Engineering*, 113, (2018), 162183.

[3] Baumann, T., Zunft, S.; Properties of granular materials as heat transfer and storage medium in CSP application, *Solar Energy Materials and Solar Cells*, 143, (2015), 3847.

[4] Ma, Z., Glatzmaier, G.C., Mehos, M; Development of solid particle thermal energy storage for concentrating solar power plants that use fluidized bed technology, *Energy Procedia*, 49, (2014), 898 907.

[5] Ratuszny, P.; Thermal energy storage in granular deposits, *E3S Web of Conferences 19*, EEMS 2017, 01022, (2017)

[6] Hoffmanna, T., Riecka, C., Bcka, A., Peglow, M., Tsotsasa, E.; Influence of granule porosity during fluidized bed spray granulation, The 7th World Congress on Particle Technology (WCPT7), *Procedia Engineering* 102, (2015), 458 467

[7] Diez, E., Meyer, K., Bckc, A., Tsotsas, E., Heinricha, S.; Influence of process conditions on the product properties in a continuous fluidized bed spray granulation process, *Chemical Engineering Research and Design*, 139, (2018), 104115.

[8] Szymanek, E.; Blaszczyk, T.; Hall, M.R.; Dehdezi, P.K.; Leszczynski, J.: Modelling and analysis of heat transfer trough 1D complex granular system, *Granular Matter*, 16(5), (2014), 687-694.

[9] Hainsworth, J.M.; Aylmore, L.A.G.: The use of computer assisted tomography to determine spatial distribution of soil water content, *Australian Journal of Soil Research*, 21(4), (1983), 435-443.

[10] Breugem, W.P.; van Dijk, V.; Delfos, R.: Flows Through Real Porous Media: X-Ray Computed Tomography, Experiments, and Numerical Simulations, *Journal of Fluids Engineering*, 136(4), (2014), 040902.

[11] Amhalhel, G.A.; Furmanski, P.: Problems of modeling flow and heat transfer in porous media, *Biuletyn Instytutu Techniki Cieplnej Politechniki Warszawskiej*, 85, (1997).

[12] Massoudi, M.: On the heat flux vector for flowing granular materials - part I,II, *Mathematical Methods in the Applied Sciences*, 29(13), (2006), 1585-1598, 1599-1613.

[13] Vargas, W.L.; McCarthy, J.J.: Heat Conduction in Granular Materials, *AIChE Journal*, 47, (2001), 1052-1059.

[14] Ferrez, J.A.; Liebling, T.M.: Parallel DEM Simulations of Granular Materials, *High Performance Computing and Networking*, Springer Verlag,(2001).

[15] Tian, K.S.; Shu, H.J.: *Progress in porous media research*, Nova Science Publishers, Inc., New York, (2009).

[16] Ordonez-Miranda, J.; Alvarado-Gil, J.J.: Thermal characterization of granular materials using a thermal-wave resonant cavity under the dual-phase lag model of heat conduction, *Granular Matter*, 12, (2010), 569-577.

[17] Fornberg, B.; Steady viscous flow past a sphere at high Reynolds numbers, *Journal of Fluid Mechanics*, 190, (1988), 471.

[18] Dixon, A.G., Taskin, M.E., Nijemeisland, M., Stitt, E.H.; Systematic mesh development for 3D CFD simulation of fixed beds: single sphere study, *Computers and Chemical Engineering*., 35, (2011), 11711185.

[19] Li,S., Yang, J., Wang, Q.; Large eddy simulation of flow and heat transfer past two side-by-side Spheres, *Applied Thermal Engineering*, 121, (2017), 810819.

[20] Qi,Z., Kuang,S., Rong,L., Yu,A.; Lattice Boltzmann investigation of the wake effect on the interaction between particle and power-law fluid flow, *Powder Technology*, 326, (2018), 208221.

[21] Fadlun, E.A.; Verzicco, R.; Orlandi, P.; Mohd-Yusof, J.: Combined Immersed-Boundary Finite-Difference Methods for Three-Dimensional Complex Flow Simulations, *Journal of Computational Physics*, 161, (2000), 35-60.

[22] Mittal, R.; Iaccarino, G.: Immersed boundary methods, *Annual Review of Fluid Mechanics*, 37, (2005), 239-261.

[23] Khadra, K.; Angot, P.; Parneix, S.: Fictitious domain approach for numerical modelling of Navier-Stokes equations, Caltagirone J-P., *International Journal for Numerical Methods in Fluids*, 34, (2000), 651-684.

[24] Tyliszczak, A.: High-order compact difference algorithm on half-staggered meshes for low Mach number flows, *Computer and Fluids*, 127, (2016), 131-145.

[25] Fletcher, C.A.J.: *Computational Techniques for Fluid Dynamics*, Springer-Verlag, (1991).

[26] Tyliszczak, A.: A high-order compact difference algorithm for half-staggered grids for laminar and turbulent incompressible flows, *Journal of Computer Physics*, 276, (2014), 438-467.

[27] Kadoch, B.; Kolomenskiy, D.; Angot, P.; Schneider, K.: A volume penalization method for incompressible flows and scalar advection diffusion with moving obstacles, *Journal of Computer Physics*, 231, (2012), 4365-4383.

[28] Suekane, T.; Yokouchi, Y.; Hirai, S.: Inertial flow structures in a simple-packed bed of spheres, *AIChE J.*, 49, (2003), 10-17.

Address: Faculty of Mechanical Engineering and Computer Science, Czestochowa University of Technology.
Al. Armii Krajowej 21, 42-201 Czestochowa, Poland
email: `ewaszym@imc.pcz.pl` email: `atyl@imc.pcz.pl`

DOI: 10.24352/UB.OVGU-2019-010 TECHNISCHE MECHANIK, 39, 1, (2019), 97 - 112
submitted: July 6, 2018

Modelling of Breathing Phenomena within Large Storage Tanks During Rapid Cooling with Ambient Rain

N. Schmidt, J. Denecke, J. Schmidt, M. Davies

Storage tanks in the process industry are often filled with hazardous media under atmospheric conditions. Due to heavy rain showers the tank content is cooled down and the system temperature drops significantly. During this process the pressure decreases and condensate forms. It is known that "vacuum" can cause serious damage on storage tanks due to undersized venting devices. To describe the transient storage tank behaviour modelling of complex inbreathing fluid flow, heat transfer, condensation, retrograde gas states or thermodynamic non-equilibrium is needed. Conservative sizing of protection devices for storage tanks is only possible if the influencing phenomena and their couplings are well understood. The influence of heat transfer through film condensation as an example phenomenon is mentioned by several authors in science and industry, but not included in common models.

With the new approach of ARTEM (advanced reactor and storage tank emission model) phenomena, like condensation or complex heat transfer will be considered for transient vessel venting. Experience and preparatory work have shown that detailed modelling with computational fluid dynamic (CFD) tools is necessary to analyse the complex multiscale phenomena accurately and in sufficient detail. As a first step towards ARTEM, an analytical parameter study on tank breathing with common sizing models and a CFD study on heat transfer through a tank wall is presented.

1 Introduction

Storage Tanks are used in many different sections of industry, e.g. chemical, petrochemical, food industry or agriculture. In these tanks, liquids, gases and mixtures are stored under atmospheric conditions. Many of these tanks are located outdoors and thus exposed to sudden weather changes. The occurrence of temperature variations causes tank venting to compensate volume contraction or expansion of the bulk phase. Common storage tanks buckle at pressure changes of 10 mbars due their relatively thin wall-thickness of 5 mm (Fullarton et al., 1987). To prevent damage, breathing valves (vacuum / pressure valves) are installed on the rooftop to enable inbreathing and outbreathing for non-hazardous tank content. If the content is inflammable or toxic, inert gas blanketing or vapor recovery units are required. For proper sizing of these compensation devices, the ventilation volume flow rate due to weather effects must be considered besides filling or emptying scenarios.
The sizing of venting devices is covered in many standards, like API 2000 (American Petroleum Institute, 2014) or DIN EN ISO 28300 (Deutsches Insitut fuer Normung, 2012). The standard models are simplified in a physical and mathematical manner to allow quick manual calculations. Many investigations in literature have shown, that these models are not sufficient for conservative sizing of venting devices (Moncalvo et al., 2016 and Holtkoetter et al., 1997). The basic assumptions of these models are valid only for non-condensable gases. Other tank breathing phenomena, e.g. film condensation, fog formation or convection are excluded. Considering these effects, breathing valves may be significantly undersized (Moncalvo et al., 2016 and Abou-Chakra, 2016).

A sizing method for breathing valves for non-condensable gases was first developed by Nauman in his unpublished report "vacuum and pressure valves on tanks". Therefore, the maximum inbreathing rate is calculated in dependency of the tank volume. Based on this work and the PTB report "Mathematical estimations of venting operations on roofed-over tanks" written by Foerster and Schampel in 1979, Sigel et al. (Sigel 1980 and Sigel et al. 1981) developed the extended "Hoechst formula" for non-condensable gases. To validate their model, Sigel et al. performed measurements on a 618 m^3 air filled tank. The measured inbreathing volume flow rate was significantly lower than predicted with their calculation model but still an improvement to Naumann. Foerster, Schampel and Steen (Foerster et al., 1984) published a model which was focused on weather dependent breathing phenomena. Their method was not only created for inbreathing predictions but also to calculate outbreathing as a result of temperature rise due to sunshine. Common standards as API 2000 are based on this work. This model is based on the assumption, that condensation is not a dominant phenomenon in tank breathing and therefore is neglectable. This consideration was revised by several authors in the following years.

Gosslau, Mueller and Weyl (Gosslau et al, 1985) developed a model for thermal tank ventilation including inbreathing and outbreathing. In contrary to Foerster et al., they considered film condensation inside the tank with the conclusion that the impact of condensation on ventilation is not as significant as initially assumed. They validated their model on the measurements of Sigel. Fullarton et al. (Fullarton, 1986) considered film condensation in their inbreathing model. A recognition of this work is, that the Naumann formula leads to significantly oversized venting devices and therefore is too conservative for correct sizing calculations. Based on this knowledge, Fullarton, Evipidris and Schluender (Fullarton et al., 1987) published an extended inbreathing model for condensable vapours. Davies et al. (Moncalvo et al., 2016) applied an enhanced approach to Fullarton's model. They were first to consider the temperature difference between the inflowing air and the bulk phase.

Holtkoetter, Shang and Schecker (Holtkoetter et al., 1997) developed a model that includes film condensation at the tank wall and homogeneous condensation in the vapor space. They validated their model on a tank of 1.18 m^3 and concluded, that the submission of condensation heat has a damping effect on cooling of the bulk phase. Salatino, Volepicelli and Volpe (Salatino et al., 1999) introduced a model with regard to the heating process of storage tanks due to sunshine. They compared their results to API 2000 4th edition, Sigel et al. and Naumann. According to their calculations, the API 2000 model underestimates the inbreathing volume flow rate, in contrast to the overestimating Sigel and Naumann model. Vapor condensation was not included in the model but was mentioned as potential source of influence. Abou-Chakra et al. (Abou-Chakra, 2016) validated the implemented calculation model for tank ventilation in the commercial software SuperChems Expert^{TM} (IoMosaic, 2015). According to their model, venting devices are overdesigned by up to 60% for non-condensable gases and underestimated by up to 270% for condensable gases using API 2000 6th ed..

The scope of this work is to show, that not only the heat transfer through film condensation has a major impact on tank cooling but also other phenomena like fog formation, convection and flow considerations on the inside. Deeper knowledge about the processes and phenomena inside of tanks is necessary to understand the physical behaviour and to calculate tank ventilation due to weather changes precisely. As first approach towards the overall calculation model ARTEM (advanced reactor and storage tank emission model), a validation of common literature sizing models is presented for condensable and non-condensable contents. In addition, a study on influencing parameter on tank breathing was performed. Further, a two-dimensional CFD simulation of the heat transfer through a tank wall, considering a rain film on the outer surface, is carried out.

The aim of ARTEM in the future is an accurate overall calculation model considering breathing phenomena inside of storage tanks to enable an exact prediction of ventilation flows. Prospectively, the ARTEM model will be extended with the emptying and filling process and additional weather effects, like pressure drop, wind flow or ambient temperature change which need to be considered for the sizing of compensation devices.

2 Phenomena of Storage Tank Cooling

Storage tank venting is caused by thermal pressure changes and load cycles. Regarding thermal changes, two leading scenarios are specified. First, the content of the tank is heated up and second, a hot tank is cooled down by a cooler environment, as depicted in figure 1. This paper focuses on the cooling process with thermal inbreathing which is described below. Other venting phenomena, like pressure changes from a depression, emptying or filling and heating of a tank are not considered in this work but will be in the future. For a proper design of compensation devices, these effects must be considered.

The cooldown of a tank exposed to sun begins when the sun is obscured by clouds with a sudden heavy rain shower. Therein, the ambient temperature drops rapidly and the pressure changes due to the depression. The first raindrops evaporate on the tank wall, causing a local cooldown while the tank wall releases radiant heat. In the course of the shower, the rain intensity may vary over time and the tank is exposed to transient environmental conditions. When wind gusts appear as side effect, a complex wind field is caused, depending on the tank location, that redirects the droplet tracks. Assuming vertical rainfall, the tank roof is covered in droplets. The developing rain film runs down the tank wall and increases the heat transfer significantly. During this process, the film is consistently heated up and partly vaporizes until reaching the ground. Assuming side wind, parts of the shell surface are moistened by forming an unstable rain film. Depending on the surface roughness and environmental conditions, the rain film builds waves until a stable rain film is formed. With rising rain intensity, the film thickness increases and varies over the tank surface. The film velocity accelerates towards the ground and hastens the cooldown of the tank wall. Incoming rain drops suppress the film locally and cause a turbulent mixing of the fluid. With impact on the rain film, the local heat transfer on the surface increases. Some storage tanks are insulated, which can reduce breathing significantly. Thus, due to inhomogeneities in the tank insulation, wind, sun and rain around the tank, the heat transfer changes locally. To summarize, the heat transfer on the outer tank surface is time- and location-dependent due to rainfall and surface quality.

At the cold tank wall, the boundary layer of gas inside the tank cools down significantly. The density of the cold boundary layer is larger than the density in the middle of the tank and therefore sinks to the tank bottom. By this, convection rolls are formed that increase mixing and mass transfer processes in the tank. The free jet from the inbreathing device acts against the free convection. It depends on the initial bulk fluid and wall temperatures, which ever dominates the flow. Due to wall cooling, the free convection also occurs in the liquid phase. The liquid has a higher heat capacity and cools down more slowly than the gas phase. In addition, the liquid experiences heat transfer through the tank bottom.

Regarding the cool gas boundary layer, a local oversaturation of the gas phase develops and condensate is formed. In the beginning of the condensation process some nuclei stay smaller than the critical drop diameter and vaporize instantaneously. The drop nuclei grow as a result of the cooling conditions to a condensate film, starting at the location with the heaviest subcooling, which is the tank roof. Due to gravity the condensed mass rans down the tank wall to the bottom causing an increase in heat exchange. Depending on the velocity profile, the inside condensate film forms a wavy surface until it is fully stabilized. In some tanks, drops formed on the rooftop are dropping to the bottom when exceeding a critical diameter.

Depending on the stored medium, the gas phase is composed of components with different vapor pressure and diffusion coefficients so that mixing thermodynamics have to be considered in the condensation process. By condensing the gas inside the tank, the mass of the gas phase is reduced and increases the vacuum.

The vacuum is compensated by inbreathing. Wet air loaded with fine particles enters from the environment and cools down the gas at the inlet nozzle. Due to the local oversaturation, heterogeneous condensation on the particle surface and homogeneous condensation, both visible as fog, occur. The associated volume contraction of the tank atmosphere increases the inbreathing airflow. Large aerosol drops sink to the ground, starting a mixing process in the bulk phase that also might accelerate the tank cool-down.

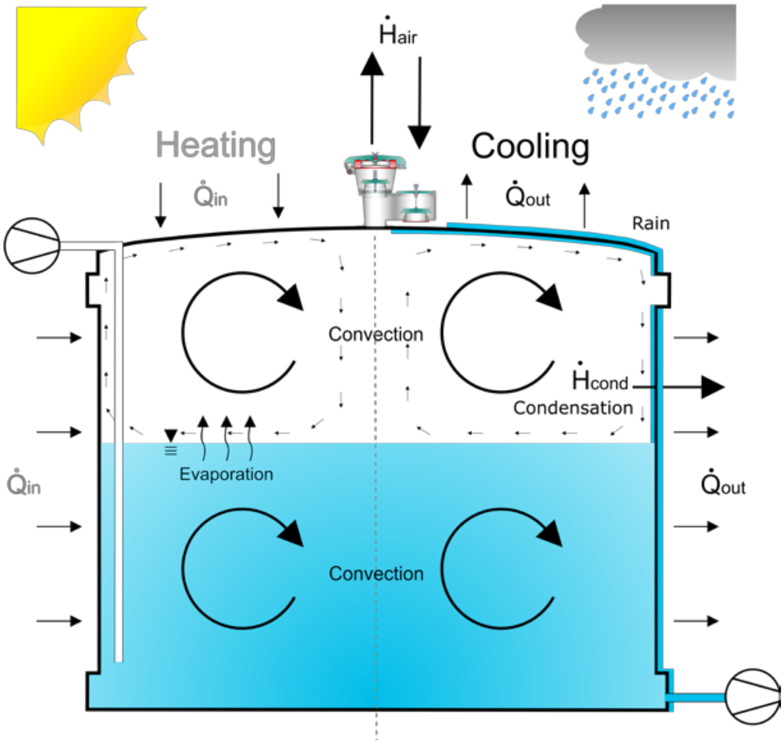

Figure 1. Storage tank venting phenomena to be considered in calculation models.

Most of the phenomena described above are not considered in any model because their interaction is quite complex. To take every phenomenon into account computational fluid dynamics (CFD) is necessary, because the phenomena are not only time but also location dependent. In literature considered effects are heat and mass transfer in the tank, e.g. inbreathing, condensation effects excluding heat conduction through the film, a rain film on the outer surface and heat transfer to the ambience. Momentum effects are entirely neglected.

3 Governing Equations in Common Venting Models

For an accurate calculation of inbreathing, the phenomena described above have to be considered. Thus, common calculation models are governed by many simplifications to economise calculation effort. In the following, a general derivation of governing equations of leading tank venting models for thermal inbreathing is given.

Commonly, the system boundary, as depicted on the right side of Figure 1, is subdivided into four different regions. The first region contains the bulk phase including condensate at the tank wall. The second region is the continuous liquid phase on the bottom of the tank. Region three is governed by the tank wall and the rain film with the environment constitutes region four. In most cases, the liquid phase is neglected because it mitigates the inbreathed air volume flow rate and therefore, the calculation is on the conservative side.

The inbreathing volume flow rate $Q_{v,air}(t)$ is determined by the thermal contraction of the gas phase (Moncalvo et al., 2016; Fullarton, 1986 and Holtkoetter et al., 1997):

$$Q_{v,air}(t)=\frac{V_{bulk}}{T_{bulk}(t)}\frac{dT_{bulk}(t)}{dt}+Q_{v,cond}(t)+Q_{v,cond,sp}(t) \tag{1}$$

Herein, V_{bulk} is the bulk volume, $T_{bulk}(t)$ is temperature of the bulk and $Q_{v,cond}(t)$ is the volume flow rate of the condensate. Holtkoetter et al. (Holtkoetter et al., 1997) also considered homogeneous condensation in their mass balance with an additional term $Q_{v,cond,sp}(t)$. This mass balance is valid for the assumption, that the temperatures of bulk and ambience are equal. Davies extended Fullarton's model among other considerations by assuming different temperatures between bulk and ambience and therefore to take the enthalpy of the inbreathed air into account. By this, the variation of the bulk temperature over time is estimated with an energy balance. The change of internal energy $U_{bulk}(t)$ in the bulk is governed by the enthalpy flux of the inbreathed air $\dot{H}_{air}(t)$, the enthalpy flux of the condensate film $\dot{H}_{cond}(t)$, the enthalpy flux of the spontaneously formed condensate $\dot{H}_{cond,sp}(t)$ and by a heat flux through the tank wall due to the cooler environment $\dot{Q}_{out}(t)$:

$$\begin{aligned}\frac{dU_{bulk}(t)}{dt}&=(M_{cond}(t)c_{p_{cond}}+M_{cond,sp}(t)c_{p_{cond}}+M_{vap}(t)c_{p_{vap}}+M_{air}(t)c_{p_{air}})\frac{dT_{bulk}(t)}{dt}\\&=\dot{H}_{air}(t)-\dot{H}_{cond}(t)-\dot{H}_{cond,sp}(t)-\dot{Q}_{out}(t)\end{aligned} \tag{2}$$

Thereby, $M_i(t)$ is the mass of the components described above and c_{p_i} is the specific heat capacity of the components which are assumed to be constant. The enthalpy flux of the inbreathed air is calculated as it follows:

$$\dot{H}_{air}(t)=\rho_{air}Q_{v,air}(t)c_{p_{air}}(T_{bulk}(t)-T_{amb}) \tag{3}$$

With ρ_{air} as air density and T_{amb} as ambient air temperature, both assumed to be constant. The condensation enthalpy flux is:

$$\dot{H}_{cond}(t)=\rho_{cond}Q_{v,cond}(t)\Delta h_{v,cond} \tag{4}$$

Thereby, ρ_{cond} is the constant density of the condensate and $\Delta h_{v,cond}$ is the constant specific condensation enthalpy of the condensate film. The condensation mass flow rate is usually calculated with the Lewis' formula in combination with Antoin's law and the assumption of saturated vapor inside the tank (Moncalvo et al., 2016 and Fullarton et al., 1987). In Holtkoetters model, the enthalpy flux caused by spontaneous condensation is:

$$\dot{H}_{cond,sp}(t)=\rho_{cond}Q_{v,cond,sp}(t)\Delta h_{v,cond} \tag{5}$$

On the basis of their measurements, Holtkoetter et al. determined the volume flow rate of spontaneous condensation $Q_{v,cond,sp}(t)$ by means of the proportional aerosol mass fraction. The heat flux leaving the tank is defined by the heat transfer from the bulk to the wall:

$$\dot{Q}_{out}(t) = k_{in} A(T_{bulk}(t) - T_{wall}(t)) \tag{6}$$

The decrease in gas volume due to condensation is included in the mass balance but the heat conduction through the film is neglected in the energy equations in the literature models. Thus, the condensation enthalpy of the film is taken into account.

The tank wall temperature $T_{wall}(t)$ depends on the heat transfer between the bulk phase and the wall k_{in}, the heat transfer between the wall, the rain film k_{rain} and the condensation enthalpy due to the film:

$$M_{wall} cp_{wall} \frac{dT_{wall}}{dt} = k_{in} A(T_{bulk}(t) - T_{wall}(t)) - k_{rain} A(T_{wall}(t) - T_{rain}(t)) - \rho_{cond} Q_{v,cond}(t) \Delta h_{v,cond} \tag{7}$$

The temperature of the rain film $T_{rain}(t)$ is dependent on the rain intensity and the heat transfer to the ambience (Fullarton et al., 1987 and Holtkoetter et al., 1997). In some models, effects like wind cooling, the warm up of the cold rain and tank wall insulation are considered (Moncalvo et al., 2016 and Foerster et al., 1984).

All models mentioned above are derived for single components. For mixtures, there is currently no ventilation model published in literature.

4 Measurements of Inbreathing

Sigel (Sigel et al., 1981) performed measurements on a storage tank with a height of 11.16 *m* and a diameter of 8.5 *m*. The tank contained a volume of 618 m^3 and was filled up with dry air. During the measurements, the tank was heated up by the sun until a maximum temperature was reached. Afterwards the outer tank surface of 340 m^2 was cooled down with water from a sprinkler. Thereby, Sigel et al. expected 10% of the water to bounce off the tank wall. In 1980 and 1981 eleven measurements were taken and recorded. The measurements differed in the following points:

- Initial temperature
- Measurement duration
- Temperature of the sprinkle water
- Temperature difference between the initial and end temperature

Despite these differences, the temporal progression of the graphical measurement display was quite similar. The maximum inbreathing volume flow rate over all measurements was situated between 71 m^3/hr and 114 m^3/hr. The size of the tank was sufficient to illustrate a realistic cooling scenario but with a maximum sprinkling intensity of 69 kg/m^2hr, only rain showers to occur every second year on average were simulated (Sigel et al. 1983). Foerster et al. (Foerster et al., 1984) considered rain showers to occur every 100 years on average with an effective rain intensity of 143.7 kg/m^2h. Unfortunately, information is missing to simulate the realistic setup, e.g. the exact measurement day time, the ground temperature, the temperature and moisture level of the inbreathed air, wall temperature in the beginning, property data of the tank wall and a reliable technical drawing of the tank.

Holtkoetter (Holtkoetter et al., 1997) performed measurements on a 1.18 m^3 laboratory tank. The bulk phase was heated up to 328 *K* and cooled down by 40 *K*. The cooling was accomplished with a sprinkler mounted on top of the tank which produced a rain flow intensity of 10 kg/m^2h, according to Abou-Chakra (Abou-Chakra, 2016). The measurements were conducted with three different media inside the tank: water, methanol and isopropanol. Holtkoetter observed besides film condensation also fog formation in the tank through small windows in the tank wall. The liquid mass of the spontaneously condensed aerosol phase was measured with a filter module. Before and after the measurements the mass of the filter was weighted to determine the amount of homogeneous condensate. The highest inbreathing rate was observed in the methanol measurements. During the water measurements, 22% of the overall condensation mass was associated to fog formation, where only 9% of spontaneous condensation mass occurred during the measurements with methanol. The fog formation has a damping effect on the cooldown, due to the emission of condensation heat. Because the measurements were performed on a laboratory tank, the observation of Holtkoetter should be reproduced on a large tank to evaluate the scale up effects. In addition, information about the exact measurement conditions is missing, e.g. the properties of the tank material, the rain temperature and intensity, the location and size of the breathing device and a technical drawing of the tank. Without this information an accurate simulation of the measurements is not possible. These uncertainties are considered in the subsequent validation of the literature models.

5 Comparison of Measurements and Models for Inbreathing

In the following, three relevant inbreathing models are compared to the measurements described above: the model of Fullarton et al. (Fullarton et al., 1987) and Davies et al. (Moncalvo et al., 2016) which both are based on the model of Foerster et al. (Foerster et al., 1984). While Foerster did not consider condensation as governing effect of tank breathing, Fullarton derived a model with condensation as significant parameter. This model was extended by Davies. The models are based on the equations and assumptions described in chapter 3.

The validation of the models on the Sigel measurements, relies on the following assumptions: A steel tank with a height of 8.5 m and a H/D-ratio of 0.8 was used. The tank atmosphere was exclusively filled with air. An inner heat transfer coefficient of 5 W/m^2K (bulk to wall), a liquid heat transfer coefficient of 5000 W/m^2K (wall to rain film) and an outer heat transfer coefficient of 25 W/m^2K (rain film to ambience) were considered. The tank wall thickness was assumed to be 5 mm.

Compared to the measurements of Sigel et al. (Sigel et al. 1981) from 9th July, 1981, the calculation with the Foerster model shows a discrepancy of 43%, see Figure 2. A weakness of the Foerster model is the assumption that film condensation and fog formation are not of significant importance on influencing the inbreathing rate. This statement was revised by Fullarton et al. (Fullarton et al., 1987). Therefore, the data of Sigel are mirrored with an accuracy of 1% by Fullarton's model and Davies' model. The two curves coincide exactly in figure 2.

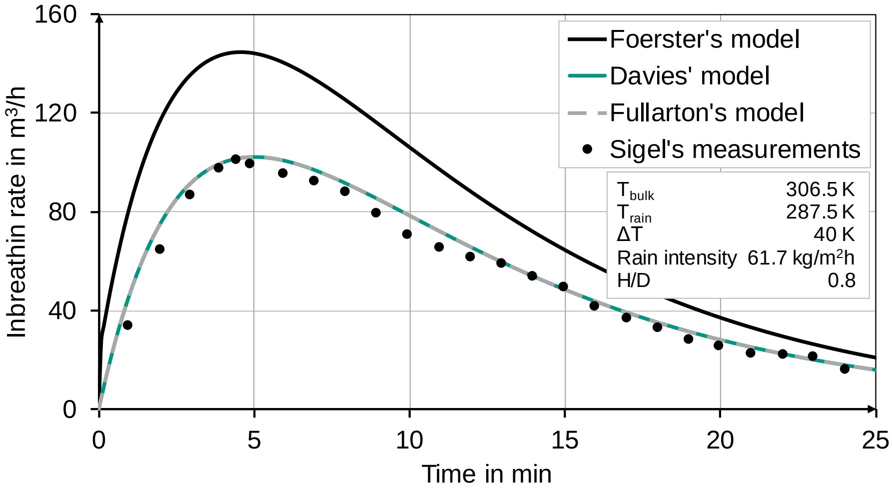

Figure 2. Inbreathing models of Foerster (Foerster et al., 1984), Davies (Moncalvo et al., 2016) and Fullarton (Fullarton et al., 1987) for non-condensable gases compared to Sigel's measurements (Sigel et al. 1981).

However, a critical error consideration of the measurement data is not negligible. Sigel assumed in his measurements that 10% of the water sprayed onto the tank rebounds from the tank surface and therefore does not contribute to cooling the surface. This assumption has not been verified. In addition, the breathing of the tank was facilitated by a long supply line. The pressure loss in this supply line is not known. Finally, weather information is incompletely listed in the experimental protocols, e.g. data on humidity, solar radiation or wind influences are missing.

A contrary situation occurs by the comparison of the models for condensable vapours to the measurement of Holtkoetter. Therefore, a steel tank with a height of 1,5 m and a H/D-ratio of 1.5 was used. The tank atmosphere was assumed to be saturated with vapor, the liquid inside the tank was neglected. An inner heat transfer coefficient of 5 W/m^2K (bulk to wall), a liquid heat transfer coefficient of 5000 W/m^2K (wall to rain film) and an outer heat transfer coefficient of 25 W/m^2K (rain film to ambience) were considered.

In Figure 3, Holtkoetter's measurements for water compared to Davies' and Fullarton's model are displayed.

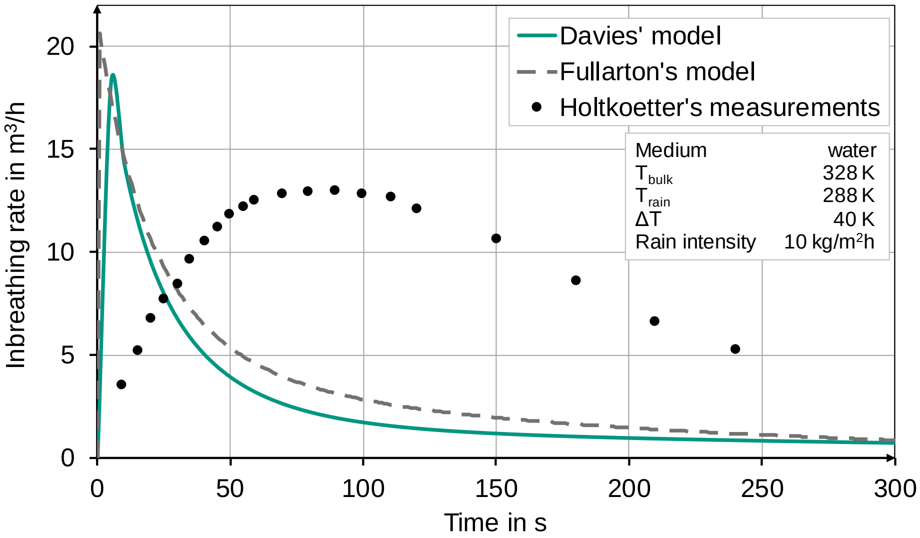

Figure 3. Inbreathing models of Davies (Moncalvo et al., 2016) and Fullarton (Fullarton et al., 1997) for condensable vapours compared to Holtkoetter's (Holtkoetter et al. 1997) measurements of water.

As to be seen from the figure, the calculated inbreathing volume flow rate is much larger than expected from the measurements. The deviation of the maximum inbreathing rate is at 55% with the Fullarton model and at 40% with the Davies model. The same calculations were performed with the medium methanol. With the Fullarton model, a deviation of 14% was noticed and a 5% underestimation with the Davies model, as depicted in figure 4. Regarding the time dependency, the maximum inbreathing rates were calculated right in the beginning whereby in the measurements the maximum rate was delayed by 90 seconds. As error analysis, two reasons seem to be obvious. The first one is related to the experimental conditions. The experimental conditions of Holtkoetter's measurements were not completely published and some assumptions were over taken from Abou-Chakra et al. (Abou-Chakra, 2016). The second reason is the occurrence of fog formation inside the tank that was observed by Holtkoetter and which is not included in Fullarton's and Davies' model. The formation of aerosols has a damping effect on the cooling process because condensation heat is released and therefore less condensate at the tank wall is formed. This effect causes a much lower maximum inbreathing rate and a widening of the curve. The intensity of this effect depends on the amount of fog that is formed.

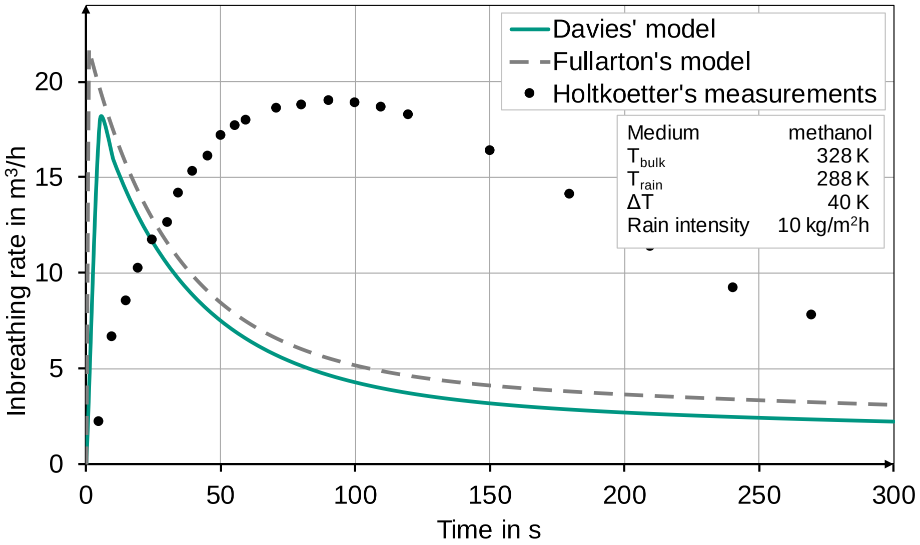

Figure 4. Inbreathing models of Davies (Moncalvo et al., 2016) and Fullarton (Fullarton et al., 1997) for condensable vapours compared to Holtkoetter's (Holtkoetter et al. 1997) measurements of methanol.

Since methanol forms less fog compared to water, the maximum inbreathing rate of the Holtkoetter measurements are more precisely predictable by literature models.

The validations of Fullaton's and Davies' model have shown that they are well qualified for inbreathing calculations with non-condensable gases for this particular measurement. For an accurate validation, a decent study on all measurements of Sigel is necessary. The comparison to the Holtkoetter's measurements demonstrated that the models are not valid for condensable vapours in small tanks, especially for stored media with high vapor pressure. It is questionable if the results are transferable to large tanks. A similar comparison to Holtkoetter's measurements was performed by Abou-Chakra et al. for the SuperChems Expert^{TM} model. The SuperChems Expert^{TM} model showed deviations of 1.7% with water vapor but 20% with methanol vapor (Abou-Chakra, 2016). A disadvantage of Fullarton's model is, that for the derivation of the mass balance the inbreathed air must be equal to the bulk phase, which is doubtful considering the temperature drop within sudden weather changes. If the air is assumed to be colder than the tank, the cooling process is accelerated. In Davies' model, the disadvantages of the temperature difference between the inbreathed air in the bulk phase was revised. The results show an improvement compared to Fullarton especially for gases with a low vapor pressure but without a satisfying solution. The Davies model is not always conservative, as the results in figure 4 have shown. Despite, the heat conduction through the condensate film is neglected in both models. For accurate sizing of compensation devices, it is necessary that the assumptions made within the calculation models are sufficiently conservative to prevent damage on the tank. Therefore, the heat transfer in particular is investigated in the CFD simulation in chapter 7.

6 Parameter Study on Inbreathing

For an evaluation of other impact factors, a parameter study with the model of Fullarton et al. (Fullarton et al., 1997) is performed. Therefore, a tank with a size of 2 651 m^3 is assumed, filled up with a vapor/air mixture of different compositions and with different media. Seven parameters are examined in total: the tank wall thickness, the tank geometry, the tank volume, the tank material, the rain intensity, the vapor proportion and the storage medium.

As result, obviously a thinner tank wall is beneficial for the heat transfer between the bulk phase and the environment so that a tank with a lower wall thickness cools down faster than a tank with a higher wall thickness. By varying the height to diameter ratio of the tank from 0.5 to 2 no remarkable deviations are noted. The discrepancy of inbreathing rates is less than 1%. In contrast, the tank volume has major impact on the inbreathing rate, see figure 5.

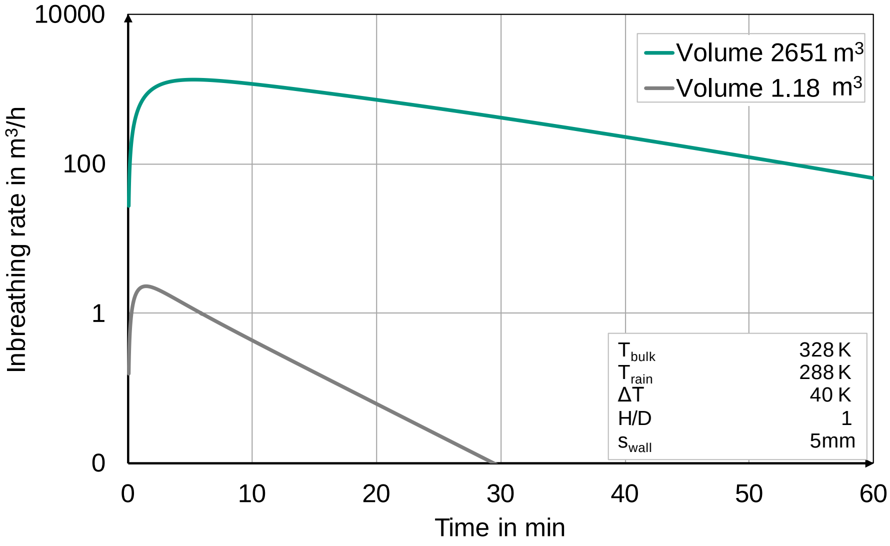

Figure 5. Inbreathing rates for a tank volume of 2651 m^3 and 1.18 m^3 over time.

The inbreathing rate in the small tank increases and mitigates faster compared to the large tank. A reason for this behaviour is the faster cooldown of the small tank, see figure 6. Due to the poor heat transfer ability of gas, the volume of the large tank is cooled down very slowly, even though the wall temperature drops quickly in the beginning.

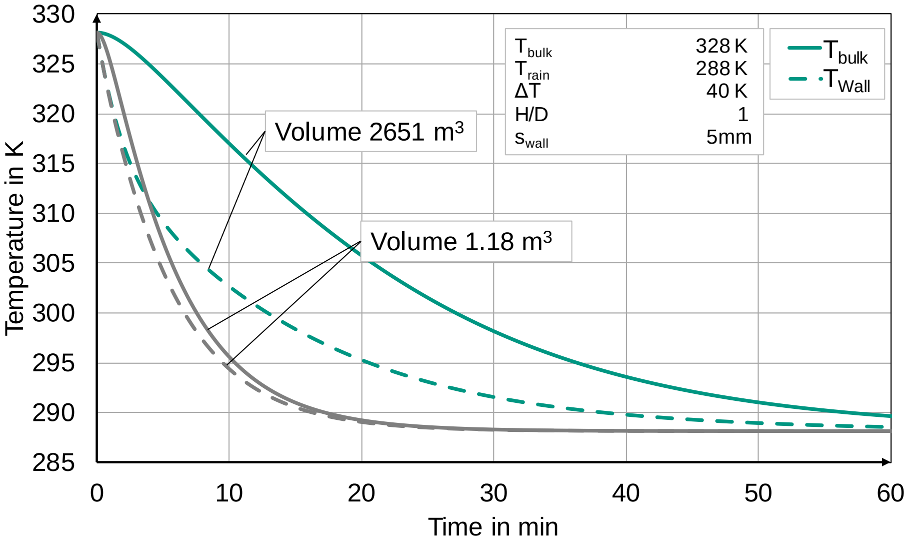

Figure 6. Wall and bulk temperature inside a storage tank with a volume of 2651 m^3 and 1.18 m^3 over time.

For an evaluation on the influence of the tank material, steel, stainless steel and steel concrete are compared. The inbreathing rates in the steel concrete tank is 17% higher compared to the other tanks, because of the slower cooldown of the concrete wall. As expected, the cooling process accelerates with increasing rain intensities and causes higher inbreathing rates, due to the faster decrease in temperature. With varying vapor content (11.8%, 50%, 100%) inside the tank, poor deviations of 6% are detected. As result, the influence of vapor content on inbreathing is negligible. A change of medium has a visible effect, as depicted in figure 7. The inbreathing rate is the highest for acetone and the lowest for water.

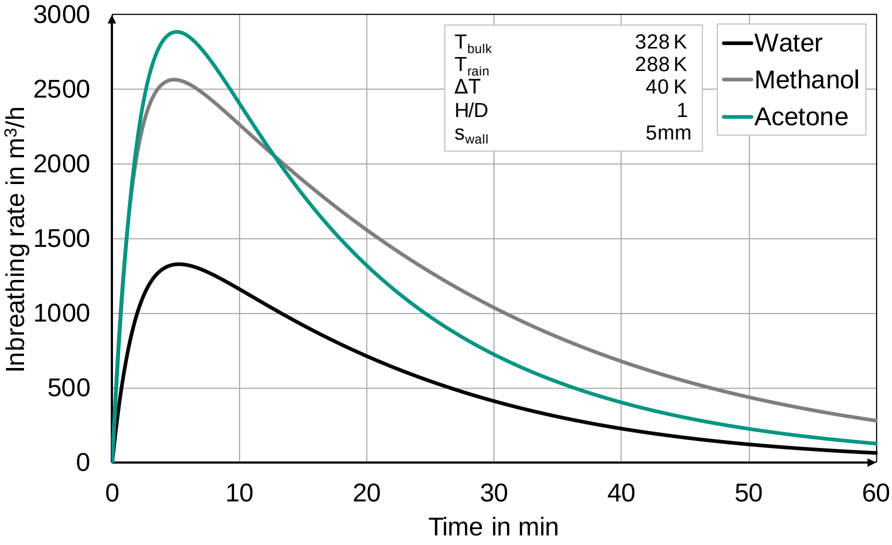

Figure 7. Inbreathing rates for acetone, methanol and water over time.

As mentioned by Holtkoetter et al. (Holtkoetter et al., 1997), homogeneous condensation is one impact factor on inbreathing. Due to the vapor pressure, acetone forms fog poorly compared to water and methanol which causes an increase in the inbreathing rate.

On the basis of this parameter study, some influences on inbreathing were pointed out. To receive a more accurate model, a detailed look on breathing phenomena with computational fluid dynamics (CFD) is necessary, considering location-dependent effects. In particular, the heat transfer simulation through the tank wall as first step to an overall calculation model is performed in the next chapter.

7 Simulation of Heat Transfer on a Storage Tank Wall

Breathing phenomena of low-pressure storage tanks have not been simulated with CFD yet. As a basis for a feasibility study for the further simulations in the ARTEM model, the two-dimensional (2D) cooling of a tank wall by heavy rainfall was performed with the *chtMuliregionFoam* solver of the OpenFOAM software, based on Sigel's measurements (Sigel et al., 1981). This solver uses the PIMPLE-Algorithm as a combination of PISO (Pressure Implicit with Splitting of Operator) and SIMPLE (Semi-Implicit Method for Pressure-Linked Equations) for the fluids with the following governing equations. A detailed description of the solver is outlined by el Abbassi et al. (el. Abbassi et al., 2017).

The mass transfer is described by:

$$\frac{\partial \rho}{\partial t} + \nabla \cdot (\rho w) = 0 \tag{8}$$

ρ is the fluid density and w the velocity of each phase. The momentum and energy transport are calculated with:

$$\frac{\partial \rho w}{\partial t} + \nabla \cdot (\rho w w) = -\nabla p + \nabla \left\{ \eta \left[\nabla w + \left(\nabla w \right)^T \right] \right\} - \nabla \left(\frac{2}{3} \eta (\nabla \cdot w) \right) \tag{9}$$

$$\frac{\partial \rho h}{\partial t} + \nabla \cdot (\rho w h) + \frac{\partial \rho K}{\partial t} + \nabla \cdot (\rho w K) - \frac{\partial p}{\partial t} = \nabla \left(a \nabla h \right) + \rho w g \tag{10}$$

Therein, p is the phase pressure, η is the dynamic viscosity of the fluid, h is the specific enthalpy of the fluid, a is the thermal diffusivity and the kinematic energy K is calculated with:

$$K = \frac{w^2}{2} \tag{11}$$

The system of equations is solved for both fluids, while the bulk phase is compressible and the liquid phase is incompressible. In both fluids a laminar flow condition is assumed. In the solid phase, only the energy equation has to be solved which is described by Fourier's law:

$$\frac{\partial \rho h}{\partial t} = \nabla (a \nabla h) \tag{12}$$

The heat transfer between the phases is coupled with the assumption that the temperature between the solid and the fluid phases at the interface is equal. Furthermore it is assumed, that the heat flux entering one region at one side of the interphase is equal to the heat flux leaving the other region in the other side of the domain.

The setup for the two-dimensional (2D) cooldown of the tank wall is shown in Figure 8, including the rain film of a constant width and the boundary layer of the bulk phase. The height of the simulated system is 10.6 *m* considering atmospheric pressure. As the aim of the study is to investigate the heat transfer through the tank wall, the bulk phase has a relatively small width of 430 *mm* to save computation time. The initial temperature of the bulk was 306.5 *K*. For top and bottom, an inlet-outlet boundary condition for velocity and temperature is assumed. From the bulk phase to the wall, a no slip condition is applied. The tank wall, with a width of 5 *mm* has the initial temperature of the bulk phase and a zero-gradient boundary condition for temperature on top and bottom. The rain film has a constant width of 2 *mm* over the height of the tank, an initial temperature of 287.5 *K* and an initial velocity of 0.37 *m/s* at the inlet at the top. The velocity was calculated with the Reynolds approach due to the assumption of a constant rain intensity of 65 kg/m^2h. On the bottom, the inlet-outlet boundary condition is applied.

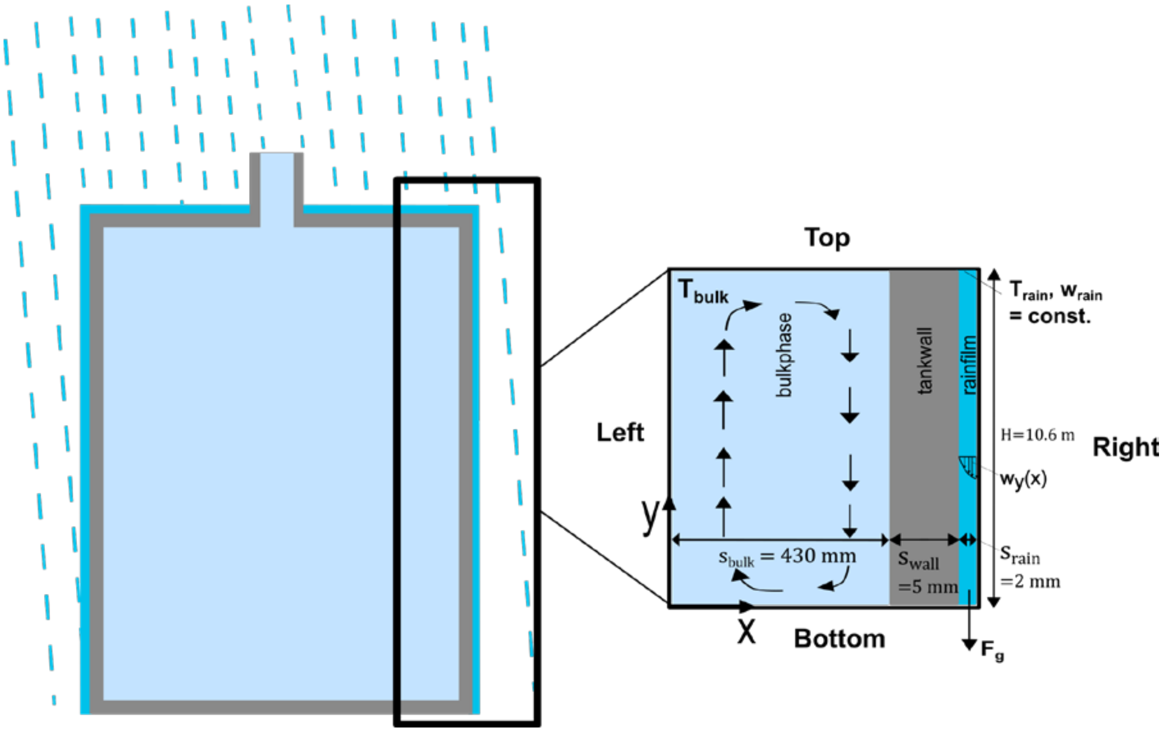

Figure 8. Simulation setup.

On purpose of saving calculation time, a grid study on a small section of 0.5 *m* height was performed. The results are depicted in Figure 9 and 10.

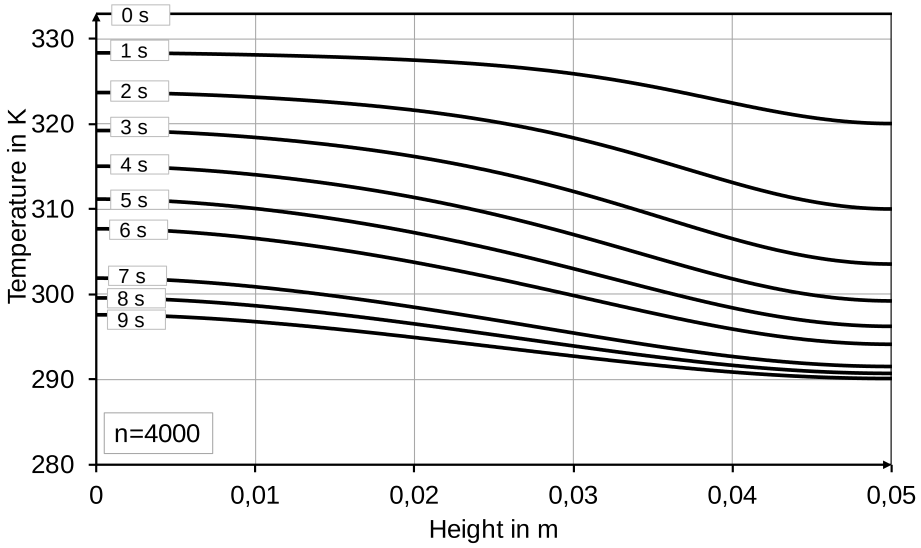

Figure 9. Temporal cooldown of the wall surface inside the tank over the tank height.

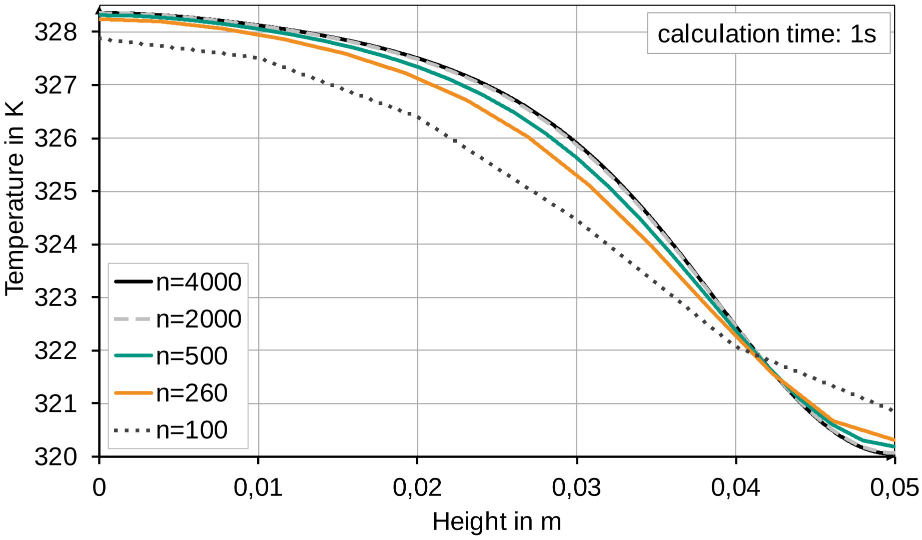

Figure 10. Grid study on the cooldown of the wall surface over the tank height at a simulation time of 1 s.

The grid study was performed using 100 cells per meter in x-direction and varying 4000 to 100 cells per meter in y-direction. The maximum deviation between 4000 cells and 100 cells is 1.51 *K* that corresponds to 0.46%. For further calculations of the heat transfer between bulk, wall and rain, the number of grid points in y-direction was set to 260 cells per meter what complies with an error of 0.19%.

The focus of the simulation is on the calculation of the heat transfer coefficient between bulk and wall and rain. In figure 11 the development of the heat transfer coefficients between the bulk, the wall and the rain are displayed.

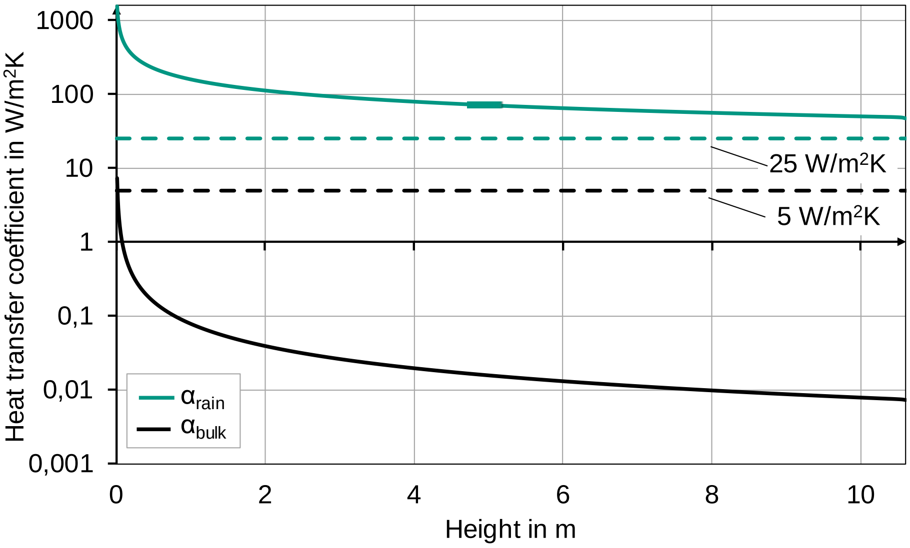

Figure 11. Heat transfer coefficients of rain, bulk and the tank wall over the tank height.

As expected, the heat transfer from the rain film to the ambience is slightly higher than in the bulk phase. Starting at 1565 W/m^2K at the tank bottom, the heat transfer coefficient decreases to 48 W/m^2K on the top. Literature models assuming a heat transfer coefficient of 25 W/m^2K (Fullartion et al., 1987, Moncalvo et al., 2016), underestimate heat transfer by 48%. In the bulk phase, the heat transfer coefficient starts at 7 W/m^2K and drops to 0.007 W/m^2K. With a condensation film on the inside of the tank, the heat transfer from the bulk to the condensation film is on the same scale as the heat transfer coefficients at the outer surface and the heat flux increases. Considering heat conduction through the film, the heat flux is even higher. Therefore, it is questionable if the assumption of a heat transfer coefficient of 5 W/m^2K (Fullartion et al., 1987, Moncalvo et al., 2016) and the neglection of the heat conduction through the condensate film is always conservative.

On heat conduction, further investigation is needed in future work. Subsequent these simulations will be extended with a pressure gradient from the depression of the weather change and the emptying and filling process of tanks.

8 Conclusion and Outlook

The results have shown, that many phenomena regarding inbreathing of storage tanks have neither been considered in common calculation models nor in the standards. As this study and the research of multiple authors of (Fullarton et al., 1987, Holtkoetter et al., 1997, Moncalvo et al., 2016) demonstrate, condensation has a major impact on the inbreathing volume flow rate. The models in the standards (API 2000 - American Petroleum Institute, 2014 or DIN EN ISO 28300 - Deutsches Insitut fuer Normung, 2012) are derived for non-condensable tank content and are therefore not conservative or applicable to tanks containing condensable vapours.

A large disadvantage of the literature models is, that the condensation mass flux is included in the mass balance though, but the heat transfer is calculated with the assumption of a dry wall by considering a heat transfer coefficient of 5 W/m^2K and a neglection of heat conduction (Moncalvo et al., 2016 and Fullarton et al., 1984). For non-condensable gases in the tank, this assumption is sufficiently conservative, as to be seen from figure 11, black line. For condensable vapours the heat transfer coefficient is increased considering a condensation flow at the tank wall. The heat transfer is then in the same magnitude as the rain film in figure 11, green line. Film dynamics like the shape of the film, flow effects or heat conduction might increase the heat flux through the tank wall significantly und shall therefore be investigated in further studies. In Fullarton's model, the assumption of equality between the bulk and ambience temperature in the mass balance seems to be unrealistic when it comes to sudden weather changes.

Film condensation but also fog formation has major impact on inbreathing as shown in figure 2 and 3 and the work of Holtkoetter et al. (Holtkoetter et al., 1997) for small laboratory equipment of 1.18 m^3. The transferability of the assumptions and observations to large storage tanks has to be verified in prospective measurement campaigns. Thus, further investigation on the entrainment of inbreathed air and turbulence effects causing local non-equilibrium in the bulk phase is needed, to understand the promotion of fog formation inside the tank. The governing effect of heterogeneous condensation due to particles in the inbreathed air is not yet considered and should be taken into account. Thus, with the information given in Holtkoetter and Sigel, it is hardly possible to simulate the measurement conditions, accurately, because of many uncertainties and inconsistencies. Therefore, new measurement campaigns are necessary.

All models mentioned above are derived for single components, predominantly water and air. In industry, liquids like naphtha, gasoline or other multi components are stored in those tanks. The impact of mixing properties on inbreathing and the transferability to common breathing models needs to be validated. Currently there is no multi component model published in literature. The influence of those effects shall be verified in subsequent models.

All the different conditions of breathing will be coupled as overall model in the new CFD approach ARTEM (advanced reactor and storage tank emission model). Regarding the overall model, some inbreathing phenomena, e.g. the boundary layer at the tank wall, drops and particles inside the tank or the rain film on the outer surface, cannot be resolved in sufficient detail on purpose of computational costs. Therefore, a multi scale approach must be developed to enable the coupling of the phenomena described in chapter 2. The model is currently under development and will be validated with especially designed measurements on a storage tank with a volume of 200 m^3. Lastly, the environmental aspects, like the formation of a rain film, wind flow and other local aspects need to be defined in a standardized way for a reliable and detailed modelling of breathing phenomena.

Acknowledgements

We would like to thank the Braunschweiger Flammenfilter GmbH for funding this research project. In addition, we would like to thank Markus Stueven and Kathi Heithausen for supporting the work within their master thesises.

Nomenclature

A	$[m^2]$	tank shell surface
a	$[m^2/s]$	thermal diffusivity
$c_{p_{cond}}$	$[J/kgK]$	specific heat capacity condensate
$c_{p_{wall}}$	$[J/kgK]$	specific heat capacity tank wall

$c_{p_{air}}$	$[J/kgK]$	specific heat capacity air
$c_{p_{vap}}$	$[J/kgK]$	specific heat capacity vapor
F_g	$[N]$	gravity force
$\dot{H}_{air}$	$[J/s]$	enthalpy flux air
$\dot{H}_{cond}$	$[J/s]$	enthalpy flux film condensate
$\dot{H}_{cond,sp}$	$[J/s]$	enthalpy flux fog
H/D	[-]	height to diameter ratio of the tank
h	$[W/m^2]$	specific enthalpy of the fluid phase
K	$[m^2/s^2]$	kinetic energy of the fluid phase
k_{in}	$[W/m^2K]$	heat transfer coefficient bulk to wall
M_{air}	$[kg]$	air mass inside the tank
M_{cond}	$[kg]$	film condensate mass
$M_{cond,sp}$	$[kg]$	fog mass
M_{vap}	$[kg]$	vapor mass inside the tank
p	$[Pa]$	pressure in the fluid phase
$Q_{v,air}$	$[m^3/hr]$	inbreathed air volume flow rate
$Q_{v,cond}$	$[m^3/hr]$	film condensate volume flow rate
$Q_{v,cond,sp}$	$[m^3/hr]$	fog volume flow rate
$\dot{Q}_{out}$	$[J/s]$	heat flux from bulk to wall
s_{bulk}	$[K]$	bulk thickness in the CFD simulation setup
s_{rain}	$[K]$	rain film thickness
s_{wall}	$[K]$	tank wall thickness
T_{amb}	$[K]$	ambient temperature
T_{bulk}	$[K]$	bulk temperature
T_{cond}	$[K]$	condensate temperature
T_{rain}	$[K]$	rain temperature
T_{wall}	$[K]$	tank wall temperature
t	$[s]$	time
U_{bulk}	$[J/s]$	bulk internal energy
V_{bulk}	$[m^3]$	bulk volume
w	$[m/s]$	rain film velocity
x, y, z	$[m]$	directions of the coordinate system
$\Delta h_{v,cond}$	$[J/kg]$	specific vaporisation enthalpy of the condensate
α_{air}	$[W/m^2K]$	heat transfer coefficient from bulk to the tank wall
α_{rain}	$[W/m^2K]$	heat transfer coefficient from rain film to the ambience
ρ_{air}	$[kg/m^3]$	density of air
ρ_{cond}	$[kg/m^3]$	density of the condensate
η	$[Pa\ s]$	dynamic viscosity

References

el Abbassi, M. ; Lahaye, D. J. P.; Vuik, C.: *Modelling turbulent combustion coupled with conjugate heat transfer in OpenFOAM,* Conference Paper from MCS 10, Neaple, Italy (2017).

Abou-Chakra, D.: *Dynamic Modeling of Inbreathing Requirements for Low-Pressure Storage Tanks,* Master of Science, Northeastern University, Boston, Massachusetts, (2016).

American Petroleum Institute: Venting Atmospheric and Low-pressure Storage Tanks. API STANDARD 2000 (2014).

Cronin, K. and Davies, M.: Analysis of the variability in collapse time of a process storage vessel due to internal steam condensation. *Proceedings of the Institution of Mechanical Engineers, Part E: Journal of Process Mechanical Engineering*, vol. 222, no. 3 (2008), pp. 171–181.

DIN Deutsches Institut für Normung e. V.: Erdoel-, petrochemische und Erdgasindustrie – Be- und Entlueftung von Lagertanks mit atmosphaerischem Druck und niedrigem Ueberdruck (ISO/DIS 28300:2011). Deutsche Fassung EN ISO 28300:2011 (Februar 2012), no. 28300.

Ennis, T.: Pressure relief considerations for low-pressure (atmospheric) storage tanks. *IChemE Symposium 151,* (2006).

Foerster, H., Schampel K., and Steen H.: Atmungsvorgänge infolge von Witterungseinflüssen an Lagertanks für brennbare Flüssigkeiten. Physikalisch Technische Bundesanstalt (Technical Report), (1984).

Fullarton, D.: Sicherheitstechnische Ueberlegungen bei Atmungsvorgängen in Lagertanks - Einfluß der Kondensation von Produktdaempfen. *Chemie Ingenieur Technik*, vol. 58, no. 1 (1986), pp. 38–40.

Fullarton, D.; Evripidis, J. and Schluender, E.U.: Influence of product vapour condensation on venting of storage tanks. *Chemical Engineering and Processing: Process Intensification*, vol. 22, no. 3 (1987), pp. 137–144.

Goßlau, W.; Mueller, E.; Weyl, R.: Thermodynamische Grundlagen der Behaelteratmung aufgrund von Witterungseinflüssen," *Technische Ueberwachung*, vol. 1, no. 26 (1985), pp. 16–22.

Holtkoetter, T.; Shang, J. and Schecker, H.-G.: Behaelteratmung - Experimentelle Untersuchungen und Entwicklung eines Vorhersagemodells. *Chemie Ingenieur Technik*, vol. 69, no. 3 (1997), pp. 361–366.

ioMosaic Corporation, *SuperChems Expert™ component of Process Safety Office™*, (2015).

Moncalvo, D.; Davies, M.; Weber, R. et al.: Breathing losses from low-pressure storage tanks due to atmospheric weather change. *Journal of Loss Prevention in the Process Industries*, vol. 43 (2016), pp. 702–705.

Salatino, P.; Volpicelli, V. and Volpe, P.: On the Design of Thermal Breathing Devices for Liquid Storage Tanks. *Process Safety and Environmental Protection,* vol. 77, no. 6 (1999), pp. 354–359.

Sigel, R.: Auswertung der Tankabkühlungsversuche 1980 und 1981 im Werk Höchst. Technical Report (Hoechst AG), (1980).

Sigel, R.; Schwarz, H., Kuxdorf, B. et al.: Maximaler Volumenstrom bei der Abkuehlung von Festdachtanks. Technical Report (Hoechst AG), (1981).

Sigel, R.; Schwarz, H.; Kuxdorf, B. et al.: Praktische und theoretische Untersuchung der Beatmung von Festdachtanks. *Chemie Ingenieur Technik*, vol. 55, no. 5 (1983), pp. 377–379.

Address: Natalie Schmidt, M.Sc; CSE Center of Safety Excellence gGmbH, Joseph-von-Fraunhofer-Straße 9, 76327 Pfinztal, Germany
email: natalie.schmidt@cse-institut.de

Prof. Dr.-Ing. Jens Denecke, CSE Center of Safety Excellence gGmbH, Joseph-von-Fraunhofer-Straße 9, 76327 Pfinztal, Germany
email: jens.denecke@cse-institut.de

Prof. Dr.-Ing. Juergen Schmidt, CSE Center of Safety Excellence gGmbH, Joseph-von-Fraunhofer-Straße 9, 76327 Pfinztal, Germany
email: juergen.schmidt@cse-institut.de

Dr.-Ing. Michael Davies, Braunschweiger Flammenfilter GmbH, Industriestr. 11, 38110 Braunschweig, Germany
email: michael.davies@protego.com

DOI: 10.24352/UB.OVGU-2019-011

TECHNISCHE MECHANIK, 39, 1, (2019), 113 - 124
submitted: July 6, 2018

Numerical and Experimental Investigation of Flow in Partially Filled Sewer Pipes

M. Alihosseini, P.U. Thamsen

Complex phenomena in wastewater systems, such as flow pattern in sewers and sediment transport could be investigated in detail using computational fluid dynamics (CFD). However, it is not easy to find an appropriate CFD model for a specific problem. This paper aims to develop and validate a CFD model to correctly predict the free-surface turbulent flow passing through a circular pipe. In this study, the multiphase model Volume of Fluid (VOF) of the software Ansys-Fluent was used to capture the interface between air and water. Different variants of the k-ε turbulence model of the RANS group and meshing approaches were investigated. To validate the CFD model, a set-up of an acryl-glass pipe in a closed system was constructed under laboratory conditions. The centre-plane velocity profile was used to compare the CFD model results and Laser Doppler Velocimetry (LDV) measurements. Furthermore, the values of the average velocity and shear stress from the experiments were compared to the results of the CFD model. The best results were obtained using a Cutcell mesh combined with the RNG k-ε turbulence model. The validated model was used to investigate the influence of the bed roughness on the velocity and shear stress distribution in partially filled pipes. The velocity decreases while increasing the bed roughness, however the shear stress becomes greater over a rough bed than over a smooth bed.

1 Introduction

The complex process of flow and sediment transport in sewer systems has been investigated using in-situ measurements, laboratory experiments and numerical modelling. All of these methods have some shortcomings. In-situ measurements are mostly site-specific and are not predictive. The flow in the channel is non-stationary and unsteady, which prevents representing the measurements (Yan et al., 2014). In contrast, the laboratory experiments are more representative and precise. However, the results from the small-scale physical models are not always transferable to real complex systems. With increasing computational resources and advancements in numerical methods, computational fluid dynamics (CFD) provides a good alternative to investigate complicated phenomena in a less expensive and more flexible way. In the following, a review of the application of CFD concerning the simulation of sewer systems is briefly presented.

Schmitt et al. (1999) studied the bed load sediment traps in sewer systems using the Volume of Fluid (VOF) method of the software Ansys Fluent. The numerical results were in good agreement with previous empirical findings and led to a better design of sediment traps.

Berlamont et al. (2003) calculated boundary shear stresses for circular pipes with a flat-bed using CFD. They used experimental data from the literature to verify the CFD model of a package PHONICS. The *k-ε* turbulence model was used. The results were satisfying, although secondary currents were neglected, since they do not have significant influence on the shear stress distribution but rather on sediment transport.

He et al. (2004) studied the behaviour of flow and sediment in a combined sewer overflow (CSO) facility using CFD. They used the VOF and the Discrete Phase Method (DPM) of Fluent to investigate different flow fields and particle capture rates in order to assess flow conditioning baffles implemented in the CSO facility. They found CFD modelling as an attractive alternative for optimizing the existing CSO facilities.

Schaffner et al. (2004) studied the application of CFD for the calculation of flush waves in sewers using the software StarCD. VOF and the *k-ε* turbulence model were used. They concluded that the results of CFD lead to a better design and dimensioning of flushing devices. Kirchheim et al. (2005) used the same CFD package to calculate different scenarios for a flushing device used in combined sewers to avoid deposits and investigate the cleaning capacity. The parameters influencing the shear stress produced by flushing waves were numerically analysed.

Bardiaux et al. (2006) obtained the velocity profiles through a sewer channel using the software Fluent. They compared the *k-ε* and Reynolds Stress (RS) turbulence models as well as the monophasic approach obtained with the symmetry plane boundary condition and the VOF method. The comparison with the experimental data showed that RSM and VOF together could accurately simulate the water behaviour in open channels. The anisotropic RS model could represent the secondary currents better than the isotropic *k-ε* model.

Bares et al. (2006) verified a 3D CFD model of Fluent to obtain the flow pattern of a combined sewer overflow. The free surface was simulated as a wall without friction and the standard k-ω turbulence model was chosen as the best suited model. They used the Ultra Doppler Method (UDM) to visualize the 2D flow field and compared the results with numerical results. The time-averaged velocity flow field could be obtained in a good way.

Bardiaux et al. (2008) used VOF combined with the RS turbulence model to simulate turbulent flows to improve sewer net instrumentation. They modelled different flows in rectangular, circular and egg-shape sections. The method presented allows determining the local velocity of a flow in any point of a cross section.

Jarman et al. (2008) reviewed the application of CFD in modelling of urban drainage systems. In all of the reviewed studies, the flow was assumed to be turbulent and the RS or k-ε turbulence models were used. They found the VOF approach very accurate in simulating the free surface, but computationally expensive. The review showed that by growing the computational resources, CFD is becoming increasingly utilized as part of larger simulation schemes for multi-physical systems.

Dufresne et al. (2009) studied the flow, sedimentation and solids separation in a combined sewer detention tank using Fluent. They used the particle tracking facility of the software to study the location of the deposited particles and the pollutant load. Agreeable results showed that CFD is a good way to model sediment transport in sewer systems.

Chen et al. (2013) developed a 3D numerical model for optimizing design changes of a combined sewer system. The VOF method and the RNG k-ε turbulence model were used to simulate the turbulent free surface. A particle tracking approach was used to model the behaviour of suspended solids. They concluded that CFD is effective in designing a combined sewer system to reduce pollutant discharge into the receiving waters.

Bonakdari et al. (2015) numerically studied the minimum velocity required to prevent sediment deposition in sewer systems. They simulated a three phases flow (water, air, sediment) in a circular pipe using the k-ε turbulence model of Ansys-CFX. The modelled longitudinal velocity profile pattern of flow and volumetric sediment concentration were in good agreement with the experimental data.

Mohsin and Kaushal (2016) used VOF and DPM of Fluent to predict the efficiency of an invert trap. They commented that the realizable k-ε turbulence model is an appropriate choice for transferring turbulence among the phases.

Regueiro-Picallo et al. (2016) analysed the open channel flow in egg-shaped pipes for small combined sewer systems using the Ansys CFX 3D model. The VOF model was used to track the interface between water and air. The shear stress and velocity profiles obtained from the CFD model were in good agreement with the experimental results.

However, there are limited studies investigating the behaviour of flow in a partially filled circular pipe using CFD. Compared to the velocity distribution in the full-filled pipe flow, the velocity distribution in a partially filled pipe has been less researched (Jiang et al., 2016). Due to the fact that the free surface is always changing with time and space, it is much more difficult to model the flow in open channels. Most of the studies investigating the flow in open channels have been done in prismatic channels, which make the calculations simpler. It is very difficult to investigate the velocity distribution along the width of an open channel theoretically (Gandhi et al., 2010).

This study aims to develop a CFD model to predict the free-surface turbulent flow in a circular pipe. The investigations have examined the influence of grid size, structure and turbulence model. After obtaining the best suited CFD model, this model is used to investigate the influence of the bed roughness on flow behaviour in open channels.

2 Materials and Methods

2.1 Laboratory Experiment

To validate the CFD model, in the laboratory of the Chair of Fluid System Dynamics of the Technische Universität Berlin, a set-up of an acryl-glass-pipe in a closed system was constructed. The model consists of a 6000 *mm* long circular pipe with an internal diameter (d) of 342 *mm*. At the beginning of the pipe, an inlet tank and at the downstream, a collecting tank are placed. Figure 1 shows the experimental set-up. The bed slope S_0 is variable; it is 0.37% for this study.

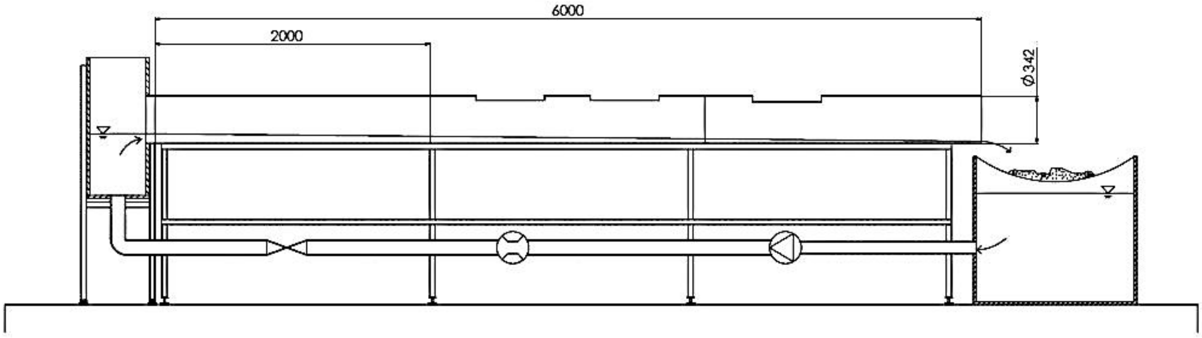

Figure 1. Construction of the experimental set-up (in *mm*)

The values of discharge (Q) were obtained using an MID flowmeter (Krohne Altometer SC 80 AS) and a compact echo sounder (NivuCompact Echolot) was used to determine the water height (h). The average flow velocity (V) and shear stress over the wetted perimeter (τ) can be expressed using the experimental data as follows:

$$V = \frac{Q}{A} \tag{1}$$

$$\tau = \rho g R_h S_f \tag{2}$$

where A is the cross-sectional area of flow which is dependent on the opening angle of the water (θ) and the radius of the pipe (r), ρ is the fluid density, g the gravitational acceleration and R_h is the hydraulic radius. In practice, the energy slope S_f is often replaced by the bed slope S_0. The parameters of the partially filled flow in a circular cross section are shown in Fig. 2.

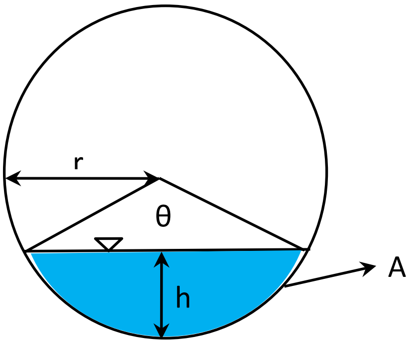

Figure 2. Partially filled flow in a circular cross section

Three experiments were conducted with different flow rates. All experiments were carried out over a smooth bed in turbulent and subcritical flow regimes. The Reynolds number (Re) was greater than 35000 and the Froude number (Fr) less than 1. The Reynolds number and the Froude number were calculated using the equations (3) and (4), respectively:

$$Re = \frac{VD_h}{\nu} \tag{3}$$

$$Fr = \frac{V}{\sqrt{hg}} \tag{4}$$

where D_h is the hydraulic diameter and ν is the kinematic viscosity.

Furthermore, the centre-plane velocity profiles were measured using Laser-Doppler-Velocimetry (LDV) at a distance of 3200 *mm* from the pipe inlet. The measurement section was selected at this point to ensure a uniform flow condition. LDV is a widely accepted and used tool for fluid dynamical investigations of gases and liquids. It is a well-established technique that gives information about the flow velocity.
Table 1 shows the characteristics of the three experiments.

Test	**I**	**II**	**III**
***Q* [*l/s*]**	2.5	3.5	4.5
***h* [*mm*]**	33	40	45
Re	35333	44764	54117
Fr	0.97	0.93	0.95

Table 1. Variable parameters from the experiment

2.2 CFD Simulation

For the numerical part of this study, the geometry consisted of the inlet tank and the pipe. The geometry should be discretized in meshes, in which the equations will be calculated. Here, a Cutcell mesh is compared to a mesh of tetrahedral elements. Using tetrahedral elements has the advantage that the mesh of the complex domain, consisting of cubes and cylinders, can be generated more easily. However, the same element size results in much more grid cells in a tetrahedral mesh compared to the Cutcell mesh. On the other hand, a Cutcell mesh can capture the interface between air and water more accurately. The CutCell mesher converts a volume mesh into a predominantly Cartesian mesh, which consists of mostly hexahedral elements with faces that are aligned with the coordinates axes. Fig. 3 shows the Tetrahedral and the Cutcell mesh. The mesh should be fine enough to capture the features of the flow. In general, the finer the mesh the more accurate are the results, but also the longer is the calculation time. Therefore, it is important to find a balance between the number of elements and the accuracy of the results. The refinement of the mesh should be done until the solutions from two meshes do not differ significantly. To obtain a sufficient mesh resolution at the wall, the values of y^+ are observed. Ansys Fluent user's guide (2016) suggests that the standard wall function should exhibit a y^+ value between 30 and 300, whereby a value close to the lower bound is most desirable. The here investigated meshes exhibit y^+ values between 40 and 195 near the wall in the measurement section. In addition, the skewness and the orthogonal quality of the mesh are considered to check its quality. The maximum skewness should be less than 0.97 and the minimum orthogonal quality more than 0.01 (Ansys, 2016). Table 2 summarizes the three investigated meshes in this study.

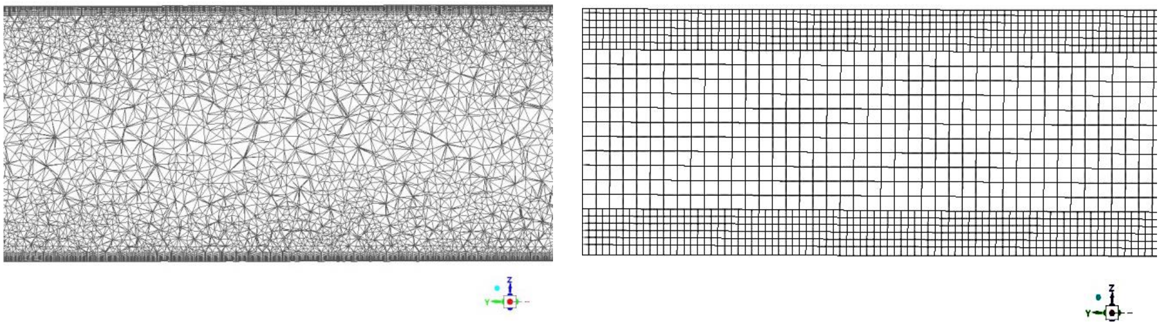

Figure 3. Tetrahedral mesh (left) and Cutcell mesh (right) in the middle cut plane

Mesh	**Elements**	**Maximum skewness**	**Minimum orthogonal quality**
Tetrahedral	2890604	0.9	0.09
fine Cutcell	1426914	0.95	0.28
coarse Cutcell	376097	0.78	0.33

Table 2: Summary of investigated meshes

The mostly used and validated multiphase solver Volume of Fluid (VOF) is used to simulate the interaction of air and water in partially filled pipes. VOF is able to describe the deformation of the free surface very well and therefore has been used successfully by a lot of researchers (Schmitt et al., 1999; He et al., 2004; Schaffner et al., 2004; Kirchheim et al., 2005; Bardiaux et al., 2006; Bardiaux et al., 2008; Chen et al., 2013; Mohsin and Kaushal, 2016; Regueiro-Picallo et al., 2016; Gandhi et al., 2010). VOF can model two or more immiscible fluids by solving a single set of momentum equations and tracking the volume fraction of each of the fluids throughout the domain. In each computational cell, the volume fractions of all phases sum to unity. The volume-averaged values in each cell are either representative for one phase or for a mixture of the phases. The mixture density (ρ_{mix}) concept in VOF for a domain containing water and air is as follows:

$\rho_{mix} = \rho_{air}, \alpha_{air} = 1, \alpha_{wat} = 0$ (The cell is empty of water)

$\rho_{mix} = \rho_{wat}, \alpha_{wat} = 1, \alpha_{air} = 0$ (The cell is empty of air)

The density of the gas-liquid mixture fluid (at the interface of water and air) is:

$$\rho_{mix} = \alpha_{air}\rho_{air} + \alpha_{wat}\rho_{wat} \tag{5}$$

where ρ_{air} and ρ_{wat} are the density of the air and water, respectively. α_{air} and α_{wat} are the volume fraction of air and water, respectively.

The continuity equation for the volume fraction of the secondary phase (here air) neglecting the mass source has the following form:

$$\frac{\partial}{\partial t}(\alpha_{air}\rho_{air}) + \nabla(\alpha_{air}\rho_{air}V_{air}) = 0 \tag{6}$$

The volume fraction equation will not be solved for the primary phase (here water). The primary phase volume fraction is computed based on $\alpha_{air} + \alpha_{wat} = 1$.

The momentum depends on the volume fractions of the phases through ρ and μ and is calculated as follows:

$$\rho\frac{\partial V}{\partial t} + \nabla.(\rho VV) = \nabla.[\mu(\nabla V + \nabla V^T)] - \nabla p + \rho g \tag{7}$$

where ρ is the fluid density, V is the fluid velocity, μ is the dynamic viscosity, p is the pressure and ρg is the gravitational body force. Only one set of momentum equations will be solved for the mixture fluid and the resulting velocity is shared among the two phases. Turbulence is also the same as in single phase flows. A single set of transport equations will be solved and the turbulence variables (here *k* and *ε*) are shared by the phases throughout the field.

The choice of the turbulence model is dependent on several factors such as the physics of the flow, the available computational resources and time for the simulation, the required accuracy, etc. Therefore, different turbulence models have been investigated. The Reynolds-averaged Navier-Stokes (RANS) approach reduces the required computational effort and resources and is widely adopted for practical engineering applications. The *k-ε* model of the RANS group is the most widely used and validated turbulence model (Stovin et al., 2002). The model is based on the Boussinesq assumption that Reynolds Stresses can be linked to the mean rates of fluid deformation. The *k–ε* model uses two quantities, the turbulent kinetic energy, *k*, and its rate of dissipation per unit mass, *ε*, to calculate the eddy viscosity. There are three variants of the *k-ε* model available in Fluent: standard, realizable and RNG, which require more computational effort respectively. They differ in:

- the method of calculating turbulent viscosity
- the turbulent Prandtl numbers governing the turbulent diffusion of *k* and *ε*
- the generation and destruction terms in the *ε* equation

The theory behind these models is well descried in Ansys Fluent Theory Guide (2016). In this study, the three variants are investigated and compared with each other. In all cases the standard wall function is selected. Table 3 summarizes different CFD models used in this study. Other turbulence models available in the Fluent package like the Reynold stress model (RSM) could give more accurate predictions for complex flows and particularly for the effects of the secondary flow. However, they are not as well validated as the k-ε model. Furthermore, in circular channels where the secondary flow is more of a result of the geometrical shape than of the turbulence, the k-ε model could more accurately predict the flow than the RS model (Knight et al., 2005).

Model	Mesh	Turbulence model
1	Tetrahedral	*k-ε* standard
2	fine Cutcell	*k-ε* standard
3	coarse Cutcell	*k-ε* standard
4	coarse Cutcell	*k-ε* RNG
5	coarse Cutcell	*k-ε* realizable

Table 3. Summary of investigated CFD models

The boundary conditions and the solution methods are set based on experiences and suggestions of the ANSYS User's Guide. At the inlet, a mass flow inlet is selected for the liquid phase with mass flow rates from the experimental data and zero for the gas phase. The turbulent intensity and viscosity ratio have been set to remain at 5% and 10, respectively at the inlet as well as at the outlet. The open top of the inlet tank and the outlet of the pipe have a pressure outlet boundary condition. The backflow value of the volume fraction is 1 for the gas phase. For the wall boundary conditions, the no-slip wall condition is used. Fig. 4 shows the computational domain and the boundary conditions.

Based on the implicit scheme for VOF, the following solution methods are selected: The PISO algorithm for the pressure-velocity coupling, the PRESTO discretization for pressure and Second Order Upwind for momentum. The interface between fluids is represented with the Modified HRIC scheme, because when calculating implicitly, all other discretization schemes will normally lead to numerical diffusion. The First Order Upwind scheme is selected for turbulent kinetic energy and turbulent dissipation rate.

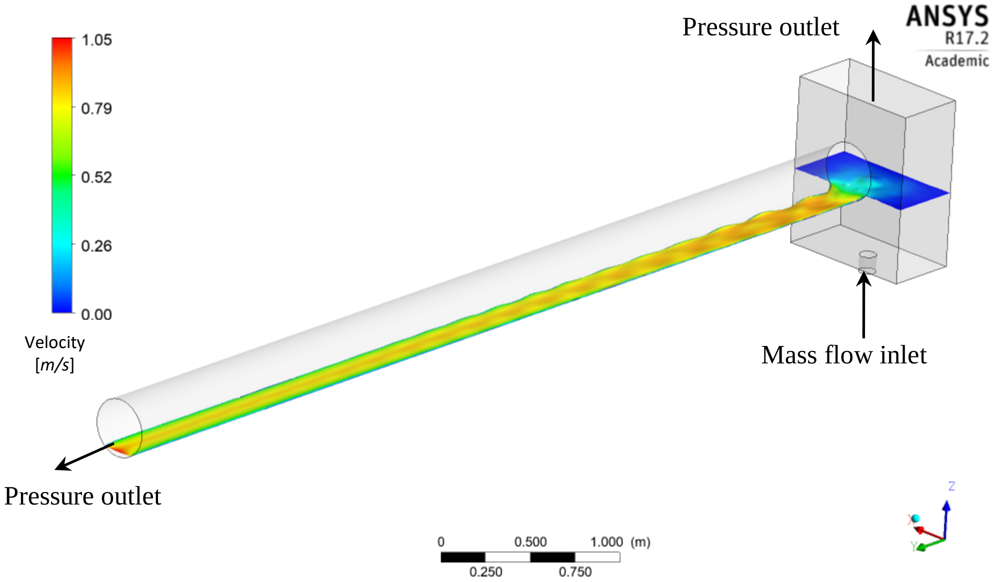

Figure 4. Sketch of the computational domain and the boundary conditions

3 Results and Discussion

3.1 Validation

First, the flow in the pipe with an inlet flow rate of 3.5 *l/s* is simulated. The CFD model centre-plane velocity profiles are compared with the LDV measurements at the middle-section of the pipe in a position of 3200 mm from the inlet. The comparison between the results of the first two models (Model 1 and 2) and the LDV measurements shows that the Cutcell mesh gives a better estimation of the centre-plane velocity profile. However, the mesh of tetrahedral cells was able to predict the values of the velocity in the near wall region. In the next step, the Cutcell mesh is coarsened (Model 3) and its velocity profile is compared to the model with a finer mesh (Model 2). Since there is no significant difference between the results and a coarser mesh leads to faster simulations, the coarser Cutcell mesh is selected as the best mesh. To choose the best turbulence model, three variants of the k-ε model are compared (Model 3, 4 and 5). The RNG model (Model 4) estimated the velocity profile with least error. Fig. 5 shows the comparison of the centre-plane velocity profile from the five CFD models and the LDV measurements.

Second, the Cutcell mesh and the RNG k-ε model (Model 4) are used to simulate the two other tests with flow rates of 2.5 and 4.5 *l/s*. Fig. 6 shows the comparison of the centre-plane velocity profiles simulated with Model 4 and LDV measurements of these two tests. As seen, the model was able to reasonably predict the velocity profile for different flow rates or rather different filling ratios in a circular pipe.

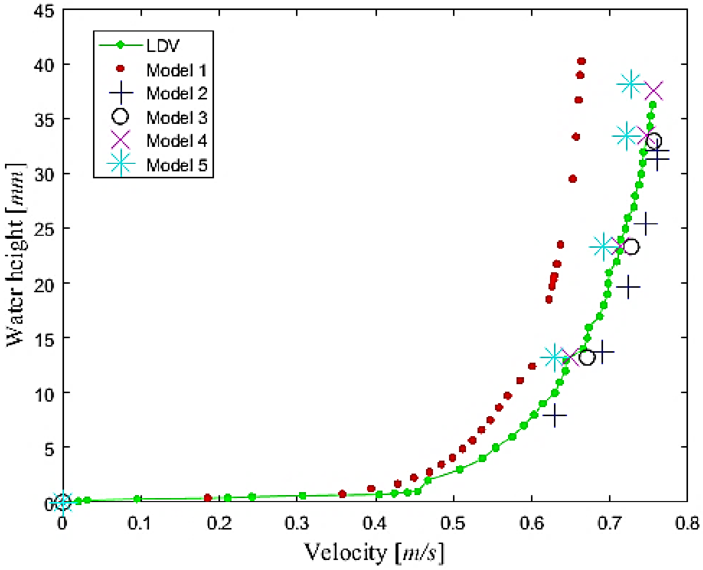

Figure 5. Experimental and numerical comparison of the centre-plane velocity profiles for an inlet flow rate of 3.5 *l/s* with different meshes and turbulence models

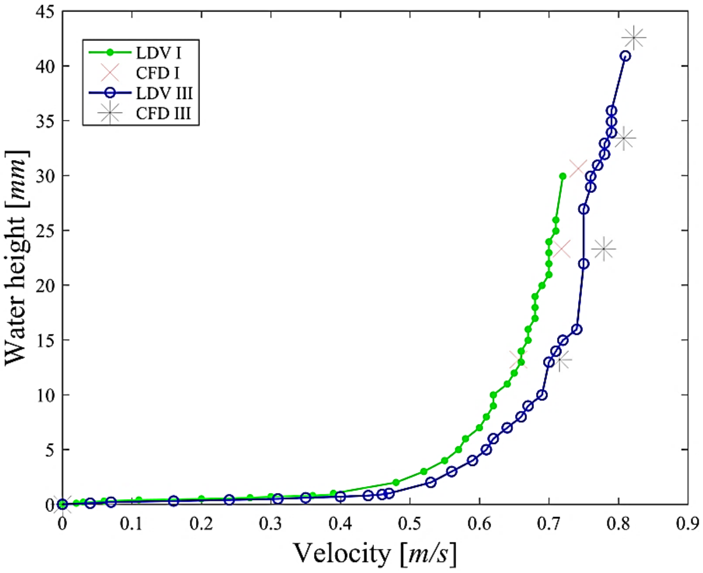

Figure 6. Experimental and numerical comparison of the centre-plane velocity profiles for Test I and III with an inlet flow rate of 2.5 *l/s* and 4.5 *l/s*, respectively using Model 4

Furthermore, the average velocity and shear stress over the wetted perimeter are used in order to validate the best model (Model 4) for three different flow rates. Table 4 shows the values of the experimental and numerical velocity and shear stress as well as the relative error between these two data sets. It is noticeable that the CFD model overestimates the values of the velocity. This could be explained by the fact that the k-ε model delivers better results for near free surface flows rather than flows close to the wall. Therefore, the small velocity values near the wall may not be very well estimated, which causes an overestimation of the mean velocity. Another alternative could be the Shear Stress Transport (SST) turbulence model which is a combination of the k-ε and k-ω turbulence models. The k-ω model is better suited for near wall regions. It was not possible within the frame of this work to test this model. On the other hand, this model underestimates the values of the shear stress. The reason could be that the experimental shear stress is an estimation of the average shear stress in the pipe. However, the value of the shear stress from the CFD model is the mean shear stress on a selected cross section. By the way, the relative error between experimental and numerical values is not more than 10% (except for V in test I).

Test	V_{EXP} **[m/s]**	V_{CFD} **[m/s]**	τ_{EXP} **[Pa]**	τ_{CFD} **[Pa]**
I	0.55	0.61	0.76	0.70
II	0.58	0.63	0.91	0.84
III	0.63	0.68	1.02	0.98

	Error V [%]	Error τ [%]
I	10.90	-7.89
II	8.62	-7.69
III	7.94	-3.92

Table 4. Comparison of the values of mean velocity and shear stress from experiment (EXP) and CFD

3.2 Velocity

As the bed roughness plays a major role in sediment transport in sewers, the validated CFD model is used to investigate its influence on the flow behaviour. Three different values for the roughness height are simulated and compared together for the same discharge (3.5 *l/s*) and bed slope (0.37 %); Smooth bed (k_s = 0), medium coarse bed (k_s = 0.5 *mm*) and rough bed (k_s = 1 *mm*) which represent plastic, concrete and stoneware as the sewer bed material, respectively. Fig. 7 shows the velocity contours on a wetted cross section with different roughness heights. The average velocity on the smooth bed is 0.63 *m/s*, on medium coarse bed 0.54 *m/s* and on the rough bed 0.49 *m/s*.

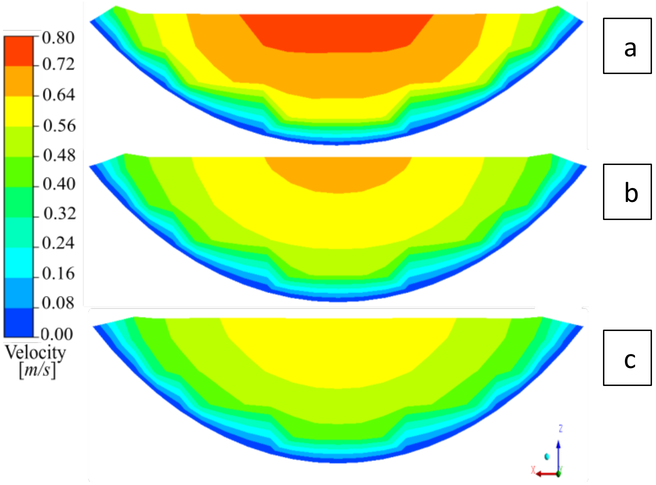

Figure 7. Longitudinal velocity contours on wetted cross section for (a) k_s = 0, (b) k_s = 0.5 *mm* and (c) k_s = 1 *mm*

In addition, the centre-plane velocity profiles are plotted against the water height. Fig. 8 shows the comparison for three different bed roughness heights. In the near wall region, the difference is not significant. However, the difference becomes greater with increasing water height. In the free-surface region, it is easy to see that the bed roughness has a great influence on the velocity profiles in the pipe. From the Figs. 7 and 8, it can be concluded that the velocity decreases while increasing the bed roughness, especially in the free surface region.

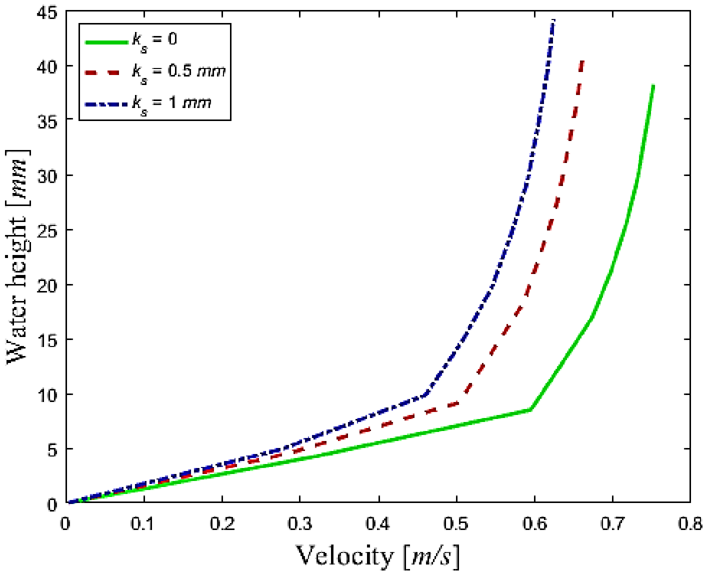

Figure 8. Numerical comparison of centre-plane velocity profiles for an inlet flow rate of 3.5 *l/s* and bed roughness of 0, 0.5 and 1 *mm*

3.3 Shear Stress

Simulated boundary shear stress distributions are plotted as a function of the lateral distance from the centre-plane for three different flow rates (Fig. 9) and three different roughness heights (Fig. 10). The *x*-axis represents the distance along the wetted perimeter of the pipe. It is visible in the figures and also concluded by (Knight and Sterling, 2000) that the shear stresses on the bottom of the channel are larger than the shear stresses on the walls. As shown in Fig. 9, increasing the flow rate leads to higher values for the shear stress. It can be observed that the distribution of the shear stress becomes more uniform by increasing the filling ratios. This is due the fact that, when the pipe is running full, the shear stress on any section of the boundary is constant. For higher flow depth ratios, the shear stress reaches its maximum value (1.2 *Pa* for 4.5 *l/s*) in the centre of the pipe; while for lower flow depth ratios, this maximum (1.05 *Pa* for 3.5 *l/s* and 0.83 *Pa* for 2.5 *l/s*) is reached in two symmetrical points of the wetted perimeter. The existence of two maxima on either side of the centreline in an open channel flow indicates the presence of secondary flows, which draws high momentum fluid away from the channel centre towards the corners. However, the strength of the secondary currents decreases with an increase in depth (Hoohlo, 1994). That’s why for higher flow rates, the maximum occurs in the centre. In addition, it is to be seen that the distribution becomes less uniform by increasing the roughness height. The shear stress on the bottom increases up to 20% while increasing the bottom roughness height by 1 *mm*.

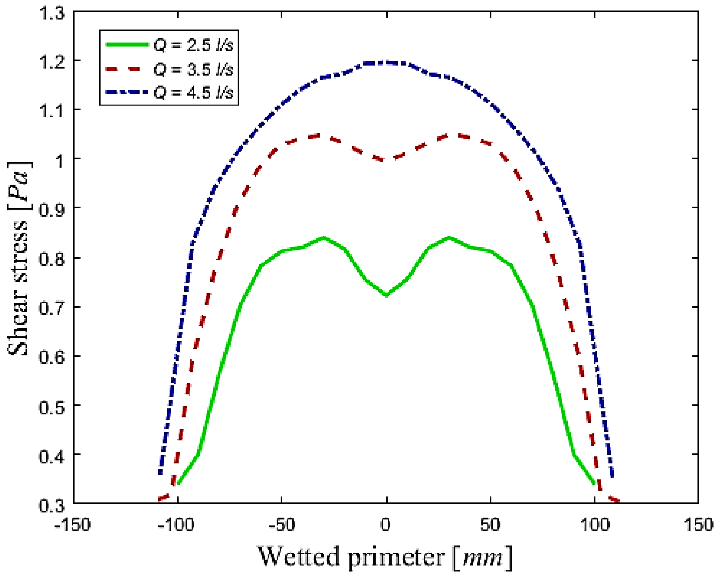

Figure 9. Boundary shear stress distribution in a cross section for different flow rates under smooth bed conditions

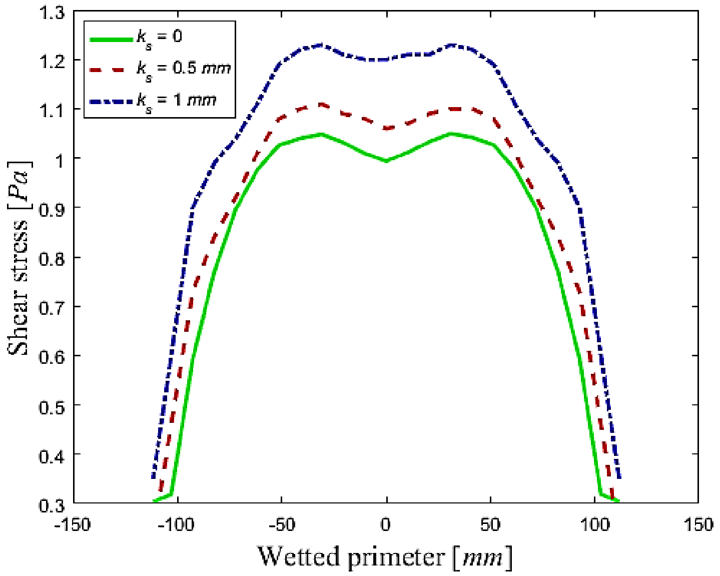

Figure 10. Boundary shear stress distribution in a cross section for different roughness heights with a flow rate of 3.5 *l/s*

4 Conclusions and Future Works

The aim of this study was to investigate various mesh approaches and turbulence models for the simulation of the flow in a partially filled pipe. A mesh of tetrahedral elements and two Cutcell meshes were compared. Additionally, three variants of the k-ε model were studied. The centre-plane velocity profiles obtained with different CFD models were compared to LDV measurements. The best results were obtained from a Cutcell mesh combined with the RNG k-ε turbulence model. Furthermore, the mean velocity and shear stress of experimental results were compared to the values of the best CFD model. The relative error was under 10%. The validated CFD model was used to analyse the influence of the bed roughness on the velocity distribution in pipes. The velocity decreases while increasing the bed roughness, particularly in the free surface region. In addition, the distribution of the boundary shear stress was investigated under different flow rates and bed roughness heights. The distribution becomes more uniform as the flow rate increases and less uniform while increasing the bed roughness. The shear stress over the rough bed is larger than that over the smooth bed. The results showed that the CFD model could reasonably simulate the flow in open channels under different boundary conditions. This paper can be seen as a preliminary study for working on more complicated problems. The results of this study have been used for investigations on the modelling of sediment transport in sewer systems using a coupled method of CFD and Discrete Element Method (DEM). The first results of this study are presented in (Alihosseini and Thamsen 2018).

5 Acknowledgments

This work has been funded and supported by Climate-KIC. Climate-KIC is supported by the European Institute of Innovation and Technology (EIT), a body of the European Union.

References

Alihosseini, M.; Thamsen, P.U.: Experimental and numerical investigation of sediment transport in sewers. *5th Joint US-European Fluids Engineering Division Summer Meeting (FEDSM 2018 ASME)*, Quebec, Canada (2018).

Ansys: *Ansys Fluent User's Guide, Release 17.2.* Southpointe, Canonsburg, ANSYS, Inc. (2016).

Ansys: *Ansys Fluent Theory Guide, Release 17.2.* Southpointe, Canonsburg, ANSYS, Inc. (2016).

Bardiaux, J.B.; Bonakdari, H.; Larrarte, F.; Mose, R.; Vazaquez, J.: Velocity Profiles Through a Sewer Channel: Using CFD to Obtain Velocity Fields. *Dresdner Wasserbauliche Mitteilungen*, 32, (2006), 327-335.

Bardiaux, J.B.; Mose, R.; Vazquez, J.; Wertel, J.: Two Turbulent Flow 3D-Modelings to Improve Sewer Net Instrumentation. *11th International Conference on Urban Drainage*, Edingburgh, Scotland, UK, (2008).

Bares, V.; Pollert, J.; Srnicek, P.: Flow Pattern Visualization of Combined Sewer Overflow. *5th International Symposium on Ultrasonic Doppler Methods for Fluid Mechanics and Fluid Engineering*, Zürich, Switzerland, (2006), 25-28.

Berlamont, J.E.; Trouw, K.; Luyckx, G.: Shear Stress Distribution in Partially Filled Pipes. *Journal of Hydraulic Engineering*, 129, (2003), 697-705.

Bonakdari, H.; Ebtehaj, I.; Azimi, J.: Numerical Analysis of Sediment Transport in Sewer Pipe. *International Journal of Engineering (IJE)*, 28, (2015), 1564-1570.

Chen, Z.; Han, S.; Zhou, F.; Wang, K.; A CFD Modeling Approach for Municipal Sewer System Design Optimization to Minimize Emissions into Receiving Water Body. *Water Resources Management*, 27, (2013), 2053-2069.

Dufresne, M.; Vazquez, J.; Terfous; A.; Ghenaim, A.; Poulet, J.B. Experimental Investigation and CFD Modelling of Flow, Sedimentation, and Solids Separation in a Combined Sewer Detention Tank. *Computers & Fluids*, 38, (2009), 1042-1049.

Gandhi, B.K.; Verma, H.K.; Abraham, B.: Investigation of Flow Profile in Open Channels Using CFD. *IGHM.* IIT Roorkee, India, (2010), 243-251.

He, C.; Marsalek, J.; Rochfort, Q.: Numerical Modelling of Enhancing Suspended Solids Removal in a CSO Facility. *Water Qual. Res. J. Canada*, 39, (2004), 457-465.

Hoohlo, C.: *A Numerical and Experiemntal Study of Open-Channel Flow in a Pipe of Circular Cross-Section with a Flat Bed.* Doctoral Thesis: Newcastel University Library, (1994).

Jarman, D.S.; Faram, M.G.; Butler, D.; Tabor, G.; Stovin,V.R.; Burt, D.; Throp, E.: Computational Fluid Dynamics as a Tool for Urban Drainage System Analysis: A Review of Applications and Best Practice. *11th International Conference on Urban Drainage,* Edinburgh, Scotland, UK, (2008).

Jiang, Y.; Bin, L.; Chen, J.: Analysis of the Velocity Distribution in Partially-Filled Circular Pipe Employing the Principle of Maximum Entropy. *PloS ONE*, 11, (2016), 1-17.

Kirchheim, N.; Schaffner, J.; Oberlack, M.: Parameter study of a flush wave using numerical modeling. *10th Internationl Conference on Urban Drainage,* Copenhagen, Denmark, (2005).

Knight, D.W.; Sterling, M.: Boundary Shear in Circular Pipes Running Partially Full. *Journal of Hydraulic Engineering*, 126, (2000), 263-275.

Knight, D.W.; Wight, N.G.; Morvan, H.P.: *Guidelines for applying commercial CFD software to open channel flow.* http://www.nottingham.ac.uk/cfd/ocf/guidelines.pdf, (2005), 1-32.

Mohsin, M.; Kaushal, D.R.: 3D CFD Validation of Invert Trap Efficiency for Sewer Solid Management using VOF Model. *Water Science and Engineering*, 9, (2016), 106-114.

Regueiro-Picallo, M.; Naves, J.; Anta, J.; Puertas, J.; Suarez, J.: Experimental and Numerical Analysis of Egg-Shaped Sewer Pipes Flow Performance. *MDPI - Water*, 8, (2016), 1-9.

Schaffner, J.; Oberlack, M.; Kirchheim, N.: The Application of Numerical Modeling (3-D) for the Calculation of Flush Waves in Sewer Channels. *6th International Conference on Urban Drainage Modelling (UDM'04),* Dresden, Germany, (2004), 1-8.

Schmitt, F.; Milisic, V.; Bertrand-Krajewski, J.-L.; Laplace, D., Chebbo, G.: Numerical Modelling of Bed Load Sediment Traps in Sewer Systems by Density Currents. *Water Science and Technology*, 39, (1999), 153-160.

Stovin, V.R.; Grimm, J.P.; Buxton, A.P.; Tait, S.J.: Parametric Studies on CFD Models of Sewerage Structures. *Proc. 9th International Conference on Urban Drainage*, Portland, Oregon, USA, (2002), 1-15.

Yan, H.; Lipeme Kouyi, G.; Gonzalez-Merchan, C.; Becouze-Lareure, C.; Sebastian, C.; Barraud, S.; Bertrand-Krajewski, J.-L.: Computational Fluid Dynamics Modelling of Flow and Particulate Contaminants Sedimentation in an Urban Stormwater Detention and Settling Basin. *Environmental Science and Pollution Research*, 21, (2014), 5347-5356.

Address: Department of Fluid Mechanics, Faculty of Mechanical Engineering, Berlin University of Technology. Straße des 17. Juni 135, 10623 Berlin, Germany
email: m.alihosseini@tu-berlin.de

DOI: 10.24352/UB.OVGU-2019-012 TECHNISCHE MECHANIK, 39, 1, (2019), 125 - 137
submitted: July 6, 2018

Smoothed Particle Hydrodynamics for Navier-Stokes Fluid Flow Application

P. Sabrowski, S. Przybilla, F. Pause, L. Beck, J. Villwock, P. U. Thamsen

The aim of this publication is to introduce the particle based computational fluid dynamics (CFD) method smoothed particle hydrodynamics (SPH) and introduce an applicable and valid SPH implementation for practical cases. For this purpose, current research approaches are combined regarding performance and numerical stability.

The principles of the method, the mathematical basics and the discretization of the Navier-Stokes equations are clarified. Furthermore, the implementation of method-specific boundary conditions, wall, inlet and outlet, as well as several correction procedures and a surface tension setup into the present code framework are described.

The advantages and validity of the method are shown based on different cases. The free surface fluid behavior of a dam break is compared to experimental data of the time dependent water level of selected positions. A Karman vortex street is validated by its Strouhal number for different Reynolds numbers. The frequency of an oscillating drop is analysed and compared to the analytical solution.

The SPH is utilized for pipe flows influenced by a backward facing step and shows an expected qualitative flow field.

1 Introduction

The method smoothed particle hydrodynamics is particle based and has its origin in the applications of astrophysics (Gingold and Monaghan, 1977; Lucy, 1977). Today, it is efficiently applied for liquid flows. A frequently used form is the weakly compressible smoothed particle hydrodynamics (WCSPH). It treats fluids as stiff media and adds an equation of state.

Due to the meshfree properties, the main advantage of the method is the simple applicability to free surface flows, moving geometries and multiphase phenomena. Where classical CFD methods usually require dynamic remeshing, SPH benefits from its Lagrangian definition. Due to its high parallelization capability, it is well suited for high performance computing (Braun et al., 2017).

Nevertheless, SPH still has some deficiencies. Although there are several working approaches of modelling turbulence, it is still a present research topic. Another feature that is still in development is the variable resolution in predefined areas, as adaptive refinements. For the implementation splitting and merging algorithms are utilized. The most advanced approaches are given by Vacondio et al. (2016) and Chiron et al. (2017). In some cases, boundary conditions may cause undesired behavior, for instance penetrations in wall BCs or backflows for inlet and outlet BCs (Tafuni et al., 2017). Another aspect is the existing proof of convergence which only holds for regular distributed particles (Violeau, 2012).

Due to the efficient approximation of the Navier-Stokes equations, especially for free surface flows, SPH has its primary application fields in coastal flows and atomization processes, among others. A typical SPH application that stems from the advantages in simulating complex and moving geometries are gear boxes.

The goal of this work is to introduce an applicable and valid SPH tool for practical cases. Hence, the most promising results of the latest SPH research are combined regarding performance and numerical stability. For this purpose, latest open and wall boundary approaches are implemented into the present code framework and enhanced as well as numerical stabilizing methods.

This software framework, the utilized models and their advantages are expounded as a foundation for the subsequent work in the field of wastewater treatment. The simulation of waste water systems and optimization of pump stations regarding sedimentation is a research topic that stems from the EFRE funded project OPuS ("Optimization of pump stations due to the Simulation of Sedimentation Processes") at Beuth University of Applied Sciences.

2 Physical Model

The Lagrangian form of the Navier-Stokes equations is used to describe the fluid flow, with the mass balance in Eq. (1) and the momentum balance in Eq. (2)

$$\frac{d\rho}{dt} = -\rho\nabla\cdot\underline{v}, \tag{1}$$

$$\frac{d\underline{v}}{dt} = \frac{1}{\rho}\left(-\nabla p + \mu\nabla^2\underline{v}\right) + \underline{g}, \tag{2}$$

where ρ and p are density and pressure, $\underline{v}$ and $\underline{g}$ are velocity and gravitational acceleration. μ denotes the dynamic viscosity of the fluid.

Weakly compressible smoothed particle hydrodynamics (WCSPH) is often used to model incompressible fluids. For the weakly compressible behavior an equation of state is necessary. The Cole equation describes water as a stiff medium and is usually utilized in SPH (Monaghan, 1994)

$$p = \frac{\rho_0 c^2}{\gamma}\left(\left(\frac{\rho}{\rho_0}\right)^{\gamma} - 1\right) + p_0. \tag{3}$$

The material parameter γ is set to 7 for water (Cole, 1948). c is the speed of sound, ρ_0 the reference density and p_0 the background pressure. When acoustics can be neglected, an artificial speed of sound is often introduced. This allows the increase of the time step without degrading the quality of the result. Usually a change in density of 1% is permitted which leads to an artificial speed of sound ten times bigger than the maximum expected velocity. The letter can be derived by an educated guess or simpler analytical approaches such as Torricelli's law (Monaghan, 1992).

Modelling turbulence is a not yet a mature discipline using SPH. Next to costly direct numerical simulations (DNS), large eddy simulations (LES) were introduced to SPH (Adami et al., 2013; Dalrymple and Rogers, 2006). A more practical approach to industrial application involves Reynolds-averaged Navier-Stokes (RANS) models based on a first-order eddy viscosity closure (Violeau, 2004). A detailed overview of turbulence modelling in SPH was presented by Violeau and Rogers (2016).

An alternative approach is the incompressible smoothed particle hydrodynamics (ISPH) method were incompressible fluids and therefore divergence free velocity fields are handled. This introduces necessary iterative solving procedures (Cummins and Rudman, 1999).

3 Numerical Model

In 1992, Monaghan (1992) successfully applied SPH to fluid dynamics. The mesh-free method is based on smoothing physical fields and their gradients at defined particle positions.

Using the Dirac delta distribution δ, every value of a continuous function f can be described at a position $\underline{r}$ in Ω through the following convolution integral:

$$f(\underline{r_i}) = (\delta * f)(\underline{r_i}) = \int_{\Omega} f(\underline{r})\delta(\underline{r_i} - \underline{r})d\Omega, \qquad \forall\underline{r} \in \Omega \tag{4}$$

Thereby, the Dirac delta distribution holds the following characteristics:

$$\delta(\underline{r} - \underline{r_i}) = \begin{cases} \infty, & \underline{r} = \underline{r_i} \\ 0, & \underline{r} \neq \underline{r_i} \end{cases}, \tag{5}$$

$$\int_{\Omega} \delta(\underline{r})d\Omega = 1. \tag{6}$$

In SPH the Dirac delta distribution is approximated by the so-called kernel function w_h. It must satisfy specific requirements, see Eqs. (7) to (9). The third property limits interpolation consistency to an order of one (Violeau, 2012).

$$\lim_{h\to 0} w_h = \delta, \tag{7}$$

$$\int_{\Omega} w_h(\underline{r})d\Omega = 1, \tag{8}$$

$$w_h(\underline{r}) \geq 0, \qquad \forall \underline{r} \in \Omega. \tag{9}$$

The simplest kernel function is the Gaussian. The introduced solver on the other hand uses the Wendland kernel shown in Eq. (10) is used,

$$\begin{gathered} w_h\left(\underline{r}_{ij}\right) = w_h(r_{ij}) = \frac{\alpha_d}{h^d}\begin{cases}\left(1-\frac{r_{ij}}{2h}\right)^4\left(1+\frac{2r_{ij}}{h}\right), & \frac{r_{ij}}{h} \in [0,2] \\ 0, & else\end{cases} \\ \left(r_{ij} = \left\|\underline{r}_i - \underline{r}_j\right\|, \underline{r}_{ij} = \underline{r}_i - \underline{r}_j, \qquad i,j = 1,\dots,n\right), \end{gathered} \tag{10}$$

where d is the number of dimensions, h is the smoothing length, α_d is a dimension dependent constant factor (Wendland, 1995). The underlying interpolation procedure is demonstrated in Figure 1.

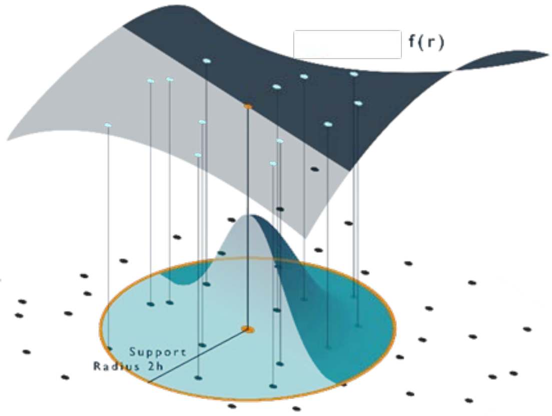

Figure 1. Reference and actual configuration of a binary mixture (Sabrowski et al., 2017)

The next step is the discretization of the integral in Eq. (4) through a Riemann sum. n is the number of particles, N the number of neighbour particles, m_j is the mass and ρ_j the density of neighbour particle j

$$[f]_d(\underline{r_i}) = \sum_{j=1}^{N} \frac{m_j}{\rho_j} f(\underline{r_j}) w_h(r_{ij}). \tag{11}$$

Applying the SPH methodology to the Navier-Stokes equations leads to a system of ordinary differential equations (ODE). For the discretization a representation of the gradient, divergence and Laplacian is required. To determine the gradient in the simplest SPH manner the interpolation described above is applied on the gradient of a sufficiently smooth function f. Together with partial integration the following identity holds

$$\nabla f(\underline{r_i}) = \int_{\Omega} \nabla f(\underline{r}) w_h(\underline{r_i} - \underline{r}) d\Omega = \int_{\partial\Omega} f(\underline{r}) w_h(\underline{r_i} - \underline{r}) \underline{n}(\underline{r}) d\Gamma \; - \; \int_{\Omega} f(\underline{r}) \nabla w_h(\underline{r_i} - \underline{r}) d\Omega \tag{12}$$

Assuming the point $\underline{r_i}$ is not close to $\partial\Omega$, the surface integral vanishes due to the compact support of w_h. With the identity $\nabla_i w_h(\underline{r_i} - \underline{r}) = -\nabla w_h(\underline{r_i} - \underline{r}\ )$ the gradient can thus be rewritten as

$$\nabla f(\underline{r_i}) = \int_{\Omega} f(\underline{r}) \nabla_i w_h(\underline{r_i} - \underline{r}) d\Omega. \tag{13}$$

This generic calculation can equally be applied to the divergence and results for sufficiently smooth g in

$$\nabla \cdot \underline{g}(\underline{r_i}) = \int_{\Omega} \underline{g}(\underline{r}) \cdot \nabla_i w_h(\underline{r_i} - \underline{r}) d\Omega. \tag{14}$$

Now this continuous representation can be spatially discretized. With additional algebra, more formulations for the differential operators can be derived (Watkins et al., 1996). These formulations hold properties that make them advantageous over the formulation above. The most frequently used formulations are the so-called symmetric divergence

$$\nabla \cdot \underline{g_i} = -\frac{1}{\rho_i}\sum_{j=0}^{N} m_j \underline{g_{ij}} \cdot \nabla_{\mathrm{i}} w_h(r_{ij}) \tag{15}$$

and the anti-symmetric gradient operator

$$\nabla f_i = \rho_i \sum_{j=0}^{N} m_j \left(\frac{f_i}{\rho_i^2} + \frac{f_j}{\rho_j^2}\right) \nabla_{\mathrm{i}} w_h(r_{ij}). \tag{16}$$

The continuity and the momentum equation are examined separately using the advantages of the different discretization schemes available for the differential operators. The divergence in the continuity equation is usually determined by the symmetric operator due to its improved mathematical consistency (Violeau, 2012)

$$\nabla \cdot \underline{v_i} = -\frac{1}{\rho_i}\sum_{j=1}^{n} m_j (\underline{v_i} - \underline{v_j}) \cdot \nabla_{\mathrm{i}} w_h(r_{ij}). \tag{17}$$

On the contrary, the anti-symmetric formulation is used to describe the pressure gradient in the momentum equation because of its favorable strict conservation of linear and angular momentum guaranteed by this operator (Monaghan, 1988)

$$\nabla p_i = \rho_i \sum_{j=1}^{n} m_j \left(\frac{p_i}{\rho_i^2} + \frac{p_j}{\rho_j^2}\right) \nabla_{\mathrm{i}} w_h(r_{ij}). \tag{18}$$

To model the viscous term, many approaches exist. The most obvious idea is to use the operators derived above and apply the divergence on the gradient operator. This comes with a high computational overhead and leads to inaccurate velocity fields (Watkins et al., 1996). Instead the viscous operator by Monaghan and Kos (1999) is used in this work

$$\nu \Delta \underline{v_i} = \sum_{j=1}^{n} \frac{4(d+2) m_j \nu \underline{v_{ij}} \cdot \underline{r_{ij}}}{(\rho_i + \rho_j)({r_{ij}}^2 + (0.1h)^2)} \nabla_{\mathrm{i}} w_h(r_{ij}). \tag{19}$$

It conserves linear and angular momentum while introducing an artificial bulk viscosity. Another frequently used approach is based on a finite differences gradient coupled with a SPH divergence formulation (Morris et al., 1997). The resulting system of ODEs reads as follows:

$$\frac{d\rho_i}{dt} = \sum_{j=1}^{n} m_j (\underline{v_i} - \underline{v_j}) \cdot \nabla w_h(r_{ij}), \tag{20}$$

$$\frac{d\underline{v_i}}{dt} = -\sum_{j=1}^{n} m_j \left(\frac{p_i}{\rho_i^2} + \frac{p_j}{\rho_j^2} - \frac{4(d+2)\nu \underline{v_{ij}} \cdot \underline{r_{ij}}}{(\rho_i + \rho_j)({r_{ij}}^2 + \eta^2)}\right) \nabla_{\mathrm{i}} w_h(r_{ij}) + \underline{f_i}. \tag{21}$$

where $\underline{f_i}$ includes external accelerations like gravity and $\eta = 0.1h$ is introduced to avoid zero nominators. Instead of utilizing the continuity equation the density can be computed directly using the SPH identity (Monaghan, 1992)

$$\rho_i = \sum_{j=1}^{n} m_j w_h(r_{ij}). \tag{22}$$

Using this identity saves an additional step in the time integration scheme and gives good results applied to particles inside the fluid. Close to the surface, however a non-negligible error is introduced by the truncated kernel support and it thus needs special consideration when applied (Morris et al., 1997).

To advance in time, the system of ODEs achieved by the SPH discretization can be solved by any time integration scheme. The explicit nature of WCSPH leads to small timesteps and as a result, many timesteps have to be computed. To reduce the introduced error, it is beneficial to use a symplectic scheme (Violeau, 2012). In this work the velocity Verlet scheme (Swope et al., 1982) is used adjusted by the additional density equation as follows:

$$\begin{aligned}
\underline{v}\left(t+\frac{\Delta t}{2}\right) &= \underline{v}(t)+\frac{\Delta t}{2}\frac{d\underline{v}}{dt}(t),\\
\underline{r}\left(t+\frac{\Delta t}{2}\right) &= \underline{r}(t)+\frac{\Delta t}{2}\underline{v}\left(t+\frac{\Delta t}{2}\right),\\
\rho(t+\Delta t) &= \rho(t)+\Delta t\frac{d\rho}{dt}\left(t+\frac{\Delta t}{2}\right),\\
\underline{r}(t+\Delta t) &= \underline{r}\left(t+\frac{\Delta t}{2}\right)+\frac{\Delta t}{2}\underline{v}\left(t+\frac{\Delta t}{2}\right),\\
\underline{v}(t+\Delta t) &= \underline{v}\left(t+\frac{\Delta t}{2}\right)+\frac{\Delta t}{2}\frac{d\underline{v}}{dt}(t+\Delta t).
\end{aligned} \tag{23}$$

To dynamically determine the timestep, the well-known CFL condition is applied (Courant et al., 1929)

$$\Delta t \leq \omega_1 \frac{h}{c}. \tag{24}$$

In addition, two more conditions are used to take the current acceleration and viscosity in consideration (Morris et al.,1997)

$$\Delta t \leq \omega_2 \sqrt{\frac{h}{\max\limits_{i=1,\dots,n}\left(\left\|\frac{d\underline{v}_i}{dt}\right\|\right)}}, \tag{25}$$

$$\Delta t \leq \omega_3 \frac{h^2}{\max\limits_{i=1,\dots,n} \nu_i}. \tag{26}$$

Typical values are $\omega_1 = 0.25$, $\omega_2 = 0.25, \omega_3 = 0.125$. The new timestep is the maximal timestep that holds for all three conditions.

To guarantee more stable pressure fields and closely fitted fluid particles near the boundary, the boundary condition proposed by Adami et al. (2012) is utilized. It is based on the pressure extrapolation from surrounding fluid particles and has the claim to ensure $\nabla p = 0$. This approach allows the proper modelling of wall boundaries.

The implemented inlet and the outlet boundary condition are also based on this pressure interpolation principle. The inlet pressure interpolation works exactly like the boundary condition by Adami et al. (2012). For the outlet, a particle is defined as a slave particle when undercutting a defined distance from predefined fixed outlet particles. For those slave particles, the pressure is interpolated from fluid and outlet. While the outlet particles hold a pre-defined pressure. As soon as slave particles leave the outlet zone, they are deleted.

To reduce the noise in the pressure field a numerical diffusive term proposed in Antuono et al. (2010) is applied on the density calculation, hence a smoothed pressure field and makes SPH applicable for violent water flows (Marrone et al., 2011).

For several approaches a surface tracking algorithm is necessary. The technique used here is introduced by He (2014) as the gradient of the color function, defined as $c = 1$ for each particle. The color gradient ∇c_i is defined as

$$\nabla c_i = \frac{\sum_j V_j \nabla_i w_h\left(r_{ij}\right)}{\sum_j V_j w_h\left(r_{ij}\right)}, \tag{27}$$

where V_j denotes the volume of particle j. The expected value within a fluid field is approximately zero and significantly greater at a free surface. Consequently, a limit value can be defined to identify the surface particles. Other surface tracking approaches are shown by Lind et al. (2012) and Marrone et al. (2010).

After a surface tracking is established, an interface-based surface tension model can be implemented. Here, the continuum surface force by Brackbill et al. (1992) is chosen. It is based on the surface tension coefficient σ, the surface curvature κ, the inwards surface normal $\underline{n_s}$, and the surface delta function δ_Σ. The resulting surface force $\underline{f_s}$ reads as follows:

$$\underline{f_s} = \sigma\kappa\underline{n_s}\delta_\Sigma \tag{28}$$

with

$$\delta_\Sigma = |\nabla c|, \tag{29}$$

$$\underline{n_s} = \frac{\nabla c}{|\nabla c|}. \tag{30}$$

The surface curvature κ of particle i can be determined by the SPH divergence operator (Adami et al., 2010):

$$\kappa_i = -\nabla \cdot \underline{n}_i = d\,\frac{\sum_j (\underline{n}_i - \underline{n}_j) V_j \nabla_i w_h(r_{ij})}{\sum_j r_{ij} V_j |\nabla_i w_h(r_{ij})|}. \tag{31}$$

These forces can lead to instabilities that introduce particle clustering and therefore affects the mathematical consistency.

Latter can only be proved for an even particle distribution (Violeau, 2012). Therefore, various particle reordering approaches were developed. A generalized shifting technique was introduced by Lind et al. (2012) derived from Fickian diffusion. A small perturbation term $\delta\underline{v_i}$ is added to the Lagrangian velocity $\underline{v_i}$with $\delta\underline{v_i} \ll \underline{v_i}$

$$\underline{v_i^*} = \underline{v_i} + \delta\underline{v_i}, \tag{32}$$

where $\delta\underline{v_i}$ is defined as

$$\delta v_i := \begin{cases} -\underline{v}_{char} 2h\underline{n} & , \quad \underline{v}_{char} 2h\|\underline{n}\| < 0.25\|\underline{v_i}\| \\ -0.25\|\underline{v_i}\| \dfrac{\underline{n}}{\|\underline{n}\|} & , \quad else \end{cases}, \tag{33}$$

according to Oger et. al. (2015), where $\underline{n} = \sum_j \nabla_i w_h(r_{ij}) V_j$. Sun et. al. (2017b) suggests a shifting distance restriction of 5 percent of the particle diameter Δx_i.

To exclude surface particles from shifting the previously described surface tracking algorithm is utilized.

Particle properties like mass and pressure are shifted with the particle position. Therefore, mass and momentum conservation cannot be guaranteed. Oger et. al. (2015) introduces an Arbitrary Lagrangian Eulerian scheme which allows mass fluxes between particles and ensures mass and momentum conservation.

4 Validation on Standard Cases

The dam break is defined by the SPH European Research Interest Community (SPHERIC) as one of the SPH benchmark tests and is therefore used to validate the SPH free surface flow prediction. The experimental setup and the results are specified in Issa and Violeau (2006). Kleefsman (2005) provides the experimental data to which the present implementation is compared to. There, the water height is determined over time at four different positions. Figure 2 shows the case setup and the two considered water level sensors *H1* and *H2* similarly to the experimental data. Additionally, it visualizes the fluid field at time $t = 0.8\,s$. The tank has a height of 3.22 m and a length of 1 m. The initial water block has a height of 0.55 m and a length of 1.228 m. It is positioned on the left corner of the tank. As soon as the simulation begins, water dam breaks and crushes into an obstacle of 0.161 m height and width. It is located at 2.476 m distance from the left tank wall.

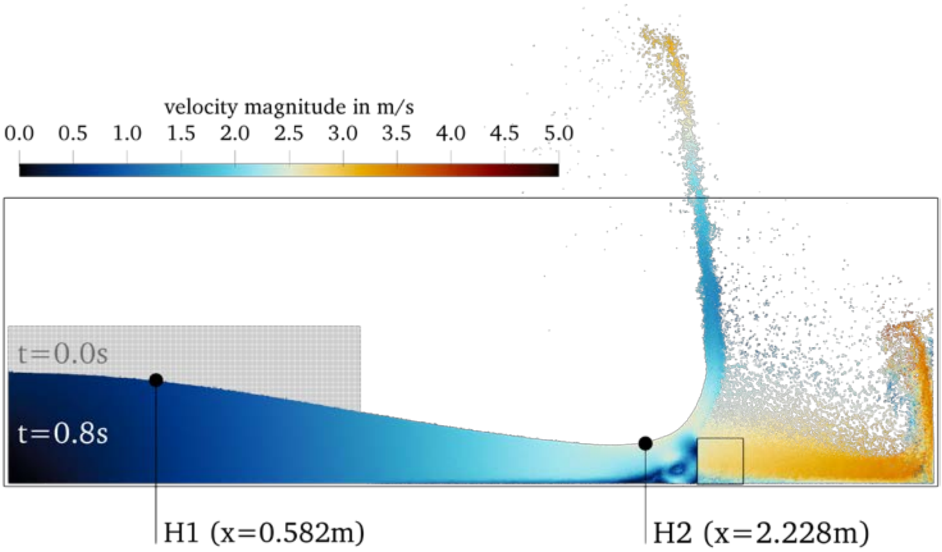

Figure 2. Velocity field for the dam break case

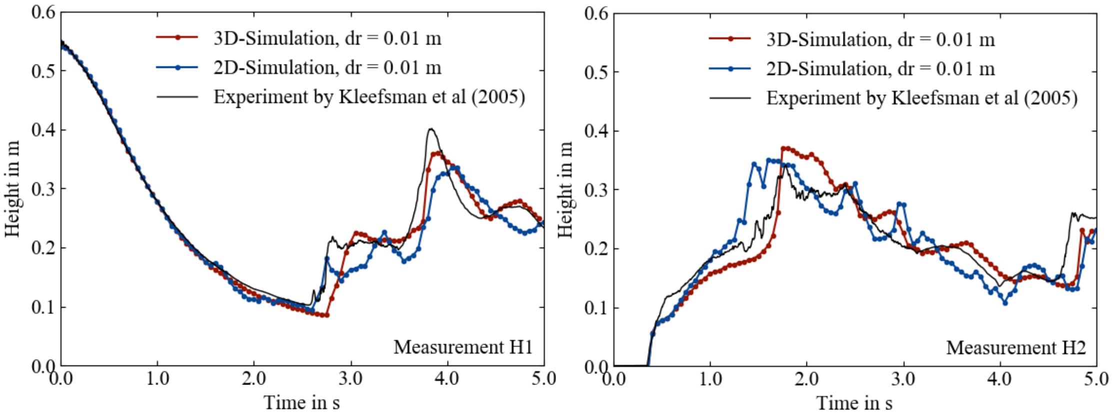

Figure 3. Variation of the water level with time at the height sensors

Figure 3 shows that the water levels resulting from the simulation are in good agreement with the experimental data. The deviations in the 2D case result from neglecting the interspaces between obstacle and wall. Moreover, turbulence modelling is not included which also causes a discrepancy to the measurements.

Nevertheless, the results of the case indicate SPH to be a suitable method for simulating highly dynamic free surface flow.

To evaluate external flows, the Karman vortex street is investigated. Although, it is not perfectly fitted to be a favorable SPH case, it can be used to validate the capabilities of SPH. For Reynolds number 100 and 200 the Strouhal number calculated from the vortex shedding frequency is determined for the present implementation which includes the incorporation of open and wall boundaries next to numerical stabilization. No-slip is used for the cylinder surface, slip for the upper and lower calculation space and open boundaries for the left and right in and outflow. Results are compared to numerical and experimental data from literature, see Table 1.

Figure 4 shows the formation of vortices with initially position-dependent marked particles.

Figure 4. Karman vortex street (position marked particles)

The frequency is examined based on a Fast Fourier Transformation on the *y*-velocity median for a fixed *x* position. The Strouhal number St can be calculated by

$$St = \frac{f_v d_c}{v}. \tag{34}$$

where f_v denotes the shedding frequency and d_c the obstacle diameter. Table 1 shows the results for Reynolds number 100 and 200 of the present work, experimental measurements by Roshko (1954) and numerical results by the references mentioned below.

Table 1. Comparison of Strouhal number with experimental and numerical data

Source	**St (Re=100)**	**St (Re=200)**
Present work	0.174	0.207
Roshko (1954)	0.170	0.185
Tafuni (2016)	0.174	0.205
Calhoun (2002)	0.175	0.202
Liu et al. (1998)	0.165	0.192

The simulation values for both Reynolds numbers show a good agreement with literature data, although the Strouhal number for Reynolds number 200 is determined higher than the compared literature values. Sun et al. (2017a) ascertain that higher Reynolds numbers cause more negative vortex pressures and therefore a less accurate representation of the physical phenomenon. Sun et al. (2017a, b) introduce approaches to avoid negative pressures which will be investigated prospectively.

Lastly, an oscillating droplet with free surface is analysed. Hence, the surrounding air is not calculated. Here, the relative pressure Δp and the oscillation frequency f of the SPH droplet simulation is compared to analytical solutions. Both are determined for a variety of particle radii R.
The analytical pressure can be determined by (Urso, 1999)

$$\Delta p = \frac{R}{\sigma} \tag{35}$$

and the oscillation frequency (Rayleigh, 1879) by

$$f = \left(2\pi\sqrt{\frac{R^3\rho}{6\sigma}}\right)^{-1} \tag{36}$$

The initial condition of the oscillating droplet and its pressure distribution can be seen in Figure 5. The particles position is initialized on a cartesian grid. As soon as the particles are set in motion, the particles distribution is uniform but less systematic. Especially at the surface, the distribution shows a characteristic but less uniform behaviour. This could influence the mathematical consistency at the surface which would also cause problems in of the physical field. The pressure field quality at the surface confirms the suspicion. The pressure values at the surface are comparatively noisy. Nevertheless, the pressure results within the droplet are in good agreement with the analytical solutions, see Figure 6. The same applies for the comparison of the simulated oscillation frequency.

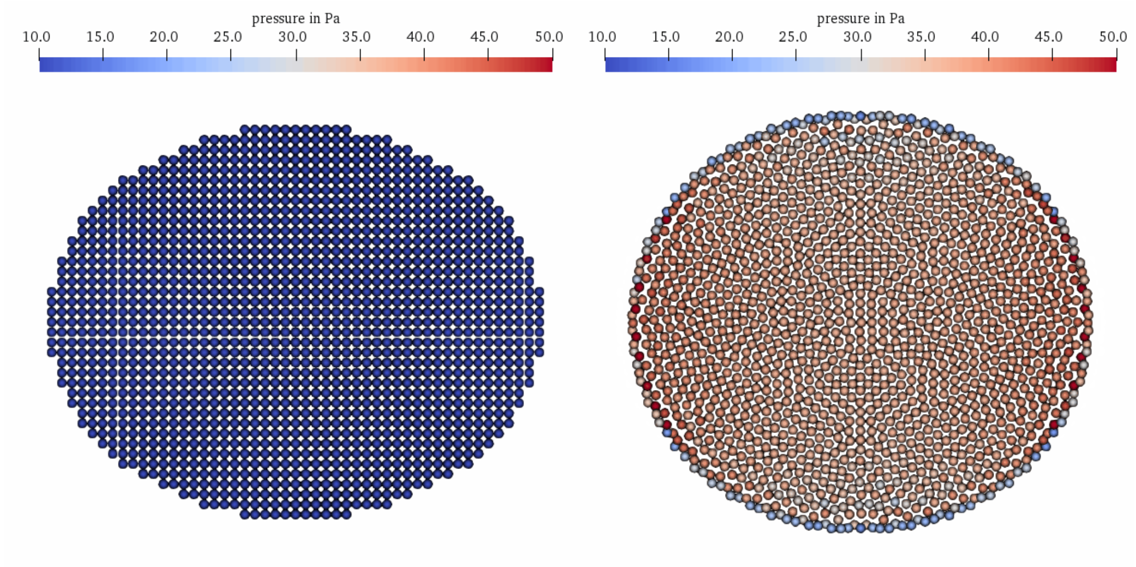

Figure 5. Initial (left) and rearranged (right) particle configuration and pressure distribution of an oscillating droplet

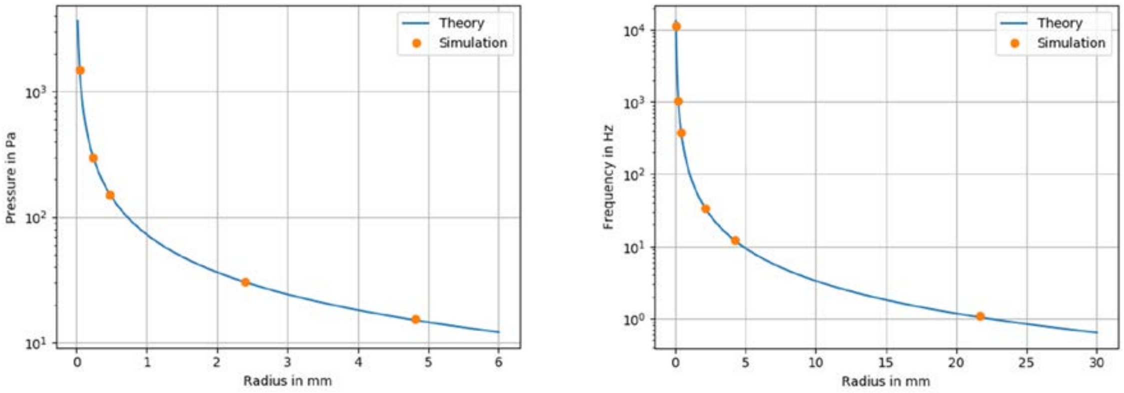

Figure 6. Comparison of analytical and numerical internal pressure (left) and oscillation frequency (right) of a droplet using WCSPH simulation

5 Application Feasability

The EFRE funded research project OPuS at Beuth University of Applied Sciences aims to optimize the geometry of wastewater systems and prevent sedimentary deposition. As a first step, a simplified experimental setup was built at Technische Universität Berlin to investigate flow and sedimentation phenomena in pipes with different inline components. Here, the applicability of the shown methodological software setup is examined as a first feasibility study to assess the occurring physical phenomena and stability. The described test rig with a backward facing step, see Figure 7, is utilized with a length of 85.5 cm between inlet and outlet, a maximum height of 16 cm and a step of 4 cm.

The presented implementation provides all necessary functionalities to approach this setup.

Figure 7 shows the pressure field in the backward facing step. The introduced open boundaries at the inlet and outlet avoid reflections of internal pressure waves, which in the past caused unphysical resonance effects. Furthermore, the wall boundary condition and the density diffusion term improve the pressure field significantly.

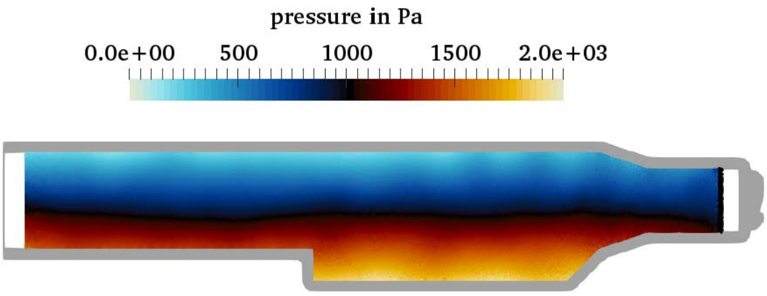

Figure 7. Pressure field of the backward facing step

A first glimpse at the vortex, which is induced by the velocity field at the backward facing step, shows the expected characteristics, see Figure 8. The vorticity and the dimensioning of the occurring flow phenomena will be further analysed in future work.

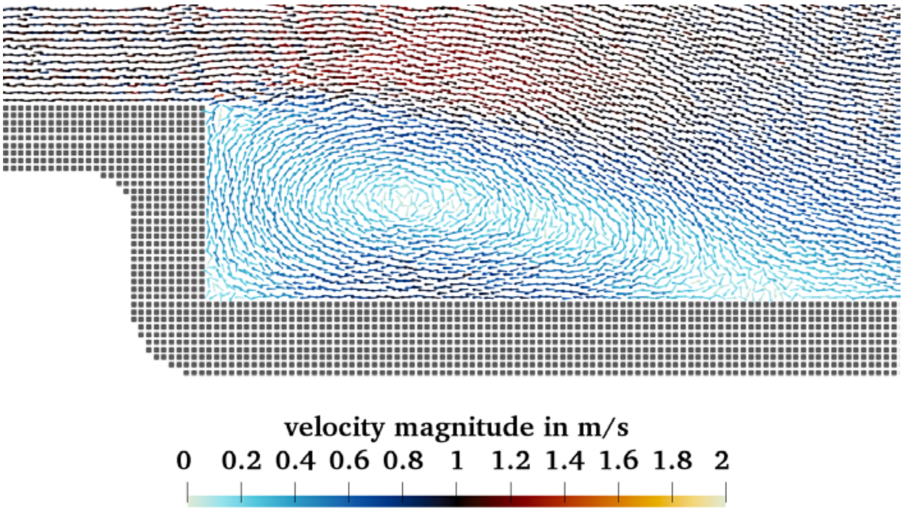

Figure 8. Velocity field of the backward facing step

Building on those approaches, the velocity field will be validated by comparing to experimental particle image velocimetry measurements.

6 Conclusion and Perspective

In this work a combined implementation of several of the latest approaches and improvements in the field of SPH is presented to allow the challenging of real world flow problems. It was possible to validate the incorporation of density diffusion schemes, improved wall treatments and the extension of the wall boundary consideration to open boundary problems for violent free surface flows as well as on an internal flow case.

The simulations of the validation cases are in good agreement with literature and experimental data. Simulations that involve free surface flows as well as external and internal flows were observed to validate the numerical quality of SPH. First pipe simulations are promising for future industrial applications.

Based on the displayed work performed with the described software setup, the application of pipe flow with varying internal features will be continued and compared to data of a corresponding experimental setup. To guarantee the necessary performance, an MPI framework will be established. Especially the pipe flow, adaptive refinements will be further developed to increase resolution in several areas of interest. Moreover, the mentioned turbulence models will further be investigated. To reach the aims of the project, a multiphase and a sedimentation model will be included and geometry studies for avoiding sedimentation in pump stations will be performed.

Acknowledgments

The presented results were established in the EFRE funded research project OPuS at Beuth University of Applied Sciences in close cooperation with Technical University Berlin using the software dive.sph. We want to thank all supporters to our research work.

References

Adami, S.; Hu, X. Y.; Adams, N. A. A new surface-tension formulation for multi-phase SPH using a reproducing divergence approximation. *Journal of Computational Physics*, 229, (2010), 5011–5021.

Adami, S.; Hu, X. Y.; Adams, N. A.: A generalized wall boundary condition for smoothed particle hydrodynamics. *Journal of Computational Physics*, 231, (2012), 7057-7075.

Adami, S.; Hu, X. Y.; Adams, N. A.: Simulating 3D turbulence with SPH. *8th International SPHERIC Workshop*, (2013), 377-382.

Antuono, M.; Colagrossi, A.; Marrone, S.; Molteni, D.: Free-surface flows solved by means of SPH schemes with numerical diffusive terms. *Computer Physics Communications*, 181, (2010), 532-549.

Braun, S.; Holz, S.; Wieth, L.; Dauch, T. F.; Keller, M. C.; Chaussonnet, G.; Schwitzke, C.; Bauer, H.-J.: HPC Predictions of Primary Atomization with SPH: Validation and Comparison to Experimental Results. *12th International SPHERIC Workshop*, (2017), 314-321.

Brackbill, J.; Kothe, S.; Zemach, C.: A continuum method for modeling surface tension. *Journal of Computational Physics*, 100, (1992), 335–354.

Calhoun, D.: Cartesian Grid Method for Solving the Two-Dimensional Streamfunction-Vorticity Equations in Irregular Regions. *Journal of Computational Physics*, 176, (2002), 231-275.

Chiron, L.; Oger, G.; de Leffe, M.; Le Touzé, D.: Analysis and improvements of Adaptive Particle Refinement (APR) through CPU time, accuracy and robustness considerations. *Journal of Computational Physics*, 354, (2017), 552-575.

Cole, H. R.: *Underwater Explosions*. Princeton University Press, Princeton (1948).

Courant, R.; Friedrichs, K.; Lewy, H.: Über die partiellen Differenzengleichungen der mathematischen Physik. Mathematische Annalen, 100, (1929), 32–74.

Cummins, S. J.; Rudman, M.: An SPH Projection Method. *Journal of Computational Physics*, 152, (1999), 584-607.

Dalrymple, R. A.; Rogers, B. D.: Numerical modeling of water waves with the SPH method. *Coastal Engineering*, 53, (2006), 141-147.

Gingold, R. A.; and Monaghan, J. J.: Smoothed particle hydrodynamics:theory and application to non-spherical stars. *Monthly Notices of the Royal Astronomical Society*, 181, (1977), 375-389.

He, X.; Wang, H.; Zhang, F.; Wang, H.; Wang,G.; Zhou, K.: Robust Simulation of Small-Scale Thin Features in SPH-based Free Surface Flows, *ACM Transactions on Graphics*. 34, (2014), 1-9.

Issa, R.; Violeau, D.: Test-case 2 3D dambreaking. *ERCOFTAC, SPH European Research Interest Community SIG*, Electricité De France, Laboratoire National d‘Hydaulique et Environnement, (2006).

Kleefsman, K. M. T.; Fekken, G.; Veldman, A. E. P.; Iwanowski, B.; Buchner, B.: A Volume-of-Fluid based simulation method for wave impact problems. *Journal of Computational Physics*. 206, (2005), 363-393.

Lind, S. J.; Xu, R.; Stansby, P. K.; Rogers, B. D.: Incompressible smoothed particle hydrodynamics for free-surface flows: A generalised diffusion-based algorithm for stability and validations for impulsive flows and propagating waves. *Journal of Computational Physics*. 231, (2012), 1499-1523.

Liu, C.; Zheng, X.; Sung, C. H.: Preconditioned Multigrid Methods for Unsteady Incompressible Flows. *Journal of Computational Physics*, 139, (1998), 35-57.

Lucy, L. B.: A numerical approach to the testing of the fission hypothesis. *Astronomical Journal*, 82, (1977), 1013-1024.

Marrone, S.; Antuono, M.; Colagrossi, A.; Colicchio, G.; Le Touzé, D.; Graziani, G.: δ-SPH model for simulating violent impact flows. *Computer Methods in Applied Mechanics and Engineering*, 200, (2011), 1526-1542.

Marrone, S.; Colagrossi, A.; Le Touzé, D.; Graziani, G.: Fast free-surface detection and level-set function definition in SPH solvers. *Journal of Computational Physics*. 229, (2010), 3652-3663.

Monaghan, J. J.: An introduction to SPH. *Computer Physics Communications*, 48, (1988), 89-96.

Monaghan, J. J.: Smoothed Particle Hydrodynamics. *Annual Review of Astronomy and Astrophysics*, 30, (1992), 543-574.

Monaghan, J. J.: Simulating Free Surface Flows with SPH. *Journal of Computational Physics*, 110, (1994), 399-406.

Monaghan, J. J.; Kos, A.: Solitary Waves on a cretan beach. *Journal of Waterway, Port, Coastal, and Ocean Engineering*, 125, (1999), 145-155.

Morris, J. P.; Fox, P. J.; Zhu, Y.: Modeling Low Reynolds Number Incompressible Flows Using SPH. *Journal of Computational Physics*, 136, (1997), 214-226.

Oger, G.; Marrone, S.; Le Touzé, D.; de Leffe, M.: SPH accuracy improvement through the combination of a quasi-Lagrangian shifting transport velocity and consistent ALE formalisms. *Journal of Computational Physics*. 313, (2016), 76-98.

Rayleigh, L.: On the Capillary Phenomena of Jets. *Proceedings of the Royal Society of London*, 29, (1879), 71–97.

Roshko, A.: On the Development of Turbulent Wakes from Vortex Streets. *Tech. rep. 1191. National Advisory Committee for Aeronautic*, (1954).

Sabrowski, P.; Paschedag, A. R.; Przybilla, S.; Kray, S.; Gutekunst, J.: Smoothed Particle Hydrodynamics – ein neuer Ansatz in der CFD. Jahrestreffen der ProcessNet-Fachgruppen Computational Fluid Dynamics, (2017).

Sun, P. N.; Zhang, A. M.; Colagrossi, A.; Marrone, S.; Antuono, M.: Targeting viscous flows around solid body at high Reynolds numbers with the δ plus-SPH model. *12th International SPHERIC Workshop*, (2017a), 1-8.

Sun, P. N.; Colagrossi, A.; Marrone, S.; Zhang, A. M.: The δ plus-SPH model: simple procedures for a further improvement of the SPH scheme. *Computer Methods in Applied Mechanics and Engineering*, Vol. 315, (2017b), 25-49.

Swope, W. C.; Andersen, H. C.; Berens, P. H.; Wilson, K. R.: A Computer Simulation Method for the Calculation of Equilibrium Constants for the Formation of Physical Clusters of Molecules Application to Small Water Clusters. *The Journal of Chemical Physics*, 78, (1982), 637-649.

Tafuni, A.: Smoothed Particle Hydrodynamics: Development and Application to Problems of Hydrodynamics. *Dissertation*, New York University Tandon School of Engineering, (2016).

Tafuni, A.; Domínguez, J. M.; Vacondio, R.; Crespo, A. J. C.: Accurate and efficient SPH open boundary conditions for real 3-D engineering problems. *12th International SPHERIC Workshop*, (2017), 346-354.

Urso, M. E.; Lawrence, C. J.; Adams, M. J.: Pendular, Funicular, and Capillary Bridges: Results for Two Dimensions. *Journal of colloid and interface science*, 220, (1999), 42–56.

Vacondio, R.; Rogers, B. D.; Stansby, P. K.; Mignosa, P.: Variable resolution for SPH in three dimensions: Towards optimal splitting and coalescing for dynamic adaptivity. *Computer Methods in Applied Mechanics and Engineering*, 300, (2016), 442-460.

Violeau, D.: One and two-equations turbulent closures for Smoothed Particle Hydrodynamics. *Proceedings of the 6th International Conference on Hydroinformatics*, (2004), 87-94.

Violeau, D.: *Fluid Mechanics and the SPH Method Theory and Applications*. Oxford University Press, Oxford (2012).

Violeau, D.; Rogers, B. D.: 2016, “Smoothed particle hydrodynamics (SPH) for freesurface flows: past, present and future”, *Journal of Hydraulic Research*, Vol. 54, pp. 1-26.

Watkins, S. J.; Bhattal, A. S.; Francis, N.; Turner, J. A.; Whitworth, A. P.: A new prescription for viscosity in Smoothed Particle Hydrodynamics. *Astronomy and Astrophysics Supplement Series*, 119, (1996), 177–187.

Wendland, H.: Piecewise polynomial, positive definite and compactly supported radial functions of minimal degree. *Advances in Computational Mathematics*, 4, (1995), 389-396.

Addresses: Technische Universität Berlin, Straße des 17. Juni 135, 10623 Berlin
Beuth Hochschule für Technik Berlin, Luxemburger Str. 10, 13353 Berlin
dive solutions GmbH, c/o Maik Störmer, Gudrunstr. 10, 10365
email: pierre.sabrowski@tu-berlin.de
sabine.przybilla@beuth-hochschule.de
pause@dive-solutions.de
lennart.beck@beuth-hochschule.de
villwock@beuth-hochschule.de
paul-uwe.thamsen@tu-berlin.de

DOI: 10.24352/UB.OVGU-2019-013

TECHNISCHE MECHANIK, 39, 1, (2019), 138-148
submitted: July 6, 2018

Impact of the Initial Flow Conditions on the Wetting Efficiency on a Flat Inclined Surface

D. Asendrych

The paper presents a numerical study of a liquid flow on a flat inclined surface using a 3-dimensional unsteady Eulerian multiphase model. Application of a VOF (Volume of Fluid) technique, a surface tracking method, allowed to reconstruct a flow structure and determine surface wettability revealing their dependence on the liquid flow rate. The critical Reynolds number value corresponding to the transition from the rivulet flow to the fully wetted surface was found to agree quite well with the reference literature data. Detailed calculations showed that the solution is sensitive to the initial conditions, i.e. it may change when the dry plate is replaced by a surface covered with a liquid film. Such a behaviour results from variation of the dynamic contact angle between the receding and the advancing contact angles corresponding to the dewetting and wetting conditions, respectively.

1 Introduction

Packed bed columns are commonly used in various industrial installations in chemical, process, petrochemical and the other sectors. The efficiency of such processes like absorption (Niegodajew and Asendrych, 2016), drying, distillation, or rectification (Haroun et al., 2014) is strongly dependent on the ability of the column packing to enlarge the contact area between co- or counterflowing phases and in turn to enhance the mass, momentum and heat transfer processes. Among the factors influencing the effective area of the liquid free surface, one can mention the packed bed characteristics (porosity, specific surface area, liquid spreading ability), gas and liquid properties (Lappalainen et al., 2008) as well as their loads (Asendrych and Niegodajew, 2017). The complexity of the problem makes the optimisation of packed bed columns challenging. That is why a deeper understanding of the flow hydrodynamics for much simpler geometries as flat or textured surfaces is required.

In the existing literature a number of studies is devoted to the liquid flow structure on flat surfaces, just to mention the works of Haroun et al. (2012), Haroun et al. (2014), Xu et al. (2008) or Xu et al. (2012). The main finding of these works is the evolution of the liquid flow structure upon the flow rate or Reynolds number. With its increase flow evolves from droplet-like flow through the system of rivulets up to film flow completely covering the surface. The other papers approach more complex systems. For instance Xu et al. (2014) investigated gas-liquid-liquid system consisting of two immiscible liquids of significantly different surface tensions. Moreover, the influence of a counterflowing gas phase on liquid behaviour was taken into account. In order to capture that effect the drag force was included in the momentum equation with the drag force coefficient proposed by Stephan and Mayinger (1992). Another important aspect approached in the literature is the influence of liquid properties on the wetting efficiency. The surface tension and the contact angle turned out to be of special importance as they may cause significant change of the morphological flow structure and in turn the portion of wetted surface. These parameters were investigated parametrically by Singh et al. (2017) and Asendrych (2018) showing the relevance of the Weber and Kapitza numbers in quantifying these effects.

A step forward was to consider corrugated surface shape in the model (see e.g. Iso et al., 2013, Subramanian and Wozny, 2012, Szulczewska et al., 2003 and Haroun et al., 2012) imitating the geometry of industrially available structured packings. The geometrical constraints of the flow were usually limited to a single element of the packing of relatively small extents, thus ensuring reasonable computational times. Sebastia-Saez et al. (2015a) and Haroun et al. (2012) employed CFD to determine the liquid holdup and the gas pressure drop. Another direction of numerical works was to include physical (Haroun et al., 2012, Sebastia-Saez et al., 2013, Sebastia-Saez et al., 2014b and Xu et al., 2009) and reactive (see e.g.: Haroun et al., 2010, Sebastia-Saez et al., 2014a and Sebastia-Saez et al., 2015b) mass transfer processes taking place at gas-liquid interface. The most advanced model incorporating various aforementioned phenomena was proposed by Sebastia-Saez (2016) and it was employed to predict the carbon dioxide capture in the aqueous solution of amine solvent.

In the present paper a numerical model enabling the reconstruction of the flow structure on a flat surface was developed. The aim of the research was to test the model for simple geometry and make it ready to apply to more complex cases simulating industrial designs of structured packings for various flow conditions. Additionally the influence of initial conditions on the solution and wetting efficiency was studied.

2 Numerical Model

The liquid flow structure was simulated with the use of a 3-dimensional (3D) multiphase Eulerian model. The flow was considered as unsteady, isothermal and laminar, with water as the liquid phase and air as the surrounding medium being in rest. Both fluids were treated as Newtonian and incompressible and not interpenetrating. Therefore the Volume of Fluid (VOF) model was employed to track the interface (i.e. liquid free surface) between immiscible fluids. The mutual interactions between fluidic phases were neglected. The properties of fluids, i.e. density, viscosity and surface tension were assumed to be equal to those at ambient conditions. In particular the water surface tension σ and the static contact angle α of the water-stainless steel system were set to 72.8 mN/m and 70°, respectively.

2.1. Governing Equations

The VOF formulation is based on the assumption that the phases are not interpenetrating. For the i^{th} phase an additional variable called volume fraction γ_i is introduced. It is defined as the ratio of the i^{th} phase volume and the total volume:

$$\gamma_i = V_i / \sum_i^n V_i \tag{1}$$

where n is a number of phases. Obviously in each cell the volume fractions of all mixture components meet the following condition:

$$\sum_{i=1}^n \gamma_i = 1 \tag{2}$$

When VOF model is employed all flow variables and mixture properties (i.e. density ρ and viscosity μ) are shared by phases and represent volume-averaged values with local γ_i values used as weighting coefficients. Thus, for instance, the mixture density is given by:

$$\rho = \sum_{i=1}^n \gamma_i \rho_i \tag{3}$$

With the use of the VOF method the tracking of the interface between two phases is carried out by solving the continuity equation for the volume fraction of one of the phases (Ansys Inc., 2016). For the i^{th} phase this equation takes the following form:

$$\frac{\partial(\gamma_i \rho_i)}{\partial t} + \nabla(\gamma_i \rho_i U_i) = 0 \tag{4}$$

Momentum equation is formulated for the mixture of phases. Except for the typical terms, it includes additionally the surface tension and the gravity forces:

$$\frac{\partial(\rho U)}{\partial t} + \nabla(\rho U \cdot U) = -\nabla p + \nabla\left[\mu\left(\nabla U + \nabla U^T\right)\right] + \rho g + S \tag{5}$$

Surface tension, being a result of forces attracting the fluid molecules, is implemented according to the model proposed by Brackbill et al. (1992). Continuum surface model (CSM), allowing to convert a surface force to a volumetric one, leads to the following expression for the source term S for the mixture composed of two fluids:

$$S = \sigma \frac{\rho \kappa \nabla \gamma_L}{(\rho_L + \rho_G)/2} \tag{6}$$

In order to define adequately the boundary condition at the inlet, an expression for the liquid film thickness δ was adopted from the work of Nusselt (1916):

$$\delta = \left[\mathrm{Re}_L \frac{3(\mu_L / \rho_L)^2}{g \sin \varphi} \right]^{1/3} \tag{7}$$

where φ is the plate's inclination angle and Re_L is the liquid Reynolds number given by the following definition

$$\mathrm{Re}_L = \frac{\rho_L U_{mean} \delta}{\mu_L} \tag{8}$$

based on the liquid film thickness and its mean velocity U_{mean}.

2.2. Computational Domain and Boundary Conditions

Computational domain was defined as a cuboid (see Figure 1) of the following dimensions: 60mm (length), 50mm (width) and 10mm (height). The length and width were chosen to fit the dimensions of the experimentally studied cases (Haroun et al., 2014 and Hoffmann et al., 2006), while the height had to ensure no impact of the top boundary on the liquid behaviour. Inclination angle was set to φ=60° for consistency with literature. The coordinating system was adjusted to the plate inclination (as shown in Figure 1) with its origin attached to the centre of the inlet plate's edge. Thus the abscissa is parallel to the surface and the ordinate perpendicular to it.

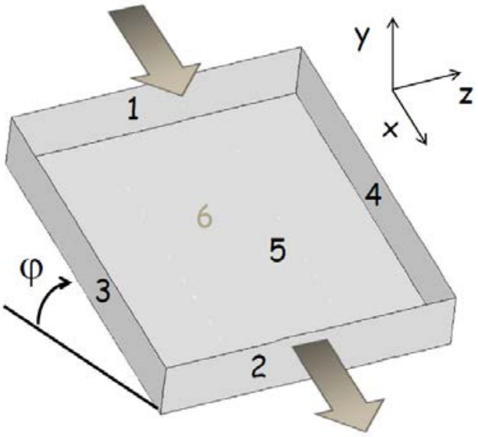

Figure 1. The view of the computational domain showing the plate's inclination angle φ and the flow boundaries with numbers corresponding to the boundary conditions (see Table 1): inlet (1), outlet (2), side walls (3) and (4), top boundary (5) and plate (6)

No	Boundary Condition	Settings
1	Velocity Inlet	i) near-wall zone, i.e. $0 < y \le \delta$ - liquid volume fraction = 1 - parabolic velocity profile ii) outer zone, i.e. $y > \delta$ - liquid volume fraction = 0 - velocity = 0
2	Pressure Outlet	overpressure $p = 0$
3,4,5	Wall	non-slip condition, specified shear stress = 0, static contact angle = 70°
6	Wall	slip condition, static contact angle = 70°

Table 1. Boundary conditions set at the boundaries of the computational domain

In order to simulate the flow behaviour in a realistic way a system of boundary conditions was set at the domain boundaries which are summarized in Table 1. The velocity inlet boundary condition (liquid volume fraction distribution and parabolic velocity profile within the liquid film) was set with the use of a User Defined Function (UDF), a set of subroutines written in C language and linked to the solver. The UDF could be additionally utilised to initialize the solution with a liquid film covering the entire plate. Its thickness and velocity distribution were then set identically as at the inlet to the domain to avoid flow disturbance and speed up the convergence.

2.3. Numerical Tools and Settings

Ansys Workbench v.17 commercial simulation package was employed to solve the problem. Ansys DesignModeller was used to create a geometry, Ansys Mesher for discretization of computational domain and Ansys Fluent to solve the fluid flow. The VOF multiphase model was used with explicitly formulated volume fraction. The air was treated as a primary phase and water as a secondary one. Spatial discretization was performed with second-order upwind scheme for momentum, while the PRESTO! algorithm was used for pressure. Relaxation factors were kept at default levels, i.e. 0.7 for momentum, 0.3 for pressure, and 1.0 for density and body forces. Pressure-velocity coupling was done with the use of the PISO method. For the reconstruction of air-water interface the "geo-reconstruct" scheme was employed. For the time advancement a first order implicit scheme was utilised.

3 Simulation Results

Before the model was used for the simulations of surface wettability it had been tested in terms of spatio-temporal discretization. In order to better control the space discretization the computational domain was divided into 2 zones separated by the plane parallel to the plate. The position of the demarcation surface (4mm above the plate) was chosen in a way to ensure that the gas-liquid interface is completely included in a wall-adjacent region. Various meshing strategies were applied to ensure sufficient spatial resolution in that sensitive zone. Several meshes were tested with a total number of cells varying between 320 thousand and 1.46 million. Finally the mesh comprising 1.13 million cells was chosen as ensuring the grid-independent solutions for entire range of Reynolds numbers foreseen for analysis. Figure 2 presents the view of the final mesh, with the cell size progressively refined towards the surface, allowing to resolve the flow where the highest gradients of flow quantities (velocity, volume fraction) were expected. Above the demarcation surface the uniform coarse mesh was applied - see top part in Figure 2.

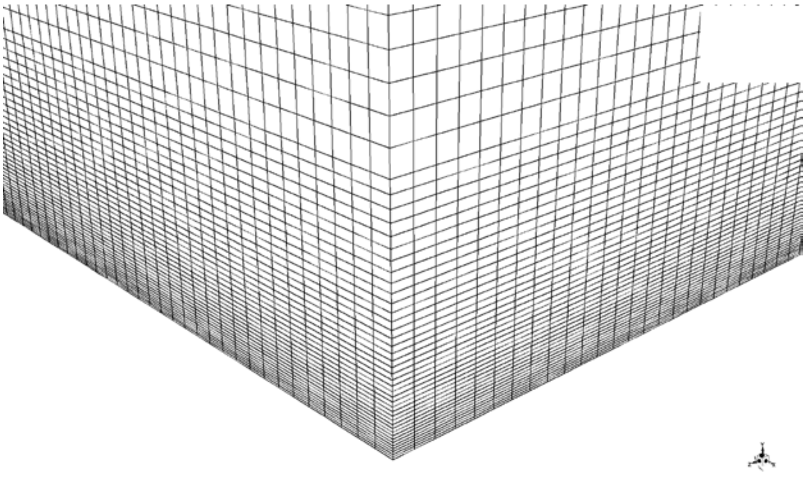

Figure 2. Magnified view of the numerical grid in the wall-adjacent corner of the domain

The time step tests were conducted in the range $10\mu s$ - $300\mu s$. A step of $25\mu s$ was found to ensure the best compromise between accuracy and computational times for all the Reynolds numbers planned for simulations.

3.1. Flow structure versus Reynolds Number

In order to identify the morphological structure of liquid flow in detail a series of simulations were performed for varying Reynolds number, constant inclination angle φ = 60° and water with its material properties corresponding to the ambient conditions.
The 3-dimensional views of the gas-liquid interfaces for *Re* = 50, 90, 130 are presented in Figure 3. For all the cases the solution was initialized with "wetted" plate, i.e. the domain was filled in with a water film of relevant thickness and velocity profile. The interfaces are shadowed to provide the information about their elevations over the plate's surface. Black colour corresponds to the plate's level, while white one to the highest altitude. The same scale is applied to all three images shown in Figure 3.

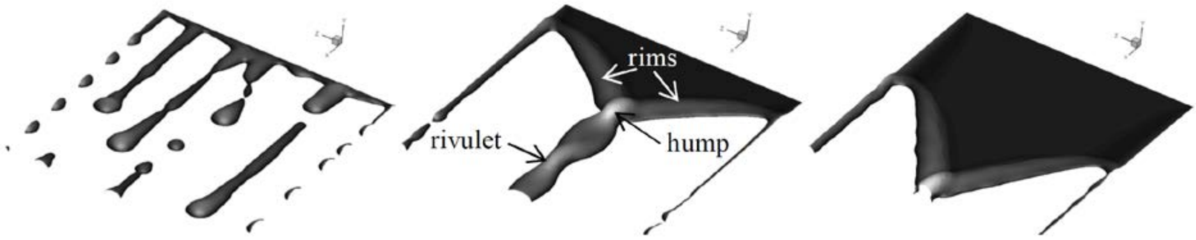

Figure 3. Flow structure evolution with Reynolds number: *Re* = 50 - droplet-like flow (left), *Re* = 90 - rivulet flow (centre), *Re* = 130 almost film flow (right)

The flow structure for *Re* = 50 (see Figure 3, left) is characterised by the presence of small rivulets breaking up into droplets. The liquid film is practically invisible. Such a flow behaviour indicates domination of the surface tension forces over the liquid inertia resulting in low wettability of the surface. When the Reynolds number increases to *Re* = 90 inertial effects become stronger, thus a portion of plate's surface is covered by the liquid film (see Figure 3, centre) with perfect wettability. At certain distance downstream the inlet edge the capillary pressure leads to formation of a stationary front resulting in liquid accumulation in elevated rims. Then liquid is redirected towards the plate's centre where two streams meet together creating a hump (with a whitish top). As a consequence local velocity rises giving finally birth to a rivulet. Further increase in the Reynolds number moves downstream the rivulet formation. Consequently portion of the plate covered with the liquid film enlarges and improves surface wettability. For *Re* = 130 (see Figure 3, right) inertial forces are strong enough to move the hump to the outlet edge further increasing the wetted surface. The presented morphological flow structure evolution with the Reynolds number is fully consistent with the observations of Xu et al. (2014) and Haroun et al. (2014).

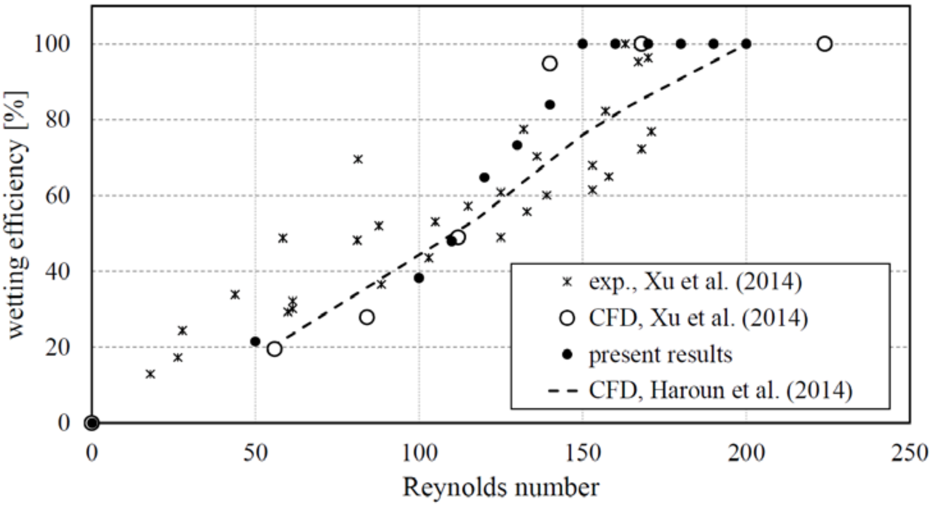

Figure 4. Dependence of the wetting efficiency on the Reynolds number; comparison of the present CFD results with the reference numerical and experimental data of Xu et al. (2014) and Haroun et al. (2014)

The qualitative results of Figure 3 are summarized quantitatively in Figure 4 as a dependence of the wetting efficiency on the Reynolds number. As a reference the already mentioned results of Xu et al. (2014)

(experimental data represented by the asterisks and numerical ones by the empty circles) and Haroun et al. (2014) (CFD data - dashed line) are included in Figure 4. The simulation results obtained in the present work (solid circles) are in a very good agreement with the reference CFD data of Xu et al. (2014). In both cases wetting efficiency increases in a slightly nonlinear way with *Re* reaching 100% for *Re* ≈ 150. Although the experimental results are characterised by noticeable uncertainty (see scatter of points), they in principle indicate linear dependence on *Re* and deviate from the present results and the CFD data (Xu et al., 2014) which is especially evident in high *Re* regime. As a consequence critical Reynolds number value, i.e. corresponding to the transition from partially to completely wetted surface, reaches *Re* ≈ 200. In contrast good correspondence is found between the experiment of Xu et al. (2014) and the CFD predictions of Haroun et al. (2014). The discrepancies between various CFD data collected in Figure 4 seem to be too large and they require reasonable explanation.

3.2. Impact of the Initial Conditions on the Surface Wettability

The results of the simulations presented in the previous section were obtained for the flow initialized with "wetted" plate, i.e. with the liquid film covering entirely the surface with relevant thickness (see equation 7) and parabolic velocity profile. Similarly Xu et al. (2014) applied "wet plate" initial condition. Although the final solution should be independent of its initialization, it was decided to check whether it may influence the surface wettability. So a series of simulations were conducted for the "dry" plate, i.e. with air filling completely the computational domain.

Temporal evolution of the liquid volume fraction at the plate's surface for both cases and *Re* = 50 is shown in Figure 5 for the selected time instants. Black colour is used here to indicate the liquid phase while white one corresponds to the gas phase. One may easily notice that starting from completely different liquid distributions both flow cases evolve finally to the same morphological structure characterised by a system of short rivulets breaking up into droplets (see Figure 5e). Although the "wetted" plate initialization promotes the formation of a single rivulet (see Figure 5b, bottom), the surface tension forces are strong enough (when compared to inertia) to reduce the rivulet (see Figure 5c, bottom) and to produce a system of droplets originating from different transverse locations of the inlet edge (see Figure 5d, bottom). As a result the wetted portion of the plate is progressively reduced.

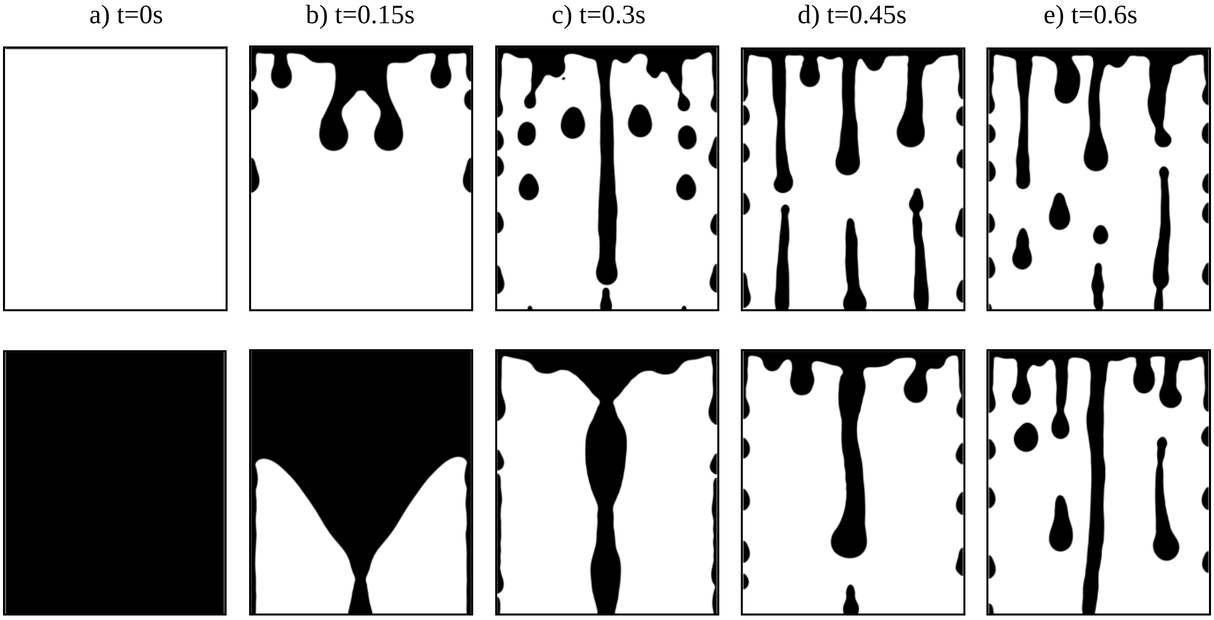

Figure 5. Temporal evolution of liquid flow structure for *Re* = 50 and different solution initializations: the top sequence corresponds to the flow initialized with a "dry" plate, while the bottom one to the flow initialized with a liquid film ("wetted" plate)

Similar consistency between "dry" and "wetted" plate initialization can be observed for *Re*=100. The corresponding time histories are presented in Figure 6. For both cases a quasi-steady state was established with a rivulet formed in the plate's centre. Thus the final flow structure as well as the surface wettability turned out to be independent of the initial condition applied. This rule turned out to be true for the limited Reynolds number range only. When it exceeded 100 the portion of wetted surface for "dry" initialisation started to decrease when compared to originally "wet" plate. This behaviour was consequently continued for the other Reynolds number values.

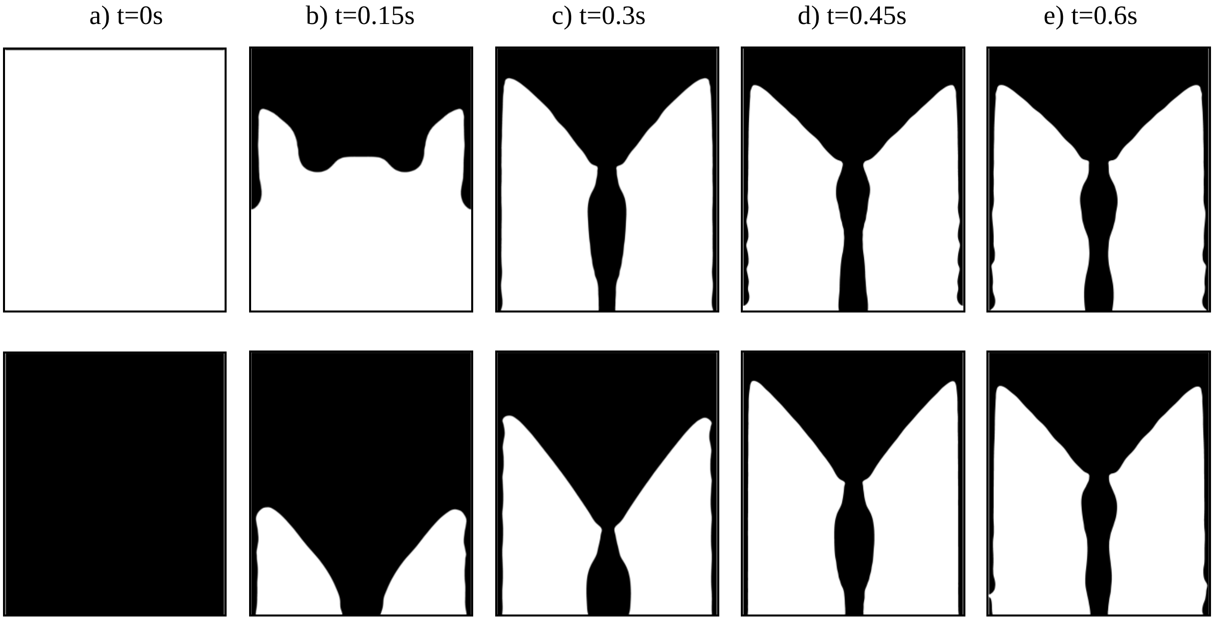

Figure 6. Temporal evolution of liquid flow structure for *Re* = 100 and different solution initializations: the top sequence corresponds to the flow initialized with a "dry" plate, while the bottom one to the flow initialized with a liquid film ("wetted" plate)

The effect of initial condition on the wetting efficiency is shown in Figure 7. However, it is presented here as a function of Weber number, i.e. a group number commonly used to analyse the flow phenomena influenced by surface tension. It is defined as:

$$We = \frac{\rho_L U_{mean}^2 \delta}{\sigma} \tag{9}$$

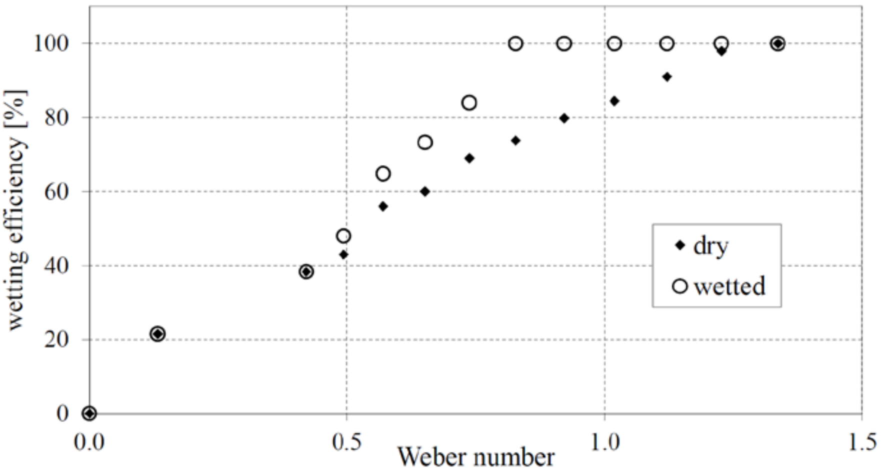

Figure 7. Hysteresis of the surface wettability resulting from different initial conditions

As can be seen from Figure 7 the "gap" between 2 differently initialized solutions exists in a quite wide range, i.e. 0.45 < *We* < 1.3 and it reaches its maximum extent (equal to 25%) at *We* = 0.8. In order to achieve full wettability for originally dry plate the Weber number had to be increased to 1.3. Such a duality in the evolution of a flow structure seems to explain the discrepancies identified between various CFD simulations presented in section 3.1 (see Figure 4). Although it is not explicitly stated in their paper Haroun et al. (2014) applied "dry" plate initialization, so their results indicate reduced wettability when compared to the present results and the data of Xu et al. (2014).

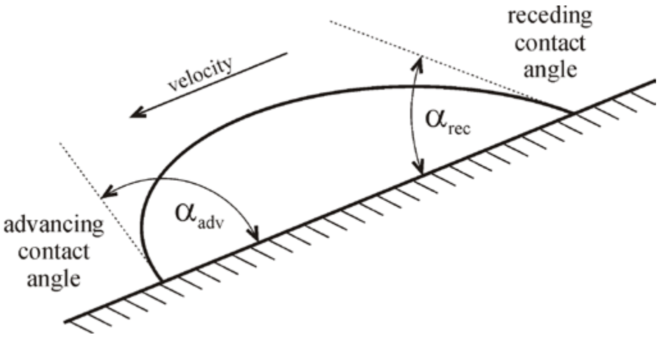

Figure 8. Illustration of the advancing and the receding contact angles for the droplet moving at the inclined flat surface

The hysteresis of the surface wettability could be explained with the variation of the contact angle during the motion of the liquid front. As commonly known the dynamic contact angle of the liquid free surface changes around its static value during the motion of a droplet (Eral et al., 2013). Front of the droplet due to capillary forces is characterised by advancing contact angle while the rear part by the receding one (see Figure 8). The local value of the contact angle depends on many factors and may vary quite significantly. For water the difference between receding and advancing contact angles may even exceed 20 degrees (Eral et al., 2013, Malgarinos et al., 2014).

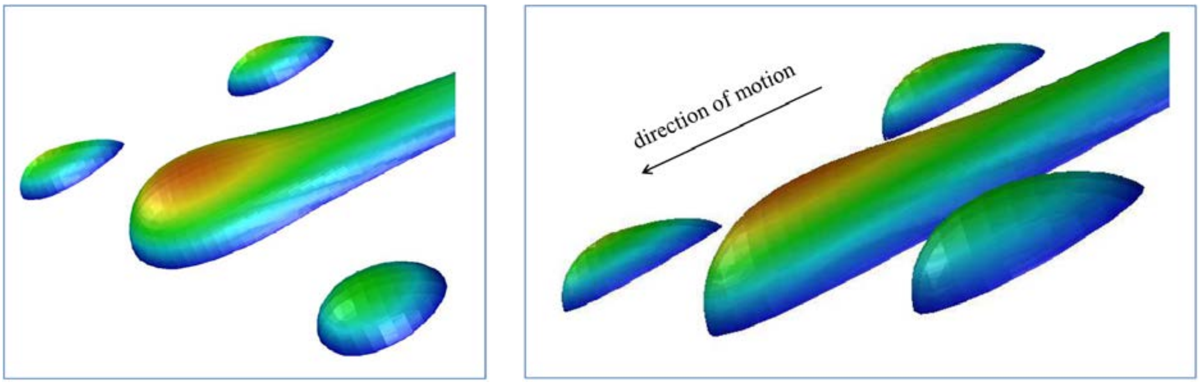

Figure 9. Sample views of the droplet-like flow structure showing the increase of the contact angle in the front of the droplets and rivulet and its decrease at the droplets' rears

Figure 9 presents the sample views of the flow structure for the Reynolds number Re = 50 (We = 0.13), i.e. for the droplet flow. One can easily notice the observable differences between the contact angles corresponding to the fronts and the rears of the droplets. Magnified views of the free surfaces allowed to estimate the range of the contact angle to $\Delta\alpha = \alpha_{adv} - \alpha_{rec} \approx 15°$. The variation of the contact angle has no consequence on the wetting efficiency for $We < 0.5$ (see Figure 7) with the morphological flow structure dominated by droplets. Regardless the initial conditions (wet or dry plate) the flow has to evolve from the liquid film through the system of rivulets to the cloud of droplets. When the flow structure is finally established and becomes quasi-stationary then the flow "forgets" about its origin and the droplets flow down wetting and dewetting the surface. Reduced wetting at the front of the droplet is compensated by the increased wetting in its rear part. The situation changes for the $We \geq 0.5$ when droplets disappear and the flow becomes stationary with a part of a surface covered with a film (see Figure 3, centre and Figure 3, right). Depending on the flow initialisation the position of the liquid rims are slightly different. For the initially dry surface they are shifted up due to higher contact angle values as the liquid front is moving down during surface wetting. Inversely, for the wetted surface, the liquid front is travelling up, thus the surface is dewetted with lower contact angles. Such a mechanism explains the hysteresis of the wetting efficiency observed for the rivulet-like flow structure.

4 Summary

Three-dimensional simulations of the liquid flow structure and the surface wettability on a flat inclined plate were carried out for varying Reynolds/Weber number and the initial flow conditions. An Eulerian multiphase one-fluid approach was employed to develop a CFD model in Ansys Fluent environment. Gas-liquid interface was reconstructed with the use of a Volume of Fluid technique. The results were found to be in a good qualitative and quantitative agreement with the available experimental and numerical reference data. It was also shown that the change of the initial condition from the "dry" to the "wetted" plate leads to the increased wettability in the higher Reynolds/Weber number range, in particular for the flow structure dominated by the rivulets. It results in noticeable change of a critical Re/We value determining the upper limit of partial surface wetting. The variation of the dynamic contact angle of the liquid front between the receding and the advancing levels has been found to be responsible for such a wetting efficiency hysteresis.

Full consistency of the results with the reference numerical and experimental data proved the model relevance and its appropriateness for studies of surface wettability. The model is planned to be used in future work to analyse the flow structure and the wetting efficiency for complex geometries of the commercially available structured packings.

Acknowledgements

The present research work was funded by the Polish National Science Centre under the grant UMO-2014/15/B/ST8/04762. PL-Grid Infrastructure is gratefully acknowledged for providing its computational resources.

References

Ansys Inc.: ANSYS Fluent User’s Guide. Release 17.0, (2016).

Asendrych D.: Numerical study of surface wettability - the influence of surface tension and contact angle, Proc. 8th International Conference from "Scientific Computing to Computational Engineering", 8th IC-SCCE, Athens, 4-7 July, (2018), 319-326

Asendrych, D.; Niegodajew, P.: Numerical study of the CO_2 absorber performance subjected to the varying amine solvent and flue gas loads. *Chemical Engineering Communications*, 204, 5, (2017), 580-590.

Brackbill, J.U.; Kothe, D.B.; Zemach, C.: A continuum method for modelling surface tension, *Journal of Computational Physics*, 100, (1992), 335-354.

Eral, H.B.; 't Mannetje, D.J.C.M.; Oh, J.M.: Contact angle hysteresis: a review of fundamentals and applications. *Colloid and Polymer Science*, 291, (2013), 247-260.

Haroun, Y.; Legendre, D.; Raynal, L.: Volume of fluid method for interfacial reactive mass transfer: Application to stable liquid film. *Chemical Engineering Science*, 65, (2010), 2896-2909.

Haroun, Y.; Legendre, D.; Raynal, L.: Mass transfer and liquid hold-up determination in structured packing by CFD. *Chemical Engineering Science*, 75, (2012), 342-348.

Haroun, Y.; Raynal, L.; Alix, P.: Prediction of effective area and liquid hold-up in structured packings by CFD. *Chemical Engineering Research and Design*, 92, (2014), 2247-2254.

Hoffmann, A.; Ausner, I.; Repke, J.-U.; Wozny, G.: Detailed investigation of multiphase (gas-liquid and gas-liquid-liquid) flow behaviour on inclined plates. *Chemical Engineering Research and Design*, 84, A2, (2006), 147-154.

Iso, Y.; Huanga, J.; Katoa, M.; Matsunoa, S.; Takano, K.: Numerical and experimental study on liquid film flows on packing elements in absorbers for post-combustion CO_2 capture. *Energy Procedia*, 37, (2013), 860-868.

Lappalainen, K.; Alopaeus, V.; Manninen, M.; Aittamaa, J.: Improved hydrodynamic model for wetting efficiency, pressure drop and liquid holdup in trickle-bed reactors. *Industrial & Engineering Chemistry Research*, 47, (2008), 8436-8444.

Malgarinos, I.; Nikolopoulos, N.; Marengo, M.; Antonini, C.; Gavaises, M.: VOF simulations of the contact angle dynamics during the drop spreading: Standard models and a new wetting force model. *Advances in Colloid and Interface Science*, 212, (2014), 1–20.

Niegodajew, P.; Asendrych, D.: Amine based CO_2 capture - CFD simulation of absorber performance. *Applied Mathematical Modelling*, vol. 40, issues 23-24, (2016), 10222-10237.

Nusselt, W.: Die Oberflächen-kondensation des Wasserdampfes, *Zeitscrift des Vereines Deutschem Ingenieure*, 60, (1916), 541-546.

Sebastia-Saez, J.D.: CFD modelling of post-combustion carbon capture with amine solutions in structured packing columns, *PhD thesis*, Cranfield University, (2016).

Sebastia-Saez, D.; Gu, S.; Ranganathan, P.; Papadikis, K.: 3D modeling of hydrodynamics and physical mass transfer characteristics of liquid film flows in structured packing elements. *International Journal of Greenhouse Gas Control*, 19, (2013), 492-502.

Sebastia-Saez, D.; Gu, S.; Ranganathan, P.: Volume of fluid modeling of the reactive mass transfer of CO_2 into aqueous amine solutions in structured packed elements at microscale. *Energy Procedia*, 63, (2014a), 1229-1242.

Sebastia-Saez, D.; Gu, S.; Ranganathan, P.; Papadikis, K.: Micro-scale CFD study about the influence of operative parameters on physical mass transfer within structured packing elements. *International Journal of Greenhouse Gas Control*, 28, (2014b), 180-188.

Sebastia-Saez, D.; Gu, S.; Ranganathan, P.; Papadikis, K.: Meso-scale CFD study of the pressure drop, liquid hold-up, interfacial area and mass transfer in structured packing materials. *International Journal of Greenhouse Gas Control*, 42, (2015a), 388-399.

Sebastia-Saez, D.; Gu, S.; Ranganathan, P.; Papadikis, K.: Micro-scale CFD modelling of reactive mass transfer in falling liquid films within structured packing materials. *International Journal of Greenhouse Gas Control*, 33, (2015b), 40-50.

Singh, K.R.; Galvin, E.J.; Sun, X.; Singh, K.R.; Galvin, E.J.; Sun, X.: Three-dimensional simulation of rivulet and film flows over an inclined plate: Effects of solvent properties and contact angle. *Chemical Engineering Science*, 142, (2016), 244-257.

Stephan, M.; Mayinger, F.: Experimental and analytical study of countercurrent flow limitation in vertical gas/liquid flows. *Chemical Engineering Technology*, 15, (1992), 51-62.

Subramanian, K.; Wozny, G.: Analysis of hydrodynamics of fluid flow on corrugated sheets of packing. *International Journal of Chemical Engineering*, 2012, (2012), 1-13.

Szulczewska, B.; Zbicinski, I.; Górak, A.: Liquid flow on structured packing: CFD simulation and experimental study. *Chemical Engineering Technology*, 26, (2003), 580-584.

Xu, Y.; Paschke, S.; Repke, J.-U.; Yuan, J., Wozny, G.: Portraying the countercurrent flow on packings by three-dimensional computational fluid dynamics simulations. *Chemical Engineering Technology*, 31, 10, (2008), 1445-1452.

Xu, Y.; Paschke, S.; Repke, J.-U.; Yuan, J.; Wozny, G.: Computational approach to characterize the mass transfer between the counter-current gas-liquid flow. *Chemical Engineering Technology*, 32, 8, (2009), 1227-1235.

Xu, Y.; Repke, J.-U.; Yuan, J.; Wozny, G.: CFD study on liquid flow behaviour on inclined flat plate focusing on effect of flow rate. *Engineering Applications of Computational Fluid Mechanics*, 6, 2, (2012), 186-194.

Xu, Y.; Zhao, M.; Paschke, S.; Wozny, G.: Detailed investigations of the countercurrent multiphase (gas-liquid and gas-liquid-liquid) flow behavior by three-dimensional computational fluid dynamics simulations. *Industrial & Engineering Chemistry Research*, 53, (2014), 7797-7809.

Address: Institute of Thermal Machinery, Częstochowa University of Technology, al. Armii Krajowej 21,
42-200, Częstochowa, Poland
email: darek@imc.pcz.czest.pl

DOI: 10.24352/UB.OVGU-2019-014 TECHNISCHE MECHANIK, 39, 1, (2019), 149 – 161
submitted: July 6, 2018

Modelling of Spark Ignition in Turbulent Reacting Droplet-laden Temporally Evolving Jet using LES

J. Stempka, L. Kuban, A. Tyliszczak

The turbulent jet flames in fuel sprays are of a great importance and are used in many practical applications, e.g., aircraft and automotive direct fuel injection systems. In this work we analyse the process of spark ignition in two-phase temporally evolving jet which carries the fuel spray. We focus on a dependence of the ignition on local flow structures, spark parameters and fuel droplets size. The fuel (n-Heptane) spray evaporates and mixes with the co-flowing oxidizer (air) creating a flammable mixture. The spark is modelled as a source term added to the energy equation. The goal of the research is to investigate the forced ignition and subsequent flame propagation/extinction in the low Mach number turbulent flow. The computations are carried out using Implicit Large Eddy Simulation (ILES) method by the high-order in-house LES solver. Liquid droplets are modelled in Lagrangian reference frame as point sources of mass, momentum and energy. The results show that combined effect of local fuel concentration, strain rate and scalar dissipation rate plays a main role in ignition. On the other hand, high rates of strain at the spark position cause substantial flame stretching leading to its extinction.

1 Introduction

Recent experimental and numerical research of reacting two-phase flows that comprise dispersed fuel spray and gaseous carrier medium have led to the new developments in combustion science. Advances help to improve overall efficiency of practical devices (e.g., gas turbines, jet engines and automotive internal combustion engines) and promote reduction of pollutant combustion products (fuel-lean operation, reheat systems). With the advent of expansion of the computational resources more advanced and realistic numerical simulations are now reachable. From that reason the numerical results of spray combustion appear more frequently in last years. Such analyses are desirable since such processes are highly complicated and not yet fully understood. Because of a large complexity of turbulent spray combustion, experimental research in this field is mostly limited to the fundamental studies. Some new and more detailed analyses has appeared recently (Mastorakos (2016); O'Loughlin and Masri (2011)). Such experiments often require very sophisticated measuring apparatus and therefore, the numerical simulations facilitate further research. Predominantly two numerical approaches are used to study such phenomena, i.e, direct numerical simulations (DNS) (Neophytou et al. (2010)) and large eddy simulations (LES) (Jones and Prasad (2010); Kuban et al. (2017); Stempka (2018)). The DNS provides detailed insight into the turbulent, reacting two-phase flows but, due to high computational cost, it is limited mainly to low Reynolds number flows and simplified domains. Thus, the LES boosts further advancements in spray combustion research since the computing demands are much lower which allows broadening the range of modelled physical phenomena. In the current work the numerical study of the forced ignition in the temporally evolving jet carrying fuel spray is undertaken. A relative motion, between the jet carrying fuel spray and external air co-flow, is imposed by a hyperbolic tangent velocity profile. The simplified configuration reduces the computational effort and allows to investigate the flow-flame interactions typical for real cases. The goal of the current work is threefold, for different initial flow fields: (i) to asses an effect of droplets spray on the flow and flame structure, (ii) to explore the relevance of spark position on ignition and (iii) to recognize causes of the flame extinction. An in-house numerical LES solver (Tyliszczak (2016)) is used to carry out the computations. It is based on high-order compact differences spatial discretisation and predictor-corrector time integration schemes. The continuous flow field is defined in Eulerian manner while the discrete phase is tracked in the Lagrangian framework. In spite of the fact that various strategies for capturing sub-grid turbulence-combustion interactions can be employed along with the sophisticated solving techniques such as: Lagrangian Particles, transported PDFs with Monte Carlo solving method, a simpler approach, namely Implicit LES (ILES) (Duwig et al. (2011)) is used for modelling the reaction kinetics. A global one-step mechanism is applied with the reaction rates calculated based on filtered values. The ILES was proven (Duwig et al. (2011)) to provide reliable solutions as far as adequate spatial resolution is achieved. The chemical reaction is initiated by additional source term in the enthalpy equation, imitating the electrical spark (energy deposition model of Lacaze et al. (2009)).

2 Mathematical Model

The Favre-filtered continuity and Navier-Stokes equations in the framework of LES for two-phase low Mach number flows are given as:

$$\frac{\partial \bar{\rho}}{\partial t} + \frac{\partial \bar{\rho}\tilde{u}_j}{\partial x_j} = \bar{\dot{S}}_{\text{mass}} \,, \tag{1}$$

$$\frac{\partial \bar{\rho}\tilde{u}_i}{\partial t} + \frac{\partial \bar{\rho}\tilde{u}_i\tilde{u}_j}{\partial x_j} = -\frac{\partial \bar{p}}{\partial x_i} + \frac{\partial \bar{\sigma}_{ij}}{\partial x_j} + \frac{\partial \tau_{ij}^{\text{sgs}}}{\partial x_j} + \bar{\dot{S}}_{m,i} \,. \tag{2}$$

The terms appearing in Eq. (2) represent the viscous stress tensor σ_{ij} and the sub-grid stress tensor τ_{ij}^{sgs}. The latter is related to the strain rate tensor $\tilde{S}_{ij}$ by $\tau_{ij}^{\text{sgs}} = \mu_{\text{sgs}}\tilde{S}_{ij}$, where the sub-grid viscosity μ_{sgs} is calculated using the Vreman model (Vreman (2004)). The species mass fractions ($\tilde{\phi}_\alpha$) and the enthalpy (h) transport equations are given by:

$$\frac{\partial \bar{\rho}\tilde{\phi}_\alpha}{\partial t} + \frac{\partial \bar{\rho}\tilde{\phi}_\alpha\tilde{u}_j}{\partial x_j} = \frac{\partial}{\partial x_j}\left[\left(\frac{\mu}{\sigma} + \frac{\mu_{\text{sgs}}}{\sigma_{\text{sgs}}}\right)\frac{\partial \tilde{\phi}_\alpha}{\partial x_j}\right] + \bar{\dot{S}}_\alpha + \overline{\rho\dot{\omega}\left(\phi_\alpha\right)} \,, \tag{3}$$

$$\frac{\partial \bar{\rho}\tilde{h}}{\partial t} + \frac{\partial \bar{\rho}\tilde{h}\tilde{u}_j}{\partial x_j} = \frac{\partial}{\partial x_j}\left[\left(\frac{\mu}{\sigma} + \frac{\mu_{\text{sgs}}}{\sigma_{\text{sgs}}}\right)\frac{\partial \tilde{h}}{\partial x_j}\right] + \bar{\dot{S}}_h + \dot{Q} \,. \tag{4}$$

The ILES (Duwig et al. (2011)) technique is used for computing the reaction rates $\overline{\dot{\omega}\left(\phi_\alpha\right)}$, the energy deposition model (Lacaze et al. (2009)) is applied for modelling the spark source term $\dot{Q}$ and sub-grid scalar fluxes are calculated with the use of Schmidt and Schumann (1989) model. The symbol σ_{sgs} refers to the turbulent Schmidt number. Species are calculated assuming Lewis number equal to unity.

2.1 Source Terms

The dispersed phase is coupled with the flow field through the source terms appearing in Eqs. (1) to (4). They represent averaged sums of the contributions from all particles at each computational cell, i.e., $\bar{\dot{S}} = 1/\Delta^3 \sum_{p=1}^{N_p} \dot{S}_p$ where the Δ and p refer to the spatial filter width and p-th droplet, respectively. The expressions for the source terms are formulated as:

$$\bar{\dot{S}}_{\text{mass},p} = \bar{\dot{S}}_{\alpha,p} = -\frac{d}{dt}m_{d,p} \,, \tag{5}$$

$$\bar{\dot{S}}_{m,p} = -\frac{d}{dt}\left(m_d v_d\right)_p \,, \tag{6}$$

$$\bar{\dot{S}}_{h,p} = -\left(c_f m_d \frac{T - T_d}{\tau_d^T} + \frac{dm_d}{dt}h_f\right)_p \,, \tag{7}$$

$$\tau_d^T = \frac{\rho_f D_d^2}{6\text{Sh}}\frac{\text{PrLe}}{\mu_f}\frac{\text{B}_\text{T}}{ln(1+\text{B}_\text{M})}\frac{c_f}{c_{f,v}} \,, \tag{8}$$

where m_d, v_d and T_d are the droplet mass, velocity and temperature respectively, c_f and $c_{f,v}$ are the fuel and fuel's vapour heat capacities, τ_d^T is the relaxation time, h_f and μ_f are the fuel specific enthalpy of vaporization and fuel dynamic viscosity, Pr and Sh are Prandtl and Sherwood numbers and B_T and B_M represent Spalding heat and mass transfer numbers.

2.1.1 Dispersed Phase

Motion of the dispersed phase is described in Lagrangian reference frame as:

$$\frac{dx_d}{dt} = v_d \,, \tag{9}$$

$$\frac{dv_d}{dt} = \frac{\tilde{u} - v_d}{\tau_d^v} \,, \tag{10}$$

where $\tilde{u}$ is the gas phase velocity at the droplet's position, the particle relaxation time τ_d^v is expressed as

$$\frac{1}{\tau_d^v} = \frac{3}{8}\frac{\rho_f}{\bar{\rho}}\mathrm{C_D}\frac{|\bar{u} - v|}{r_d} \,, \tag{11}$$

in which the symbol $\mathrm{C_D}$ denotes the drag coefficient and r_d is the droplet radius.

2.1.2 Evaporation Model

The droplets act as point-sources of evaporating species. Following the formulation of infinite conductivity evaporation model proposed by Miller et al. (1998) the droplet temperature and mass rates of change during evaporation are computed from:

$$\frac{dT_d}{dt} = \frac{1}{3}\frac{\mathrm{Nu}}{\mathrm{Pr}}\left(\frac{c_{p,g}}{c_f}\right)\frac{T - T_d}{\tau_d^e} + \left(\frac{h_f}{c_f}\right)\frac{\dot{m}_d}{m_d} \,, \tag{12}$$

$$\frac{dm_d}{dt} = -\frac{1}{3}\frac{\mathrm{Sh}}{\mathrm{Sc}}\left(\frac{m_d}{\tau_d^e}\right)\mathrm{H_M} \,, \tag{13}$$

$$\tau_d^e = \frac{\rho_f D_d^2}{18\mu_g} \,, \tag{14}$$

where $c_{p,g}$ is the fuel vapour-gas mixture, τ_d^e is a particle relaxation time and D_d is the drop's diameter. The dimensionless numbers (Prandtl, Schmidt, Nusselt and Sherwood) are computed as $\mathrm{Pr} = \mu_g c_{p,g}/k_g$, $\mathrm{Sc} = \mu_g/\rho_g\Gamma_g$, the Nu and Sh are computed using correlations for non-stationary droplets. The $\mathrm{H_M}$ term accounts for the mass transfer potential, i.e., in the current work the "D^2 law" model (Spalding (1953)) is used and it is defined as $\mathrm{H_M} = ln\,(1 + \mathrm{B_M})$. The term $\dot{m}_d = dm_d/dt$ is the droplet mass rate of change. Physical quantities denoted by the subscript g are calculated adopting the "1/3 rule" of mixing. Such quantities are calculated at the reference temperature and mass fraction. This procedure makes them dependent on spatial and thermal variations of flow variables for the physical consistency.

2.1.3 Spark

The spark is modelled using the energy deposition (ED) model of Lacaze et al. (2009). The local amount of heat transferred into the flow during deposition is denoted as $\dot{Q}$. The contribution of the spark is accounted in the enthalpy equation as an additional source term. Energy deposition model follows the Gaussian distribution in time and space and is defined as

$$\dot{Q} = \frac{\epsilon}{4\pi^2\sigma_s^3\sigma_t}\exp^{-\frac{1}{2}\left(\frac{r}{\sigma_s}\right)^2}\exp^{-\frac{1}{2}\left(\frac{t - t_0}{\sigma_t}\right)^2} \,, \tag{15}$$

where r is the radial distance to the center of the spark, t denotes time and t_0 is the instant of time when the power density function reaches a maximum. The model is controlled by three parameters: the transmitted energy ϵ, $\sigma_s = \Delta_s/a$ and $\sigma_t = \Delta_t/a$ where Δ_s and Δ_t are characteristic size and time duration of the spark, respectively. The coefficient $a = 4\sqrt{ln\,(10)}$ is chosen so that 98% of the deposited energy finds in the domain $\Delta_s^3 \cdot \Delta_t$. The parameters describing the spark are given in Tab. 1.

Table 1: Spark parameters

Δ_s	Δ_t	t_0	ϵ	Δ_s/d_j
3 mm	0.5 ms	1.5 ms	5 mJ	0.65

The size and duration of the spark were taken based on an experimental work of Ahmed and Mastorakos (2006) devoted to analysis of an ignition probability map of methane jets. In the ED model of the spark the selected values guarantee relatively steep rise of the temperature up to the level 3500 K approximately. The time when the spark reaches the maximum intensity (t_0) corresponds to the time instance after the initial transient phase when the vortical structures start to be seen (see Fig. 7) and when small droplets start to concentrate in the vortex cores.

2.1.4 Reaction Terms

The main difference between LES and Implicit LES (ILES) relies on treatment of the reaction source terms. In ILES the sub-filter scales resulting from the filtration of the convective terms are modelled by eddy viscosity model, but the chemical source terms $\overline{\dot{\omega}(\phi_\alpha)}$ are modelled assuming $\overline{\dot{\omega}(\phi_\alpha)} \approx \dot{\omega}(\tilde{\phi_\alpha})$ (Duwig et al. (2011)). In the current analysis reaction rates are obtained from the Arrhenius formula using one-step global chemistry according to the following reaction

$$C_7H_{16} + 11(O_2 + 3.76N_2) = 7CO_2 + 8H_2O + 41N_2\,, \tag{16}$$

for which the reaction rate is tuned to give a reasonable prediction of the strain rate extinction (Fernandez-Tarrazo et al. (2006)). It was chosen to reasonably minimize the computational expense. However, this approach is known from over-predicting the flame speed for rich mixtures, yet it still can reproduce correct trends in the analysis of turbulence impact on the ignition and flame propagation without resolving the flame speed at all equivalence ratio range in details (Chakraborty and Mastorakos (2007)). The ILES assumptions would certainly fail in the Reynolds Averaged Navier-Stokes (RANS) framework as the fluctuations in RANS models are large. On the other hand, the ILES is valid for laminar flow simulation and in DNS where all turbulent flow scales are resolved. Hence, one may assume that for sufficiently dense computational meshes, when the grid cells are comparable with the Kolmogorov length scale, the ILES approach is appropriate. This is verified in preliminary computations.

3 Numerical Approach

Computations were carried out using an in-house academic LES solver for low-Mach numbers flows (SAILOR, Tyliszczak (2016)) which is based on high-order compact difference method combined with the projection method for pressure-velocity coupling on half-staggered meshes and 2nd order Total Variation Diminishing (TVD) scheme. Even though the low order TVD schemes are known from dumping the small-scales in the current work the scheme is used only for species convective terms discretisation to assure boundedness of the species fluxes and gave satisfactory results in the previous works (Wawrzak and Tyliszczak (2016)). Time integration is performed with the use of predictor-corrector approach as a combination of Adams-Bashforth and Adams-Moulton methods. For resolving the dispersed phase motion 1st order integration scheme is applied. The two-way velocity coupling is realized using 2nd order accurate method for the momentum source terms approximation and 4th degree Lagrangian polynomials for the interpolation of the flow field velocity at the droplets positions. The simulations were carried out with a varying time-step and Courant-Friedrichs-Lewy condition set to 0.1. The numerical code was thoroughly tested in the previous studies (Kuban et al. (2017); Wawrzak and Tyliszczak (2016)).

4 Configuration

The configuration used in the current study is schemtically showed in Fig. 1. The computational domain has following dimensions: $Lx = 0.025\ m$, $Ly = 0.04\ m$ and $Lz = 0.01\ m$. The periodic boundary conditions are applied in X and Z directions while the upper and lower walls are assumed adiabatic. Initially the flow, similarly as the droplets had temperatures equal to $300\ K$. The flow of the oxidizer and fuel spray is initiated by imposing hyperbolic tangent velocity profile similarly as in Hawkes et al. (2007). In effect the temporally evolving plane jet is constituted in the middle part of the domain. The jet velocity profile is defined as

$$u(y) = -\frac{U}{2} \cdot \tanh\left(\frac{d_j}{8\Theta}\left(\frac{2|y|}{d_j} - \frac{d_j}{2|y|}\right)\right)\,, \tag{17}$$

where symbol U denotes the free stream velocity of the co-flow outside the jet, $d_j = 4.6\ mm$ is the initial width of the jet and Θ denotes the momentum thickness. The Θ defines the gradient of the velocity profile at the jet edge what is shown schematically in Fig. 1. Currently the effect of two different values of Θ resulting in the ratios $d_j/\Theta = 20$ and 50 is studied among other parameters.

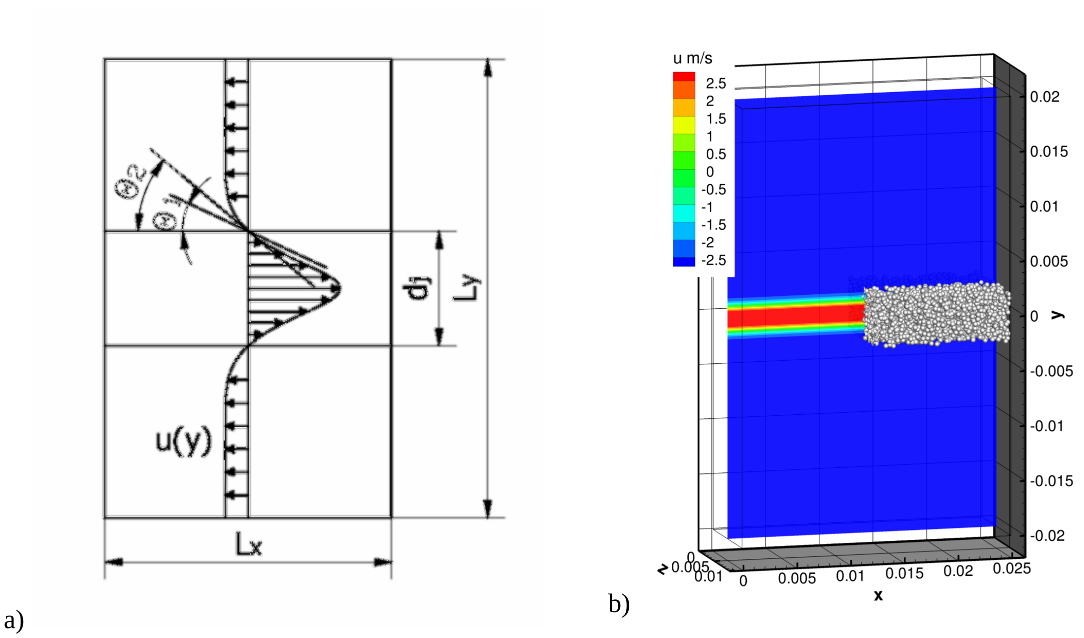

Figure 1: (a) Scheme showing the effect on the velocity profile resulting from using two different values of Θ. (b) Computational domain at the initial state, showed are: contours of streamwise velocity and white dots indicating droplets positions (only right half).

Initially, a homogeneous isotropic turbulence field (HIT) was imposed on the flow field. The HIT is characterized by the Passot and Pouquet (1987) energy spectrum

$$E(k) = 16\sqrt{2/\pi}\frac{u'^2}{k_0}\left(\frac{k}{k_0}\right)^4 \exp^{-2\left(\frac{k}{k_0}\right)^2}, \tag{18}$$

where $u' = \left\langle\sqrt{u'u'}\right\rangle$ is the RMS of initial velocity fluctuations and k_0 is an adjustable wave number used to generate turbulent field with a required Taylor microscale $\lambda =< u'u' > / < \partial(u'u')/\partial x >$. The HIT provides temporal evolution of the jet and the velocity fluctuations are wiped out anywhere outside the jet region. The initial fluctuations for both jet Reynolds numbers Re_{d_j} studied (where $\mathrm{Re}_{d_j} = Ud_j/\nu$) were adjusted such that $\mathrm{Re}_\lambda = \lambda u'/\nu \approx 7$ while the Taylor microscales are $\lambda \approx 4e-4$ and $7e-4$ for the flows characterized by $\mathrm{Re}_{d_j} = 1000$ and 5000, respectively. In both cases the turbulence intensities are equal to $\mathrm{Ti} = 1\%$. The computational mesh consists of $120 \times 192 \times 48$ nodes distributed uniformly in each direction. The resulting grid spacings are close to 200 μm which is comparable with the Kolmogorov length scales, i.e., $\eta_K = 125$ μm and 469 μm for $\mathrm{Re}_{d_j} = 5000$ and 1000. Hence, it can be assumed that applied mesh of such can fulfil the ILES requirement of well stirred reactor.

The fuel (n-Heptane) spray with droplet sizes following the modified Rosin-Rammler size distribution is imposed into the middle part of the domain. Initially, the spray is distributed as a rectangular slab placed within the planar jet region and during the time it spreads due to the momentum coupling. The two distinct distributions of the droplets characterised by different Sauter mean diameters are taken into account. These are equal to (i) $d_{32} = 20$ μm with diameters within 10-30 μm range and (ii) $d_{32} = 50$ μm with diameters spreading from 20-80 μm. The initial mass loading is chosen in order to obtain a global equivalence ratio equal to $\phi = 1.5$ in each case. These resulted in liquid fuel mass loading equal to $m_f = 5.47$ g with two different initial number of droplets, i.e., $\mathrm{N_d} = 993372$ and 132919. Additional small portion of gaseous fuel of mass fraction equal to $\phi_f = 0.01$ is present within the jet region. The inter-droplet forces due to collisions are not taken into account because for the current study the ratio of the liquid fuel volume to that of the gaseous medium is of order 10^{-3}, which is close to the threshold value below which the droplets collisions do not strongly affect the flow (Elghobashi (1994)).

5 Results

Table 2 summarizes all investigated parameters. Each setup differs by at lest one parameter, e.g. jet Reynolds number Re_{d_j}, Sauter mean diameter d_{32} (μm) or momentum thickness Θ. Figure 2 highlights the locations of sparks events. These are labelled as (e.g. S1, S2, ..., S6) used thereafter to denote different cases. For example symbol CS4 denotes initial flow field characterised by $\mathrm{Re}_{d_j} = 5000$ with the spray for which $d_{32} = 50$ μm,

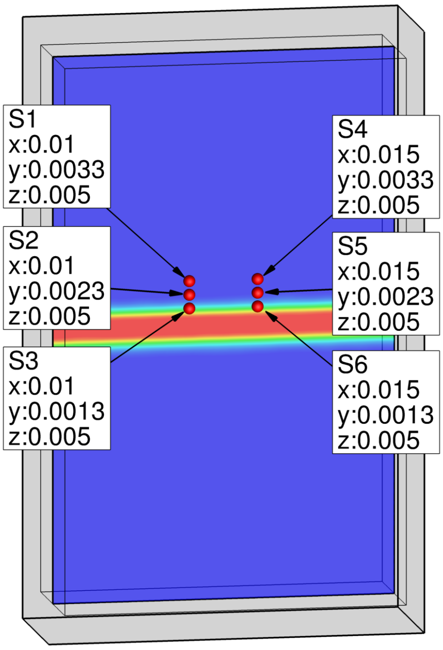

Figure 2: Picture showing spark positions with its numbering.

parameter $d_j/\Theta = 20$ and spark located at point S4 (see Fig. 2) with coordinates equal to: $x = 0.015\ m$, $y = 0.0033\ m$ and $z = 0.005\ m$. Occurrence of the ignition events for most relevant cases described in the following section are summarised in Table 3.

It can be observed that two global parameters are crucial for the successful ignition, i.e. transversal spark location and the jet Reynolds number. Comparison of the results obtained for setups A and B is shown in Figure 3 and for setups C and G in Figure 4. The plots present instantaneous local maximum temperature, fuel mass fraction and the flame volume which is defined as the volume occupied by the gas which temperature is higher than $1200\ K$. The computations of setups C to D and G to H led to analogical observations.

Apparently, the shear layer thickness d_j/Θ has marginal effect on ignition while slight change in spark location relative to the jet region along with the change of Re_{d_j} are the most influential parameters. In both cases (A and B setups) independently on the momentum thickness, sparking at the locations S3 and S6 lead to unsuccessful ignition. In opposition to locations S3 and S6 spark events in other locations result in successful ignition, (again) independently of d_j/Θ. From above results, it is seen that shifting spark location along the shear layer (x-direction) has marginal impact on likelihood of the ignition. This can be attributed to the use of temporally evolving jet rather than spatially evolving one. The turbulence intensity of HIT seems to be too weak to have a substantial impact on the flow field in different axial sparks locations. On the contrary, moving the spark transversely (y-direction) results in different ignition scenario. Changing the spark location may result either in ignition or its lack depending on the mixture composition and velocity gradient along transversal direction.

Table 2: Simulation setups

Case	Re_{d_j}	d_{32}	d_j/Θ
A	5000	20	20
B	5000	20	50
C	5000	50	20
D	5000	50	50
E	1000	20	20
F	1000	20	50
G	1000	50	20
H	1000	50	50

Table 3: Results summary

Case	S1	S2	S3
A	ignition	ignition	no ignition
B	ignition	ignition	no ignition
C	no ignition	no ignition	no ignition
D	no ignition	no ignition	no ignition
E	ignition	ignition	no ignition
F	ignition	ignition	no ignition
G	ignition	ignition	no ignition
H	ignition	ignition	no ignition

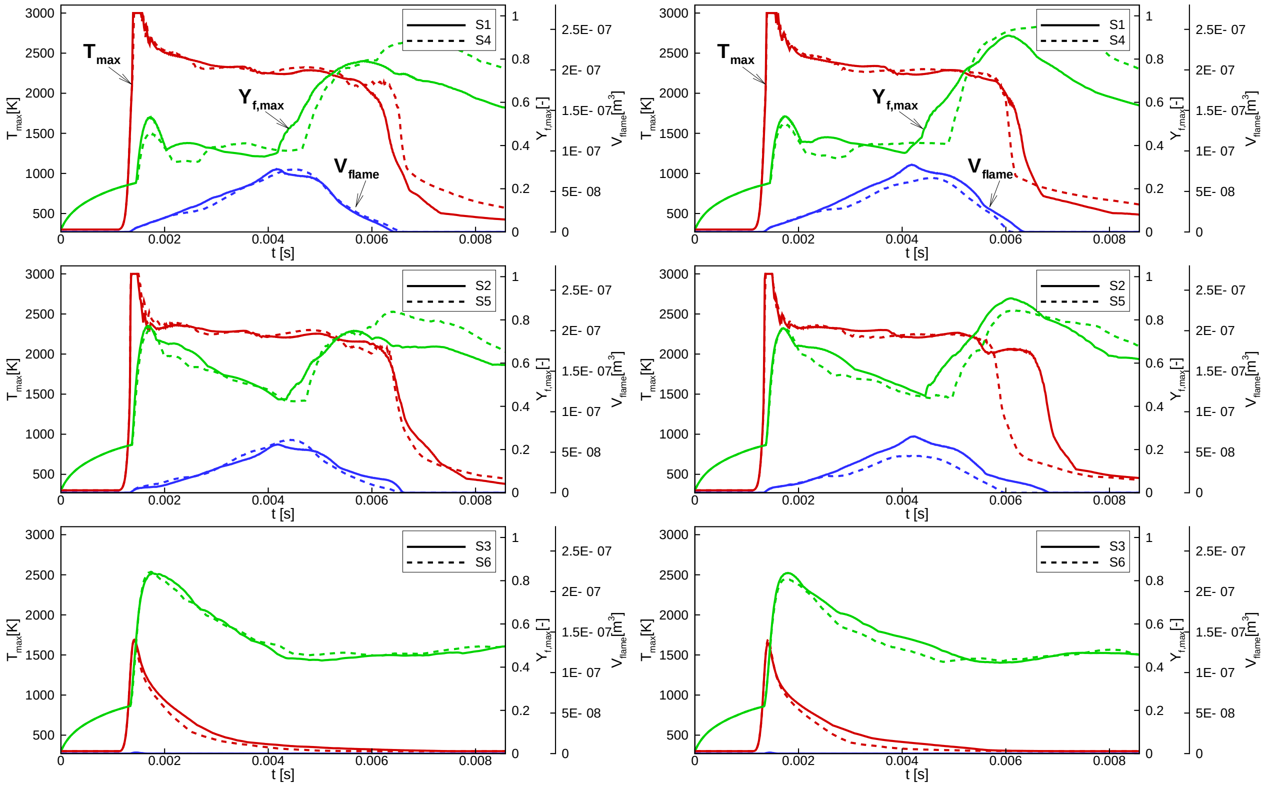

(a) Cases: AS1/AS4, AS2/AS5, AS3/AS6

(b) Cases: BS1/BS4, BS2/BS5, BS3/BS6

Figure 3: Plots showing instantaneous maximal temperature, fuel mass fraction and flame volume.

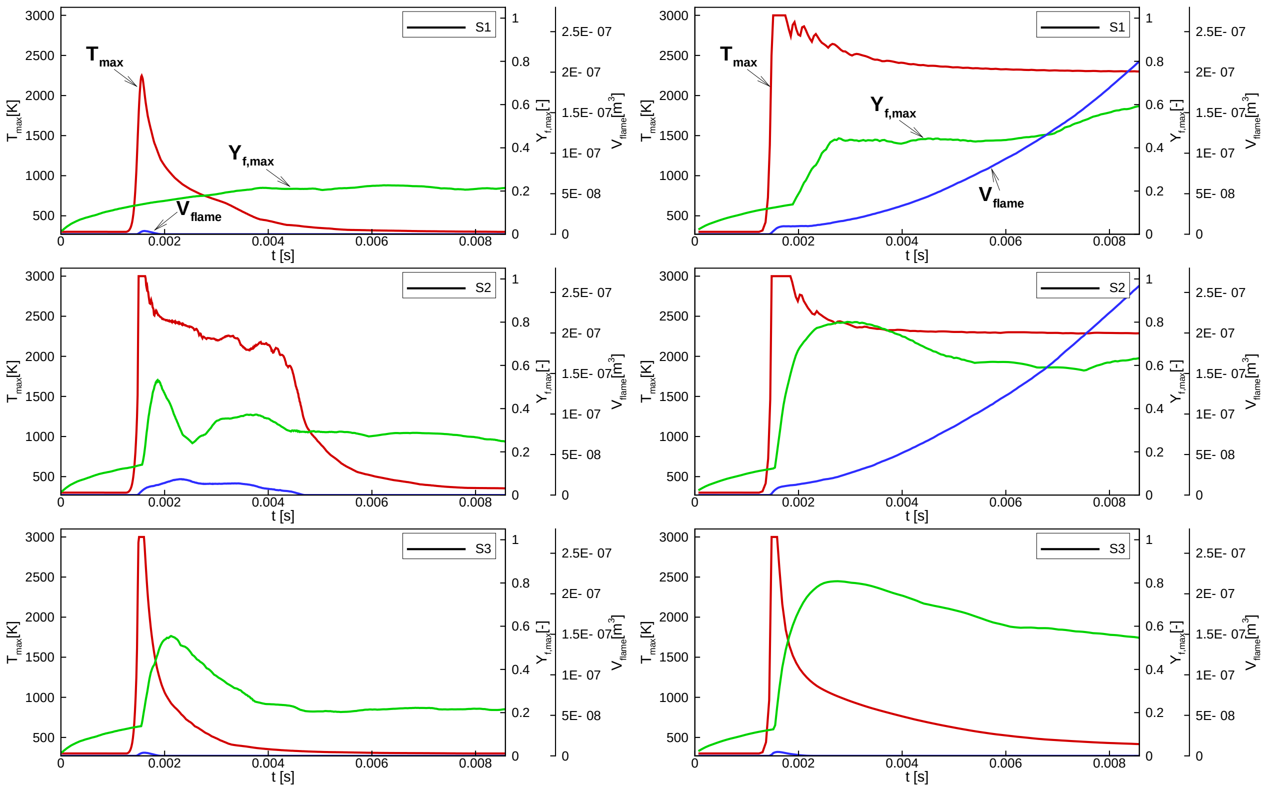

(a) Cases: CS1, CS2, CS3

(b) Cases: GS1, GS2, GS3

Figure 4: Plots showing instantaneous maximal temperature, fuel mass fraction and flame volume.

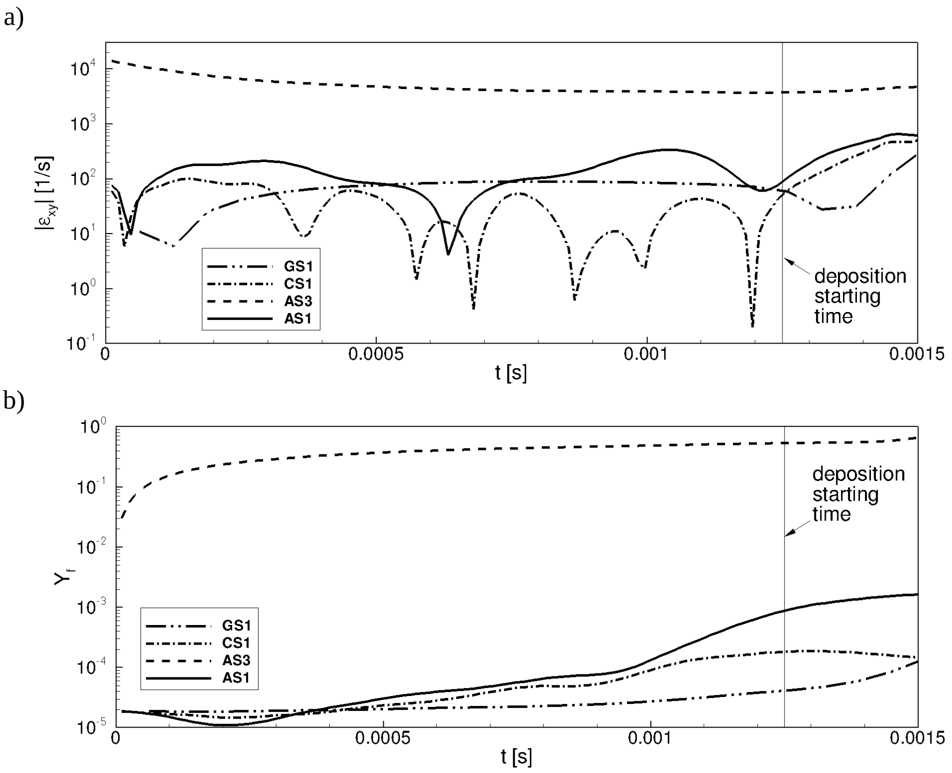

Figure 5: (a) Plot showing the instantaneous absolute values of the xy component of strain rate tensor. (b) Plot showing the instantaneous values of the local fuel mass fraction.

Figures 3a) and b) show that hot kernel survives only few Δ_t for setups A and B, excluding the S3 and S6 locations for which the flame kernel development is unsuccessful. An indication for that fact can be found in flame volume plot which shows slight growth during time period from 1.5 ms to 4 ms for which the temperature values reach maximum and then starts to fall. One can also notice that spark events in positions S3 and S6 led to only slight rise of maximal temperature comparing to positions S1, S2, S4 and S5. That could be due to the intense cooling effect of cold gas flowing in the vicinity of the spark. The heat from hot gaseous kernel is convected to the jet stream so the thermal energy deposited locally is lower than the activation energy preventing the initiation of chemical reactions. Figure 4 presents comparison of the results obtained for setups with Reynolds numbers $\mathrm{Re}_{d_j} = 5000$ (Fig. 4a) and Re_{d_j}=1000 (Fig. 4b) characterized by the same Sauter mean diameter of fuel droplets ($d_{32} = 50\,\mu m$). Evidently cases CS1, CS2, CS3 (Fig. 4a), did not succeed in ignition neither in the flame kernel initiation. On the

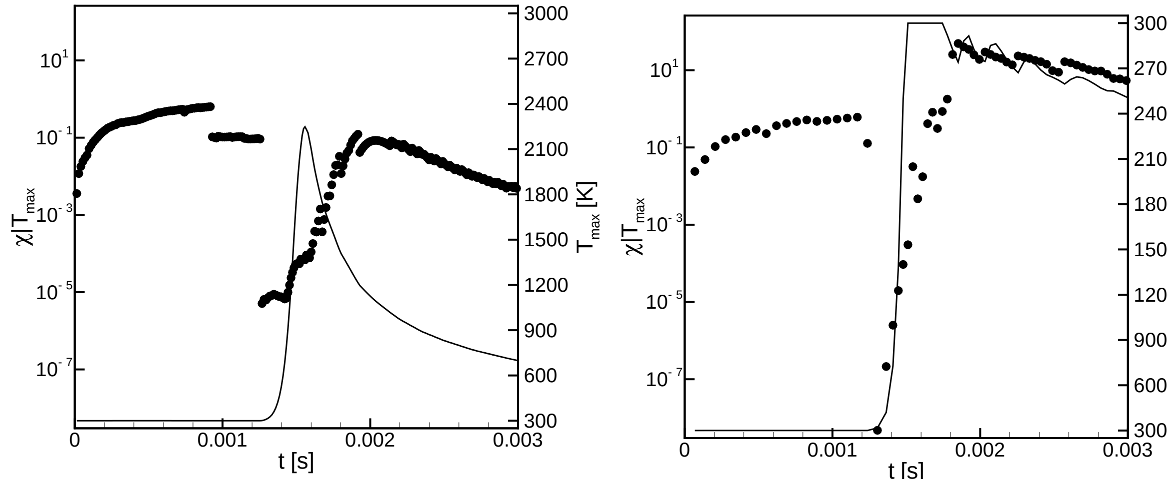
(a) Case CS1

(b) Case GS1

Figure 6: Plots showing time variations of scalar dissipation rate conditioned by the maximum temperature $\chi|T_{max}$ (dots) along with maximum temperature growth (lines).

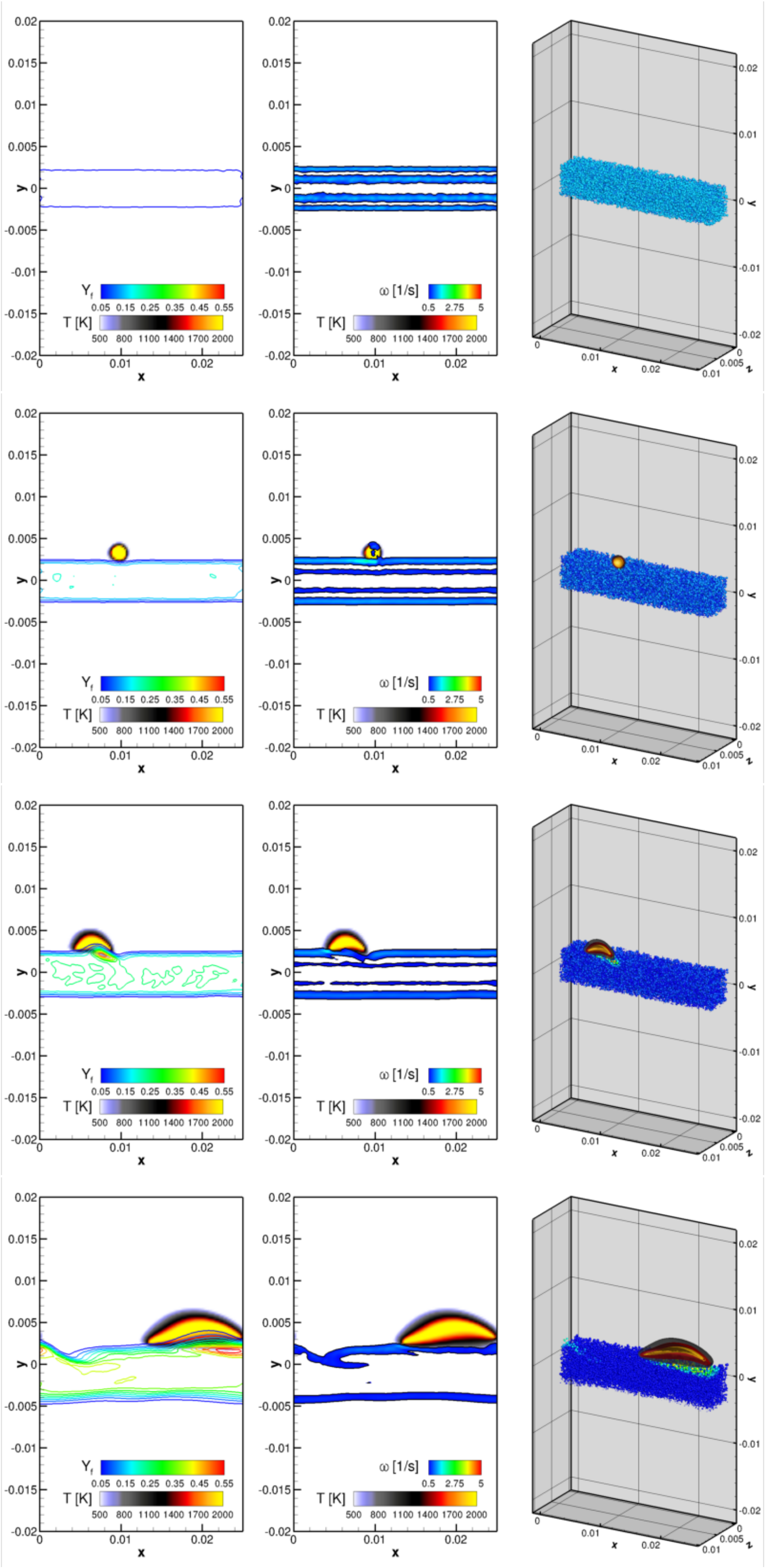

Figure 7: Contour plots of temporal evolution of temperature and vorticity magnitude with indication of spray stream depicted as spheres, showing flame initiation and propagation in setup GS1. The subfigures are given for time instances: 0.07, 0.35, 0.83 and 1.74 ms from top to the bottom one, respectively.

contrary, the cases that differ only in droplets diameter (setups AS1, AS2) have led to successful ignition. Hence, the importance of droplet diameter on ignition likelihood emerges. This agrees comparing the results of $\mathrm{Y_f}$ (setups A and C) for which the amount of maximum fuel content just before the energy deposition is lower when larger droplets are considered. Analysis of the isolated effect of Re_{d_j} for the same initial $d_{32} = 50\ \mu m$ (Fig. 4) leads to the observation that when larger droplets are present - ignition still may occur but only for lower Re_{d_j}. This manifests the case that the effect of evaporation rate cannot be itself viewed as the key reason for the lack of ignition. For higher Re_{d_j} three ignitions events are not successful. Steep velocity gradients cause fluid elements to strain and lead to increase in shear stresses within the shear layer between jet and co-flow thus preventing the ignition. Indeed, analysis of plots showing the instantaneous local values of strain rate tensor component ϵ_{xy} (Fig. 5a) and fuel content $\mathrm{Y_f}$ (Fig. 5b) before the energy deposition reveals differences in local flow conditions for cases CS1 and GS1. Monitored $\mathrm{Y_f}$ at the location S1 for this two setups differ only slightly, this was expected since the droplet diameters are the same while ϵ_{xy} shows completely different bahaviur for both Re_{d_j}. For higher Re_{d_j} the plot reveals highly irregular path while for lower Re_{d_j} is more smooth. Sharp oscillations of ϵ_{xy} values with amplitude of about 2 orders of magnitude preceeding the energy depostion event cause substantial straining of the hot kernel for higher Re_{d_j}. These findings are similar to the ones shown by Lacaze et al. (2009) where the effect of higher streamwise velocity on spark ignition resulted in lower ignition probability. Cases with lower Re_{d_j} (GS1, GS2) (Fig. 4b) lead to successful flame initiation and further flame propagation as can be seen from the plots of maximal temperature and flame volume. After the spark energy deposition is terminated, the maximum temperature falls slightly and reaches steady, near-adiabatic level while the flame volume continues to rise.

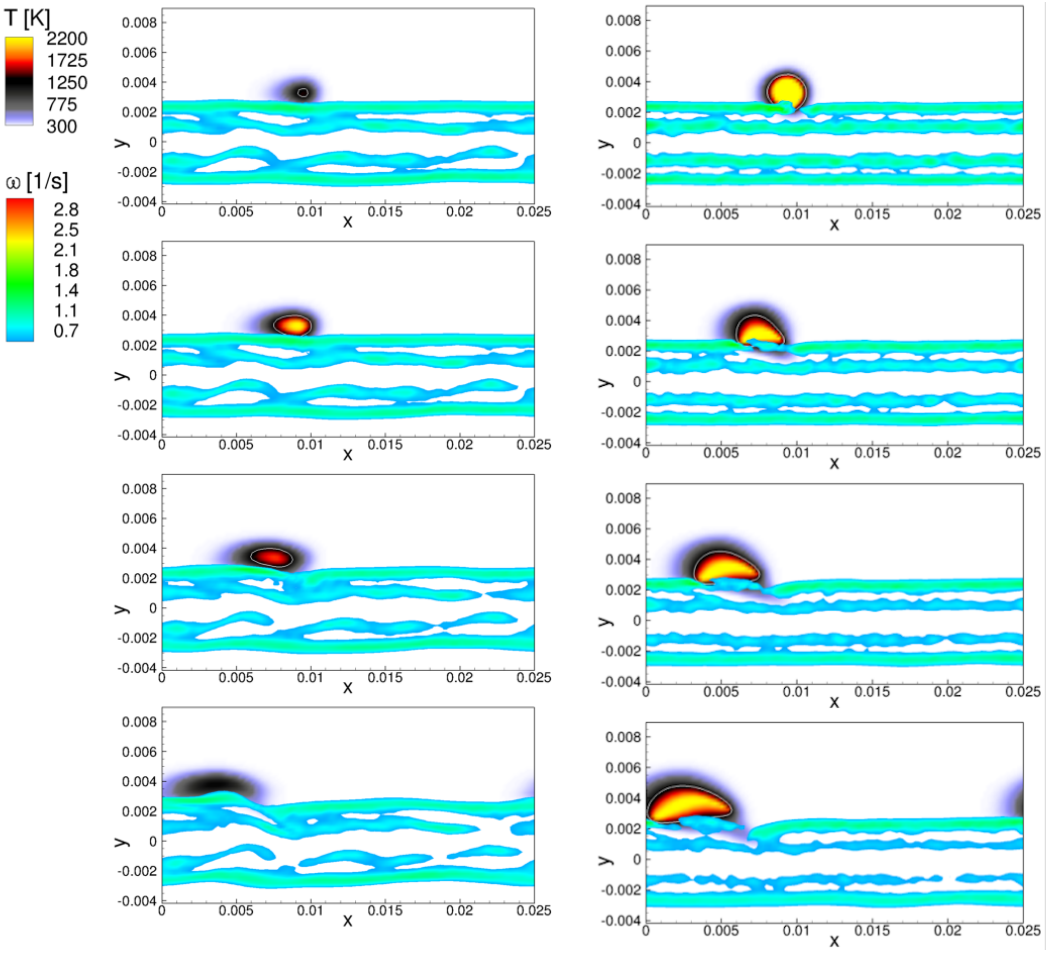

(a) (b)

Figure 8: Contours of temporal evolution of temperature and vorticity magnitude for setup: (a) CS1 and (b) GS1. The subfigures are given for time instances: 0.35, 0.48, 0.79 and 1.5 ms from top to the bottom one, respectively.

Figure 7 shows exemplary process of flame initiation and propagation in setup GS1. It is drawn along with contours of fuel mass fraction, vorticity magnitude and fuel spray indicated by the blue dots coloured by the droplets temperature. It can be seen that flame after its initiation grows in spherical manner until it starts to interact with upper edge of the slab of droplets. From that moment the thermal expansion of highly heated gas causes deviations from spherical shape because the velocity of expanding gas is different towards the co-flow and spray. The spray also affects the flame kernel by a rapid absorption of the heat because at that side convection is intense due to higher flow rates of cold gas towards the jet axis. Flame initially can not penetrate the spray rather than that it only slides on the edge of the droplet slab being fed by weakly evaporating fuel. Flame starts to penetrate the spray after it is dispersed by large flow structures. On the other hand, the cases GS3 and CS3 result in a rapid decrease of the maximum temperature shortly after the spark event. Indicating again, that the position S3 is not suitable for igniting the mixture. This is also manifested by a very intense strain rate and high local fuel load at point S3 (see AS3 in Fig. 5). However, the major cause of a misfire in case of setup GS3 was found to be attributed to the high local fuel content when the spark is placed within droplets stream. The fuel mass fraction exceeds the upper flammability limit for n-Heptane during spark deposition. Further analysis of setups CS1 and GS1 for which the only difference was in Re_{d_j} basis on a comparison of scalar dissipation rates χ accompanying spark energy deposition. Figure 6 shows scatter plots of χ conditioned with local maximum temperature $\chi|T_{max}$. It can be seen that at the beginning of the energy deposition the $\chi|T_{max}$ are more than 2 orders of magnitude lower for GS1 than for CS1, since χ is proportional to mixture fraction gradient, it indicates that the reactants are well stirred.

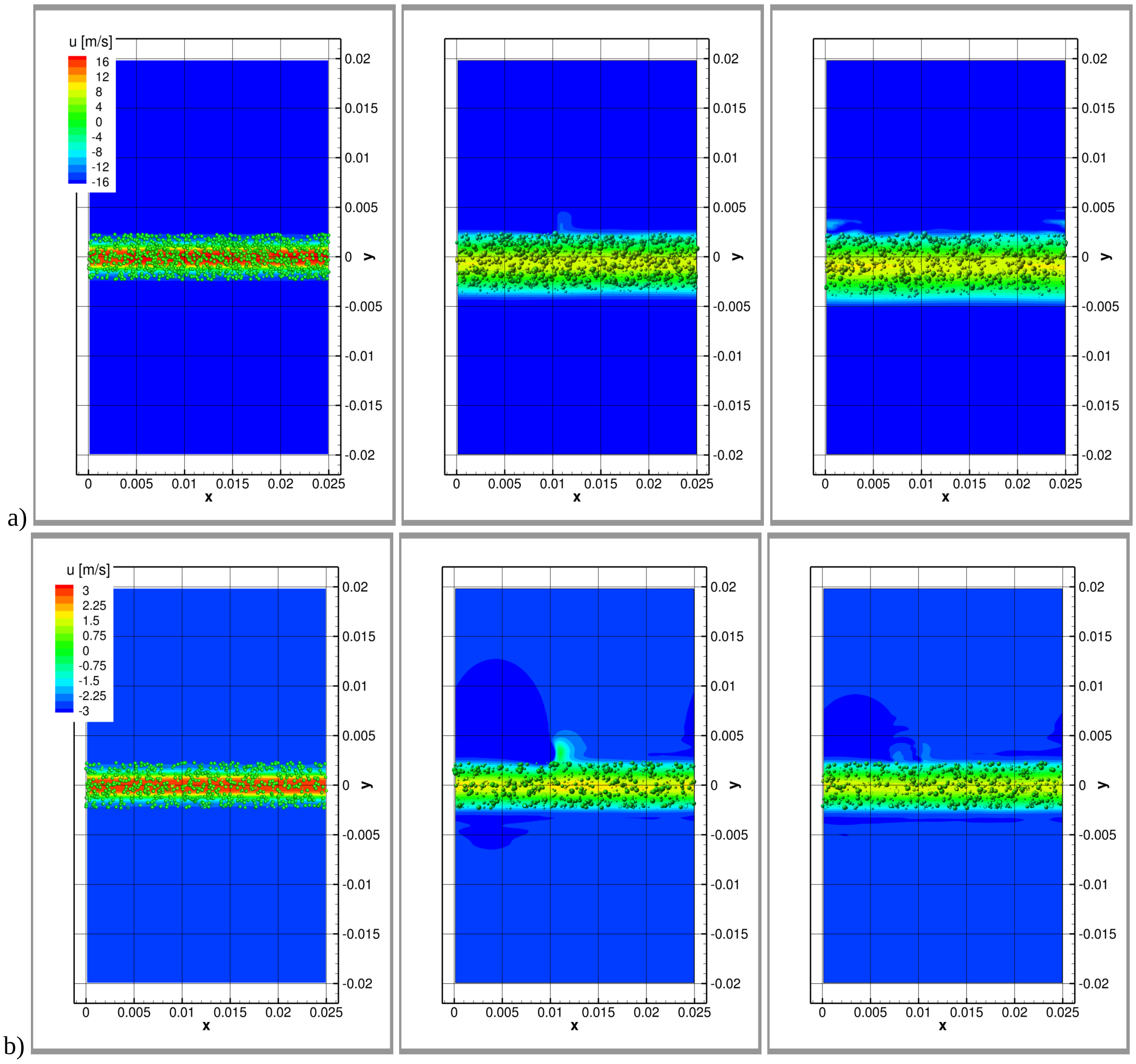

Figure 9: Contours of temporal evolution of axial velocity with imposed spray indicated by spheres of different size. Droplets are scaled with the D_d and coloured by its axial velocity component. Presented setups: (a) CS1, (b) GS1. The subfigures are given for time instances: 0.07, 1.5 and 2 ms from left to the right one, respectively.

The graphical representation of the vorticity and temperature fields presenting the flame kernel initiation (CS1) and its development (GS1) are shown in Figure 8. Initially, in both cases the flame kernel has spherical shape and is growing until reaching the jet shear layer. The kernel is further subjected to the steep velocity gradient that stretches it intensively. Being stretched by the shear forces the flame starts to propagate along the upper shear layer. The cold jet stream of droplets as well as high velocity inside the jet cause substantial heat convection from the flame kernel so its entrance inside the fuel stream is prevented. The flame slides along the shear layer until the jet is developed and spray is more dispersed. Further, bigger flow structures start to develop within the jet. These structures along with the thermal expansion of hot gasses lead to droplet dispersion and allow the flame to penetrate the spray slab. At that point the differences between CS1 and GS1 are more pronounced. Rapid heat convection in case of setup CS1 caused by higher flow rate adjacent to the hot gas kernel causes the kernel's temperature to drop. The flame kernel of GS1 survives because the reaction is self-sustained and heat release is higher than the heat loses. This allows the flame to continue its growth primarily in the upper side of droplet slab with gradual penetration through the fuel jet.

By analysing the results from cases CS1 and GS1 shown in Figure 9 one can learn about droplet dispersion caused by the flow. Pictures of several succeeding time instances present contour plots of axial velocity with imposed spheres indicating the fuel spray which are scaled by the D_d and coloured by its axial velocity values. It can be seen that in case of higher Re_{d_j} (Fig. 9a) the inertia of the droplets is quickly overtaken by the jet stream so the spray follows the flow as it is indicated by the same colors of droplets and contours. For flow with lower Re_{d_j} (Fig. 9b) at the same time instances, the temporal development of the jet region is weaker resulting in lower spray slab width than observed for higher Re_{d_j}. It can be also noticed that at this point, the inertia of the droplets is more pronounced because even for furthest time instance the velocity differences between droplets and flow are noticeable. Both cases indicate that even at flow times two times greater than t_0 (third picture) spray is not dispersed anywhere in the domain but rather trapped by the shear layers on both sides of the jet. The initial width of the spray slab only slightly increases until later times when larger flow structures breaks the slab and throw droplets elsewhere (not shown here). This occurs faster in the case with higher Re_{d_j}. It can be also seen that smaller droplets with the smaller Stokes numbers mostly migrate towards the jet axis, where the velocity is highest. On the other hand, the large droplets travel rather near the shear layers.

6 Summary

The paper presents a numerical ILES study of a spark forced ignition in temporally evolving two-phase planar jet that is subjected to the strong shear forces acting at the shear layer, which along with growing turbulent fluctuations cause development of the large turbulent structures. The current parametric studies include examination of several different spark locations, two different initial droplets distributions and selected flow parameters, i.e. momentum thickness and jet Reynolds numbers. The obtained results allowed to formulate conclusions that are consistent with the findings from the previous studies on turbulent spray flames:

- marginal effect of streamwise spark locations is observed due to the low initial turbulence intensity and use of temporally developing jet configuration;
- the opposed is observed for the transversal spark locations; igniting very close to the droplets stream or within it can lead to the substantial heat absorption by the droplets, preventing formation of the high temperature kernel that would be sufficient to drive chemical reaction and heat release;
- igniting in regions of high strain rate can lead to the flame quenching even if fuel mass fraction does not exceed the flammability limits;
- hot kernel initiated in high Reynolds number flows is subjected to intense stretching, resulting in expansion of the heated region what causes heat diffusion into the greater volume thus decreasing the peak temperature;
- the flame firstly slides along the surface of the droplets stream until the spray is dispersed by the large flow structures and afterwards penetrates the spray;
- smaller droplets with lower Stokes numbers gather in the vicinity of the jet axis while larger droplets are shifted near the shear layers what augments the evaporation rates and fuel diffusion outside the spray stream.

Acknowledgements

This work was supported by grant 2015/17/B/ST8/03217 (National Science Centre, Poland) and statutory funds BS/PB-1-103-3010/11/P. PL-Grid infrastructure was used to carry out the computations.

References

Ahmed, S.; Mastorakos, E.: Spark ignition of lifted turbulent jet flames. *Combust. Flame*, 146, (2006), 215 – 231.

Chakraborty, N.; Mastorakos, E.: Direct numerical simulations of localised forced ignition in turbulent mixing layers: The effects of mixture fraction and its gradient. *Flow Turbul. Combust.*, 80, (2007), 155 – 186.

Duwig, C.; Nogenmyr, K.; Chan, C.; Dunn, M.: Large eddy simulations of a piloted lean premix jet flame using finite-rate chemistry. *Combust. Theor. Model.*, 15, (2011), 537 – 568.

Elghobashi, S.: On predicting particle-laden turbulent flows. *Appl. Sci. Res.*, 52, (1994), 309 – 329.

Fernandez-Tarrazo, E.; Sanchez, A.; Linan, A.; Williams, F.: A simple one-step chemistry model for partially premixed hydrocarbon combustion. *Combust. Flame*, 147, (2006), 32 – 37.

Hawkes, E.; Ramanan, S.; Sutherland, J.; Chen, J.: Scalar mixing in direct numerical simulations of temporally evolving plane jet flames with skeletal CO/H2 kinetics. *Proc. Combust. Inst.*, 31, (2007), 1633 – 1640.

Jones, W.; Prasad, V.: Large eddy simulation of the sandia flame series (d-f) using the eulerian stochastic field method. *Combust. Flame*, 157, (2010), 1621 – 1636.

Kuban, L.; Stempka, J.; Wawrzak, A.; Tyliszczak, A.: DNS and ILES study of ethanol spray forced-ignition in a time-evolving mixing layer. *MCS-10: Tenth Mediterranean Combustion Symposium*, Naples, 2017.

Lacaze, G.; Richardson, E.; Poinsot, T.: Large eddy simulation of spark ignition in a turbulent methane jet. *Combust. Flame*, 156, (2009), 1993 – 2009.

Mastorakos, E.: Forced ignition of turbulent spray flames. *Proc. Combust. Inst.*, 000, (2016), 1 – 17.

Miller, R.; Harstad, K.; Bellan, J.: Evaluation of equilibrium and non-equilibrium evaporation models for many-droplet gas-liquid flow simulations. *Int. J. Multiph. Flow*, 24, (1998), 1025 – 1055.

Neophytou, A.; Mastorakos, E.; Cant, R.: DNS of spark ignition and edge flame propagation in turbulent droplet-laden mixing layers. *Combust. Flame*, 157, (2010), 1071 – 1086.

O’Loughlin, W.; Masri, A.: A new burner for studying auto-ignition in turbulent dilute sprays. *Combust. Flame*, 158, (2011), 1577 – 1590.

Passot, T.; Pouquet, A.: Numerical simulation of compressible homogeneous flows in the turbulent regime. *J. Fluid Mech.*, 181, (1987), 441 – 466.

Schmidt, H.; Schumann, U.: Coherent structure of the convective boundary layer derived from large eddy simulation. *J. Fluid Mech.*, 200, (1989), 511 – 562.

Spalding, D.: The combustion of liquid fuels. *Proc. Combust. Inst.*, pages 847 – 864.

Stempka, J.: Impact of subgrid modelling and numerical method on autoignition simulation of two-phase flow. *Arch. Thermodyn.*, 39, (2018), 55 – 72.

Tyliszczak, A.: High-order compact difference algorithm on half-staggered meshes for low mach number flows. *Comput. Fluids*, 127, (2016), 131 – 145.

Vreman, W.: An eddy-viscosity subgrid-scale model for turbulent shear flow: Algebraic theory and applications. *Phys. Fluids*, 16, (2004), 3670 – 3681.

Wawrzak, A.; Tyliszczak, A.: LES-CMC simulations of a turbulent hydrogen jet in oxy-combustion regimes. *Int. J. Hydrogen Energ.*, 41, (2016), 9705 – 9717.

Address: Institute of Thermal Machinery, Czestochowa University of Technology, Faculty of Mechanical Engineering and Computer Science, Armii Krajowej 21, 42-201 Czestochowa, Poland
email: `stempka@imc.pcz.pl`

DOI: 10.24352/UB.OVGU-2019-015 TECHNISCHE MECHANIK, 39, 1, (2019), 162 – 174
submitted: July 6, 2018

One-Dimensional Turbulence Simulations for Reactive Flows in Open and Closed Systems

T. Starick, J. A. Medina M., H. Schmidt

The One-Dimensional Turbulence (ODT) model is applied to reactive flows in open and closed systems represented by a lifted jet flame in a vitiated coflow, and a constant volume autoignition configuration, respectively. ODT is a one-dimensional model for turbulent flow simulations, which uses a stochastic formulation to represent the effects of turbulent advection. Diffusion and reaction effects along the ODT domain are considered by deterministic evolution equations.

This work is an effort to verify the applicability and efficiency of the model for open and closed systems. In the open system case, ODT results are compared against experimental results of a lifted methane/air jet flame detailed in the work of Cabra et al. (2005). In the closed system case, a periodic, constant volume domain is used to investigate the sensitivity of the ignition evolution to initial temperature and composition inhomogeneities of a lean n-heptane/air mixture. In the latter context, ODT results are compared to DNS results from Luong et al. (2015). The results for the jet and constant volume configuration show a reasonable match with the experimental and DNS data, considering the reduced order of the model and the underlying assumptions for each case. At the jet configuration, a dependence of the flame evolution on the turbulence intensity parameter can be seen. For the closed system, initial temperature and composition inhomogeneities allow a mitigation of the undesirable rapid pressure rise due to locally different ignition delay times.

1 Introduction

The topic of low temperature homogeneous premixed combustion has led to the development and optimisation of Homogeneous Charge Compression Ignition (HCCI) engines. These combine the benefits of spark and compression ignition engines. They are, however, confronted with the problem of simultaneous reaction of homogeneous mixture zones entailing a rapid pressure rise, which results in pressure ringing, engine knocking, or even the destruction of the engine block. Stratification is, therefore, an aspect that needs to be considered in the design to avoid a rapid pressure rise (Luong et al., 2015). Computationally, this has been studied by means of the effects of disturbances or inhomogeneities in reactive mixtures and temperature distributions by Yoo et al. (2011) and Luong et al. (2015).

The topic of flame extinction and flame stabilisation has also central importance, and it has been traditionally addressed experimentally and theoretically by the study of simplified jet flames. Lifted jet flames are a special category of jet flames, where the stabilised flame is lifted from the burner by increasing the fuel or air coflow velocity (Lyons, 2007). These flames may allow, e.g., the minimisation of the damage provoked by the flame to the burner construction materials. Past studies of Cabra et al. (2005) have confirmed autoignition as a mechanism for flame stabilisation in lifted flames.

There are clear limitations for fully accurate computational investigations of these phenomena. The most reliable approaches, Direct Numerical Simulations (DNS), are prohibitively expensive, since they require the complete resolution of all scales of interactions between turbulence and chemistry (Yoo et al., 2011; Yu and Bai, 2013; Luong et al., 2015). In contrast, 1-D models are still attractive for research due to the broad physical insight that they might offer at the expense of their relatively cheap computational cost. In an effort to resolve all relevant scales, yet still be able to achieve realistic Reynolds number flows in numerical simulations, Alan Kerstein formulated the One-Dimensional Turbulence (ODT) model (Kerstein, 1999). ODT is an efficient alternative in comparison to DNS, and an alternative in comparison to Reynolds-Averaged Navier-Stokes (RANS) and Large-Eddy Simulation (LES) approaches, as demonstrated by several investigations done so far by Kerstein et al. (2001); Ashurst and Kerstein (2005); Lignell et al. (2013); Jozefik et al. (2015); Fragner and Schmidt (2017) and Medina M. et al. (2018).

In this study, a broad, yet brief overview of the ODT modelling framework for open and closed combustion systems is presented. Lignell et al. (2013) presented a comprehensive overview of all possible applications of ODT. The latter study, however, missed the topic of constant volume modelling completely. Initially homogeneous, yet disturbed, temperature and composition fields are evaluated with a recent ODT formulation in a constant volume, periodic configuration (Medina M. et al., 2018). Results for a lifted jet flame in a vitiated coflow, following a more traditional ODT formulation are shown as well (Echekki et al., 2001; Lignell et al., 2013).

2 ODT Model Formulation

2.1 Turbulent Advection and Eddy Event Implementation in ODT

The characteristic signature from ODT is the triplet map transformation (Kerstein, 1999). The implementation of a triplet map (eddy event) is a representation of the turbulent advection effects in an incompressible flow. This is a mere kinematic representation of the flow, and thus the analysis of the effects of a triplet map should be discussed within the framework of the momentum equation in an incompressible regime (divergence-free velocity field given by u_j, for $j = 1, 2, 3$). Starting from the momentum equation, it is possible to decompose the advection term into linear and non-linear contributions. The pressure can also be considered as a scalar field resulting from the sum of linear and non-linear contributions. Considering only linear effects, the momentum equation for incompressible flows in ODT, assuming the 1-D line direction as y, results in,

$$\frac{\partial u_j}{\partial t} = \nu \frac{\partial^2 u_j}{\partial y^2} + E_j + \mathit{\Gamma}. \tag{1}$$

A source term $\mathit{\Gamma}$ has been added to the original ODT momentum equation as described in Kerstein et al. (2001). This symbolises the linear effects of mean advection or a mean forcing pressure gradient. This convention was chosen to represent the source term treatment in ODT (Lignell et al., 2013; Fragner and Schmidt, 2017). In Eq. (1), t is the time, $\nu = \mu/\rho$ is the kinematic viscosity (μ is the dynamic viscosity and ρ the density) and E_j represent changes induced by the triplet map and pressure scrambling operations in ODT detailed in the work of Kerstein et al. (2001).

In general, the triplet map implementation causes a change in a scalar profile along the line direction, according to the transformation rule,

$$\psi(y) \rightarrow \psi[f(y)]. \tag{2}$$

Here, ψ is any scalar quantity defined in the ODT line at a position y and subsequently mapped to a position $f(y)$ by the transformation rule (Kerstein, 1999). The transformation rule is measure preserving, which for constant density and a scalar velocity component implies conservation of $\int u^0 \mathrm{d}y$, $\int u^1 \mathrm{d}y$, $\int u^2 \mathrm{d}y$; i.e., the transformation implies conservation of mass (length), momentum and energy along the line. Treating the velocity as a vector requires the use of a Kernel function, which redistributes the available kinetic energy among velocity components (Kerstein et al., 2001). Since it is clear that for this work, the previous conception of ODT with constant density is rather limited, the expansion for the variable density formulation, introduced by Ashurst and Kerstein (2005), is used for the mapping of the velocity field u_j, namely

$$u_j(y) \rightarrow u_j[f(y)] + b_j K(y) + c_j J(y). \tag{3}$$

Here, $K(y)$ and $J(y)$ are kernel functions, as described in Ashurst and Kerstein (2005), while b_j and c_j are the respective kernel coefficients for each velocity component. The reader should note that, although the introduction of two kernels for the velocity mapping in Eq. (3) allows redistribution of available kinetic energy in a variable density line, the fundamental conception of the map as a measure preserving transformation is more readily applicable for solenoidal flows (Lignell et al., 2013) (and in fact, it is formulated by Ashurst and Kerstein (2005) for flows with negligible compressibility effects). It is therefore convenient to introduce a splitting of the velocity field into its solenoidal and irrotational components. The solenoidal component (rotational part) is readily handled by the eddy event conception in ODT, while the irrotational component $u_{tot,j}$ can be decomposed into a deformation component $u_{D,j\ \text{(deformation)}}$ and a linear advection component $u_{A,j,\ \text{(net advection)}}$ as described in Medina M. et al. (2018).

$$u_{tot,j} = u_{A,j\ \text{(net advection)}} + u_{D,j\ \text{(deformation)}} \tag{4}$$

The net advection of u_j in Eq. (4) refers to the sum of mean and turbulent advection. This is the starting point for the formulation of the set of governing equations in the applicable ODT model. u_j is governed by a quasi-incompressible momentum evolution, while $u_{D,j}$ arises exclusively from the variable-density (compression and expansion) effects along the line ($u_{D,2} = u_D$ and $u_{D,1} = u_{D,3} = 0$) (Medina M. et al., 2018).

In ODT, eddy events are sampled from a joint Probability Density Function (PDF) $P(l, y_0, t)$ of eddy sizes l and positions y_0 at a given time t (Kerstein, 1999). The reconstruction of the PDF at every instant of time is prohibitively expensive, since it requires evaluating all possible potential eddies with any size l at any position y_0. A discrete approximation of the PDF is used instead, constructed by a combination of the rejection method and the thinning method (Kerstein, 1999). The sampling conforms then with a defined, statistical Poisson process. Generally speaking, an acceptance probability of the eddy $P_a(l, y_0, t)$ is obtained by the expression,

$$\frac{\lambda(l, y_0, t)}{f(l)g(y_0)}\Delta t_{sampling} = P_a(l, y_0, t). \tag{5}$$

Eq. (5) is able to correctly approximate the eddy sampling from $P(l, y_0, t)$, as long as the sampling time interval $\Delta t_{sampling}$ is sufficiently small ($\Delta t_{sampling} << 1$). $\lambda(l, y_0, t)$ is an eddy rate in ODT, while $f(l)$ and $g(y_0)$ are assumed PDFs for the eddy size and position, as in Lignell et al. (2013). $\lambda(l, y_0, t)$ can be modelled based on a dimensional analysis relating energetic contributions to the inverse of an eddy turnover time τ, as in Jozefik et al. (2015) and Medina M. et al. (2018),

$$\lambda(l, y_0, t) = \frac{C}{l^2\tau} = \frac{C}{l^2}\left[\frac{2K_0}{\rho_0}\left(E_{kin} - ZE_{vp} + E_{pe}\right)\right]^{1/2}. \tag{6}$$

Eq. (6) models the eddy turnover time in ODT in terms of the available (kinetic) energy E_{kin}, an energetic viscous penalty E_{vp}, and a potential energy term E_{pe}. The latter is added in order to influence the eddy selection due to the variable density line (Jozefik et al., 2015; Medina M. et al., 2018). C and Z are model parameters, which are normally calibrated for a specific flow configuration. The terms $K_0 = l^{-3}(\int_{y_0}^{y_0+l} K^2 \mathrm{d}y)$ and $\rho_0 = \int_{y_0}^{y_0+l} \rho K^2 \mathrm{d}y$, are used with the definitions of the different energies,

$$E_{kin} - ZE_{vp} + E_{pe} = \left[K_0\left(Q_1 + Q_2 + Q_3\right)\right] - Z\left[\frac{1}{2}\left(\frac{\mu_{eddy}^2}{\rho_{eddy} l}\right)\right] + \left[K_0 \int_{y_0}^{y_0+l} \frac{\partial u_D}{\partial t} K\left(\rho - \rho_{eddy}\right)\mathrm{d}y\right]. \tag{7}$$

Here, Q_1, Q_2 and Q_3 are the available energies per velocity component, as in Ashurst and Kerstein (2005). μ_{eddy} and ρ_{eddy} are line averages of the dynamic viscosity and density (averages over the eddy length).

After an eddy is implemented, a deterministic catch up takes place up to the physical time at which the eddy was deemed to be implemented. This is the instant of time t at which the eddy was accepted according to the sampling based on $P_a(l, y_0, t)$. The deterministic catch up mechanism consists of a time-advancement of the 1-D diffusion/reaction evolution equations in ODT, starting at the instant of time corresponding to the last eddy implementation, up to the time t. Therefore, time advances constantly due to the increments $\Delta t_{sampling}$. The numerical solution as a whole advances effectively with every performed catch up. The deterministic 1-D diffusion/reaction evolution equations in ODT are detailed in the next section.

2.2 ODT Diffusion/Reaction Evolution for Closed Systems (Constant Volume Configuration)

This section gives an overview of the diffusion/reaction evolution equations for closed systems used in ODT. For a detailed description of the numerical advancement for the ODT diffusion/reaction evolution equations, the reader is referred to Appendix I.

The diffusion/reaction evolution equations in ODT can be derived from the application of the Reynolds Transport Theorem (RTT) to the intensive quantities (ϵ) of mass, momentum and energy. For reference, the Lagrangian formulation of the equations, using a zero Mach number limit approximation, is obtained and explained in Lignell et al. (2013). Here, the equations obtained from Lignell et al. (2013) are only mentioned and written in an equivalent differential form. Momentum conservation in the ODT line, considering that the cell interfaces move with the mass average velocity (no ϵ property fluxes across the cells), implies, for the quasi-incompressible treatment of the velocity u_j,

$$\rho\frac{\mathrm{d}u_j}{\mathrm{d}t} = \frac{\partial}{\partial y}\left(\mu\frac{\partial u_j}{\partial y}\right). \tag{8}$$

Here, $\mathrm{d}/\mathrm{d}t$ symbolises the Lagrangian time derivative. Similarly, diffusion and reaction evolution of species mass fractions Y_k ($k \in \{1, 2, ...N\}$), is given by,

$$\rho \frac{\mathrm{d}Y_k}{\mathrm{d}t} = \frac{\partial}{\partial y}\left(\rho D_k \frac{\partial Y_k}{\partial y} + \frac{\rho D_k Y_k}{M}\frac{\partial M}{\partial y}\right) + \dot{w}_k. \tag{9}$$

In Eq. (9), D_k is the kth species mixture-averaged diffusion coefficient, M is the mean molecular weight of the mixture and $\dot{w}_k$ is the kth species reaction rate. The Hirschfelder and Curtis' approximation for the species diffusion velocities is considered here, i.e. $V_k = -D_k\left(Y_k^{-1}\partial Y_k/\partial y + M^{-1}\partial M/\partial y\right)$.

The evolution equation for the enthalpy of the mixture h is,

$$\rho \frac{\mathrm{d}h}{\mathrm{d}t} = \frac{\mathrm{d}P}{\mathrm{d}t} + \frac{\partial}{\partial y}\left(\lambda \frac{\partial T}{\partial y}\right) - \frac{\partial}{\partial y}\left[\sum_{k=1}^{N}(h_k \rho V_k Y_k)\right]. \tag{10}$$

In Eq. (10), P is the leading order thermodynamic pressure, λ is the thermal conductivity, T is the temperature of the mixture and h_k is the kth species specific enthalpy.

As in Medina M. et al. (2018), the divergence condition for the deformation velocity allows the calculation of the temporal rate of change of the thermodynamic pressure (applying an integration over the ODT line). It also allows the calculation of the dilatation of the cells, which is required to enforce mass conservation, once the new thermochemical state is known (local divergence of each cell).

$$\frac{\partial u_D}{\partial y} = -\frac{1}{\gamma P}\frac{\mathrm{d}P}{\mathrm{d}t} + \Psi. \tag{11}$$

In Eq. (11), γ is the ratio of specific heats and Ψ is defined as

$$\begin{aligned}\Psi = \frac{1}{\rho c_p T}&\left\{\frac{\partial}{\partial y}\left(\lambda \frac{\partial T}{\partial y}\right) - \frac{\partial}{\partial y}\left[\sum_{k=1}^{N}(h_k \rho V_k Y_k)\right]\right.\\ &\left.+\sum_{k=1}^{N}\left[h_k\left(\frac{\partial}{\partial y}(\rho V_k Y_k) - \dot{w}_k\right)\right]\right\}\\ &-\frac{M}{\rho}\sum_{k=1}^{N}\left\{\frac{1}{M_k}\left[\frac{\partial}{\partial y}(\rho V_k Y_k) - \dot{w}_k\right]\right\},\end{aligned} \tag{12}$$

c_p is the specific heat capacity at constant pressure. The equations for species and enthalpy evolution are solved by means of a Strang-Splitting method (Medina M. et al., 2018). The $\mathrm{d}P/\mathrm{d}t$ term used in Eq. (10) is calculated from the integration of Eq. (11). The resulting pressure at the end of the advancement is calculated by a closed form of the ideal gas law,

$$P = \frac{R\left(\int_{y=0}^{y=L}\rho \mathrm{d}y\right)_{t=0}}{\int_{y=0}^{y=L}\left(T\sum_k \frac{Y_k}{M_k}\right)^{-1}\mathrm{d}y}. \tag{13}$$

Here, L is the length of the 1-D domain and R is the universal gas constant. The quantity in the numerator in Eq. (13) indicates the initial mass of the line, which remains constant during the simulation. After the pressure update, the density is calculated by means of the ideal gas law. Momentum is integrated with an implicit Euler method prior to the pressure and density update, but with the updated temperature derived from the advancement of h and Y_k. Finally, cell sizes are adjusted to enforce mass conservation, based on the use of the definition $u_D = \mathrm{d}y/\mathrm{d}t$ in the local divergence constraint, Eq. (11) (evaluated at the new thermochemical state) (Medina M. et al., 2018).

2.3 ODT Diffusion/Reaction Evolution for Open Systems (Jet Configuration)

The diffusion/reaction equations for the open system configuration are in general the same ones as those derived for the closed system. For open systems, we have $\mathrm{d}P/\mathrm{d}t = 0$ in Eq. (10) and (11). Eq. (13) is also redundant, since the pressure stays constant.

The divergence condition is enforced in the open configuration in a slightly different way. It is possible to rewrite Eq. (11) as

$$\frac{\partial u_D}{\partial y} = -\frac{1}{\rho}\frac{\mathrm{d}\rho}{\mathrm{d}t}. \tag{14}$$

Within the Lagrangian framework of the model, it is possible to approximate numerically $\mathrm{d}\rho/\mathrm{d}t$. Using a Leapfrog time approximation and applying the definition of velocity $u_D = \mathrm{d}y/\mathrm{d}t$, while considering the midpoint time-levels as the averages of time-levels n and $n+1$, mass conservation is obtained as in Lignell et al. (2013),

$$(\rho\Delta y)^{n+1} = (\rho\Delta y)^{n}. \tag{15}$$

Eq. (15) corresponds to the integral conservation of mass within a cell. It dictates the corresponding adjustment of the cell sizes that conforms with mass conservation in an open system. Unlike Eq. (11) for closed systems, using Eq. (15) may result in changes of the overall 1-D domain length.

In this work, a comparison with stationary spatially developing round jet flames is intended. Following Echekki et al. (2001), the 1-D domain is advected in z-direction using an instantaneous bulk velocity $\overline{u}(t)$,

$$z(t) = z(t_0) + \int_{t_0}^{t} \overline{u}(t')\mathrm{d}t'. \tag{16}$$

The bulk velocity in Eq. (16) is calculated by the sum of the free-stream (coflow) velocity u_∞ and the ratio of the integrated momentum flux to the integrated mass flux,

$$\overline{u}(t) = u_\infty + \left.\frac{\int_{-\infty}^{\infty} \rho\,(u-u_\infty)^2\,\mathrm{d}y}{\int_{-\infty}^{\infty} \rho\,(u-u_\infty)\,\mathrm{d}y}\right|_t. \tag{17}$$

Unlike in the closed configuration, the open configuration is solved by means of a first-order explicit Euler advancement, as in Lignell et al. (2013).

3 Results

3.1 Closed System (Constant Volume Configuration)

Simulations for constant volume autoignition of a lean n-heptane/air mixture were performed with ODT using the same settings as in the DNS from Luong et al. (2015). The domain extends over 3.2 mm. Periodic boundary conditions are applied on the ODT line. The initial grid is discretised by a uniform distribution of 1280 cells along the line. Randomised initial fields for the velocity and scalars were generated based on a Passot-Pouquet spectrum (Passot and Pouquet, 1987) that conforms with a given mean and RMS fluctuation value, as in Oevermann et al. (2008) and Medina M. et al. (2018). The same version of the ODT code as in Medina M. et al. (2018) was used for the simulations and applies an adaptive solver that enables local temporal changes in the resolution, in order to accurately capture all scales along the ODT line (Lignell et al., 2013).

Table 1 lists the settings for mean initial temperature and equivalence ratio, T_0 and ϕ_0, and fluctuations of temperature T', equivalence ratio ϕ' and velocity u' for the investigated cases. The most energetic length scales for

Table 1: Parameters of the simulation cases 1-4, considering either temperature T or composition Φ inhomogeneities.

Case	T_0 (K)	T' (K)	ϕ_0 (-)	ϕ' (-)	l_e, l_{Te}, l_{ϕ_e} (mm)	u' (m/s)	${\tau_{ig}}^0$ (ms)
1	805	15	0.45	-	1.25	0.83	1.5
2	933	15	0.45	-	1.25	0.83	1.5
3	805	-	0.45	0.05	1.25	0.83	1.5
4	933	-	0.45	0.05	1.25	0.83	1.5

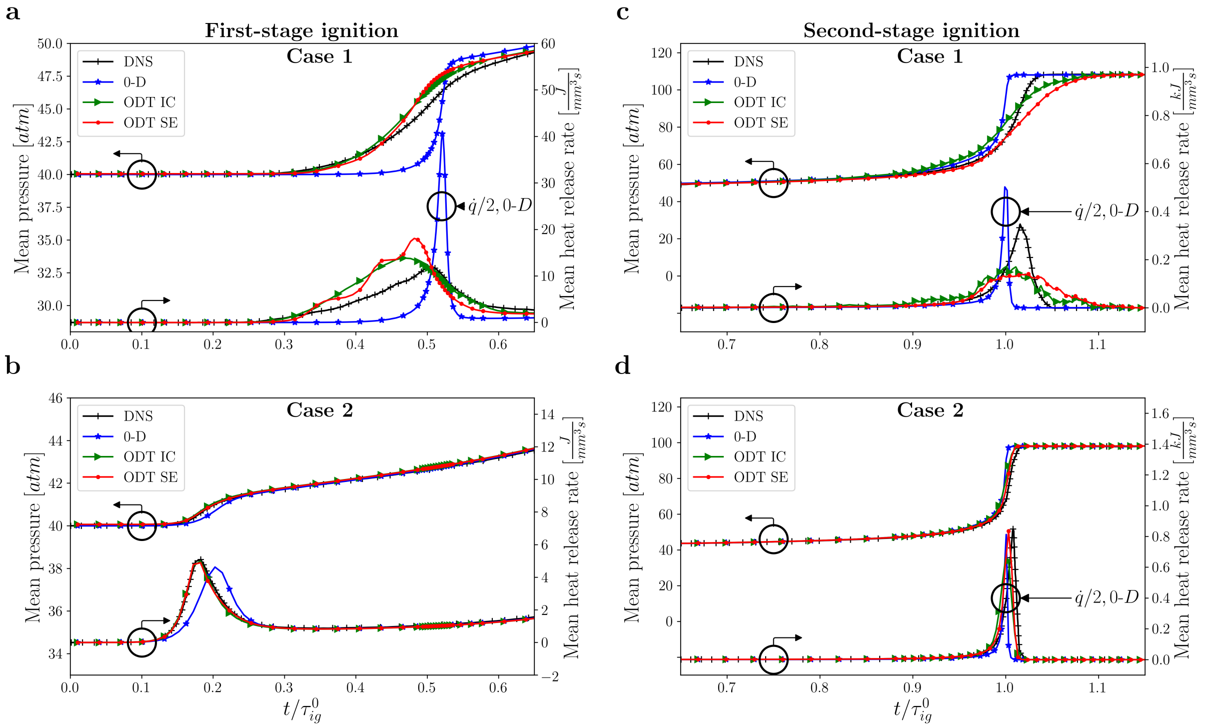

Figure 1: Temporal evolution of the spatially averaged pressure and heat release rate for case 1 and 2. These consider temperature inhomogeneities of $\boldsymbol{T' = 15}$ K at initial mean temperatures of $\boldsymbol{T_0 = 805}$ K (a and c) and $\boldsymbol{T_0 = 933}$ K (b and d).

temperature l_{Te}, composition $l_{\phi e}$ and velocity l_e are also presented, as well as the 0-D ignition delay time τ_{ig}^0, taken from Luong et al. (2015). The integral length scales are assumed to be equal to the most energetic length scales for the generation of the initial conditions. The initial pressure in the domain is $P_0 = 40$ atm, as in the DNS.

The chemistry for the n-heptane/air combustion is represented by a 58-species reduced kinematic mechanism from Yoo et al. (2011), as in the DNS. For the calculation of the thermodynamic and transport properties, the C++ interface of the Cantera software package is applied (Goodwin, 2002). During the reaction step of the splitting, the stiff chemistry is solved by means of CVODE (Hindmarsh and Serban, 2015) (the reaction component of the enthalpy is advanced simultaneously with an explicit Euler method).

ODT model parameters C and Z in Eq. (6) are taken as $C = 4$ and $Z = 0.4$. For this specific case, C represents the intensity of the turbulence in ODT, while Z is a proportionality parameter of order one for the energetic viscous penalty, as in Kerstein et al. (2001). These values were selected based on a calibration process of the model for one of the cases studied, and assumed constant for all simulations.

The initial mean temperature values of $T_0 = 805$ K and $T_0 = 933$ K were deliberately selected. The characteristic combustion behaviour of n-heptane/air mixtures with an equivalence ratio of $\phi_0 = 0.45$ leads to the same ignition delay time of $\tau_{ig}^0 = 1.5$ ms for $T_0 = 805$ K and $T_0 = 933$ K in the 0-D simulation (Luong et al., 2015).

Figure 1 shows the temporal evolution of the spatial and ensemble averaged ODT results for heat release rate and pressure. Results are shown for the first-stage ignition (left) and second-stage ignition (right). For comparison, 0-D and DNS data from Luong et al. (2015) are shown as well. The 0-D results served as a validation of the ODT code, since they were obtained by a homogeneous initialisation of the 1-D fields and by suppressing all possible eddy events. For a better visualisation, the 0-D values are sometimes shown with a normalisation factor of 0.5.

The distribution of the initial temperature and composition fields has a large influence on the combustion process and thus on the ignition delay time. This can be seen in Fig. 1, which considers random initialisations (ODT IC in the plots) and a sample size of $n = 100$ for every case detailed in Table 1.

Due to the stochastic nature of the ODT model, an evaluation of the influence of initial conditions and of the stochastic turbulent transport implementation was performed separately. In this context, an initial condition was

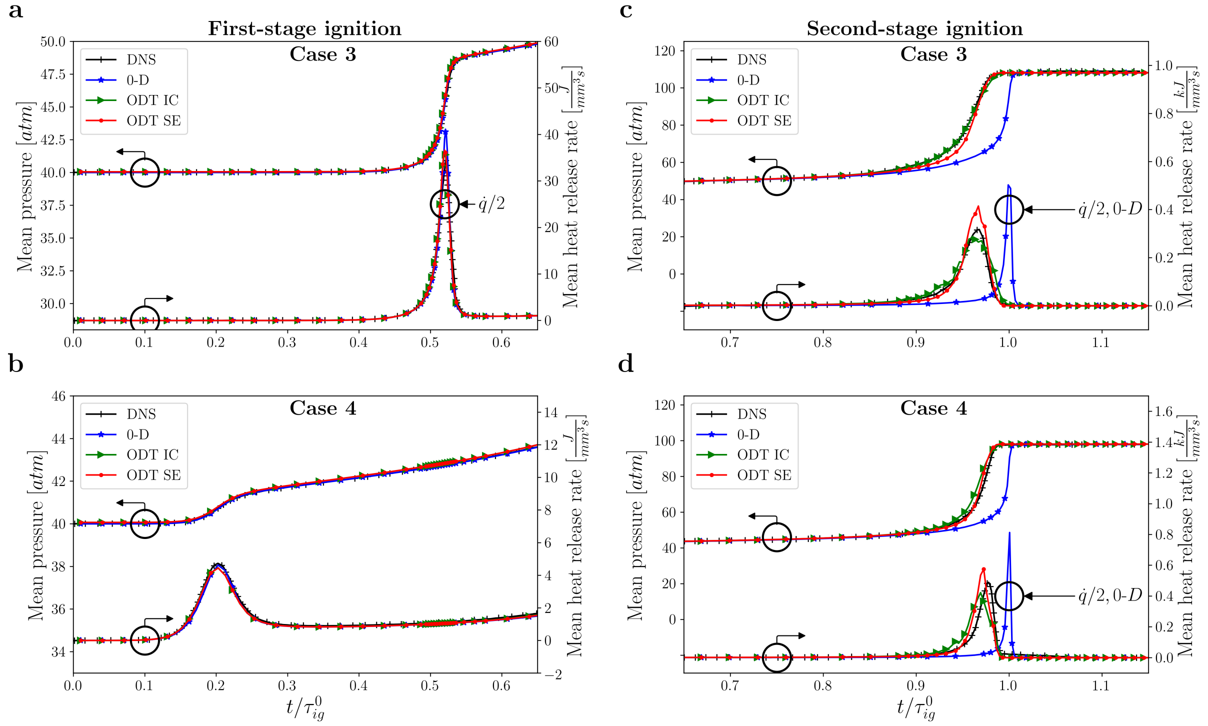

Figure 2: Temporal evolution of the spatially averaged pressure and heat release rate for case 3 and 4. These consider composition inhomogeneities of $\boldsymbol{\Phi' = 0.05}$ at initial mean temperatures of $\boldsymbol{T_0 = 805}$ K (a and c) and $\boldsymbol{T_0 = 933}$ K (b and d).

selected, which best suited the DNS data in temporal development of pressure and spatially averaged heat release rate. Several simulations were then performed and ensemble averaged. Despite the same initial conditions, the simulation results are still subject to fluctuations due to the stochastic eddy event implementation. This can also be seen in Fig. 1 (ODT SE in the plots).

In general, ODT is able to reproduce results that match the DNS data at the first and second-stage ignition. 0-D results from Luong et al. (2015) show that slight modifications in the initial mean temperature of $T_0 = 805$ K have a greater influence, in comparison to $T_0 = 933$ K, on the ignition delay time. This can be one possible reason for the wider spread of the dome of heat release rate and the less steep pressure rise of the ensemble averaged ODT results at case 1 (ODT IC, ODT SE) when comparing with DNS data. The temperature fluctuations cause a delay in combustion, whereby the pressure rise is mitigated. In case 2, initial temperature fluctuations have less influence on the combustion process. For the latter case, 0-D, ODT IC, ODT SE and DNS results have similar profiles.

Figure 2 also shows the temporal evolution of the spatially and ensemble averaged ODT results for heat release rate and pressure during first-stage ignition (left) and second-stage ignition (right). In contrast to Fig. 1, however, composition inhomogeneities of $\phi' = 0.05$ are examined. Again, ODT (ODT IC and SE) is able to produce results that are in very good agreement with the DNS trend. This applies to both the first-stage ignition and the second-stage ignition. ODT SE slightly overpredicts and ODT IC slightly underpredicts the DNS results at the moment of combustion in cases 3 and 4. The comparison with the 0-D simulations shows that the composition fluctuations lead to an earlier combustion for both investigated initial mean temperatures. The rapid pressure rise is only slightly mitigated by the composition fluctuations.

Overall, results obtained with ODT show a reasonable match with DNS data. The quality of the results is promising, considering the short simulation times and the reduced dimensionality application of this ODT model for constant volume combustion.

3.2 Open System (Jet Configuration)

The open system case is represented by a lifted methane/air jet flame in a vitiated hydrogen/air coflow. For comparison purposes, ODT simulations consider an equivalent setup and the same parameters as the experimental measurements of Cabra et al. (2005). Table 2 lists the initial conditions for the jet and coflow. Here, Re is the bulk Reynolds number based on d, the diameter, u is the velocity, T is the temperature and X the mole fraction of each species. For the initial velocity profile at the nozzle exit, a synthetic profile was used which was created by superposition of a fully developed turbulent channel flow mean profile with a turbulent Passot-Pouquet spectrum (Passot and Pouquet, 1987). The coflow was initialised with a uniform radial distribution of the velocity at $z/d = 0$ (nozzle exit), where z stands for downstream position (Eq. (16)) and d for the diameter of the jet.

Table 2: Initial conditions for the jet and coflow are listed.

-	Jet	Coflow
Re	$28,000$	$23,300$
d(mm)	4.57	140
u(m/s)	100	5.4
T(K)	320	1350
$X_{\mathrm{O_2}}$	0.15	0.12
$X_{\mathrm{N_2}}$	0.52	0.73
$X_{\mathrm{H_2O}}$	0.0029	0.15
X_{OH}(ppm)	0.0	200
$X_{\mathrm{H_2}}$(ppm)	100	100
$X_{\mathrm{CH_4}}$	0.33	0.0003

The ODT domain uses homogeneous Neumann boundary conditions and has a length of 140 mm, which is a span close to 30 jet diameters. Although the ODT formulation for open systems using a planar and temporal framework is not novel, the chosen configuration represents nonetheless a challenge for the model, given the delicate interactions and balance between the mixing of the hot coflow products and the cold unburned jet, together with the reaction and autoignition of the jet (Cabra et al., 2005).

For the representation of the methane/air chemistry, a 19-species reduced mechanism from Lu and Law (2008) is used. This mechanism is derived from a 30-species skeletal mechanism for methane/air based on the detailed GRIMech 3.0 mechanism (Smith et al., 1999).

Figure 3, on the left side, shows a two-dimensional rendering of the temperature evolution of the jet flame for one realisation. On the right side, an ensemble averaged temperature evolution of the jet flame is presented with a sample size of $n = 50$. Axis y/d corresponds to the one-dimensional domain, while axis z/d is obtained by means of the temporal-to-spatial translation, Eq.(16). The ODT model parameters were fixed to $C = 5$ and $Z = 50$. The ensemble averaged temperature evolution on the right side shows the familiar structure of a jet diffusion flame. This supports the validity of the assumption that the streamwise velocity associated with the chemically active region can be approximated by a bulk velocity, which is advecting the 1D-domain in downstream direction. The visually determined liftoff height of $z/d \approx 38$ in Figure 3 is in good agreement with the findings of Cabra et al. (2005).

In Figure 4, the concentration evolution of the OH-species is presented for a single realisation on the left side and an ensemble average on the right side. The comparison of the ensemble averaged temperature evolution in Figure 3 and OH-concentration evolution in Figure 4 shows that the highest OH-concentrations occur in the regions with the highest temperatures.

Figure 5 presents the Favre-averaged centerline profile of temperature and O_2 mass fraction for different values of the C model parameter. The averaging is based on 50 ensemble members for every case simulated with randomised initial profiles. A detailed previous study of the application of ODT for jet flames has been performed recently by Abdelsamie et al. (2017). Abdelsamie et al. showed that the model parameter C has a large influence on ignition prediction and scalar conditional means when comparing ODT results against DNS data.

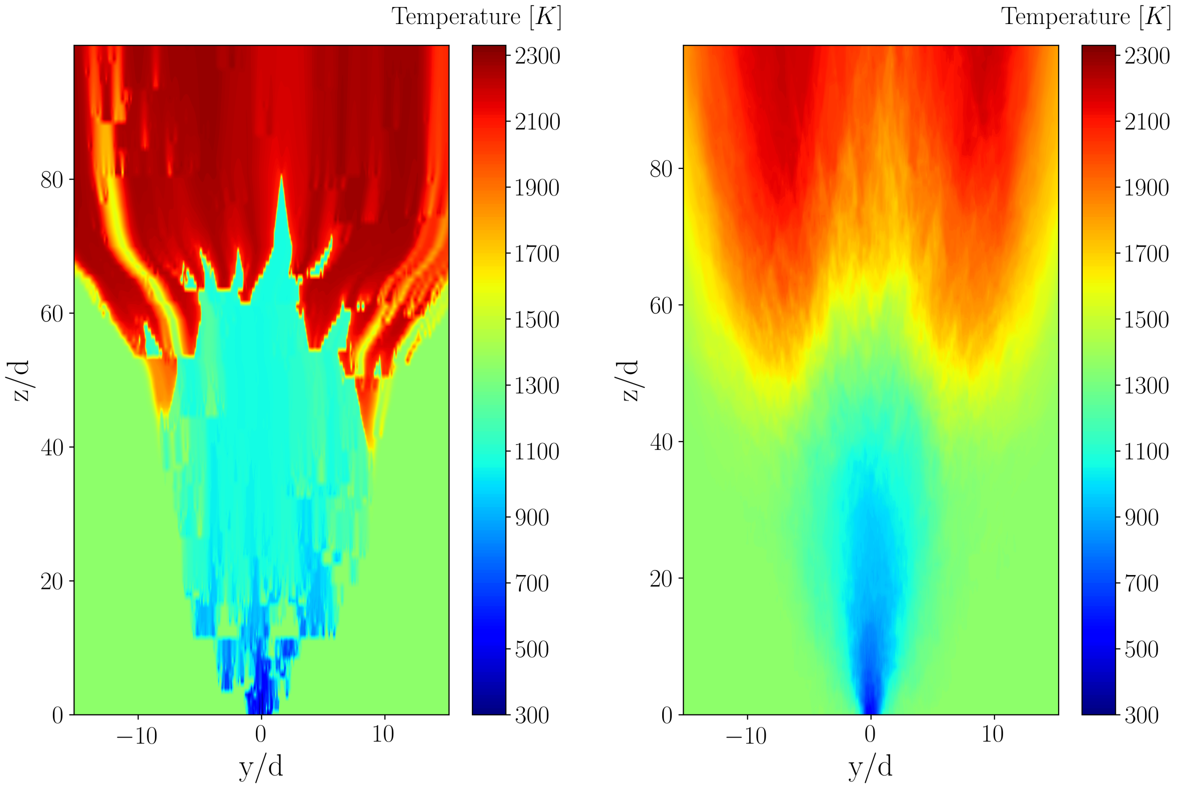

Figure 3: Two-dimensional rendering of temperature evolution for a single realisation (left) and ensemble average (right).

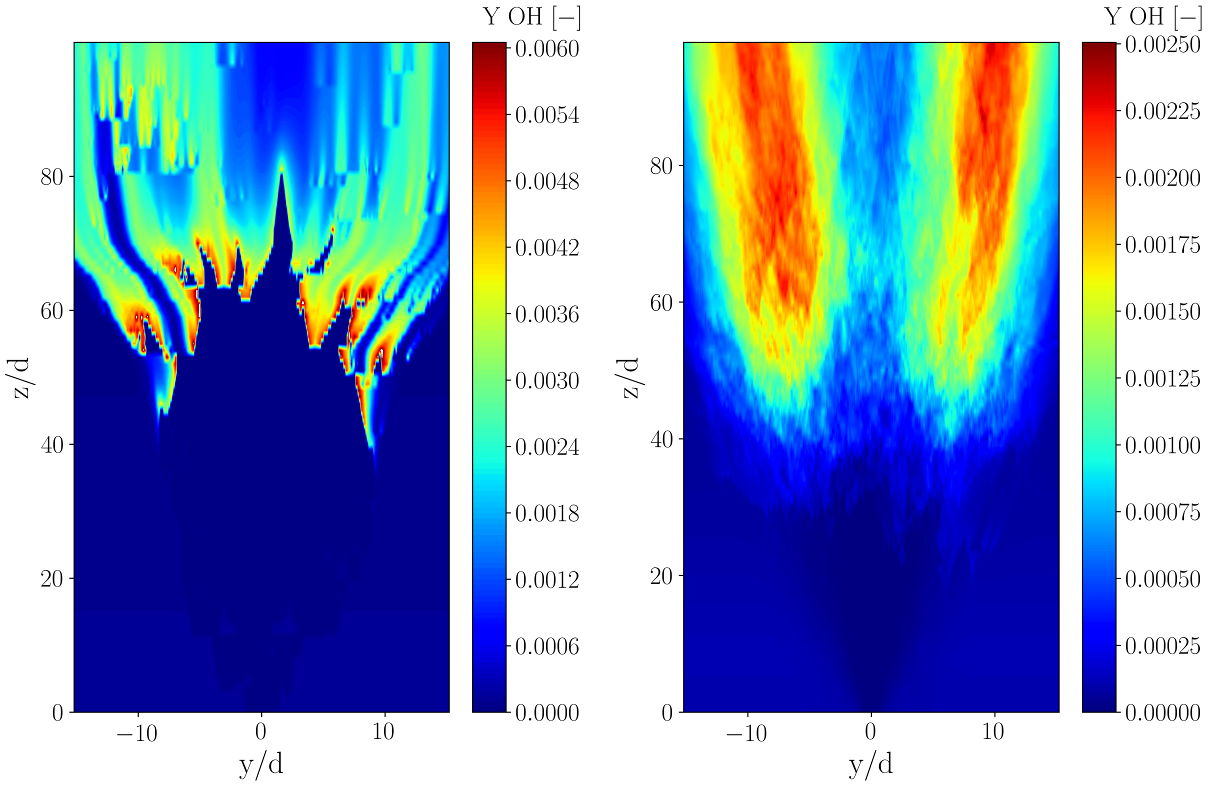

Figure 4: Two-dimensional rendering of OH-concentration evolution for a single realisation (left) and ensemble average (right).

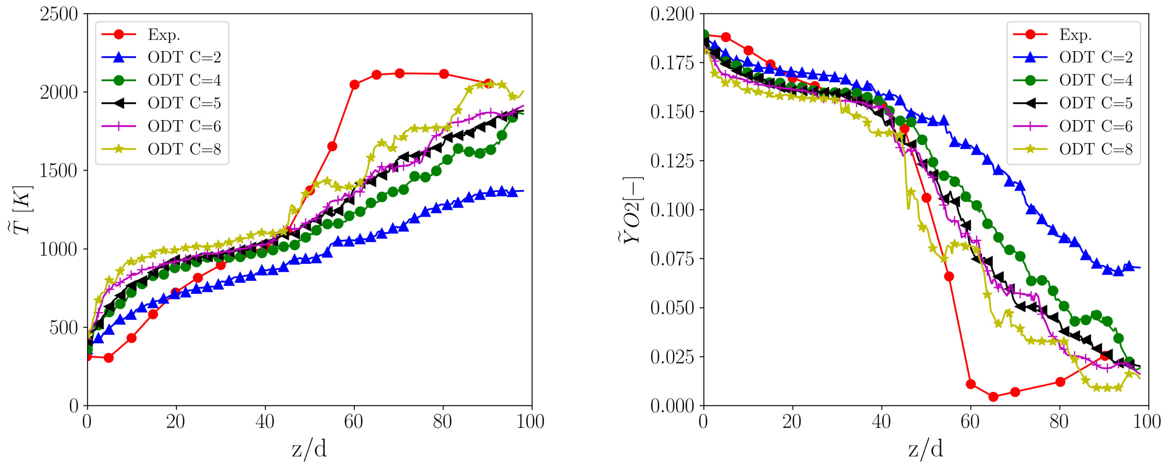

Figure 5: Comparison of simulated centerline profiles of Favre-averaged temperature (left) and Favre-averaged O_2 mass fraction (right) against experimental results (Exp.) of Cabra et al. (2005). For the ODT simulations, the model parameter C was varied.

Results shown in Figure 5 confirm the findings of Abdelsamie et al. (2017) for the C parameter. The initial stage (up to $z/d \approx 25$) characterised by mixing without reaction between jet and coflow is strongly affected by the C parameter. A high C parameter encourages the mixing and leads to a fast temperature increase at the centerline. This tends to accelerate the ignition. However, higher C parameters exaggerate the mixing in igniting zones and lead to a suppression of the ignition. In contrast, lower C parameters underestimate the mixing. The consequence of this is an insufficient mixing of the cold jet and hot coflow that results in a later ignition. A moderate C parameter of $C = 5$ and $Z = 50$ gave the best compromise for this study.

4 Conclusions

The application of ODT for simulations of a constant volume configuration and a jet is presented. The constant volume configuration is aimed at evaluating autoignition of a n-heptane/air mixture with initial temperature and composition inhomogeneities. The predicted heat release rates and pressure rises for all investigated cases are found to be in reasonable agreement with the DNS results, considering the reduced order of the model. The model is able to capture the key combustion characteristics of the examined n-heptane/air autoignition processes.

Despite the required number of ensemble members, which can be calculated in parallel following a Monte Carlo philosophy, simulation times for one ensemble member were in the order of 24 CPU-hours. These short computing times, in general, are one of the most attractive aspects of ODT. Although it is not done in detail in this work, parametric studies for different turbulent Reynolds number regimes and sensitivity analysis for reaction chemistry can be carried out with ODT, given the advantage of these short computing times. These investigations are currently not feasible with DNS due to the limitations in computing power (or only possible with great sacrifices in the reduction of chemical mechanisms). This makes ODT an efficient stand-alone model for constant volume configurations of reactive flows.

The second application of ODT is a lifted methane/air jet flame in a vitiated coflow. The spatially developing round jet flame is approximated by a planar temporally evolving jet. This assumption is not completely accurate and can be investigated in future work with a novel cylindrical ODT formulation from Lignell et al. (2018). Nonetheless, a good agreement was obtained in terms of centerline temperature evolution. The jet flame results reveal a strong influence of the C model parameter. The C parameter influences the mixing at the initial stage, which largely effects the entire combustion behaviour.

I Appendix

Numerical procedure for the constant volume configuration

In this appendix, we present additional details regarding the numerical advancement of the ODT equations already presented in Section 2. Both numerical methods used for the open and closed system have been previously explained in Lignell et al. (2013) and Medina M. et al. (2018). There are, however, some subtleties regarding the closed system implementation that may interest the reader. The reader is advised that the entire discussion in this appendix is focused on the numerical advancement of the ODT diffusion/reaction evolution equations presented in Section 2.2. The handling of the turbulent advection and eddy event implementation in Section 2.1 is out of the discussion, since the same strategy as in any previous ODT publication is applied.

Lignell et al. (2013) presented a Lagrangian ODT implementation using a Finite Volume Method (FVM) for combustion systems. Although this implementation is very appealing and fully conservative, it encounters theoretical obstacles for its application to closed systems. Especially, the compromise to displace the discrete volume interfaces in order to account for conservation of mass in the Lagrangian framework is challenging. This treatment conspires directly with the suppositions of a closed system with a fixed and constant volume. As noted in Lignell et al. (2013), a first order approximation of the continuity equation is,

$$\int_{\widehat{\Omega}} \rho \mathrm{d}V = 0 \rightarrow \rho_i \Delta y_i = Ci. \tag{18}$$

Here, $\widehat{\Omega}$ is a moving Lagrangian Control Volume (CV), ρ is the local density and Ci is a cell-wise constant. The volume elements in the 1-D domain are symbolised by the size of the discrete cells Δy_i. Eq. (18) allows the dilatation or contraction of the volume elements, and thus, of the overall Lagrangian system, in order to ensure conservation of mass. This equation conserves the mass of each cell, however, changes the volume of the cells. Summing up all volume elements results in a net volume change. This is done for open systems. This could also be applicable in closed systems with fixed volume, where mass and volume can both be conserved if a mean constant density is achieved. In such case, the calculation of the pressure that would satisfy Eq. (18) would be, in the opinion of the authors, iterative in its essence. Since the main purpose of ODT as a turbulence model is to facilitate access to turbulence states which cannot be reached by DNS, we opt to discard an iterative method for the advancement of the governing equations, and therefore choose a non-conservative formulation for the deterministic catch up of eddies in ODT. We explain this implementation in terms of Finite Difference (FD) equations, which are, in 1-D, conveniently equivalent to the discrete FVM representation.

Let us start the discussion defining the total time derivative for intensive quantities (ψ) in a Lagrangian system, $\mathrm{d}\psi/\mathrm{d}t = (\partial\psi/\partial t) + u_{tot,j}(\partial\psi/\partial x_j)$. Such a derivative is viewed in an Eulerian framework in terms of the partial rate of change and the advection of ψ. As discussed in Section 2.1, we can formally split the velocity $u_{tot,j}$ into its advective and dilatational part, in analogy to a Helmholtz decomposition. Neglecting the mean advection of the system, and considering turbulent advection only by the instantaneous eddy events in ODT, it is clear that the only effects that need to be incorporated in the total time derivative, besides the local Eulerian rate of change of ψ, are the dilatation effects by $u_{D,j} = u_D$. Due to our 1-D treatment, these dilatation effects are entirely given by the velocity divergence condition in Eq. (11). We can now relate the velocity divergence condition, and the velocity itself, to the Lagrangian interface displacement,

$$u_D = \frac{\mathrm{d}y}{\mathrm{d}t}. \tag{19}$$

Therefore, we can rewrite the divergence condition using a Central Difference Scheme (CDS) as,

$$\frac{\left.\frac{\mathrm{d}y}{\mathrm{d}t}\right|_{i+1/2} - \left.\frac{\mathrm{d}y}{\mathrm{d}t}\right|_{i-1/2}}{\Delta y_i} = -\frac{1}{\gamma_i P}\frac{\mathrm{d}P}{\mathrm{d}t} + \varPsi_i. \tag{20}$$

In order to formulate a consistent discretisation, both Left-Hand Side (LHS) and Right-Hand Side (RHS) must be frozen at the same time level. The RHS of Eq. (20) is that one of Eq. (11) and includes the time-derivative of the pressure $\mathrm{d}P/\mathrm{d}t$, which must also be calculated at the corresponding time level. Below, we list the algorithmic solution steps of the ODT equations for the closed system configuration.

1. Start with some initial conditions for the density ρ, pressure P, enthalpy h, composition Y_k and ODT velocities u_j.

2. Calculate the corresponding $\mathrm{d}P/\mathrm{d}t$ at the fixed volume initial state (integrating Eq. (11) in Section 2.2),

$$\frac{\mathrm{d}P}{\mathrm{d}t} = -\left[(u_{D,y=L} - u_{D,y=0}) - \int_{y=0}^{y=L} \Psi_i \mathrm{d}y\right] \frac{P}{\int_{y=0}^{y=L} \frac{1}{\gamma}\mathrm{d}y}. \tag{21}$$

3. Advance the local Eulerian rate of change for the chemistry (h, Y_k) and the kinematics (u_j). In this work, a Strang-Splitting method for the diffusion and reaction operators is used as in Medina M. et al. (2018). This is done in order to tackle stiff chemistry problems. In principle, a forward Euler time integration would also be possible.

4. Calculate the resulting pressure at the new thermochemical state. As suggested by Motheau and Abraham (2016), we use an integral expression for the pressure, which is derived from mass conservation and the condition of constant mean density in the system (Eq. (13) in Section 2.2). This is still a resulting pressure in an Eulerian reference frame, thus, the discrete cell volumes are still frozen at this point.

5. Calculate the resulting local density using the new pressure, by means of the ideal gas law.

6. Determine the displacement of the Lagrangian cell interfaces by Eq. (20). Note that $\mathrm{d}P/\mathrm{d}t$ must be recalculated here. In this case, by using a first-order approximation in time, the resulting cell volumes are given as

$$\Delta {y_i}^{n+1} = \Delta {y_i}^{n} + \Delta t \left[\Delta y^* \left(-\frac{1}{\gamma_i^* P^*}\frac{\mathrm{d}P^*}{\mathrm{d}t} + \Psi_i^*\right)\right]. \tag{22}$$

7. The last step conforms with a first-order Lie-Splitting treatment for the Lagrangian total time derivative; i.e. all local rates of change are first calculated on a fixed-volume basis (analogous to an Eulerian treatment), and afterwards, dilatation effects are taken into account at the end of the time-step. The star marker * in the RHS of Eq. (22) indicates the Eulerian state after the time advancement ($\Delta y^* = \Delta y^n$).

Although it would also be possible to calculate open systems with the above mentioned procedure considering $\mathrm{d}P/\mathrm{d}t = 0$, we use instead the fully conservative approach suggested by Lignell et al. (2013) in this work.

References

Abdelsamie, A.; Lignell, D.; Thévenin, D.: Comparison Between ODT and DNS for Ignition Occurrence in Turbulent Premixed Jet Combustion: Safety-Relevant Applications. *Zeitschrift fuer Physikalische Chemie*, 231(10), (2017), 1709–1735.

Ashurst, W.; Kerstein, A.: One-dimensional turbulence: Variable-density formulation and application to mixing layers. *Physics of Fluids*, 17(2), (2005), 025107 1–27.

Cabra, R.; Chen, J.-Y.; Dibble, R. W.; Karpetis, A. N.; Barlow, R. S.: Lifted methane-air jet flames in a vitiated coflow. *Combustion and Flame*, 143(4), (2005), 491–506.

Echekki, T.; Kerstein, A.; Dreeben, T.: One-Dimensional Turbulence Simulation of Turbulent Jet Diffusion Flames: Model Formulation and Illustrative Applications. *Combustion and Flame*, 125(3), (2001), 1083–1105.

Fragner, M.; Schmidt, H.: Investigating asymptotic suction boundary layers using a one-dimensional stochastic turbulence model. *Journal of Turbulence*, 18(10), (2017), 899–928.

Goodwin, D.: *Cantera C++ User's Guide*. California Institute of Technology (2002).

Hindmarsh, A.; Serban, R.: *User Documentation for CVODE v2.8.2 (SUNDIALS v2.6.2)*. Lawrence Livermore National Laboratory (2015).

Jozefik, Z.; Kerstein, A.; Schmidt, H.; Lyra, S.; Kolla, H.; Chen, J.: One-dimensional turbulence modeling of a turbulent counterflow flame with comparison to DNS. *Combustion and Flame*, 162(8), (2015), 2999–3015.

Kerstein, A.: One-dimensional turbulence: model formulation and application to homogeneous turbulence, shear flows, and buoyant stratified flows. *Journal of Fluid Mechanics*, 392, (1999), 277–334.

Kerstein, A.; Ashurst, W.; Wunsch, S.; Nilsen, V.: One-dimensional turbulence: Vector formulation and application to free-shear flows. *Journal of Fluid Mechanics*, 447, (2001), 85–109.

Lignell, D.; Kerstein, A.; Sun, G.; Monson, E.: Mesh adaption for efficient multiscale implementation of One-Dimensional Turbulence. *Theoretical and Computational Fluid Dynamics*, 27(3), (2013), 273–295.

Lignell, D.; Lansinger, V.; Medina M., J. A.; Klein, M.; Kerstein, A.; Schmidt, H.; Fistler, M.; Oevermann, M.: One-dimensional turbulence modeling for cylindrical and spherical flows: model formulation and application . *Theoretical and Computational Fluid Dynamics*, 32(4), (2018), 495–520.

Lu, T.; Law, C.: A criterion based on computational singular perturbation for the identification of quasi steady state species: A reduced mechanism for methane oxidation with NO chemistry . *Combustion and Flame*, 154(4), (2008), 761–774.

Luong, M.; Yu, G.; Lu, T.; Chung, S.; Yoo, C. S.: Direct numerical simulations of ignition of a lean n-heptane/air mixture with temperature and composition inhomogeneities relevant to HCCI and SCCI combustion. *Combustion and Flame*, 162(12), (2015), 4566–4585.

Lyons, K.: Towards an understanding of the stabilization mechanisms of lifted turbulent jet flames: Experiments. *Progress in Energy and Combustion Science*, 33(2), (2007), 211–231.

Medina M., J. A.; Schmidt, H.; Mauss, F.; Jozefik, Z.: Constant volume n-Heptane autoignition using One-Dimensional Turbulence. *Combustion and Flame*, 190, (2018), 388–401.

Motheau, E.; Abraham, J.: A high-order numerical algorithm for DNS of low-Mach-number reactive flows with detailed chemistry and quasi-spectral accuracy. *Journal of Computational Physics*, 313, (2016), 430–454.

Oevermann, M.; Schmidt, H.; Kerstein, A.: Investigation of autoignition under thermal stratification using linear eddy modeling. *Combustion and Flame*, 155(3), (2008), 370–379.

Passot, T.; Pouquet, A.: Numerical simulation of compressible homogeneous flows in the turbulent regime. *Journal of Fluid Mechanics*, 181, (1987), 441–466.

Smith, G. P.; Golden, D. M.; Frenklach, M.; Moriarty, N. W.; Eiteneer, B.; Goldenberg, M.; Bowman, C. T.; Hanson, R. K.; Song, S.; Gardiner, W. C.; Lissianski, V. V.; Qin, Z.: *GRI-MECH 3.0*. `http://www.me.berkeley.edu/gri_mech/` (1999).

Yoo, C. S.; Lu, T.; Chen, J.; Law, C.: Direct numerical simulations of ignition of a lean n-heptane/air mixture with temperature inhomogeneities at constant volume: Parametric study. *Combustion and Flame*, 158(9), (2011), 1727–1741.

Yu, R.; Bai, X.: Direct numerical simulation of lean hydrogen/air auto-ignition in a constant volume enclosure. *Combustion and Flame*, 160(9), (2013), 1706–1716.

Address: Chair of Numerical Fluid Mechanics and Gas Dynamics, Faculty of Mechanical Engineering, Brandenburg University of Technology Cottbus-Senftenberg, Siemens-Halske-Ring 14, 03046 Cottbus, Germany
email: `Tommy.Starick@b-tu.de`

TECHNISCHE MECHANIK

Scientific Journal for Fundamentals and Applications of Engineering Mechanics
Wissenschaftliche Zeitschrift für Grundlagen und Anwendungen der Technischen Mechanik

Instructions for Authors

TECHNISCHE MECHANIK publishes articles in all fields of mechanics, theoretical as well as applied, including related disciplines, and in particular also articles demonstrating practical applications. The journal publishes full length papers, as well as discussions on papers which have appeared in the journal.
TECHNISCHE MECHANIK is a non-profit (open-access) journal, founded by the Otto-von-Guericke-University. It can be freely downloaded from the website.

Manuscripts have to be written with LaTeX. The most important features of the style guidelines are implemented in the files contained in **tm-article.zip** (download from http://www.ovgu.de/techmech/).

Each submitted paper runs through a standard peer review process. Please suggest three international well known reviewers for your paper when you submit it.

Please submit your paper in electronic form by email.

Hinweise für Autoren

Die Zeitschrift TECHNISCHE MECHANIK veröffentlicht Forschungsarbeiten aus dem Gesamtgebiet der Mechanik, d. h. allen Zweigen der theoretischen und angewandten Mechanik einschließlich angrenzender Fachgebiete sowie Diskussionsbeiträge zu in dieser Zeitschrift erschienenen Arbeiten. Die Zeitschrift ist ein open-access Journal das 1980 von der Otto-von-Guericke-Universität gegründet wurde. Alle Artikel können kostenfrei von unserer Webseite herunter geladen werden.

Artikel werden ausschließlich in englischer Sprache veröffentlicht.

Die Manuskripte müssen in LaTeX geschrieben werden. Die wichtigsten Stil-Richtlinien sind in den Dateien umgesetzt, die in **tm-article.zip** (bereit gestellt unter http://www.ovgu.de/techmech/) enthalten sind.

Jeder eingereichte Beitrag durchläuft einen standardmäßigen Begutachtungsprozess. Bitte schlagen Sie bei Einreichung des Artikels drei mögliche, international renommierte Gutachter vor.

Bitte reichen Sie Ihren Beitrag elektronisch per E-Mail ein.

Internetadresse / website	http://www.ovgu.de/techmech
E-Mail / email	Technische.Mechanik@ovgu.de

Address of the editor:
Institut für Mechanik
Otto-von-Guericke-Universität
Postfach 4120

D-39016 Magdeburg

Tel.: +49-391-67-52459
Sekretariat -58608
Fax: +49-391-67-12439
-12863
e-mail: Technische.Mechanik@ovgu.de
http://www.ovgu.de/techmech/

Inhalt / Contents

ISSN 0232-3869 (print)
ISSN 2199-9244 (online)